Searching for extra-solar planets with the transit method

Johannes Koppenhöfer

Searching for extra-solar planets with the transit method

Dissertation

an der
Ludwig–Maximilians–Universität (LMU) München

Ph.D. Thesis

at the
Ludwig–Maximilians–University (LMU) Munich

submitted by

Johannes Koppenhöfer

born on 10th August 1977 in Bretten

Munich, March 27th 2009

1st Evaluator: Priv. Doz. Dr. Roberto P. Saglia
2nd Evaluator: Prof. Dr. Harald Lesch

Date of the oral exam: July 2nd 2009

Contents

List of Figures

List of Tables

Zusammenfassung

Die Suche nach extra-solaren Planeten hat in den letzten Jahren einen enormen Aufschwung erlebt. So ist die Zahl der gefundenen Planeten bereits auf 331 angewachsen (Stand: 20.3.2009). Beinahe wöchentlich werden neue Detektionen bekanntgegeben. Nicht zuletzt das starke öffentliche Interesse motiviert immer mehr Astronomen, neue Beobachtungsprojekte zu starten und sich an der Planeten-Suche zu beteiligen.

Direktes Abbilden von extra-solaren Planeten ist extrem schwierig, da in den meisten Fällen der Mutterstern den Planeten um Grössenordnungen überstrahlt. Zusätzlich ist aufgrund der großen interstellaren Entfernungen der scheinbare Abstand von Stern und Planet sehr klein, was ein direktes Abbilden erschwert. Es wird deshalb eine Vielzahl von indirekten Methoden angewandt, um extra-solare Planeten zu finden. Eine Sonderstellung hat dabei die Transit-Methode, bei der die Helligkeit eines Sterns auf periodische Schwankungen untersucht wird, die von einem vor dem Stern vorbeiziehenden Begleiter verursacht werden. Solche Transit-Planeten haben den Vorteil, dass aus der Messung des Helligkeitsabfalls während der Bedeckung ihr Radius und damit auch die Dichte bestimmt werden kann. Transit-Planeten erlauben außerdem einen Einblick in die Zusammensetzung ihrer Atmosphäre. Auf der Suche nach erdähnlichen Planeten oder gar nach Hinweisen auf Leben außerhalb des Sonnensystems sind Transit-Planeten deshalb die vielversprechendsten Ziele. Daran anknüpfend thematisiert die vorliegende Arbeit verschiedene Aspekte der Suche nach extra-solaren Planeten mit der Transit-Methode.

Im einleitenden ersten Kapitel werden die erfolgreichsten Methoden der Suche nach extra-solaren Planeten vorgestellt. Außerdem werden die für die folgenden Kapitel erforderlichen Formalismen zusammengefasst.

Das zweite Kapitel behandelt das pre-OmegaTranS-Projekt, eine photometrische Suchkampagne am 2.2m-Teleskop in LaSilla/Chile. Das Ziel dieses Projekts ist die Identifikation neuer Transit-Planeten. Insgesamt wurden dazu 16000 Sterne auf periodische, für Transit-Planeten charakteristische Helligkeitsschwankungen untersucht. Vier Kandidaten wurden gefunden, von denen einer (POTS-C1b) sehr aussichtsreich ist. Es handelt sich dabei um einen Begleiter eines massearmen Hauptreihen-Sterns, der die Größe von Jupiter besitzt. Alle Indizien weisen auf eine tatsächliche planetare Natur des Kandidaten hin. Derzeit laufen Vorbereitungen zu dessen Bestätigung mit Hilfe von photometrische und spektroskopische Nachbeobachtungen.

Kapitel 3 beschreibt einen solchen Prozess der Bestätigung eines Transit-Kandidaten am Beispiel von OGLE2-TR-L9. Mit Hilfe von spektroskopischen Nachbeobachtungen konnte die Masse des Kandidaten auf 4.5 Jupiter-Massen bestimmt werden. Zusätzliche photometrische Nachbeobachtungen lassen keinen Zweifel an der planetaren Natur des Kandidaten. OGLE2-TR-L9 ist mit einem Radius von 1.6 Jupiter-Radien größer als von Planeten-Aufbau-Modellen erwartet. Diverse Mechanismen wurden vorgeschlagen, um diese Beobachtung zu erklären, die bereits an einer Reihe von anderen

Transit-Planeten gemacht wurde. Im Vergleich zu den 56 anderen bisher gefundenen Transit-Planeten umkreist OGLE2-TR-L9 den heißesten und am schnellsten rotierenden Stern.

In diesem Jahr wird Pan-Planets, ein Transit-Projekt am PanSTARRS-Teleskop des Haleakala-Observatoriums auf Hawaii beginnen. Das Teleskop ist ausgerüstet mit der größten CCD Kamera, die bisher gebaut wurde. Mit jeder Aufnahme werden sieben Quadratgrad auf 1,4 Milliarden Pixeln abgebildet. Im Rahmen dieser Arbeit wurden detaillierte Simulationen durchgeführt, um die Beobachtungsstrategie von Pan-Planets zu optimieren und die Anzahl der Planeten zu bestimmen, die gefunden werden können (Kapitel 4). Dabei wurde festgestellt, dass bei vorgegebener Beobachtungszeit, eine hohe Anzahl von Feldern zu mehr Detektionen führt. Außerdem werden kurze Beobachtungsblöcke von 1h gegenüber 3h pro Nacht bevorzugt. Gemäß den Simulationen können im ersten Jahr insgesamt 25 Planeten der Größe von Jupiter gefunden werden. Pan-Planets ist damit eines der aussichtsreichsten Transit-Projekte in der naheliegenden Zukunft.

Die in dieser Arbeit erlangten Erfahrungen auf dem Gebiet der Transit-Suche sind sehr wichtig für alle zukünftigen Planeten-Projekte an der Universitäts-Sternwarte der LMU. Zahlreiche Kollaborationen wurden bereits iniziiert, um in Zukunft in gesteigertem Maße an der Detektion und Charakterisierung von extra-solaren Planeten teilzuhaben.

Chapter 1

Introduction

In the Solar System we know eight planets. The four rocky planets Mercury, Venus, Earth and Mars are orbiting the Sun in the inner region whereas the more massive gaseous planets Jupiter, Saturn, Uranus and Neptune are located in the outer region. All orbits are coplanar ($\Delta i \leq 4°$) and have very low eccentricities. For a very long time, the Solar System was the only known planetary system. One could therefore only speculate about the existence or frequency of extra-solar planets:

- "There cannot be more worlds than one!" (Aristoteles, 384-322 B.C.)

- "There are infinite worlds, both unlike and like this world of ours (...) we have to think of living creatures in all of these worlds." (Epikur 341-270 B.C.)

- "Innumerable suns exist. Innumerable earths revolve around these - Living beings inhabit these worlds." (Giordano Bruno 1548-1600)

The situation changed with the discovery of the first extra-solar planets in the 90s of the last century. Astronomers found planetary systems that are very different from the Solar System. Highly eccentric orbits, gaseous planets in close-in orbits (so called "Hot Jupiters") and, last but not least, the large number of planets had a high impact on the development of better planet formation and evolution theories. The discoveries have helped us to get a better understanding of the history of the Solar System although many puzzles still remain unsolved.

In §1.1 we provide a definition for an extra-solar planet. We outline the theory of planet formation in §1.2. Methods that are use for the detection of extra-solar planets are introduced in §1.3. We focus on the radial velocity and transit methods that are used in this work. In §1.4 we review the current status of extra-solar planet searches. §1.5 explains follow-up strategies that need to be done in order to confirm candidates that were detected with the transit method. The large variety of detailed follow-up studies that can be done for transiting planets are presented in §1.6. Finally, we adress the questions of whether extra-solar planets could be places for the development of life (§1.7) and what this means for our own place in the big picture of the universe.

1.1   Definition: Planet

In 2006 the International Astronomical Union (IAU) defined that in our Solar-System a planet is a celestial body that...

- ...is in orbit around the Sun, ...

- ...has sufficient mass for its self-gravity to overcome rigid body forces so that it assumes a hydrostatic equilibrium (nearly round) shape, and...

- ...has cleared the neighborhood around its orbit (IAU, 2006).

As a result of this definition, Pluto was no longer a planet. Because it has not cleared the surrounding area of its orbit, Pluto is now considered to form a new class of dwarf planets together with Ceres.

For extra-solar planets a similar definition is applied although the exoplanet, of course, does not orbit the Sun but any other star in the Universe. ”Free-floating planets” which do not orbit any star are also being discussed[1].

In addition to the three criteria above, an extra-solar planet must satisfy a fourth one that limits its mass to about 13 M_{Jup} and discriminates it from a Brown Dwarf. Brown Dwarfs do fusion of Deuterium, where a Deuterium particle and a proton unite to form a ^{3}He particle (Chabrier *et al.*, 2000)[2]. Above 65 M_{Jup} and core temperatures of about 2 million Kelvin the fusion of Lithium starts. The transition from Brown Dwarfs to H-burning main-sequence stars is at around 75-80 M_{Jup}.

The naming convention for extra-solar planets is such that the fist planet detected in a system gets the suffix 'b', the second 'c', and so on. E.g. the name of the first planet found in the 51 Peg system is 51 Peg b.

1.2   Planet Formation Theory

The theory of planet formation has changed a lot in the last decade. On the one hand, driven by the increasing number of extra-solar planet detections, on the other hand, due to an advance in computer technology that has enabled more and more precise simulations. However, many aspects of planet formation are still not understood and heavily under debate.

The formation of planets is strongly coupled to the process of star formation which starts with a collapsing molecular cloud. At the end of the fragmentation process, the gas forms disks around the young proto-stars due to angular momentum conservation. For Solar metallicity, a proto-planetary disk is assumed to carry ∼1% of heavy elements (dust grains and condensed elements). Fig. 1.1 shows two proto-planetary disks that were observed with the Hubble-Space-Telescope in the Orion nebula. The absorption by the dust in the disks is clearly visible against the bright background.

In the beginning, the dust is uniformly distributed and strongly coupled to the gas in the disk. Planet formation theories have to describe the growth of small dust particles with sizes of a few μm to planets with diameters of more than 100 000 kilometers, a growth of 14 orders of magnitude in size and 42 orders of magnitude in mass!

---

[1] in the early stages of formation, planets could be ejected out of their systems due to gravitational interactions with other planets; note, however, that such free-floating planets are very difficult to detect (see below)
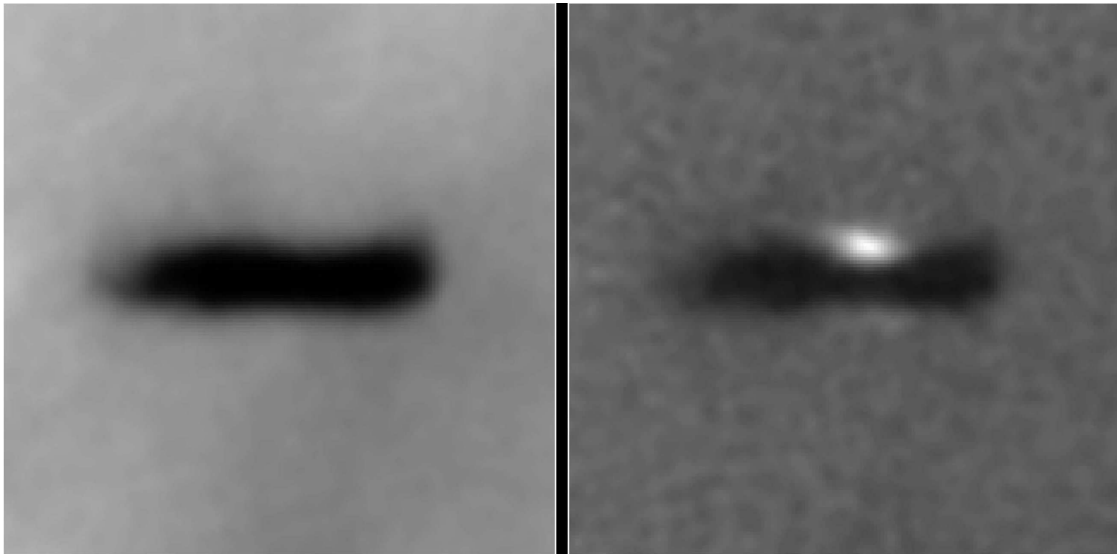
Figure 1.1: Proto-planetary disks in the Orion nebula.

Currently, two main processes of planet formation are being discussed, the core-accretion/gas-capture (GCCA) model (Pollack *et al.*, 1996; Ruden, 1999) and the disk instability (DI) mechanism (Boss, 1997) which will be discussed in the following.

1.2.1 The core-accretion/gas-capture model

As the name suggests, the CAGC model describes the formation of planets in two steps. In the core-accretion phase, the sticky dust grains grow in two body collisions and settle to a thin layer in the midplane of the disk. Ongoing collisions lead to further growth up to bodies of the size of about 1km - which are called planetesimals. This phase is comparatively short and happens on timescales of a few thousand rotation periods of the disk.

Planetesimals are big enough to decouple from the surrounding gas, therefore they move approximately with Keplerian speed on circular orbits around the proto-star. Due to inelastic collisions, the planetesimals grow further. The focusing effect of gravity is increasing the collision cross section (Safronov, 1972). The bigger the planetesimal is, the stronger it attracts smaller neighboring planetesimals and the faster it grows. This accelerated process is called runaway growth. After about 10^6 years (Aarseth *et al.*, 1993; Weidenschilling *et al.*, 1997), only the biggest bodies are left: rocky planetary cores, that comprise most of the heavy elements of the disk.

In the second phase of the CAGC model, the still growing rocky proto-planets find themselves in a dissolving gaseous disk. When a planetary core reaches about 10 Earth masses, its gravitational force is strong enough to bind Hydrogen and the rocky core begins to attract gas from the surrounding disk. This process starts slowly and becomes very efficient as soon as the mass of the gaseous envelope is comparable to the mass of the core. The core-accretion phase ends when the disk is cleared by either the accretion process itself or the increasing luminosity of the proto-star in the center that dissolves the gas.

The CAGC model explains well the observed increase of planet frequency with metallicity (Fischer & Valenti (2005), see below). A higher metallicity implies a larger amount of dust particles which can form planetary cores more easily. Also the composition of Jupiter and Saturn with cores between 10 and 20 Earth masses (Saumon & Guillot, 2004; Militzer *et al.*, 2008) is consistent with the CAGC model. However, there is one big problem which is the time scale. Observations show, that the characteristic lifetime of a proto-planetary disk is only a few 10^6 years (Haisch *et al.*, 2001). After that, no gas is left that could be accreted by the planetary cores. According to the CAGC model, the main core-accretion phase and the early gas-capture take substantially longer than 10^7 years.

One explanation could be that the core-accretion process is speeded-up by vortices in the disk that form due to perturbations generated by infall onto the disk (Barranco & Marcus, 2000) or due to hydrodynamic instabilities (Lovelace *et al.*, 1999; Klahr & Bodenheimer, 2003).

1.2.2 The disk instability model

An alternative model for the formation of gaseous planets is the disk instability (DI) model which has been proposed by Kuiper (1951) and reviewed by Boss (1997). A proto-stellar disk becomes unstable against perturbations if the following parameter (Toomre, 1964) is of order unity or less:

$$Q = c_s \kappa / \pi G \Sigma \tag{1.1}$$

where c_s is the local speed of sound, κ is the epicyclic frequency at which a fluid element oscillates when perturbed from circular motion and Σ is the surface density. If, in addition, the cooling time scale of the disk is shorter than the orbital time scale, fragmentation of the disk into planets is possible (Gammie, 2001). Both requirements indicate that the DI mechanism is favored only at relatively large distances from the star.

Detailed 3-dimensional hydrodynamic simulations were carried out by several groups (e.g. Boss (2002), Mejía *et al.* (2003) or Mayer *et al.* (2002)). The results have shown, that the DI mechanism is able to form planets on a very short time scale on the order of $1\,000$ years. However, the amount of mass needed is at the high end of the observed range of disk masses (Bodenheimer, 2004).

Boley (2009) concludes that DI is the most likely mechanism responsible for the formation of planets in orbits wider that 100 AU whereas the CAGC model better explains the formation of planets in orbits closer than 100 AU.

1.2.3 Orbital evolution of extra-solar planets

Although the CAGC and DI model can explain the formation of rocky and gaseous planets, the distribution of orbital parameters of extra-solar planets brought up several questions which have been adressed by orbital evolution models that include planet-planet and planet-disk interactions.

The formation of close-in Jupiter-sized planets with periods of a few days that were detected with the radial velocity and transit method (see below) cannot be explained by the CAGC or DI models. At small distances from the star, the disk is too hot and the amount of gas available is not sufficient to build Jupiter-sized planets. Hot Jupiters must have formed further out in the proto-planetary disk and then migrated inwards due to planet-disk interactions (Ward, 1997).

Type I migration

Already during the core-accretion phase, a proto-planet excites density waves in a disk through Lindblad and corotation resonances. As a reaction, it experiences a torque by each excited wave (Goldreich & Tremaine, 1979). Lindblad resonances, located interior to the planet, result in positive torques while outer Lindblad resonances exert negative torques. A non-zero net torque from both sides causes a radial orbital migration of the planet, known as type I migration (Tanaka *et al.*, 2002). The time scale of this process is very short ($\sim 10^5$ years) causing the planet to eventually move into the star before it could start capturing the surrounding gas (Korycansky & Pollack, 1993). To avoid this, some mechanism must be responsible for stopping or at least slowing down the inward migration.
Nelson (2005) argues that in a turbulent disc migration occurs stochastically with inwards and outwards phases which could decelerate the migration. Also departures from the linear regime for planets with masses of $\sim$10-20 M_{Earth} could reduce the inward migration (Masset *et al.*, 2006). Recent studies have shown that including non-isothermal effects in the simulations can also stop type I migration and even result in an outward migration (Paardekooper & Mellema, 2006; Kley & Crida, 2008).

Type II migration

After the planet has reached a mass of about 1 M_{Jup}, it can induce the formation of a gap in the disk. The orbital evolution of the planet is then strongly coupled to the viscous evolution of the disk in which the outward angular momentum transfer continues. The planet takes up the momentum flow from the inner disk and releases it to the outer disk. If the two processes do not balance, the planet migrates inwards and essentially follows the material of the inner disk as it evolves towards the star (Lin *et al.*, 1996; Papaloizou *et al.*, 2007). Fig. 1.2 shows the time evolution of a Jupiter-sized planet as it evolves towards the star under type II migration.
Type II migration is generally used to explain the location of Hot Jupiters. However, as in the case of type I migration, it remains to be explained which process is halting the orbital decay of the planet to avoid the planet to fall into the star. Several mechanisms have been proposed such as tidal interaction with the star and interaction with the stellar magnetosphere (Lin *et al.*, 1996) or mass-loss of the planet overflowing its Roche-lobe due to the strong heating caused by irradiation (Trilling *et al.*, 1998).
However, extra-solar planets were found at a large range of semi-major axes (see below) which suggests, that type II migration has to stop not only very close to the star but also at larger separations. A possible explanation could be the dissipation of the disk during the migration process (Trilling *et al.*, 2002). Alternatively, the planets that we observe today might only be the last of a larger number of planets that have been formed in the proto-stellar disk and subsequently migrated into the star (the last of the Mohicans principle, Lin (1997)).
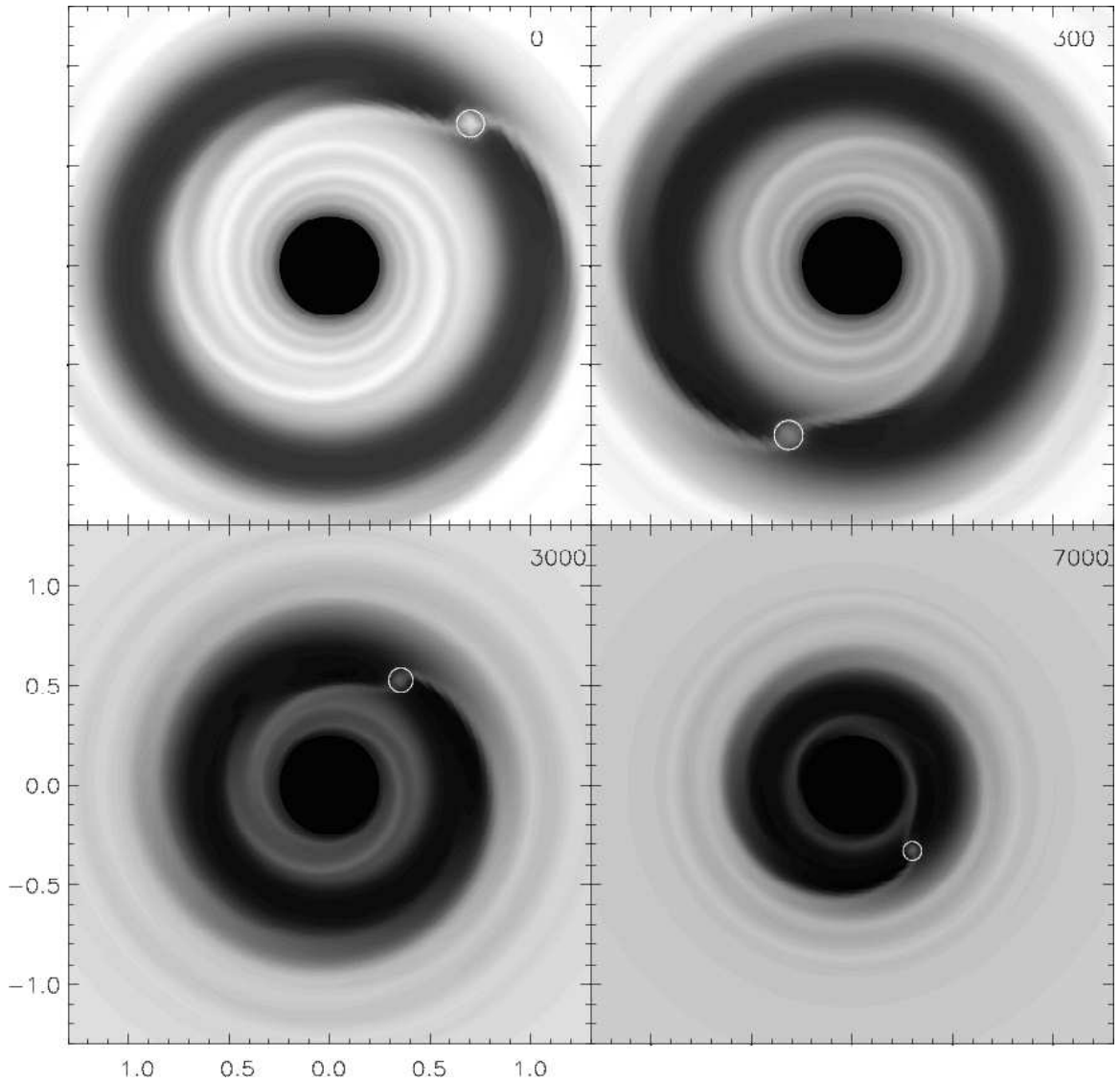
Figure 1.2: Time evolution in units of orbital periods of the disk surface density and orbital radius a gap-forming planet with initial mass of 1 M$_{Jup}$ (taken from Nelson *et al.* (2000)). After 7 000 revolutions, the planets mass has grown to 3.5 M$_{Jup}$ under the assumption of maximal accretion. The circle around the planets indicates its Roche-lobe.

Type III migration

A third migration mechanism is being discussed which is induced by coorbital torques exerted on the planet by material flowing through the orbit. Type III migration can assist or retard type II migration (Masset & Papaloizou, 2003; Artymowicz, 2004).

Orbital circularization and tidal locking

Strong tidal interaction with the central star circularize the orbits of close-in planets. Matsumura *et al.* (2008) found the median eccentricity of all planets with semi-major axes smaller than 0.1 AU to be as low as 0.013. From the nearly-circular orbits they conclude, that tidal circularization occurs on a relatively short time scale.

When a migrating planet approaches the host star, its rotation is slowed down due to the tidal interactions. This effect is a strong function of the planet-star separation ($\sim r^{-6}$, Goldreich & Soter (1966)) and leads to a synchronous rotation[3]. A direct consequence of the tidal-locking is a temperature gradient between day- and night-side of the planet. However, Knutson *et al.* (2007) derived a temperature map of the transiting planet HD189733b with a minimum temperature of 973 ± 33 K and a maximum temperature of 1212 ± 11 K indicating that energy from the irradiated day-side is efficiently redistributed throughout the atmosphere (see §1.6).

The reduced rotation rate has also severe implications for the planetary magnetic moment (due to a weaker dynamo-effect). Tidally locked planets are assumed to have comparatively weak magnetic fields and small magnetospheres which in turn can cause an enhanced particle loss (Grießmeier *et al.*, 2004).

Resonant orbits

In multi-planet systems, the orbital parameters are changing in time due to mutual gravitational interactions. Already during the core-accretion phase, elastic scattering leads to a transfer of angular momentum between proto-planets (Levison *et al.*, 1998). In the later stages, the interaction is driven by the migration of giant planets. In an extreme case close encounters could even cause planets to be ejected from the system.

Planet-disk interaction and orbital migration can trap planets in resonant orbits (Snellgrove *et al.*, 2001; Kley *et al.*, 2004). Several systems of this type were found such as the 2:1 resonant planets around Gliese 876 (Marcy *et al.*, 2001) or the 3:1 resonant planets around 55 Cancri (McArthur *et al.*, 2004).

Planet-planet interaction can also explain the eccentricity distribution of extra-solar planets detected with the radial velocity method (see below) showing that stable highly eccentric orbits are a possible outcome of long-term dynamical evolution (Ford *et al.*, 2003; Jurić & Tremaine, 2008).

1.3 The Search For Extra-Solar Planets

Many different techniques are used to search for extra-solar planets. Fig. 1.3 shows a diagram of various methods indicating the minimum planetary mass each method is sensitive to. The graph is taken from Perryman (2000) and has been updated.

In this chapter, we discuss the most successful planet detection methods in detail putting emphasis on the radial velocity and transit techniques that are used in this work.

---

[3] e.g. the Moon performs a synchronous rotation with respect to the Earth
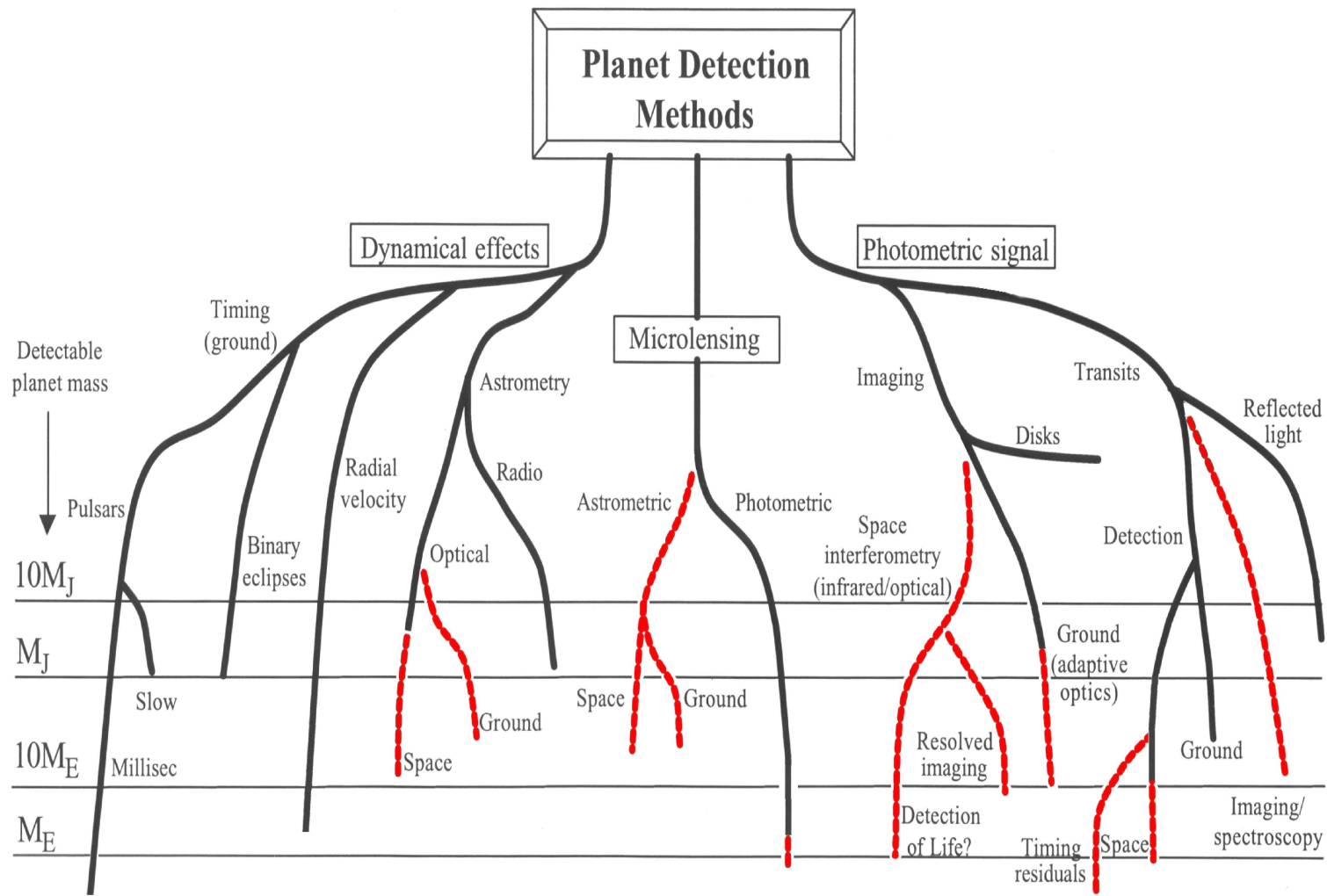
Figure 1.3: Overview of extra-solar planet detection methods.

1.3.1 Imaging

Direct detection of extra-solar planets is extremely difficult. Due to the large interstellar distances, the angular separation of an extra-solar planet and its host star is very small. In addition, an enormous brightness contrast complicates the detection. In the visual wavelength range the cool planet has very little thermal emission and we only see the light of the star that is reflected on the planet's surface. E.g. for Jupiter and Sun, the brightness contrast in the is on the order of 10^{-9}. In the infrared the brightness contrast decreases to $\sim 10^{-4}$, because in this spectral region the planet shines brighter (due to thermal emission) and the star is fainter.

In regular ground-based observations, the turbulent atmosphere of the Earth results into a broad distribution of a star's light on the detector (known as point-spread-function or PSF). Due to the small angular distance and the high brightness contrast, the star completely outshines its companion. In order to make the faint and close planet visible, adaptive optics have to be used to enhance the resolution of an image. A very powerful instrument in this respect is NACO[4] (Lenzen *et al.*, 2003; Rousset *et al.*, 2003) mounted on the VLT which has been successfully used to image several planet candidates.

Until today, 11 objects in the transition region between planets and Brown Dwarfs have been found with direct imaging. Proving that each star and its companion form a common proper motion pair, it has been ruled out that the faint planet candidates are actually background sources. In Fig. 1.4 we show the images of four planet candidates. Table 1.1 lists the parameters of all candidates found so far. The mass of each candidate can only be determined from its spectrum and brightness using evolutionary models. The problem with this method is that applying different models results in a large range of possible masses. Therefore, the real nature of most candidates is very controversial.

The semi-major axes of the orbits of directly imaged planets are generally very large (with exception of SCR 1845) which facilitated the detection. Beta Pic b has the smallest angular separation to its host star (0.41 arcseconds). All systems are quite young. Since young planets gain gravitational energy during the contraction phase, they shine brighter and are therefore easier to detect.

Direct imaging of analogs to our Solar System is presently not possible. Improvements are expected from ground based infrared interferometry and from upcoming space missions that will use interferometric and/or coronographic approaches.

---

[4] short for NAOS-CONICA: Nasmyth Adaptive Optics System - High Resolution Near-Infrared Camera
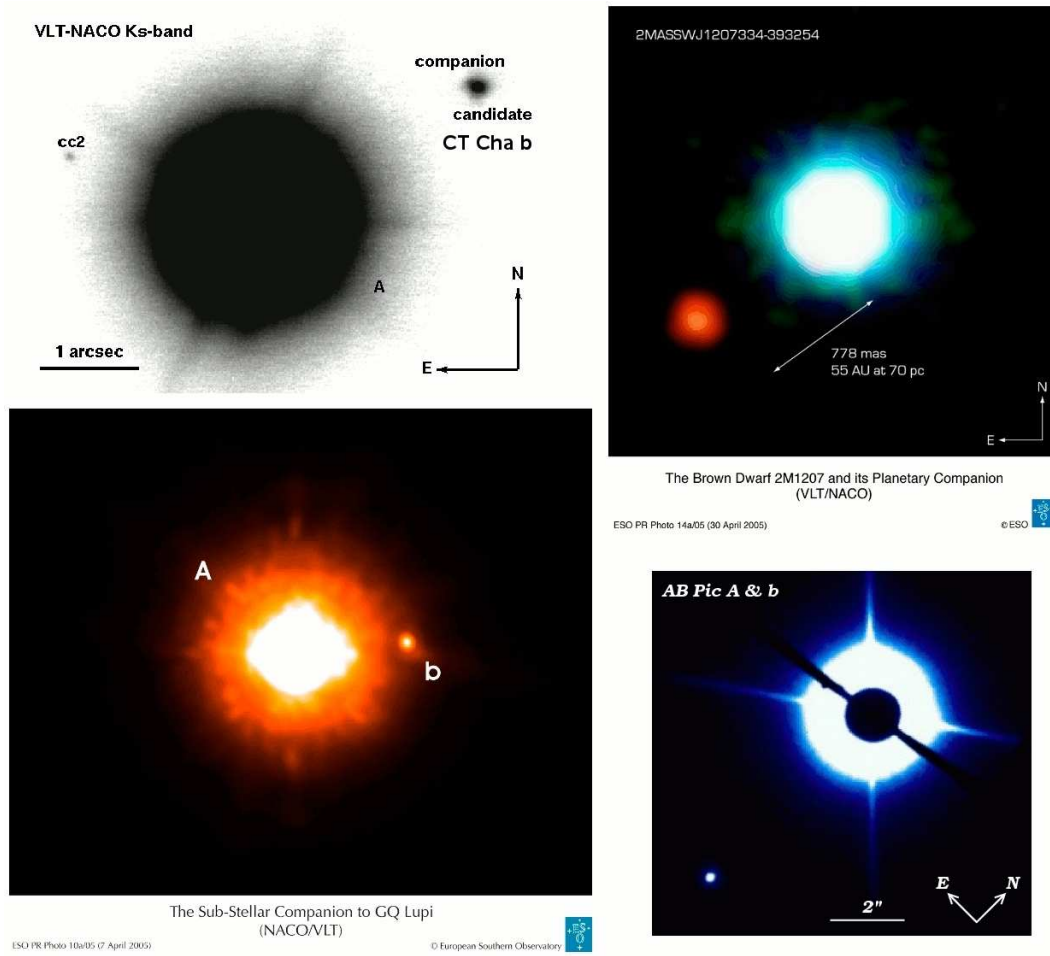
Figure 1.4: Planet candidates detected by direct imaging.

planet	host	semi-major axis	distance	mass	age	reference
2M 1207 b	M8	55 AU	70 pc	$4\,M_{Jup}$	8 Myr	Chauvin *et al.* (2004)
CT Cha b	K7	440 AU	165 pc	$17\,M_{Jup}$	2 Myr	Schmidt *et al.* (2008)
UScoCTIO 108 b	M7	670 AU	145 pc	$14\,M_{Jup}$	5.5 Myr	Kashyap *et al.* (2008)
SCR 1845 b	M8.5	>4.5 AU	3.9 pc	$>8.5\,M_{Jup}$	>0.1 Gyr	Biller *et al.* (2006)
AB Pic b	K2	275 AU	46 pc	$13.5\,M_{Jup}$	30 Myr	Chauvin *et al.* (2005)
GQ Lup b	K7eV	103 AU	140 pc	$21.5\,M_{Jup}$	1 Myr	Neuhäuser *et al.* (2005)
β Pic b	A6V	8 AU	19.3 pc	$8\,M_{Jup}$	6 Myr	Okamoto *et al.* (2004)
HR 8799 b	A5V	68 AU	39.4 pc	$7\,M_{Jup}$	60 Myr	Marois *et al.* (2008)
HR 8799 c	A5V	38 AU	39.4 pc	$10\,M_{Jup}$	60 Myr	Marois *et al.* (2008)
HR 8799 d	A5V	24 AU	39.4 pc	$10\,M_{Jup}$	60 Myr	Marois *et al.* (2008)
Fomalhaut b	A3V	115 AU	7.7 pc	$3\,M_{Jup}$	200 Myr	Kalas *et al.* (2005)

Table 1.1: Parameters of all planet candidates detected by direct imaging.

1.3.2 The microlensing method

If a foreground star in the Milky Way moves directly in front of a background star (e.g. located in the bulge of the Milky Way or in the Large Magellanic Cloud), the light of the background star is deflected due to space-time curvature and two images become visible (see Fig. 1.5). However, the large distances to the lens and the source makes the separation of the two images too small to be resolved (μ-arcseconds). Nevertheless, a net magnification of the background star (photometric microlensing) and a shift of the center of light of the combined image (astrometric microlensing) can be observed.
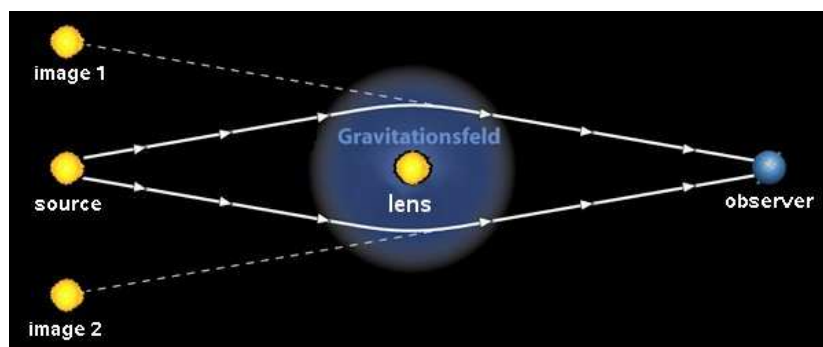
Figure 1.5: Light deflection caused by a gravitational lens (taken from http://de.wikipedia.org).

In case of a point mass lens and a point source, the exact progression of the symmetric and achromatic mircolensing amplification can be described with a Paczynski curve (see Fig. 1.6). Typical timescales for microlensing events are a few days to weeks - depending on the mass of the lensing star and the impact parameter. If the lensing foreground star has one or more planets, the microlensing event light curve may deviate from its symmetric shape and show additional features that can be quite complicated (see Fig. 1.7).
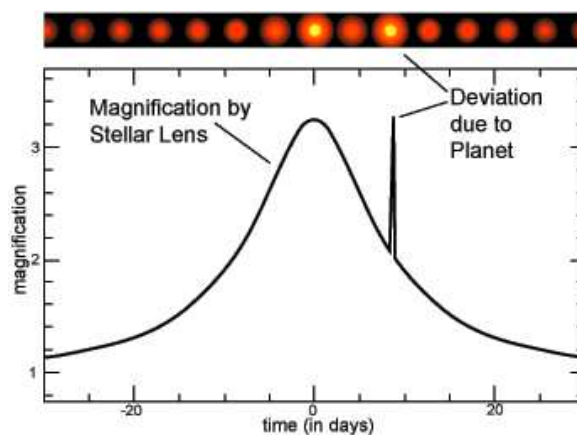
Figure 1.6: Light Curve of microlensing event with a planet. The symmetric Paczynski curve is interrupted on a short timescale due to a planetary companion of the lens star.

The chance for a source to be lensed by a foreground star is relatively low. About one in a million stars into the direction to the center of the Milky Way is lensed at a time. However, due to the high density of stars, almost always a few events are visible. Two projects, the Optical Gravitation Lensing Experiment (OGLE, Udalski (2003)) and the Microlensing Observations in Astrophysics project (MOA, Abe *et al.* (2004)) developed early warning systems which produce almost a thousand microlensing alerts per year. In case an event shows anomalies, which could be attributed to planetary companion of the lens, it is being followed-up with a high temporal resolution by large collaborations such as the Microlensing Follow-Up Network (μFun, Yoo *et al.* (2004)) or the joint venture between Probing Lensing Anomalies NETwork (PLANET, Dominik *et al.* (2002)) and RoboNet (Tsapras *et al.*, 2009). If enough observations are available, a complete modeling of the system by least-square-fitting of the light curve reveals the projected distance of the planet to the star and the planet's mass. Due to the specific geometry, microlensing towards the Galactic Bulge is most sensitive to planets with orbital separations of a few AU.

So far, seven planets have been found with the microlensing method. Table 1.2 summarizes the parameters of all detections. One event, OGLE-06-109L, is particularly interesting, since the lensing system consists of a two planet configuration that is very similar to the Jupiter-Saturn system.

One limitation of the microlensing method is the fact that an event will never occur again. This makes it impossible to confirm a detection. The lack of follow-up possibilities[5] implies that the microlensing method is only useful for the investigation of the distributions of masses and projected semi-major axes of extra-solar planets.

planet	mass	semi-major axis	reference
MOA-07-BLG-400-L b	0.9 M_{Jup}	0.85 AU	Dong *et al.* (2009)
MOA-07-BLG-192-L b	0.01 M_{Jup}	0.62 AU	Bennett *et al.* (2008)
OGLE-06-109L b	0.71 M_{Jup}	2.3 AU	Gaudi *et al.* (2008)
OGLE-06-109L c	0.27 M_{Jup}	4.6 AU	Gaudi *et al.* (2008)
OGLE-05-390L b	0.017 M_{Jup}	2.1 AU	Beaulieu *et al.* (2006)
OGLE-05-169L b	0.04 M_{Jup}	2.8 AU	Gould *et al.* (2006b)
OGLE-05-071L b	3.5 M_{Jup}	3.6 AU	Udalski *et al.* (2005)
OGLE-03-235L/MOA-03-BLG-53 b	2.6 M_{Jup}	5.1 AU	Bond *et al.* (2004)

Table 1.2: Parameters of all planet candidates detected by microlensing.

---

[5] in some cases it was possible to identify the lens star with HST
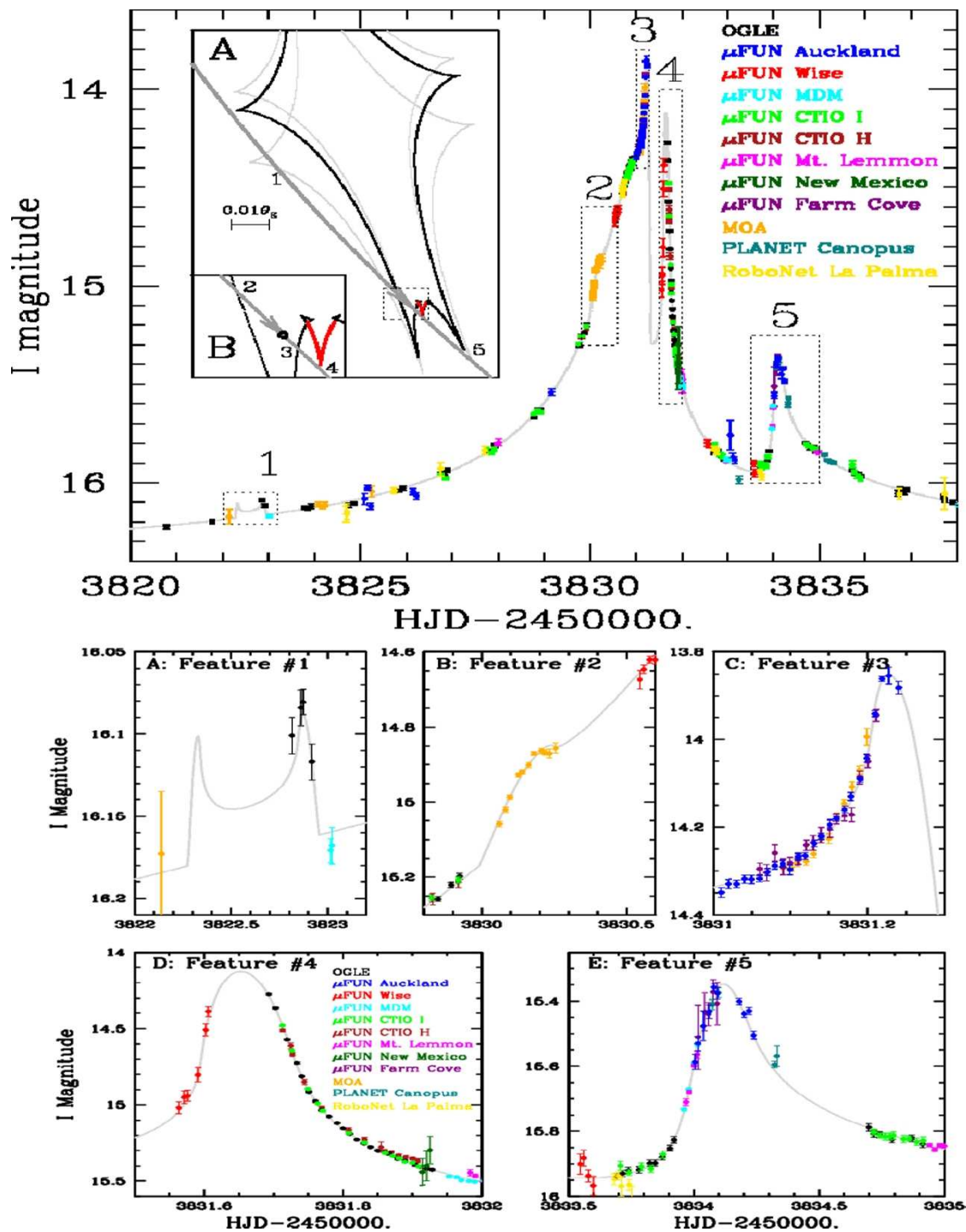
Figure 1.7: Light Curve of microlensing event OGLE-06-109L. Five anomalies reveal the presence of two companions to the lens star.

1.3.3   Timing methods

Because in a two body system both objects revolve their common center of mass, a planet causes its host star to perform a reflex motion. With the radial velocity method (see §1.3.4), the radial part of this wobble is measured directly as a redshift of the stellar spectra. However, in case the star is sending out a coherent periodical signal, even the actual radial displacement of the star caused by the planet can be measured as time delays arising from light travel time differences of the signal. In the following, we summarize 3 different timing methods that have led to the detection of extra-solar planets.

The first extra-solar planet that was detected is actually orbiting a pulsar. Wolszczan & Frail (1992) measured periodic time delays of the radio pulses of PSR B1257+12, which can only be explained by a reflex motion of the pulsar due to a system of 3 planets with 0.02, 4.3, and 3.9 Earth masses and respective orbital periods of 25, 66 and 98 days. Measuring the mutual gravitational perturbations of the outermost two planets, Konacki & Wolszczan (2003) were able to measure the inclinations (and therefore the true masses) of the two orbits. They found both orbits to be coplanar with an inclination of $\sim 50°$. The existence of pulsar planets was a big surprise[6]. It is still not fully understood, how these planets have survived the supernova explosion of their host or how they could have been captured afterwards. In addition to the 3 planets in the PSR B1257+12 system, one more planet with a mass of $M \cdot \sin i = 2.5$ M_{Jup} was found with the pulsar timing method (Thorsett et $al.$, 1999).

Silvotti et $al.$ (2007) reported the discovery of a $M \cdot \sin i = 3.2$ M_{Jup} companion to the pulsating sub-dwarf B V391 Pegasi at an orbital distance of about 1.7 AU with a period of 3.2 yr. The star is on the extreme horizontal branch of the HRD. Silvotti et $al.$ (2007) used the O-C (Observed - Calculated) diagram (Sterken, 2005) to measure the secular variation of pulsation periods in time caused by the reflex motion of the star. This technique is particularly useful for two classes of pulsators: hot sub-dwarfs and white dwarfs (Kepler et $al.$, 2005), since their short pulsation periods of a few minutes are extremely stable in time.

Recently, a planet candidate was found around the eclipsing binary system HW Vir (Lee et $al.$, 2009). The binary consists of a sub-dwarf B and an M-dwarf which revolve and eclipse each other every 2.8 hours producing a very stable periodic signal. 8 years of photometric data have revealed periodic time delays of the eclipses which can consistently be explained by the presence of two additional circumbinary companions with masses of $M \cdot \sin i = 19.2$ M_{Jup} and $M \cdot \sin i = 8.5$ M_{Jup} and orbital periods of 9.1 and 15.8 years respectively.

1.3.4   The radial velocity method

The most successful detection method so far is the radial velocity (RV) method. Already in the 1950s, Otto Struve proposed to measure the periodic RV signal that a Jupiter-sized planet would induce on its host star (Struve, 1952). The method had so far only been used to determine the masses of stellar binary systems. According to Struve, a variation of 200 m/s for a Jupiter-sized planets in close orbits could have been detectable already at that time.

---

[6] especially considering that the system is located in a globular cluster (M4)

However, it took more than 40 years until this method was applied successfully. In 1995 Michael Mayor and Didier Queloz published the discovery of the first extra-solar planet revolving a main-sequence star (Mayor & Queloz, 1995). Fig. 1.8 shows the measured RV variation of 51 Peg with a period of 4.2 days.
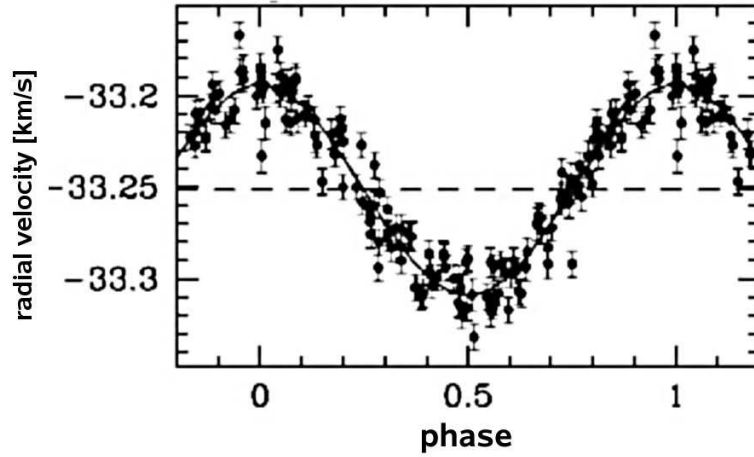
Figure 1.8: Radial velocity variations of 51 Peg, the first main-sequence star that was known to have a planet.

In the following, the most important equations and relations that connect the individual parameters of a planetary system to the measured RV amplitude are summarized .
The relation between mass and semi-major axis of a star and its planet is given by the definition of the barycenter:

$$a_* \cdot M_* = a_{pl} \cdot M_{pl} \quad , \tag{1.2}$$

where in the following the indexes pl and $*$ always refer to the planet and the star respectively.
On a circular orbit with period P, the orbital velocity of the star v_* can be calculated as:

$$v_* = 2\pi \cdot \frac{a_*}{P} = 2\pi \cdot \frac{a_{pl}}{P} \cdot \frac{M_{pl}}{M_*} \quad , \tag{1.3}$$

where the period P and the semi-major axis a_{pl} are connected by Kepler's 3rd Law:

$$\left(a_* + a_{pl}\right)^3 = \frac{G}{4\pi^2} P^2 \left(M_* + M_{pl}\right) \quad . \tag{1.4}$$

In most systems the mass of the planet is much smaller than the mass of the host star (i.e. $M_{pl} \ll M_*$). According to eq. 1.2, this implies that the semi-major axis of the stellar orbit is much smaller than the semi-major axis of the planet (i.e. $a_* \ll a_{pl}$). Using these approximations, eq. 1.4 transforms into:

$$a_{Pl}^3 = \frac{G}{4\pi^2} P^2 M_* \quad . \tag{1.5}$$

Putting this result into eq. 1.3, the orbital velocity of the star moving around the common center of mass can be calculated as:

$$v_* = \left(\frac{2\pi G}{P}\right)^{1/3} \cdot \frac{M_{pl}}{M_*^{2/3}} \quad . \tag{1.6}$$

A measurement of the true orbital velocity is not possible since the inclination angle of the system is generally unknown. As the name of the detection method suggest, only the radial component of the orbital velocity, $v_* \cdot \sin i$, can be measured. The half-amplitude K of the RV variation is therefore:

$$K = v_* \cdot \sin i = \left(\frac{2\pi G}{P}\right)^{1/3} \cdot \frac{M_{pl} \cdot \sin i}{M_*^{2/3}} \tag{1.7}$$

or in Solar System units:

$$K = 28.4 \cdot \left(\frac{P}{1yr}\right)^{-1/3} \cdot \left(\frac{M_{pl} \cdot \sin i}{M_{Jupiter}}\right) \cdot \left(\frac{M_*}{M_\odot}\right)^{-2/3} [m/s] \quad , \tag{1.8}$$

which is equivalent to

$$K = 28.4 \cdot \left(\frac{a_{pl}}{1AU}\right)^{-1/2} \cdot \left(\frac{M_{pl} \cdot \sin i}{M_{Jupiter}}\right) \cdot \left(\frac{M_*}{M_\odot}\right)^{-5/6} [m/s] \quad , \tag{1.9}$$

where we used eq. 1.5 in Solar System units:

$$P = \left(\frac{a}{1AU}\right)^{3/2} \cdot \left(\frac{M_*}{M_\odot}\right)^{-1/2} [yr] \quad . \tag{1.10}$$

The above equations were deduced under the assumption of a circular orbit. In case of non-circular orbit with eccentricity e the amplitude of the radial velocity variation is higher and eq. 1.7 has to be multiplied by an additional factor (Cumming *et al.*, 1999):

$$K = \left(\frac{2\pi G}{P}\right)^{1/3} \cdot \frac{M_{pl} \cdot \sin i}{M_*^{2/3}} \cdot \frac{1}{\sqrt{1-e^2}} \quad . \tag{1.11}$$

For eccentric orbits, the radial velocity variations are not sinusoidal as they are in the case of 51 Peg (see Fig. 1.9). A fit to the RV measurements reveals the period P, the semi-major axis a_{pl}, the eccentricity e and the minimum mass $M_{pl} \cdot \sin i$. However, as mentioned above, the inclination i and thus the true mass M_{pl} cannot be determined. Using the RV method, several systems with more than one planet have already been detected. In these cases, the RV variations are superimposed like beats in musics.

The challenge in measuring accurate radial velocities is to find a stable wavelength reference. Mainly two methods were used in the past: the simultaneous ThAr calibration and the I_2-technique.
In ThAr mode, one fiber is put on the object of interest and one fiber is fed with the light coming from a ThAr calibration lamp. The ThAr-spectrum can then be used as a wavelength reference to monitor the instrumental drifts on the detector. One problem with this method is the long term stability. Because ThAr-lamps age, the spectrum may change over time.
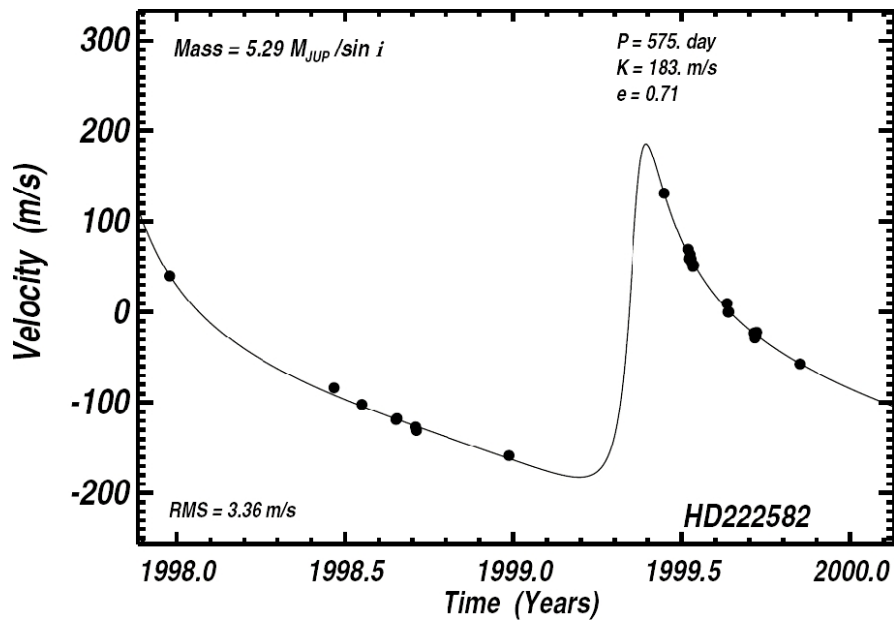
Figure 1.9: Radial velocity variations of HD222582, a star with a planet in a highly eccentric orbit ($e = 0.71$).
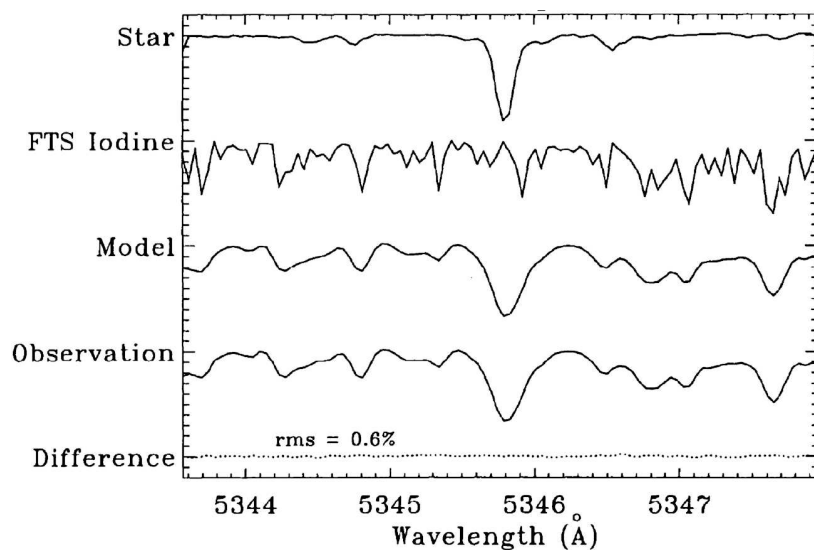
Figure 1.10: Modeling of the combined iodine and stellar spectrum. The Doppler-shifted stellar spectrum is added to a PSF-convolved iodine template spectrum that has been measured at the Fourier Transform Spectrometer (FTS) at McNath Observatory. By least-squares fitting of this model to the observed spectrum, the radial velocity of the star can be measured. The Figure shows a 5 Å region of the spectrum of HR 5019, taken from Marcy & Butler (1992)

The I$_2$-technique was proposed by Campbell & Walker (1979) and first applied in a radial velocity search for extra-solar planets by Marcy & Butler (1992). The light coming from the telescope is led through a cell filled with I$_2$-gas that is absorbing at specific wavelengths. As a result, a combined spectrum of the star and the I$_2$ absorption reaches the detector. I$_2$ has several hundred very narrow absorption lines in the optical spectral region. The radial velocity of the star can be measured by simultaneous modeling of the combined I$_2$ and Doppler-shifted stellar spectrum (see Fig. 1.10). Despite of a better long term stability, the I$_2$-technique has two major disadvantages over the ThAr-method. Firstly, the I$_2$ lines are only covering a limited wavelength range from 5 000-6 500 Å and secondly, the I$_2$ absorption reduces the S/N of the spectrum which is a problem for faint sources. A significant improvement in the precision and stability of the wavelength calibration might come from the relatively new technology of optical frequency combs, generated from mode-locked femtosecond-pulsed lasers. The 2005 Nobel Prize in physics was awarded for the pioneering on such combs (Reichert *et al.*, 1999; Jones *et al.*, 2000; Udem *et al.*, 2002). For further details on this method we refer to Murphy *et al.* (2007).

Todays best spectrographs have a spectral resolution of about 10^5 which enables the observer to measure radial velocities with a precision better than 1 m/s for bright stars. In this region, the precision is mainly limited by stellar variability acting on different timescales (Pepe & Lovis, 2008; Kjeldsen *et al.*, 2005), from minutes (p-modes) to hours (granulation) and days or weeks (activity).

Presently, the most powerful instrument for a RV search is the High Accuracy Radial velocity Planet Searcher (HARPS, Mayor *et al.* (2003)) mounted at the 3.6m telescope at LaSilla observatory. The exquisite temperature stability (a few mK) of this stationary fiber-fed high resolution (R=115 000) spectrograph has recently enabled the detection of a system with 3 planets in circular orbits which have very low minimum masses of 4.2, 6.9, and 9.2 M_{Earth} and periods of 4.3, 9.6, and 20.5 days, respectively (Mayor *et al.*, 2009).

1.3.5 The astrometric method

A complementary detection technique to the RV method is the astrometric method where the two tangential components of the reflex motion of a host star of an extra-solar planet are measured as a periodical displacement (see Fig. 1.11). The effect is very small (of the order of milli-arcseconds) and decreasing with increasing distance of the system.

No planet has been found with the astrometric method. Nevertheless, (Benedict *et al.*, 2002) achieved a confirmation of GJ876b with astrometric follow-up observations using the Find Guidance Sensor at the HST. In combination with the RV measurements, the inclination of the orbit and therefore the true mass of the planet was determined.

The astrometric method is more sensitive to planets with larger semi-major axis making the technique complementary to both the RV and transit techniques. However, the longer periods of such planets require a longer baseline of the observations.

ESA's GAIA mission (http://gaia.esa.int) is planned to be launched in 2011. The satellite is expected to deliver proper motions and radial velocities of 1 billion stars. With an expected astrometric precision of 20 μas, GAIA will be able to detect a large number of long period extra-solar planets.
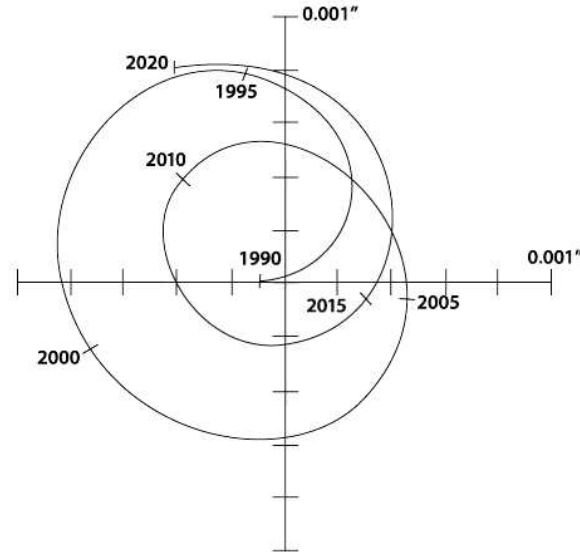
Figure 1.11: Astrometric displacement of the Sun during a 30 year period as seen from a distance of 10 pc (source: NASA/JPL).

1.3.6   The transit method

If the orbital inclination i is close to $90°$, it is possible to detect transits of an extra-solar planet. Covering a small fraction of the stellar surface, the observed brightness of the star drops by a certain amount that is (under the assumption of a constant surface brightness) equal to the square of the radius-ratio of planet and star:

$$\frac{\Delta F}{F} = \left(\frac{R_{pl}}{R_*}\right)^2 \quad . \tag{1.12}$$

For a Jupiter-sized planet transiting a Solar-type star, this is on the order of 1% whereas for an Earth-sized planet, the depth reduces to 0.01%. Note that for bright stars, a photometric precision of 1% can be achieved already with comparable small telescopes ($\sim$20 cm aperture) whereas the detection of Earth-sized planets around Sun-like stars is currently only possible from space. Exceptional cases are M-dwarf host stars which are much smaller than the Sun. Due to the reduced radius, the transit depth of an Earth-sized planet is large enough to be detected from ground.

In detail, the exact progression of the brightness change during a transit is more complicated. During ingress, the planet eclipses more and more of the star making the brightness decrease smoothly. During the transit, the shape of the light curve is determined by limb-darkening. The planet covers parts of the stellar surface with different brightnesses and the light curve gets a round bottom with the lowest point in the center when the planet covers the brightest part of the star. Analytic models for transit light curves are discussed in Mandel & Agol (2002). Fig. 1.12 shows a schematic view of a transit indicating ingress (2), transit (3) and egress (4) phases.
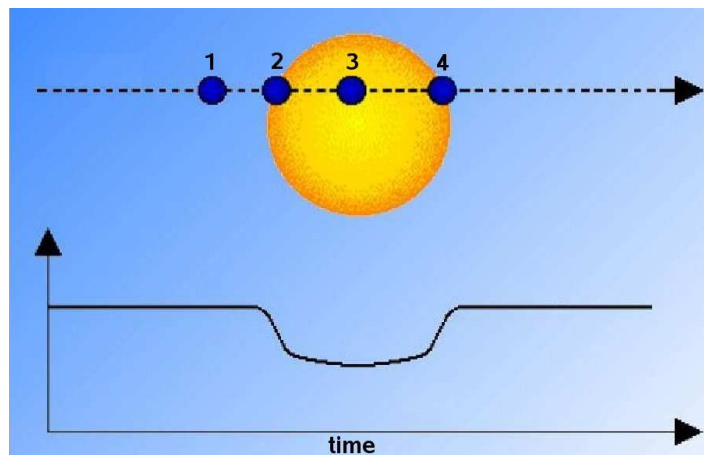
Figure 1.12: Light Curve of a transit event.

The first transit of an extra-solar planet was discovered by Charbonneau *et al.* (2000). The planetary companion of HD209458 was detected with the RV method (Mazeh *et al.*, 2000) and later found to be transiting. Since the RV curve allows to predict the exact time when a planet transits (in case the orbit is edge-on), such follow-up observations are quite easy to perform and have become a standard procedure that is applied to most planets that are detected with the RV method.

Right after the discovery of its transit, HD209458b was followed-up with the Hubble-Space-Telescope (HST Brown *et al.* (2001)). Fig. 1.13 shows the HST light curve with an exquisite photometric precision of 10^{-5} that can only be achieved from space.
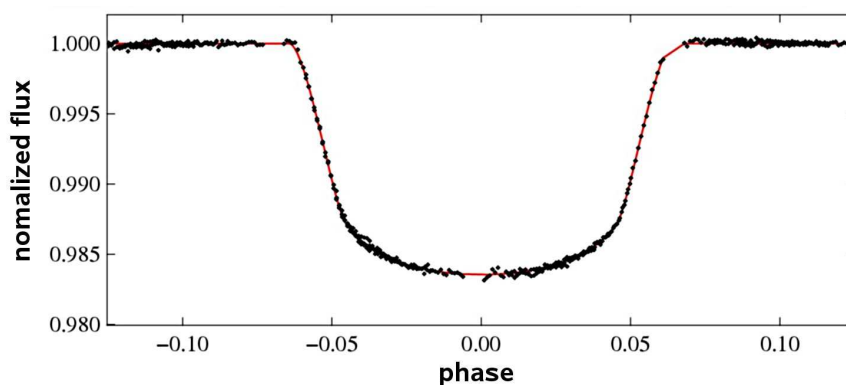
Figure 1.13: Hubble Space Telescope light curve of a transit of HD209458 b.

In the following we derive the equations that connect the most important parameters of transiting planets. As already mentioned above, the orbital inclination of a transiting planet has to be close to $90°$. In particular, it has to exceed a minimum inclination i_{min} that is depending on the orbital
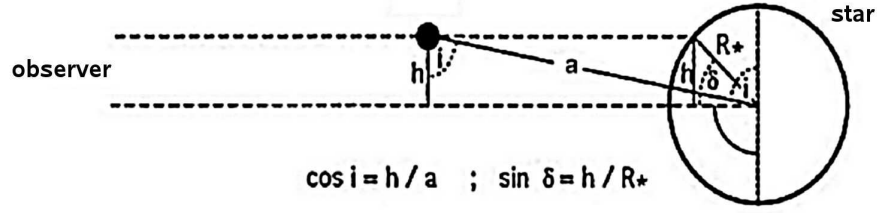
Figure 1.14: Geometry of a transit event.

semi-major axis a_{pl} and the stellar radius R_*:

$$i_{min} = cos^{-1} \frac{R_*}{a_{pl}} \quad . \tag{1.13}$$

The probability to see transits of a planet with randomly oriented inclination vector is:

$$p_{transit} = \cos i_{min} = \frac{R_*}{a_{pl}} \quad . \tag{1.14}$$

For individual objects, the probability is in fact very low. E.g. in our Solar System, the transit probability drops from 1.2% for Mercury to 0.46% for the Earth and to 0.01% for Jupiter. As a consequence, the transit method is insensitive to planets in wide orbits. Only planets with semi-major axis smaller than 0.1 AU have been detected so far[7]. In order to compensate the limited range of sensitivity and the small edge-on probability, a large number of stars need to be observed in transit surveys. This is achieved either with extremely wide angle optics or with deep observations of crowded regions of the sky such as the Milky Way disk.

The relation between inclination and stellar latitude can be derived from Fig. 1.14:

$$\cos i = \frac{R_* \sin \delta}{a_{pl}} \quad . \tag{1.15}$$

where central transits with $\delta = 0°$ correspond to an inclination of $i = 90°$ and grazing eclipses with $\delta = 90°$ correspond to $i = i_{min}$.

Another important parameter is the transit duration $t_{transit}$ which depends on the stellar and planetary radii, the orbital period and the semi-major axis as well as the stellar latitude (Deeg, 1998):

$$t_{transit} = \frac{P}{\pi} \left(\frac{R_* \cos \delta + R_{pl}}{a_{pl}} \right) \quad . \tag{1.16}$$

The transit duration can also be expressed as a function of semi-major axis using eq. 1.5:

$$t_{transit} = \sqrt{\frac{4 \cdot a_{pl}}{\pi G M_*}} \cdot \left(R_* \cos \delta + R_{pl} \right) \quad . \tag{1.17}$$

The so-called fractional transit duration τ is defined as the transit duration in units of orbital periods:

$$\tau = \frac{t_{transit}}{P} \sim a_{pl}^{-1} \quad . \tag{1.18}$$

---

[7] the transiting planets HD17156b and HD80606b found with the RV method have larger semi-major axes

For uniformly spaced light curves, the expected number of measurements taken during a transit is proportional to the fractional transit duration. In order to detect transiting planets, a sufficient number of data points in transit are needed (see §2.6.2). As a consequence, short period planets which have a longer fractional transit length will be easier to detect than long period planets. For unevenly sampled light curves, as one would expect for a ground based survey, the effect is on average the same. However, the window function introduced by the diurnal day/night cycle leads to a period dependent detection efficiency with an enhanced detection efficiency for planets with periods close to an integer number of days (about half of which show transits in each night).

In summary, the detection of transiting planets with longer orbits is more difficult in two respects: firstly, because of a $\sim a_{pl}^{-1}$ decreasing transit probability (eq. 1.14) and secondly, due to the $\sim a_{pl}^{-1}$ decreasing average number of data points taken during a transit (eq. 1.18). Compared to the RV method where the amplitude of the variation only drops $\sim a_{pl}^{-1/2}$ (eq. 1.8) the transit method is much more biased towards finding planets in close-in orbits.

Due to the large number of stars observed in a transit survey (of the order 10^5-10^6), an efficient detection algorithm is needed to identify planet candidates. In §2.6.2 we introduce the detection algorithm we used in our work.

After the selection of light curves that show transit signatures, there are still a high number of false interlopers (transiting low-mass stars, blend eclipsing binary systems) among the list of candidates (see §1.5). In order to confirm the planetary nature of a candidate selected by the detection algorithm, the mass has to be determined using RV follow-up observations.

Current transit projects can be divided into two distinct classes: wide-angle surveys using telescopes with small apertures and deep surveys using meter-class telescopes. The former observe bright stars up to 13th magnitude whereas the latter observe fainter stars in the range 13-17 mag. Table 1.3 gives an overview of the most successful ongoing and most promising future transit surveys.

survey	aperture	survey area	planets found	reference
TrES	small (various)	large (various)	4	Dunham *et al.* (2004)
super WASP	2x8x0.2m	964 sq.deg.	15	Pollacco *et al.* (2006)
HAT-Net	6x0.11m	384 sq.deg.	11	Bakos *et al.* (2004)
XO	2x0.2m	2 646 sq.deg.	5	McCullough *et al.* (2005)
OGLE	1.3m	0.3 sq.deg.	8	Udalski (2007)
CoRoT(space)	0.27m	7.8 sq.deg.	6	Baglin *et al.* (2007)
Kepler(space)	0.95m	105 sq.deg.	launched	Koch *et al.* (2004)
Pan-Planets	1.8m	49 sq.deg.	start 2009	Koppenhoefer *et al.* (2009)
OmegaTranS	2.6m	18 sq.deg.	start 2010	www.astro-wise.org/projects

Table 1.3: Overview of ongoing and future transit surveys.

In contrast to planets detected with the RV method, transiting planets reveal much more information. Not only the orbital parameters, such as period, epoch and eccentricity but also intrinsic parameters of the planet, like its true mass and radius (and therefore its density) can be determined. In addition, a variety of detailed follow-up studies can be performed during transit or eclipse of the planet (see §1.6).

1.4 Current Status of Extra-Solar Planet Searches

As of March 20th 2009, a total of 331 detections of extra-solar planets have been published[8]. Fig. 1.15 shows the number of planets detected with each of the methods described in the previous section.
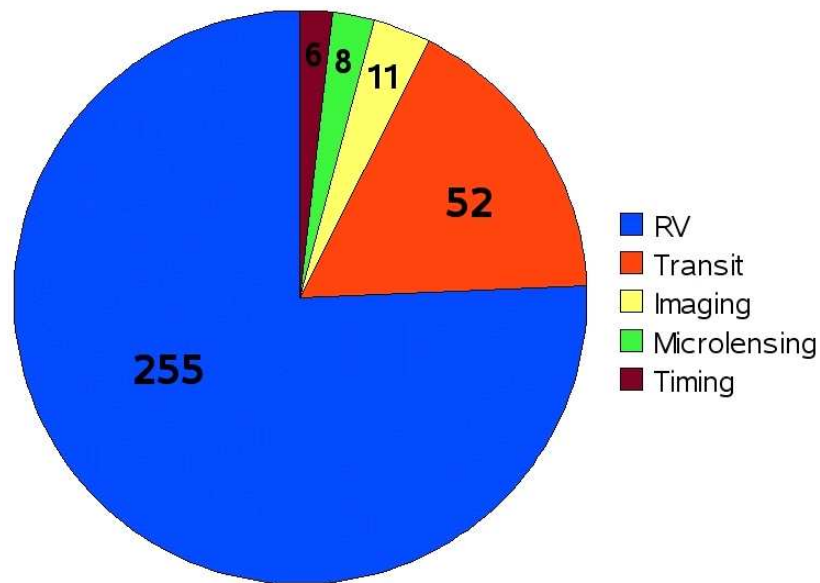
Figure 1.15: Number of planets detected with each method.

The most successful technique is the RV method which has provided 75% of all detections. Note that since only a minimum mass of the candidates can be derived, some might actually be too massive to be a planet. However, in a statistical view, most of the candidates detected by the RV method are indeed planets. Radial velocity searches will continue with focus on the detection of very low-mass planets, multi-planetary systems, planets with longer periods and planets around low-metallicity stars and giants.

A total of 57 transiting planets are known to date[9]. Remarkably, more than half of the transiting planets have been found in the past two years, making the transit method similarly successful in that period compared to the radial velocity method (see Fig. 1.15). The majority of the recently detected transiting planets were found in wide-angle surveys which target bright stars such as WASP, HAT, TrES or XO (Pollacco *et al.*, 2006; Noyes *et al.*, 2008; O'Donovan *et al.*, 2007; McCullough *et al.*, 2005). Also the space mission CoRoT has contributed by adding six new discoveries (Aigrain *et al.*, 2008). Deep surveys such as OGLE which are targeting highly crowded regions of the Milky Way disk have not been able to keep up with the increased detection rate of all-sky monitoring programs

---

[8] for a daily update see www.exoplanet.eu
[9] five of which were detected with the RV method

mainly due to limited amount of observation time and a lower number of target stars. However, upcoming projects such as Pan-Planets or OmegaTranS will presumably give rise to a revival of the deep surveys in the next years. The first detection of a transiting Earth-mass planet in the habitable zone is expected from the Kepler space mission that has been launched recently.

Although each of the other methods (imaging, timing and microlensing) has its own specific aspects and although each of the detected objects is very interesting, a large number of detections is not expected in the near future. This is mainly due to the fact that these methods are not applicable in large scale surveys but require detailed analyses of single objects. An exception might be a microlensing space mission that would have both the photometric precision and the time sampling that is needed to detect a large number of planets in a small field of view (Bennett *et al.*, 2004). Note also that the microlensing technique is currently the only method capable of detecting free-floating planets or planets outside the Milky Way (e.g. in M31).
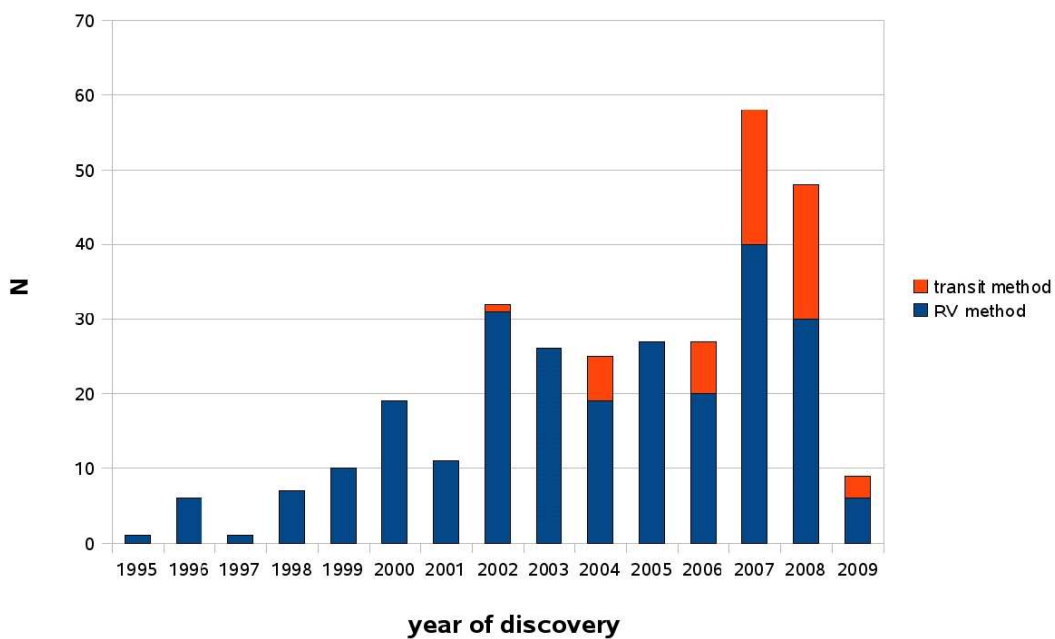
Figure 1.16: Comparing the number of planets detected with the RV and transit methods. In the last years the detection rate of transiting planets increased significantly whereas the RV detections flattened out at a rate of ∼30 detections per year.

The high number of extra-solar planets that have been found over the last decade allows a detailed statistical analysis of their parameters (see e.g. Udry & Santos (2007)). In the following we discuss the most important results that have been found.

The minimum mass distribution of RV planets

The analysis of the mass distribution of extra-solar planets (Fig. 1.17) indicates that although the RV method is more sensitive to massive companions, the frequency of planets decreases as a function of mass (Jorissen *et al.*, 2001). The distribution falls to a value close to zero for masses above 10 M_{Jup}. In the Brown Dwarf regime (between 13 and 80 M_{Jup}), there is a deficiency of companions to solar-type stars which is called the Brown Dwarf desert (Halbwachs *et al.*, 2000). Together with the shape of the mass distribution, this suggests a different formation mechanism between low-mass stars and planetary systems.
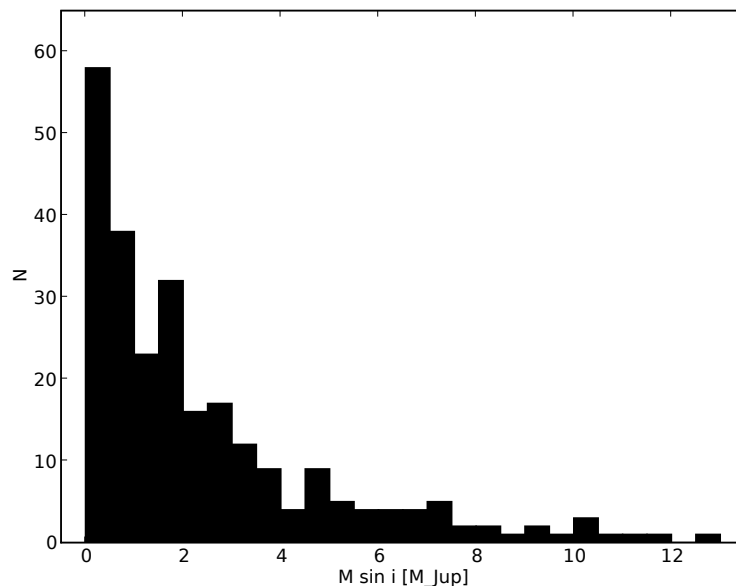
Figure 1.17: Minimum mass distribution of planets detected with the RV method.

The period distribution of RV planets

Fig. 1.18 shows the period distribution of planets detected with the RV method. Although the RV method has a selection effect towards finding short period planets (K $\sim$ a $_{pl}^{-1}$, see eq. 1.11), the resulting bias in the period distribution of Jupiter-sized planets is assumed to be low, because the precision of most RV surveys is high enough to detect most of the massive planets, even with longer periods (Cumming *et al.*, 2008).
Giant-planets with periods below 3 days have been named Very Hot Jupiters (VHJ) in contrast to Hot Jupiters (HJ) with periods between 3 and 5 days[10].

---

[10]the upper limit of 5 days is not strictly used
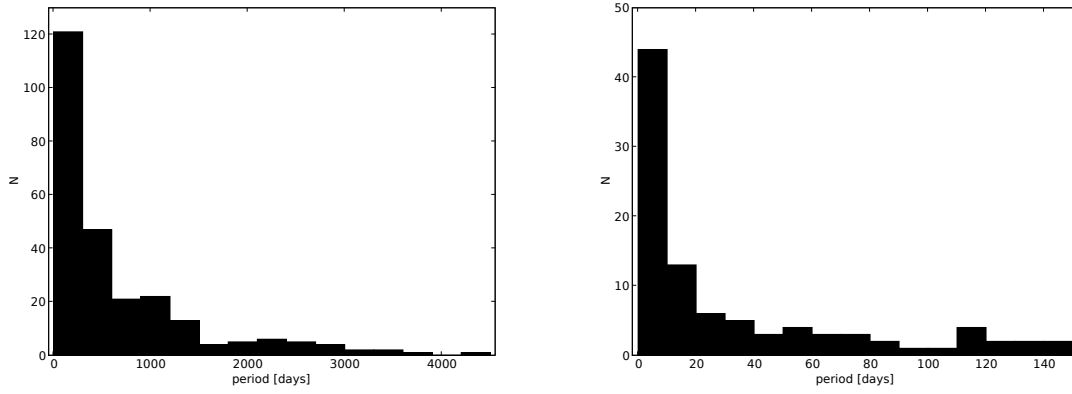
Figure 1.18: Period distribution of planets detected with the RV method.
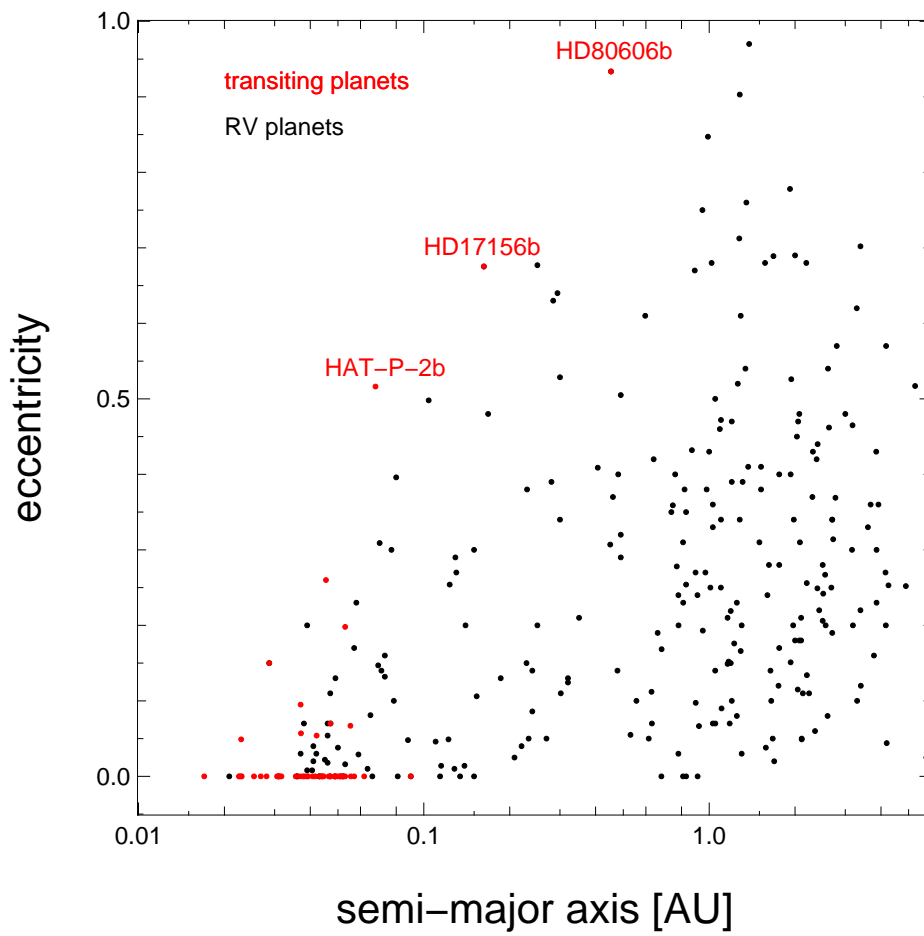
Figure 1.19: Eccentricity vs. semi-major axis of planets detected with the transit or RV method.

The eccentricity distribution of RV and transiting planets

Unlike the planets in our Solar System, extra-solar planets have been found to exhibit significant eccentricities. Fig. 1.19 shows the eccentricity distribution of all planets detected with the RV and transit method as a function of semi-major axis. For distances larger than 0.1 AU, the values range from 0 to more than 0.9 with a distribution that is similar compared to eccentricities found in binary star systems (Halbwachs *et al.*, 2005). However, the high eccentricities cannot be explained by the standard giant planet formation models. Several eccentricity pumping mechanisms have been proposed such as interactions in multiple systems (Jurić & Tremaine, 2008; Rasio & Ford, 1996) or the interactions between the planet and the disk of planetesimals (Murray *et al.*, 2002).
For orbital distances smaller than 0.1 AU, the average eccentricity drops significantly which is a result of a circularization process caused by tidal interactions of the planet with the star (see §1.2.3).

Multi-planet systems

Among the 254 planets detected with the RV technique, there are 79 planets in multi-planet systems. 23 systems with 2 planets, 8 systems with 3 planets, 1 system with 4 planets (HD160691) and 1 system with 5 planets (55 Cnc) have been detected. However, this is considered to be only a lower limit. Ongoing monitoring of most planet systems is continuously increasing the number of known multi-planet systems. Many RV curves of stars with a single planet show long term trends that indicate the presence of a second planet with a longer period (see e.g. Fischer *et al.* (2001)).
Taking these considerations into account and given the higher rate of multi-planet systems in the older long-running RV surveys, it seems likely that most stars form systems of planets rather than isolated, single planets (Udry & Santos, 2007).

The frequency of giant planets and its metallicity dependence

Analyzing the results from several RV surveys, Fischer *et al.* (2005) found a strong correlation between the frequency of extra-solar planets and the host star metallicity. Fig. 1.20 shows the frequency of planets with orbital periods less than 4 years with a RV amplitude larger than 30 m/s. The frequency rises from 4% for solar metallicity to 27% for [Fe/H]=0.5. The frequency for sub-solar metallicity is consistent with being constant (see also recent results by Sozzetti *et al.* (2009)).
There are two theories that explain the metallicity dependent frequency of Jupiter-sized planets. The first scenario is favored by the CAGC planet formation model (see §1.2.1) and is assuming that the overabundance of heavy elements in planet-hosting stars is primordial (Ida & Lin, 2004). A collapsing molecular cloud with high metallicity has a larger number of dust particles which can build more planetesimals in the agglomeration and accretion phase. Naturally, the chance for the formation of a giant planet will be higher if more planetesimals are present in the proto-planetary disk.
The second scenario assumes that the planet-hosting stars are actually not metal-rich but only the outer layers (that are observed to derive the metallicity of a star) are polluted by the debris of the planetary system (Laughlin & Adams, 1997; Gonzalez, 1998). This would be in agreement with the DI planet formation model (see §1.2.2) which predicts a very weak metallicity dependency of the giant planet frequency.
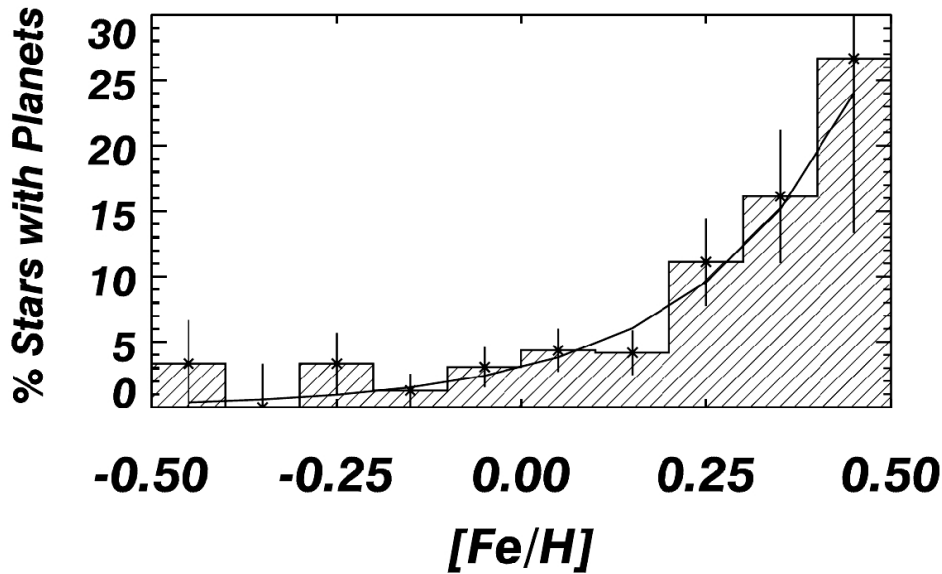
Figure 1.20: Planet frequency as a function of host star metallicity.

If the overabundance is coming from pollution of the outer layers, mixing processes in the convection zone of the stars should diminish the effect and since the depth of the convection zone depends on the spectral type of the star, there should be a trend with effective temperature. No such trend has been observed, most groups are therefore in favor of the primordial metallicity enhancement (Valenti & Fischer, 2008; Ecuvillon *et al.*, 2006; Pinsonneault *et al.*, 2001). However, Pasquini *et al.* (2007) analyzed the metallicity distribution of 14 planet-hosting giant stars and found no evidence for a metallicity dependent frequency. Since giant stars have a much larger mass of the convection zone they conclude that planet hosting main-sequence stars might indeed be polluted by infall of debris whereas the pollution disappears as soon as the convective mixing increases during the transition to the giant phase.

The masses and radii of transiting planets

Fig. 1.21 shows the radii and masses of all transiting extra-solar planets with $M < 5$ M_{Jup}. Most planets have densities in the range from 0.4 to 1.5 g/cm^3 (shown as dashed lines). Three planets have significantly larger radii than predicted by models for core-less planets densities (Fortney *et al.*, 2007; Burrows *et al.*, 2007). The origin of the large radii might be explained by additional heat sources such as more significant core heating, tidal dissipation due to a non-zero eccentricity and/or irradiation (for a detailed discussion see Liu *et al.* (2008)).
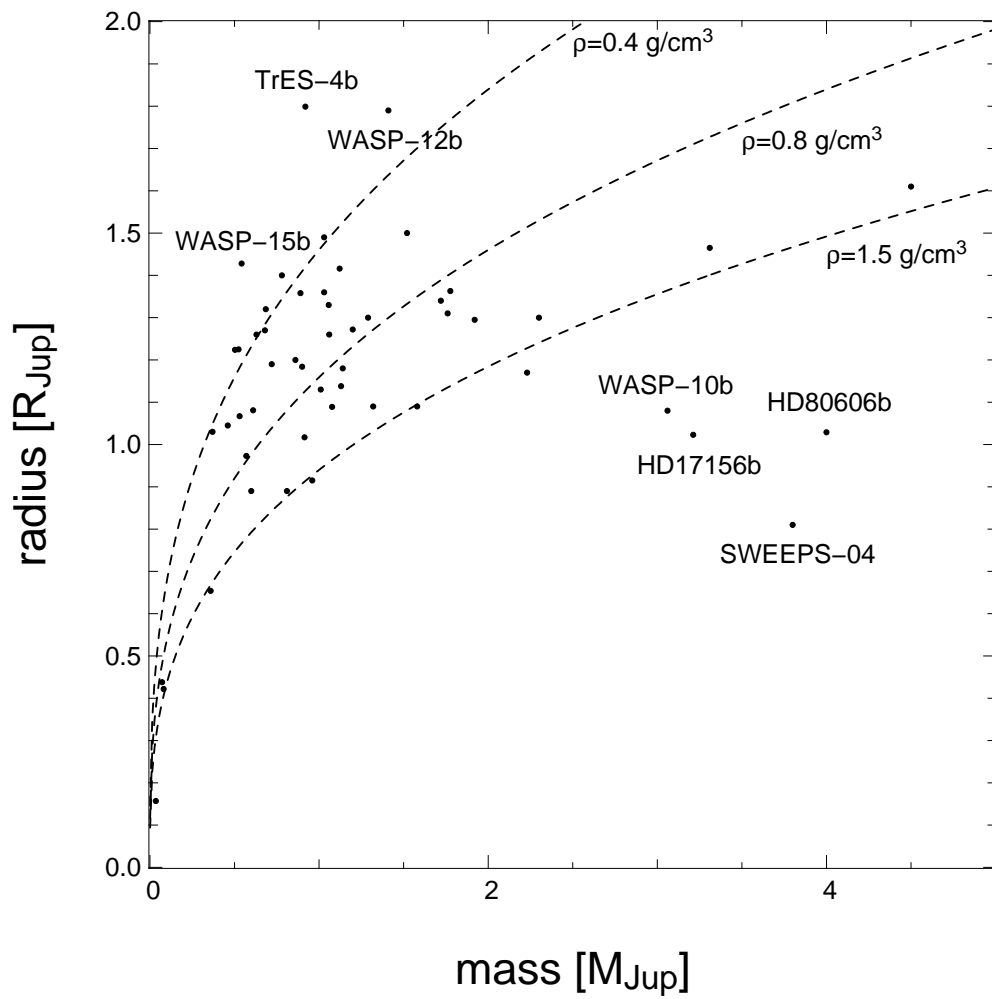
Figure 1.21: Radius and mass of all transiting planets.

1.5   Follow-up Observations of Transiting Extra-Solar Planet Candidates

The detection of a high S/N transit signature in the light curve of a star does not prove the existence of a transiting planet. In order to confirm the detection, a number of false positive scenarios with similar or identical light curves have to be ruled out (Bouchy *et al.*, 2005):

- a transiting low-mass star with radius similar to that of Jupiter

- a transiting Brown Dwarf with M $\geq$ 13 M$_{Jup}$

- an eclipsing binary system which is blend by a third star that is either physically bound or a fore- or background star within the line of sight

For the detection of an extra-solar planet with the transit method it is essential to confirm the planetary nature of a candidate with high-resolution spectroscopic follow-up observations (see §1.3.4). Since the inclination of transiting systems is known ($\sim$90°), measurement of the RV variations of the host star reveals the true mass of the transiting object, which can decide whether a candidate is really a planet or one of the three false positive cases.
However, high-resolution spectroscopy is time-consuming and large telescopes are needed (especially for faint targets). It is infeasible to follow-up all candidates found in a transit survey. An efficient preselection based on the light curve and/or low-resolution RV measurements is essential in order to reduce the number of candidates as much as possible beforehand.
In the following we present methods that were developed to reject false positive detections.

1.5.1   The Tingley-Sackett parameter

Tingley & Sackett (2005) proposed a photometric diagnostic to aid in the identification of transiting extra-solar planets on light curve basis. They derived a simple parameter η_{pl} that is the ratio between observed transit duration and the duration expected given the transit depth and orbital period. The parameter helps to rank the candidates. It can be applied even if the photometric precision or the sampling of the light curve is not good enough to resolve ingress and egress of the transit. Assuming a planetary radius of 1 R$_{Jup}$, equation (11) of Tingley & Sackett (2005) transforms into:

$$\eta_p = \frac{D_{obs}}{D} = \frac{D_{obs}}{2(1+\sqrt{1.3/d})} \cdot \left(\frac{2\pi GM_\odot}{\tau}\right)^{1/3} R_\odot^{-5/12} \left(\frac{1.3}{d}\right)^{5/24} \quad , \tag{1.19}$$

with period τ, transit duration D_{obs} and fractional transit depth d. Fig. 1.22 shows η_p for 173 transit candidates found in the OGLE-III survey (Udalski *et al.*, 2002a,c,b, 2003, 2004). All confirmed planets have a value of $\eta_p < 1.0$ (red diamonds). Applying this cut to the OGLE sample reduces the number of candidates significantly to 61.
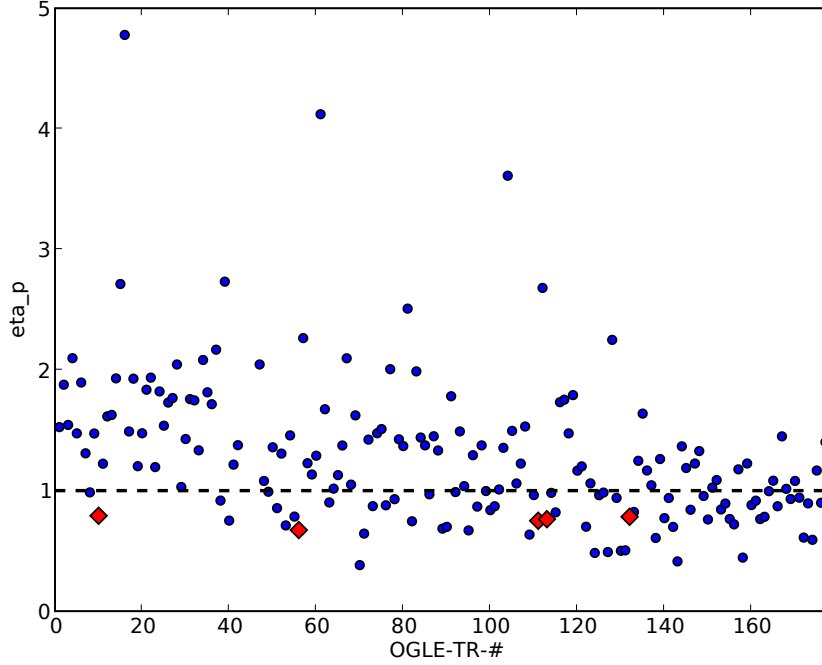
Figure 1.22: Value of the Tingley-Sackett parameter for 173 OGLE candidates. Five planets that were confirmed to be transiting planets are shown as red diamonds.

1.5.2 Ellipsoidal variations

In case of a transiting low-mass star, the system may show ellipsoidal light variations in the out-of-transit parts of the light curve (Udalski *et al.*, 2002a) with exactly half the orbital period: tidal effects cause deformations of the secondary which make the system appear the brightest at phases 0.25 and 0.75 (assuming the transit occurs at phase 0.0). This effect is stronger the more massive and closer the secondary is. Therefore, detecting ellipsoidal variations in the light curve is a good indicator for a high mass of the companion and rule out a planetary nature of the candidate. Fig. 1.23 shows the light curve of OGLE-TR-5 with strong ellipsoidal variations.
Drake (2003) demonstrated, that the sample of candidates published by the OGLE group can be reduced analyzing the out-of-transit parts of the light curves. Sirko & Paczyński (2003) extended the work of Drake (2003) improving the error estimates on the amplitudes of the variations.

For each frequency v the ellipsoidal variations can be parameterized as:

$$I(t) = <I> + a_{c,v} \cdot cos(2\pi vt) + a_{s,v} \cdot \sin(2\pi vt) \quad , \tag{1.20}$$

where $a_{c,v}$ and $a_{s,v}$ are least-square fitted in such a way that $I(t)$ matches the observations using only the out-of-transit data points of the light curve.
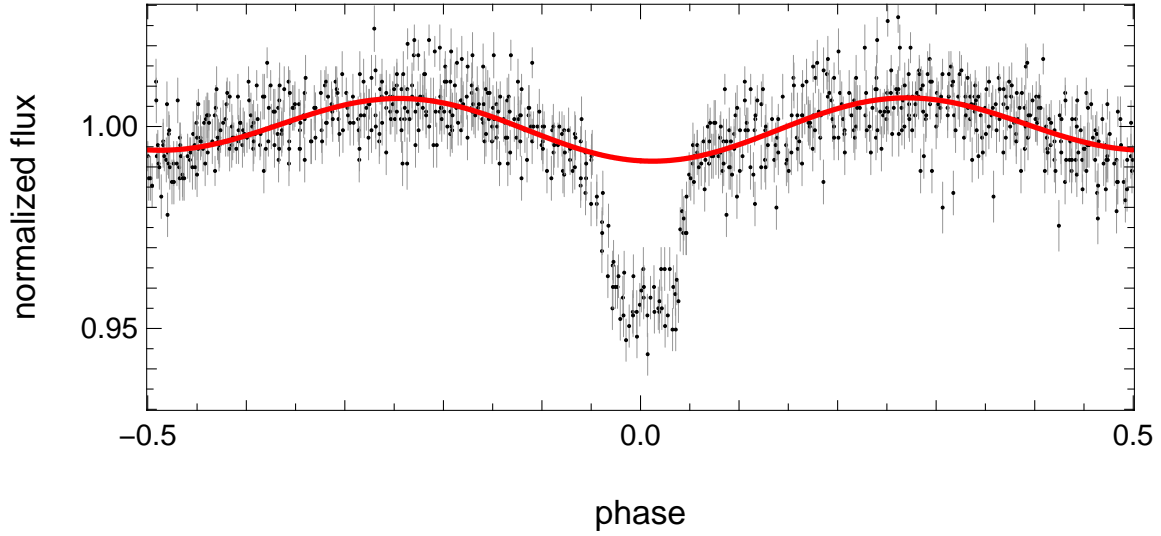
Figure 1.23: Folded light curve of candidate OGLE-TR-5 with strong ellipsoidal variations in the out-of-transit part. The solid line shows the best cosine fit excluding the points in transit phase.
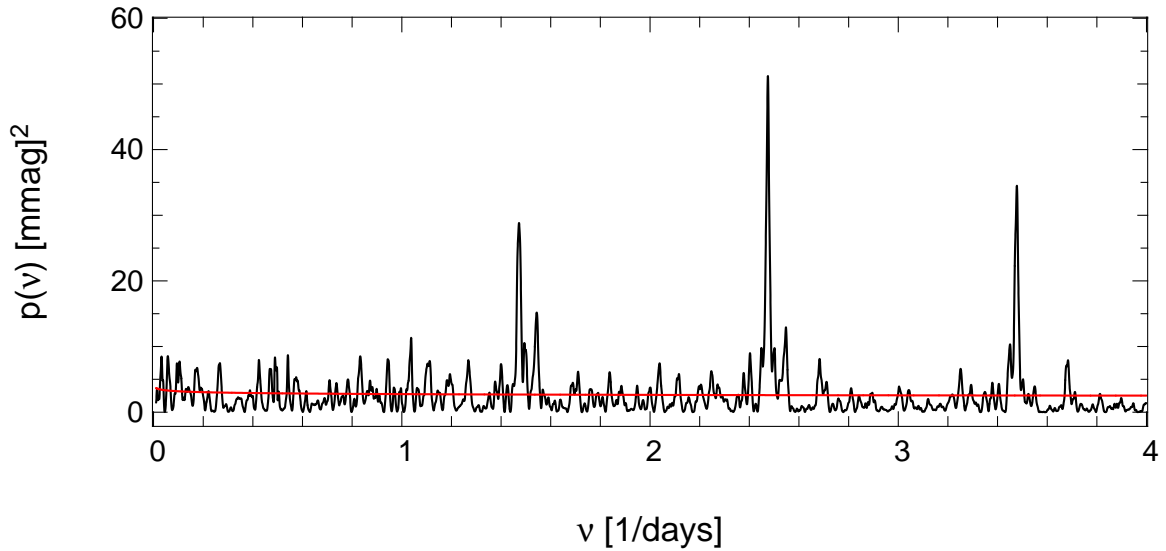
Figure 1.24: Power spectrum of candidate OGLE-TR-5. There are three peaks with $p(\nu) > 20$. The highest peak marks the ellipsoidal frequency $\nu_{c_2} = 2.475$ days^{-1} and two aliases at 1.475 and 3.475 days^{-1}. The red line shows a least-squares power law fit to the spectrum.

We calculate the power at each ellipsoidal frequency ranging from 0.22 - 3.5 d^{-1} (corresponding to orbital periods of 0.57 - 9.2 days):

$$p(\nu) = a_c(\nu)^2 + a_s(\nu)^2 \quad . \tag{1.21}$$

As an example we show in Fig. 1.24 the power spectrum of candidate OGLE-TR-5 with a clear signal
of ellipsoidal variations visible as a peak at the ellipsoidal frequency ν_{c_2}=2.475 days^{-1} (corresponding
to half the orbital period of 0.808 days).
The coefficient a_{c2} fitted at the frequency corresponding to half the orbital period is a direct indicator
for variations caused by tidal deformations of a massive secondary. Therefore, significant positive
value of a_{c2} can be used to rule out a planetary nature of a transit candidate. In order to estimate the
significance of a_{c2}, Sirko & Paczyński (2003) fit a 2 parameter power-law of the form

$$p(\nu) = p_0 \cdot \nu^{p_1} \tag{1.22}$$

to the power spectrum and estimate the statistical error σ at each frequency ν to be equal to
$\sqrt{p(\nu)/2}$. Fig. 1.25 shows the measurements of a_{c2} for 173 OGLE candidates. Rejecting candidates
with significant sinusoidal variations, the sample of transiting planet candidates can be reduced
significantly making the search for ellipsoidal variations a powerful tool in the process of eliminating
false candidates on light curve basis.

1.5.3 Low-precision spectroscopic follow-up observations

A first and low-cost step in the process of eliminating false positive candidates by follow-up
observations is to do low-resolution spectroscopy. A rough determination of the effective temperature
and surface gravity provides an estimate of the stellar radius and spectral type. The stellar radius, in
turn, can be used to determine an improved value for the radius of the candidate. If e.g. the host star
turns out to be an evolved star, the transiting object will be very large as well and the candidate is
most likely a stellar companion.
The measured stellar parameters can also be used to improve the light curve fitting. More realistic
limb-darkening coefficients and a more precise stellar radius decrease the parameter-space of the
fit. Possible false candidates will show systematic outliers in the residuals of the best fit, if the
photometric precision is good enough.

1.5.4 Medium-precision spectroscopic follow-up observations

Most false positive candidates are actually transiting low-mass stars or Brown Dwarfs which can
be excluded with medium precision RV measurements. This can be achieved either with medium
resolution spectroscopy at high S/N or with high resolution spectroscopy at medium/low S/N. Due to
the high mass, the amplitude of the RV variation is very large ($\sim$km/s) and a few measurements taken
at phases with the highest RV signal (close to phase values of 0.25 and 0.75) are sufficient to identify
and eliminate non-planetary candidates.
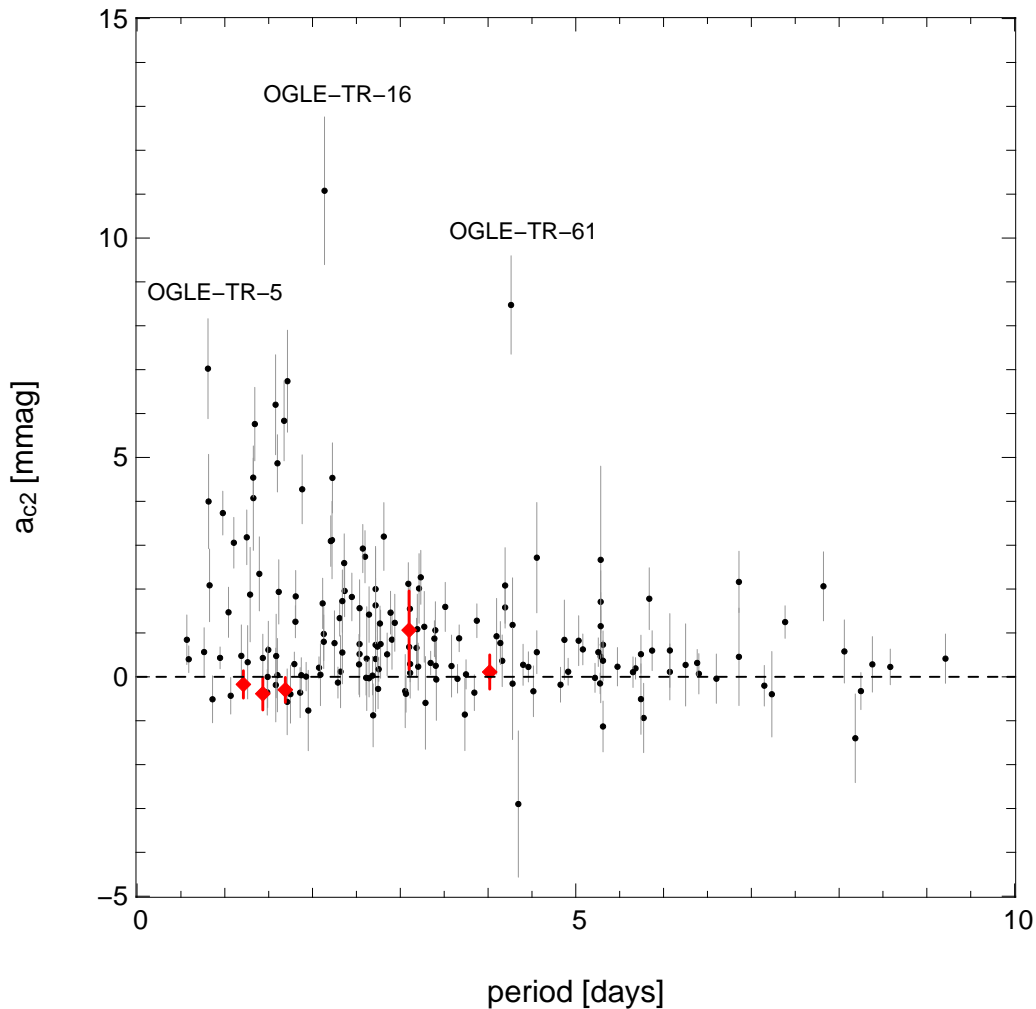
Figure 1.25: The values of the parameter a_{c2} as a function of period for 173 OGLE candidates. Positive values of a_{c2} indicate tidal deformations of a massive secondary rather than a planet. Up to 30% of all OGLE candidates show significant ellipsoidal variations. None of the negative values of a_{c2} is significant. The red diamonds represent the 5 confirmed planets found among the OGLE candidates.

1.5.5   High-precision spectroscopic follow-up observations

The final step in the follow-up process and confirmation of a transit candidate, is the accurate determination of its mass with high resolution spectroscopy. This is done as described in §1.3.4. Since the period and epoch of the transiting object are known and since most candidates are on circularized orbits, there is only one free parameter when fitting the radial velocity curve, namely the mass. Therefore, fewer measurements are required to confirm a transiting planet candidate compared to the number of measurements needed to detect planets with the RV method. Fig. 1.26 shows the RV measurements taken in order to follow-up and confirm the transiting planet WASP-2b.
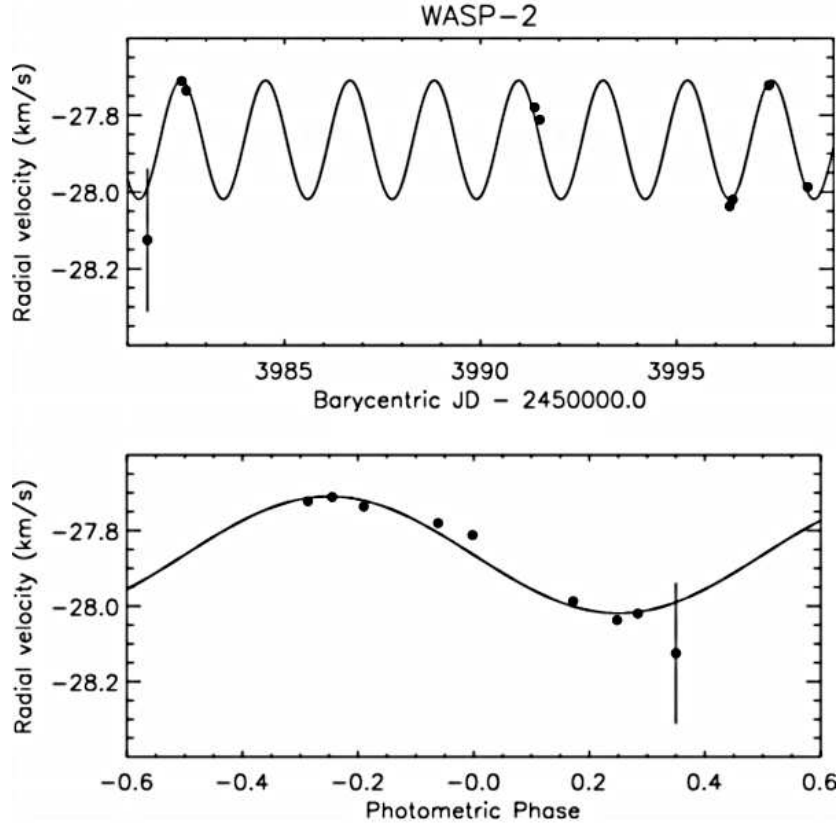
Figure 1.26: RV follow-up observations of WASP-2b. Since period, epoch and eccentricity of the orbit are known, 9 measurements suffice to derive the mass of the candidate and confirm its planetary nature (Cameron *et al.*, 2007).

Most currently detected candidates have visual magnitudes of 10 and more. The S/N of the spectra and therefore the precision of the RV measurements is generally lower than for the very bright objects targeted in RV surveys. This is particularly true for candidates found in deep surveys, such as the OGLE-III or the pre-OmegaTranS survey (see §2) where candidates down to V∼17 have been found.

The following formula provides an estimate of the expected precision of RV measurements:

$$\sigma_{RV} \approx 1.45 \times 10^9 \left(\frac{S}{N}\right)^{-1} R^{-1} B^{-\frac{1}{2}} \quad \left[\frac{m}{s}\right] \quad , \tag{1.23}$$

with the average S/N per resolution element, the resolving power of the spectrograph R and the covered spectral range B in Å. The formula was derived numerically (E. Guenther, private communications). For a typical S/N of 50, a resolution of 40 000-50 000 and a spectral coverage of ∼2 000 Å, the expected precision is 10-15 m/s. This is enough to derive masses down to 1 M_{Jup} for planets in short orbits around cool main-sequence stars.

One very important aspect in the process of confirming transit candidates with RV measurements

is the possibility that an eclipsing binary system that is blend by a foreground star may not show the expected large RV variations if the foreground source is a very large contribution the total light. In this case, the combined spectrum may be dominated by the foreground star in such a way that the varying eclipsing binary component can not be separated in the spectrum. It might only cause the spectral lines of the foreground star to become asymmetrically shifted towards higher or lower wavelengths. Cross-correlation with a template results in the detection of a small RV variation, as one would expect for a planet.

In order to rule out such a scenario, a careful analysis of line asymmetries has to be done by calculating the bisector of the cross-correlation function (see e.g. Queloz *et al.* (2001) or Santos *et al.* (2002)). The procedure has become a standard tool in excluding blend scenarios in the process of confirming transiting extra-solar planets with RV measurements (see §3).

1.5.6   Multi-band photometric follow-up observations

Multi-band photometric follow-up observations can aid in the process of eliminating candidates that are actually blend eclipsing binary systems. If the spectral type of the blending source differs significantly from the spectral type of the eclipsed primary, the amount of third light is different in each band. This results in a transit depth that is different in each band, or in other words in a color change during the transit (Tingley, 2004).

The 7-channel imager GROND is the ideal instrument for this kind of follow-up. A combined fit to the light curves in multiple bands can exclude a blended binary scenario, if the transit morphology of eclipsing binaries is found to be inconsistent with the observations (i.e. too wide and/or V-shaped or too color-dependent, see §3).

1.6 Follow-up Studies of Transiting Extra-Solar Planets

In contrast to all other detection methods, planets found with the transit method allow the observer to perform a variety of detailed follow-up studies. Analyzing the photometric and spectroscopic signals, we are able to uncover the composition of the planetary atmosphere and determine its surface temperature, an important step towards the detection of life in the universe. In the following we introduce the techniques that are currently used to study transiting extra-solar planets.
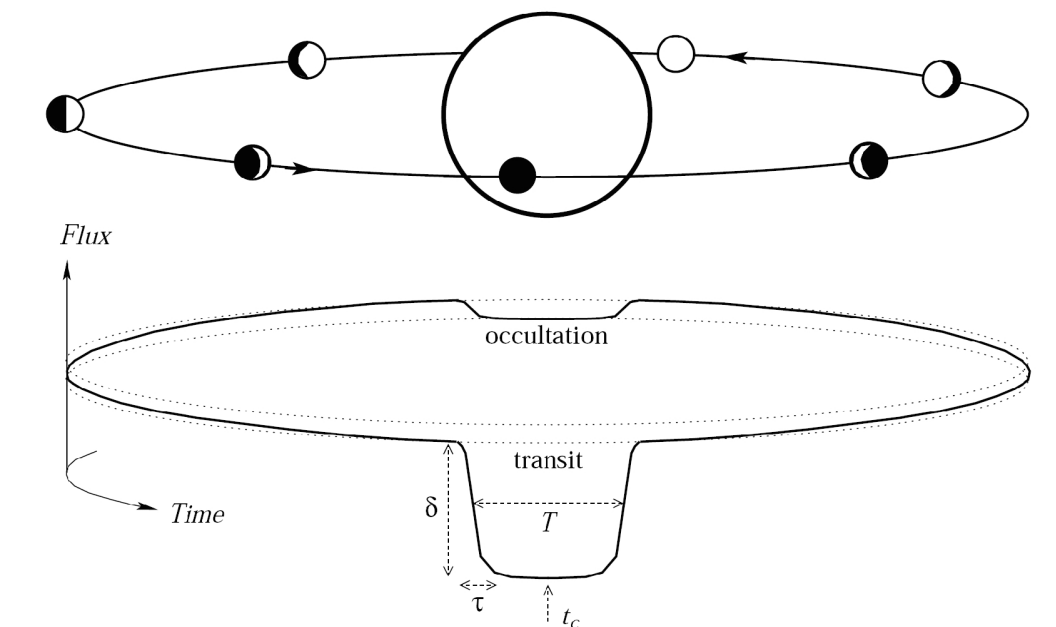
Figure 1.27: The orbit of a transiting planet (taken from Winn (2009)).

Analysis of the planetary atmosphere

During a transit, the light of the star shines through the atmosphere of a transiting planet (see Fig. 1.28). Comparing the spectra before and during the transit, the detection of additional absorption features can reveal the presence of atoms and molecules. Since the effect is very small, such measurements can presently only be done for very bright stars and exclusively from space.

Charbonneau *et al.* (2002) published the detection of sodium in the atmosphere of HD209458b. Using the Hubble-Space-Telescope STIS spectrograph, they found that the transit depth in a bandpass centered on the sodium feature is deeper by $2.32 \cdot 10^{-4}$ relative to the transit depth in comparison bands. In the following years, also atomic Hydrogen, Carbon and Oxygen have been found in the outer atmosphere of HD209458b (Vidal-Madjar *et al.*, 2003, 2004). More recently, Tinetti *et al.* (2007) detected a clear signal of water vapor in the transmission spectrum of HD189733b.
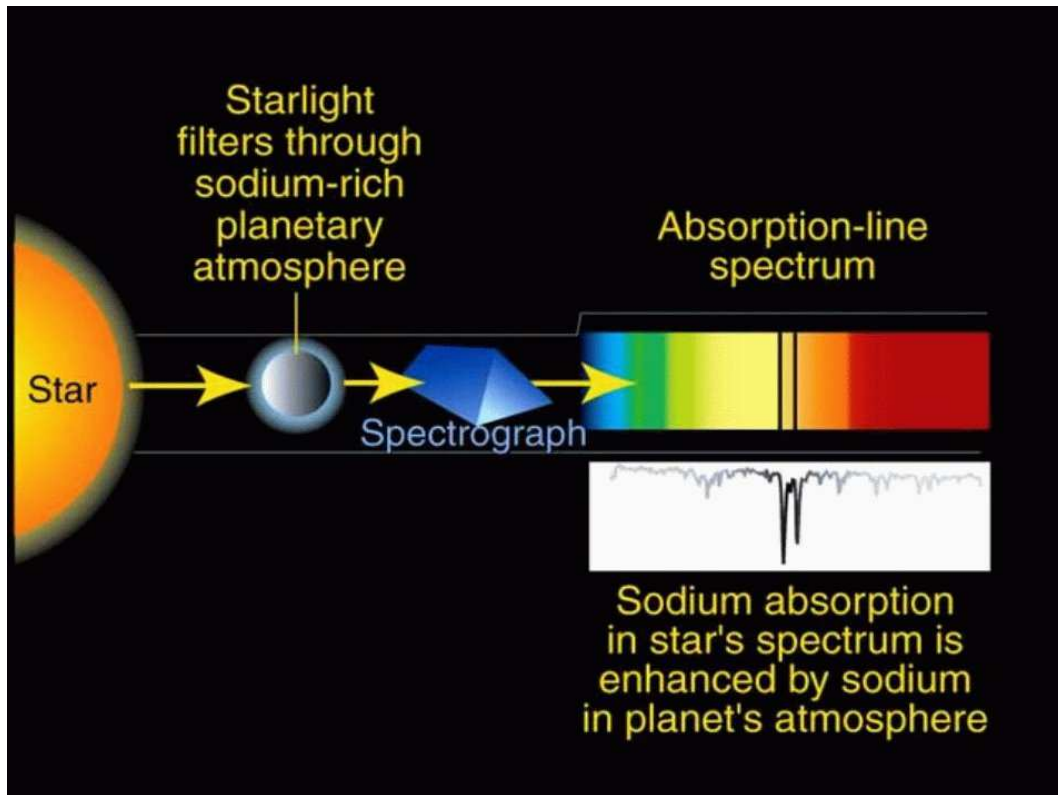
Figure 1.28:   Transmission spectroscopy of an extra-solar planet's atmosphere (taken from www.http://www.windows.ucar.edu/tour/link=/headline_universe/extrasolar.html).

Detection of thermal emission

Thermal emission of transiting extra-solar planets has been detected by several groups. During the secondary eclipse, i.e. when the planet disappears behind the star, the brightness drops by a small amount which is equal to the emitted light from the planet in the observed wavelength region. Assuming a black-body law the so-called brightness temperature of an extra-solar planet can be determined.

Infrared observations with the Spitzer Space Telescope (Werner *et al.*, 2004) have been used to successfully measure the day-side temperature of 6 planets so far. In two additional cases, TrES-3b and OGLE-TR-56b, a detection of a thermal signal was possible even from ground based observations. Table 1.4 gives an overview of the measured temperatures of extra-solar planets.

The observations of Knutson *et al.* (2007) span more than half of an orbital period, covering primary and secondary eclipse (see Fig. 1.29). Analyzing the brightness variations between both transits, they were able to derive also the night-side temperature which they found to be 973 ± 33K, indicating that the energy from the irradiated day-side is efficiently redistributed throughout the atmosphere.

planet	Temperature	wavelength	reference
GJ436b	717 ± 35K	8 μm	Demory *et al.* (2007)
	712 ± 36K	8 μm	Deming *et al.* (2007)
HD149026b	$2\,300 \pm 200$K	8 μm	Harrington *et al.* (2007)
HD189733b	$1\,117 \pm 42$K	16 μm	Deming *et al.* (2006)
	$1\,212 \pm 11$K	8 μm	Knutson *et al.* (2007)
HD209458b	$1\,130 \pm 150$K	24 μm	Deming *et al.* (2005)
TrES-1b	$1\,060 \pm 50$K	4.5 and 8.0 μm	Charbonneau *et al.* (2005)
TrES-3b	$2\,040 \pm 185$K	2.2 μm	de Mooij & Snellen (2009)
TrES-4b	$2\,290 \pm 220$K	8 μm	Knutson *et al.* (2009)
OGLE-TR-56b	$2\,718 \pm 117$K	1 μm	Sing & López-Morales (2009)

Table 1.4: Brightness temperatures of extra-solar planets derived from secondary eclipse measurements. Except for TrES-3b and OGLE-TR-56b, all observations have been done with the Spitzer Space Telescope.
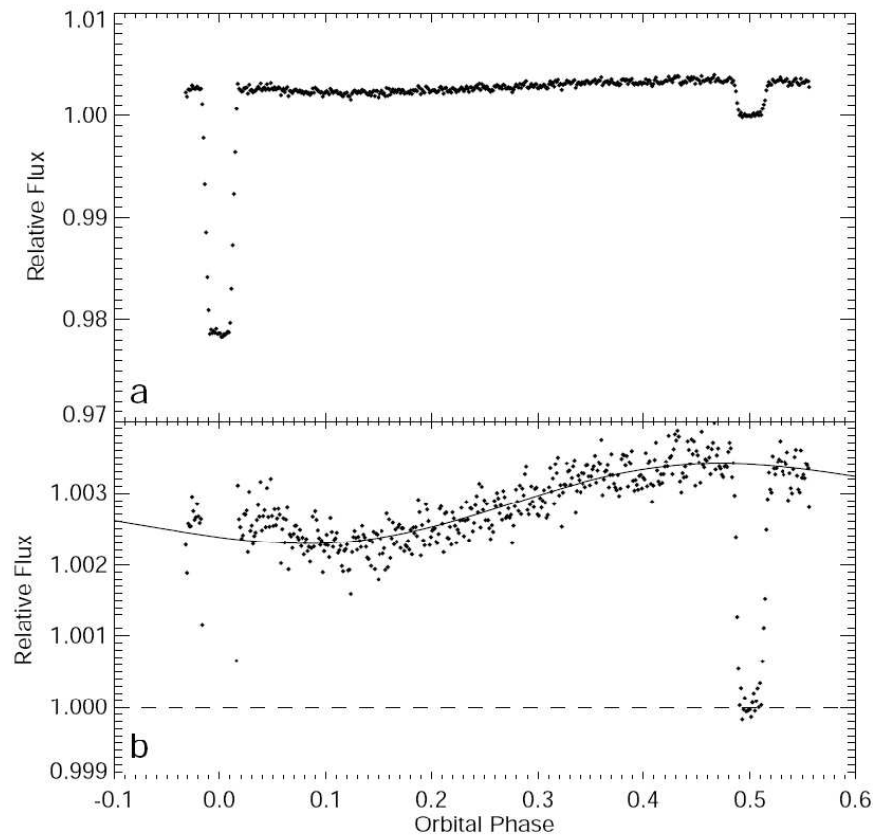
Figure 1.29: Infrared light curve of HD189733b showing primary and secondary eclipse and sinusoidal variations caused be a temperature gradient between day- and night-side.

In an advanced form, secondary eclipse measurements in multiple bands can be used to obtain a (very) low resolution emission-spectrum of a planet. Swain *et al.* (2008) measured thermal emission of HD189733b in 18 different bands between 1.5 and 2.5 μm. They conclude, that the observed intensity distribution indicates the presence of H_2O, CO_2 and CO in the planet's atmosphere (see fig. 1.30).
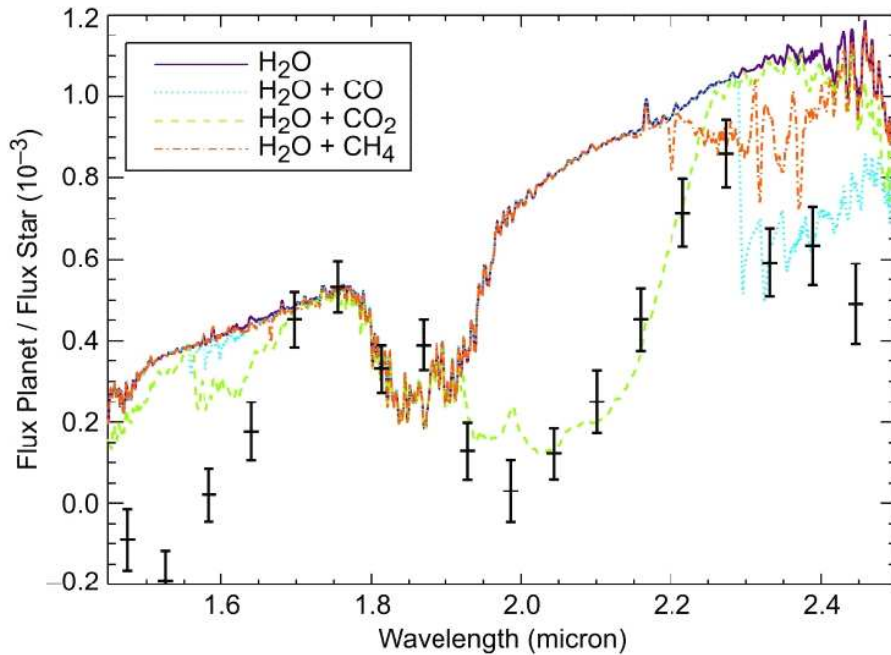
Figure 1.30: Day-side emission spectrum of HD189733b. The observed spectrum (black markers) is compared to model spectra with different components.

Analysis of the spin-orbit alignment

As the planet transits its host star, it covers different parts of the stellar surface. Since all stars are rotating, each surface element has a differential radial velocity whereas the measured radial velocity of the star is the sum of all surface elements. Blocking some fraction of the stellar light, the transiting planet causes a line-asymmetry which results in a small shift of the total stellar radial velocity that is measured during the transit (see Fig. 1.31). This is known as the Rossiter-McLaughlin-Effect (Rossiter, 1924; McLaughlin, 1924).

Using the Rossiter-McLaughlin-Effect, the alignment between the projected spin vector of the star and the orbital vector of the planet can be determined. According to planet formation theories (see §1.2), a good spin-orbit alignment is expected since the angular momentum should be the same for the star and the proto-planetary disk in which the planets form.
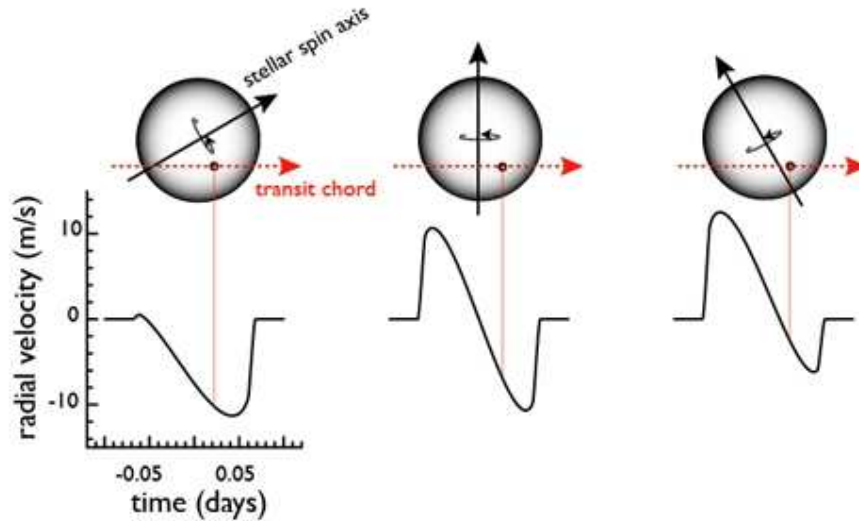
Figure 1.31: The Rossiter-McLaughlin-Effect (taken from www.oklo.org).

planet	projected spin-orbit angle	reference
HD209458b	-4.4° ± 1.4°	Winn *et al.* (2005)
	3.9° ± 20°	Queloz *et al.* (2000)
HD189733b	-1.4° ± 1.1°	Winn *et al.* (2006)
HD149026b	-12° ± 15°	Wolf *et al.* (2007)
HD17156b	62° ± 25°	Narita *et al.* (2008)
	9.4° ± 9.3°	Cochran *et al.* (2008)
TrES-1b	30° ± 21°	Narita *et al.* (2007)
TrES-2b	-9° ± 12°	Winn *et al.* (2008)
HAT-P-1b	3.7° ± 2.1°	Johnson *et al.* (2008)
HAT-P-2b	1.2° ± 13.4°	Winn *et al.* (2007)
	0.2° ± 12.3°	Loeillet *et al.* (2008)
WASP-14b	-14° ± 17°	Joshi *et al.* (2009)
CoRoT-2b	7.2° ± 4.5°	Bouchy *et al.* (2008)
XO-3b	37.3° ± 3.7°	Winn *et al.* (2009)
	70° ± 15°	Hébrard *et al.* (2008)

Table 1.5: Spin-orbit alignment of transiting extra-solar planets.

In Table 1.5 we summarize the results of all spin-orbit studies that have been done so far. In most cases there is a good alignment. Only two systems were found to be significantly misaligned: the controversial case of HD17156b and XO-3b where two authors measured a high value of the projected spin-orbit angle.

Detection of additional planets

Accurate measurement of transit timing variations (TTV) opens up the possibility to detect additional planets. The gravitational perturbation will cause the time between subsequent transits to change slightly (Holman & Murray, 2005; Agol *et al.*, 2005). The effect is especially high, if the perturbing planet is in a mean motion resonance. In this case, even Earth-mass planets can be found with current instrumentation. Fig. 1.32 shows the predicted TTV of HD209458b for a range of perturbing planets.
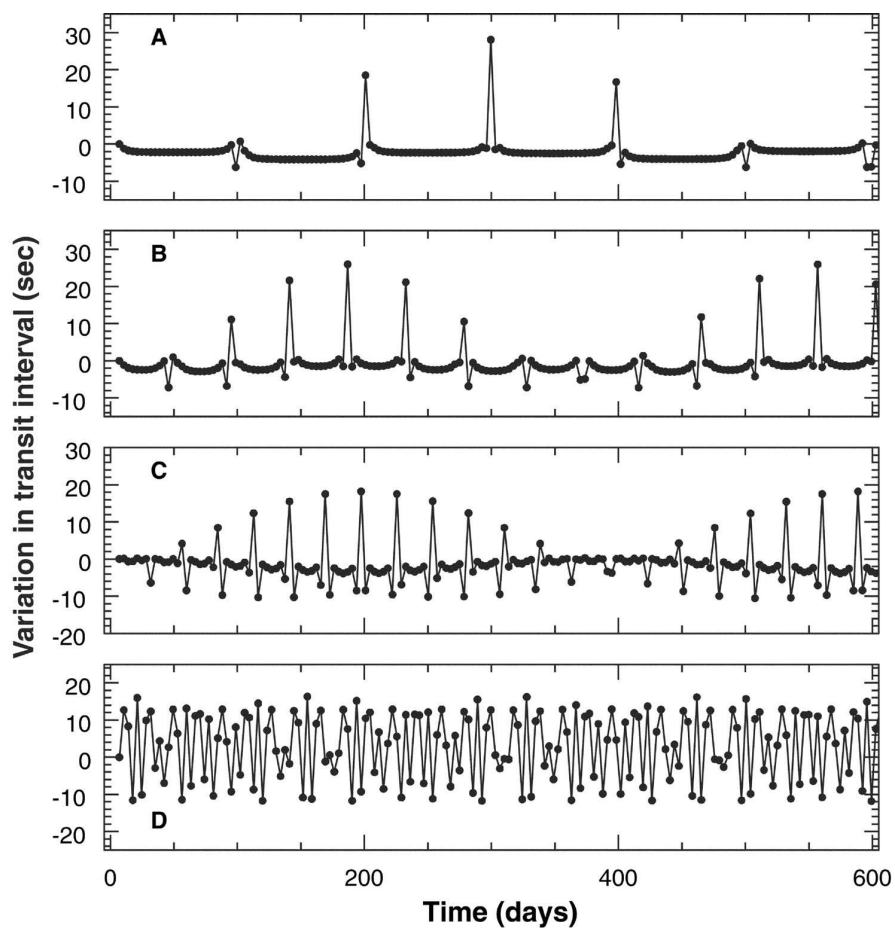
Figure 1.32: Theoretical TTV of HD209458b for a coplanar perturbing 1.05 M_{Jup} planet with an orbital period of 99.8, 46.4, 28.0, and 19.2 days (A to D) and eccentricity of 0.7, 0.5, 0.3, and 0.1 respectively (taken from Holman & Murray (2005)).

At the present time, no planet detection has been achieved by measuring TTV and only upper limits have been derived. However, a large number of groups have started to measure accurate transit times. Especially the space missions CoRoT and Kepler will be able measure TTV with a surpassing accuracy.

Detection of Moons

The detection of a photometric signal from moons of transiting extra-solar planets is extremely challenging, even from space, where the precision is enhanced by orders of magnitudes (Sartoretti & Schneider, 1999). Several authors have suggested to use TTV to search for extra-solar moons (Sartoretti & Schneider, 1999; Szabó *et al.*, 2006; Simon *et al.*, 2007). However, Kipping (2009) pointed out that the TTV amplitude is proportional to both the mass M_M and the orbital distance a_M of the moon

$$\delta_{TTV} \sim M_M \cdot a_M \quad . \tag{1.24}$$

He argues that since the period of the moon (and therefore the distance a_M) cannot be reliably determined from the TTV signal, the mass of a detected moon will remain unknown. However, he found that a moon will also cause transit duration variations (TDV) with

$$\delta_{TDV} \sim M_M \cdot a_M^{-1/2} \quad , \tag{1.25}$$

which is of a similar order of magnitude as δ_{TTV}. By combining the measurements of both TTV and TDV, the mass of the moon can be determined. According to Kipping (2009), TTV and TDV caused by a moon with 1 M_{Earth} orbiting the transiting planet GJ436b could be as large as 20s, which is within the reach of current photometric follow-up capabilities.

1.7 Habitability of Planets and the Search for Life

Mankind has always been curious about the existence of extra-terrestrial life. The discovery of the first planet around a main-sequence star (Mayor & Queloz, 1995) has caught the attention of both scientists and non-scientists and the ongoing search for extra-solar planets is now followed with great public interest. The results from the last years have shown that gaseous giant planets are common in the Galaxy and it is only a matter of time until the first rocky Earth-like planet is detected.

A new branch of science has been formed combining the two disciplines astronomy and biology. Astrobiology has been defined as "the study of the living universe" (NASA Astrobiology Institute, 2004). On purpose, this definition includes the study of life on Earth. In fact, since no extra-terrestrial life has been found so far, we have to learn from life on Earth and extrapolate our knowledge to other places in the universe.

What is life?

This is not a trivial question. There have been various attempts in the literature to find a comprehensive scientific definition of life, most of them face problems in the form of counter-examples. E.g., metabolic definitions of life find it hard to exclude fire (since it grows and reproduces through chemical reactions) and thermodynamic definitions find it hard to exclude mineral crystals (which create and sustain local order). For a more detailed discussion see Chyba & McDonald (1995) and Chyba & Hand (2005).

Maybe a purely scientific answer can never be given, since the question "what is life?" is partly philosophical. The focus of Astrobiology is therefore to study life not to find a definition for it.

Life on Earth is based on carbon chemistry. However, it would be naive to exclude the existence of life based on other elements, such as silicon (Feinberg & Shapiro, 1980). Nevertheless, several carbon-based molecules have been identified in the interstellar medium (Ehrenfreund *et al.*, 2002) whereas silicon-based molecules have not been found in a large number. This suggests that life is more likely based on carbon-chemistry. Anyway, it seems natural to first try to understand life as we know it. In the following considerations, we focus on extra-solar life that is similar to the life on Earth.

The Habitable Zone

Several groups have addressed the question of under which conditions a planet is suitable for the development of life (Rasool & de Bergh, 1970; Hart, 1979; Kasting, 1988). The presence of liquid water is an essential parameter since water acts as a polar solvent providing a medium in which molecules may dissolve and chemical reactions may occur.

The Habitable Zone (HZ) of a star has been defined as a shell in which liquid water can be present on the surface of a rocky planet (Kasting *et al.*, 1993). The inner edge of the HZ is determined by the photolysis of H_2O and the resulting H escape. The outer edge is determined by the creation of CO_2-clouds in the atmosphere of the planet which increase its albedo and cause a runaway glaciation process.

Within this range, the carbon-silicate cycle acts as a stabilizing negative feedback mechanism: CO_2 is removed from the atmosphere by weathering processes of calcium and silicon in rocks and subsequent precipitation as carbonate sediments. Vulcanism feeds back CO_2 into the atmosphere. There is a balance between both processes which stabilizes the Earth's climate (for more details about the carbon cycle we refer to Houghton (2003)). Conservative estimates for our Solar System define a HZ from 0.95 to 1.37 AU (Kasting *et al.*, 1993). Hotter stars have larger HZs.

As we know from the history of life on Earth, the development of complex organisms takes a long time. There is robust and abundant fossil evidence for life on Earth more than 3 billion years ago. In this time span, the Sun's luminosity increased by about 40%. As a consequence the HZ has evolved outwards. Kasting *et al.* (1993) define the continuous habitable zone (CHZ), as the shell around a star in which liquid water can be present over time scales of billions of years. According to conservative estimates, the 4.5 Gyr CHZ of the Earth around the Sun extends from about 0.95 AU to 1.15 AU.

The CHZ disappears for massive stars that have a main-sequence lifetime shorter than 4.5 Gyr. The development of life is therefore assumed to occur on planets around G-stars and later types. The CHZs of low-mass stars (later than mid-K) are at very close distances and lie within the tidal lock radius at which tidal interactions result in a permanent day- and night-sides of the planet and the loss of its magnetosphere. The synchronous orbit will make the planet a very harsh environment, which would very unlikely allow the development of life. In sumamry, G-Stars are the most interesting targets in the search for life because more massive stars have a shorter lifetime and less massive stars have a HZ that is too close.

The Galactic Habitable Zone

Several authors suggested that there might be a preferable region in our Galaxy for the development of life (Gonzalez *et al.*, 2001; Lineweaver *et al.*, 2004), often referred to as the Galactic Habitable Zone (GHZ). If the observed planet frequency metallicity relation for Jupiter-sized planets (see §1.4) can be extrapolated to rocky planets, the radial metallicity gradient in the Milky Way indicates that the more metal rich inner regions will bear more planets than the outer regions.

However, supernova explosions are expected to have a life-threatening effect on all neighboring stellar systems. The more dense regions in the bulge of the Galaxy and the starforming regions in the spiral arms may therefore impose a higher radiation risk for the development of life. In this context, our Solar System is located in a preferred location. At a distance of 8.5kpc from the Galactic center, the Sun is situated in the corotation zone, where it keeps pace with the spiral arms. Close supernova explosions have therefore been very rare in the past.

Taking into account both the metallicity effect and the supernova risk, Lineweaver *et al.* (2004) estimated the GHZ to extend from about 7 to 9 kpc distance from the Galactic center.

The Intelligent Universe?

Various attempts have been made to address the question whether or not intelligent species exist elsewhere in the universe. In the following, we summarize some of the most popular arguments for or against extra-terrestrial intelligence.

The Copernican principle: The Copernican principle states that the Earth is not in a central, specially favored position. This concept can be extended to say that humans are not privileged observers of the universe. As the Earth is only one of many planets in the Solar System, humans might be only one of many life forms that exist in the Universe.

The large number argument: In our universe, there are hundreds of billions of galaxies with each of them having hundreds of billions of stars. It seems natural to expect that at least some of these have planets upon which life has developed and advanced civilizations live. The famous Drake equation, which was written down as a meeting agenda for a conference held in November 1960 in Green Bank, is the mathematical representation of the large number argument:

$$N = R_\star \cdot f_p \cdot n_e \cdot f_l \cdot f_i \cdot f_c \cdot L \quad , \tag{1.26}$$

where the number of coexisting technically communicative civilizations in the Galaxy N is calculated by multiplication of the rate of star formation $R_\star$ with the fraction of stars that have a planetary system f_p, the average number of planets in each system that are suitable for the development of life n_e, the fraction of those on which life actually evolves f_l, the fraction of those on which intelligent life evolves f_i, the fraction of those which become communicative f_c and the average lifetime of such a communicative civilization L.

The problem with the Drake equation is that most of its factors can only be guessed. Only for the first three ($R_\star$, f_p and n_e) we have a reliable estimate. Probably the most uncertain factor is L, which could have a value of anything between the lifetime of a star ($\sim 10^{10}$years) and the time between the development of radio and the production of nuclear weapons ($\sim 10^2$ years). Therefore, the uncertainties in L alone frustrate any estimation of N.

Fermi's paradox: The Fermi Paradox is the apparent contradiction between a high probability of the existence of extra-terrestrial civilizations and the lack of evidence for it. If intelligent life were common, there must have been more advanced civilizations than mankind which long ago developed interstellar travel and would therefore have already populated the whole Galaxy and inevitably have reached the Earth. Since no signs of such civilizations have been found, they must not exist.
Several solutions to the Fermi paradox have been proposed. One (hopefully wrong) solution is that advanced civilizations have a high probability of destroying themselves on a short timescale. Another possibility is that we just did not look carefully enough to find other civilizations.

The Search for Extra-Terrestrial Life

The most promising scientific projects in the search for evidence of extra-terrestrial life are the ESA mission DARWIN (Cockell *et al.*, 2009) and NASA's Terrestrial Planet Finder (TPF) mission (Beichman *et al.*, 2006). Both projects aim at the detection and characterization of atmospheres of nearby Earth-like extra-solar planets using infrared interferometry and spectroscopy. In particular, the goal is to find signatures of so called biomarkers which indicate the presence of life on a planet. CO_2, H_2O are considered to be important for the habitability of a planet. Other molecules such as O_3 or CH_4 are resulting from biological activity.
Given the ambitious nature of both projects and the common problem of funding, NASA and ESA may in the end collaborate on a joint Darwin/TPF mission. Russia and Japan have also expressed their interest in contributing to the mission (according to www.esa.int).

The Search For Extra-Terrestrial Intelligence

One may ask, why take the detour of looking for biomarkers if we could as easily try to listen to signals emitted from other civilizations? In fact, the first thoughts in this direction were published by Cocconi & Morrison (1959) which is today considered to be the birthplace of SETI, the Search for Extra-Terrestrial Intelligence. Cocconi and Morrison proposed to use radio telescopes to search for signals with a narrow bandwidth close to the 21cm line of hydrogen.
A first SETI project named Ozma was conducted by Frank Drake back in 1960. In 200h he analyzed the signals of two stars with the new 85 foot radio telescope at Green Bank. Although Ozma did not find a signal from an extra-terrestrial civilization, it became the model for most future SETI projects. In November 1960, the Green Bank conference was the first place where scientists discussed the possibility of extra-terrestrial intelligence. Despite different opinions on various aspects, the general consensus was that intelligent life most likely exists outside Earth and that it was worthwhile to search for it.

However, only small surveys were conducted in the following years (e.g. Ozpa or Ozma II). One survey worth mentioning is the Big Ear project. In 1973, a radio antenna of the size of a soccer field started a continuous scan of the sky. On the 15th of August 1977, the Big Ear heard a strong signal that was recorded over a duration of 37s (which is the time needed for an object on the sky to move out of the view of the telescope). The detection became famous as the "Wow"-signal. To date there is no explanation that could rule out an alien origin. But unless the signal is detected again, we may never know for sure what the Big Ear heard.

The situation of SETI changed in the 70s, when NASA joined by sponsoring workshops and studies on the feasibility of SETI. Ambitious programs were designed such as the Cyclops mission (Oliver, 1973), a large array of radio telescopes with a diameter of a few km (see Fig. 1.33).
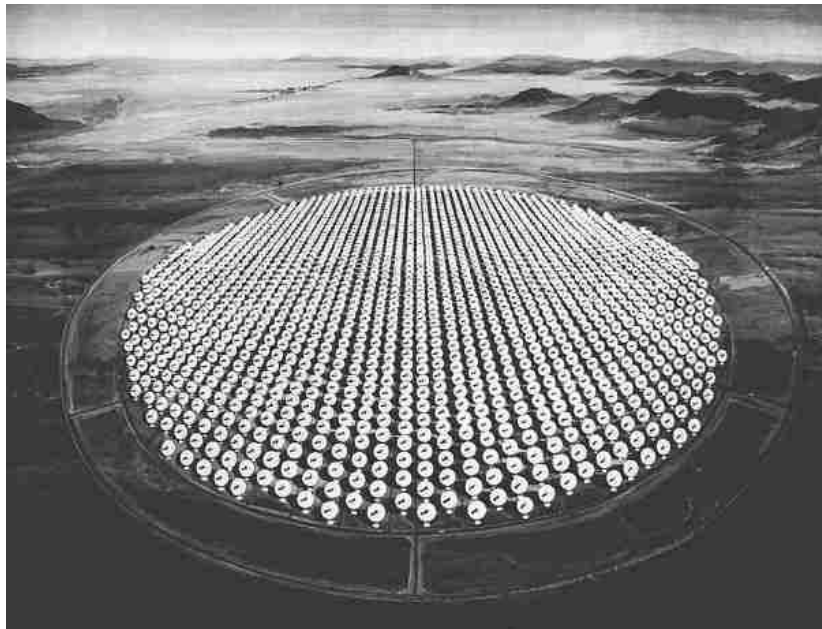
Figure 1.33: Artist's concept of the entire Cyclops system. The diameter of the antenna array is about 16 kilometers.

Ambitious projects needed extensive funding which was becoming more and more a problem for the proposed SETI. It was not until 1992 that NASA started a targeted SETI mission using the 305m Arecibo radio telescope in Puerto Rico. At the same time an all-sky radio survey began at a 34m dish at Jet Propulsion Laboratory. Surprisingly, only one year after its start, both projects were terminated. After an investment of around 60 million dollars over 23 years, and less than one year of operation, NASA's SETI project was dead.

When NASA pulled out, the SETI institute stepped in. Founded in 1984, the SETI institute sponsored and conducted research on SETI and life in the universe. The institute was able to raise enough private funding to save the targeted search that had been started at the Arecibo telescope.

From 1995 to 2004, a total of 1 000 solar-type stars closer than 200 pc were analyzed in the project Phoenix. The project was conducted on several big radio telescopes, namely the 64m telescope of Parkes Observatory in Australia, the 42m Green Bank Telescope and the 305m Arecibo telescope.

The ongoing untargeted search SERENDIP was started in 1996 at the Arecibo telescope. Permanently mounted, the SERENDIP receiver scans whatever region the telescope happens to point at. Due to a need for computational resources to analyze the enormous amount of data that is collected, the project SERENDIP invented SETI@home, a joint network of users that donate their computational resources to analyze a small subset of the recorded radio signals.

After the start of SETI@home in 1999, there was a stunning response. The idea of participating in such a fascinating process as the detection of alien life motivated computer users worldwide to let their computers run day and night with the hope of being the one who detects the first signal of an extra-terrestrial civilization.

Today, the SETI@home community has hundreds of thousands of members in more than 200 countries (see www.setiathome.org). Although no evident signal of an extra-terrestrial civilization has ever been found, people around the globe continue to let their computers search for signals from outer space, true to the motto of Cocconi and Morrison: "The probability of success is difficult to estimate; but if we never search, the probability of success is zero."

Chapter 2

The pre-OmegaTranS Survey

2.1 Abstract

In late 2004, a consortium of astronomers from INAF[1] Capodimonte (Italy), Sterrewacht Leiden (Netherlands) and MPE Garching (Germany) designed the OmegaCam Transit Survey (Omega-TranS). A total of 26 nights of guaranteed time observations with OmegaCam (Kuijken *et al.*, 2002) at the VLT Survey Telescope (Capaccioli *et al.*, 2002) were granted to this project by the three institutes. Scaling from existing surveys, OmegaTranS was expected to deliver 10-15 new detections per year with the main power being the large 1 sq.deg. field of view of the OmegaCam detector. Note that at that time only 8 transiting planets were known.

Due to ongoing delays in the construction and commissioning of the telescope, the start of the project has been delayed further and further. At the present time, we expect the telescope to be ready in 2010. Since there are already more than 50 transiting planets known today, the impact of OmegaTranS in its original design will not be very high. We therefore decided to change the strategy and optimize the survey for the detection of low-mass planets around M-dwarfs and Hot Jupiters in open stellar clusters.

In order to start the project and to collect the first data, we conducted a pre-OmegaTranS survey using the ESO Wide Field Imager (WFI) mounted on the 2.2m telescope at LaSilla observatory (Baade *et al.*, 1999). The aim of this project was, on the one hand, to finalize the set-up of the Omega-TranS data reduction pipeline and, on the other hand, to possibly find the first transit candidates.

In §2.2 we give an overview of the pre-OmegaTranS data set. Standard data reduction procedures are described in §2.3. In order to obtain absolute photometry and color information for each star in our target field, we perform a photometric calibration as explained in §2.4. The creation of the light curves using the difference imaging technique is presented in §2.5. In §2.6 we introduce our light curve analysis and candidate selection process and in §2.7 we present 4 transiting planet candidates that were detected. Simulations on the survey efficiency are summarized in §2.8. We present survey byproducts such as eclipsing binaries or other variable stars in §2.9. Finally, we draw our conclusion in §2.10

---

[1] Instituto Nazionale di Astrofisica

2.2   The Data

For the first season of the pre-OmegaTranS survey, we observed two adjacent WFI fields (OTSF-1a and OTSF-1c) which are the north-west and south-west corner of the previously selected best OmegaTranS field OTSF-1 (Barbieri, 2007). In the following seasons in 2007 and 2008, we decided to observe only OTSF-1a due to the limited amount of observing time that was available. The image center of OTSF-1a is at RA=13h35m41.6s and DEC=-66°42'21" and the field dimensions are 34'x33'.

As the outcome of 7 proposals (both for public ESO time and MPG reserved time), a total of 129h of observations were collected in the years 2006-2008. Spread over 34 nights, we obtained a total of 4433 pointings in the Johnson R-band (filter #844, see WFI user manual). The exposure time was 25s in most cases. Under very good and very bad observing conditions we slightly adjusted the exposure time in order to achieve a stable S/N and to avoid saturating too many stars. Fig. 2.1 shows the exposure time distribution of all pre-OmegaTranS images. The average cycle rate (exposure, readout and file transfer time) is 107s. There is a second much shallower peak in the cycle rate distribution (Fig. 2.2) at around 230s which is made of the few images taken in 2006 when we were alternating between two fields. In Fig. 2.3 we show the PSF FWHM (seeing hereafter) distribution of all observations. 167 images with a seeing larger than 2.5 arcsec are not used because of their bad quality.

In addition to the science images, we obtained calibration images (i.e. bias and flatfield exposures) for each of the 34 nights. The total uncompressed raw data set comprises 725 GBytes (589 GBytes science data, 136 GBytes calibration data).
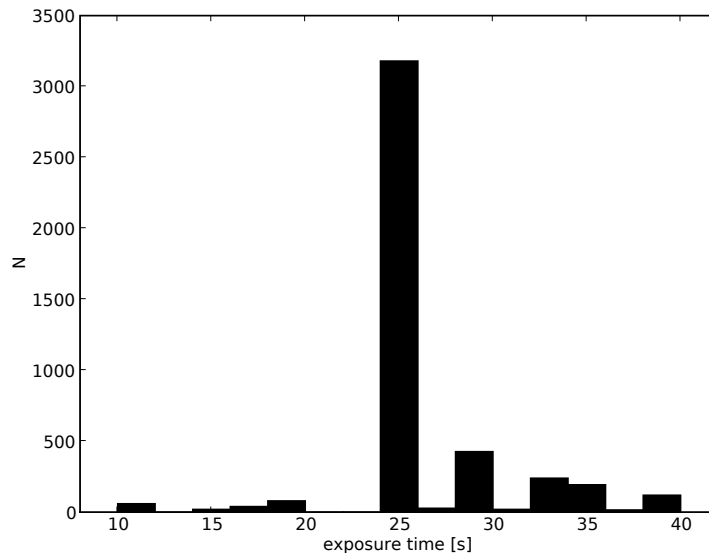
Figure 2.1: Exposure time distribution of the pre-OmegaTranS observations. Most images were exposed for 25s. Under very bad or very good seeing conditions we slightly adjusted the exposure time.
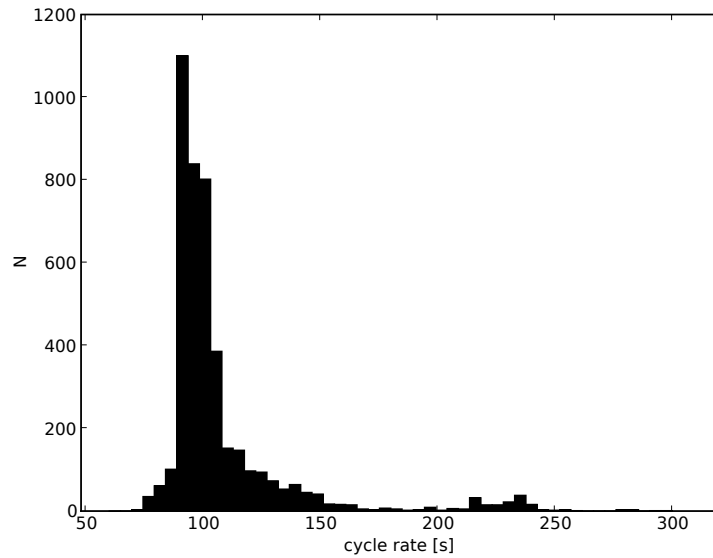
Figure 2.2: Cycle rate distribution of the pre-OmegaTranS observations. The typical time between two pointings was 100 seconds. Varying readout and data transfer times resulted in a broadening of the distribution. In 2006 we were alternating between 2 fields which roughly doubled the cycle rate, visible as a second much shallower peak at around 230s.
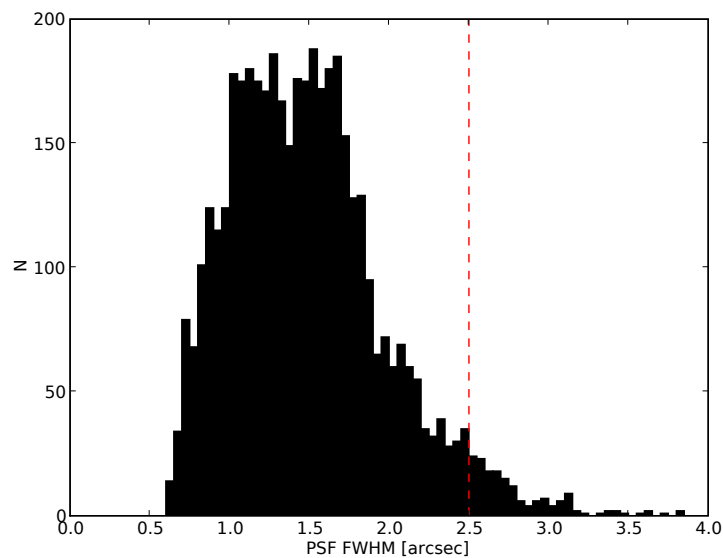
Figure 2.3: Seeing distribution of the pre-OmegaTranS observations. 167 pointings with a seeing larger than 2.5 arcsec are not used.

CCD	gain (e$^-$/ADU)	readout noise	bad pixel fraction
ccd50	1.98	5.68 e$^-$	2.56%
ccd51	1.95	5.62 e$^-$	0.58%
ccd52	2.24	5.62 e$^-$	0.75%
ccd53	1.95	5.50 e$^-$	2.49%
ccd54	1.99	5.75 e$^-$	0.45%
ccd55	2.00	6.00 e$^-$	6.77%
ccd56	2.13	5.39 e$^-$	2.28%
ccd57	2.14	5.37 e$^-$	0.97%

Table 2.1: WFI CCD characteristics. All CCDs have a size of 2kx4k pixel with a pixel scale of 0.238 arcsec/pixel.

2.3   Standard Reduction

The basic CCD data reduction steps were done using the Astro-WISE[2] standard calibration pipeline. For a complete description of all tasks we refer to the Astro-WISE User and Developer manual[3]. The data reduction pipeline treats all CCDs as independent detectors. Throughout this chapter, the term 'image' refers to the pixels of one single CCD.

2.3.1   The gain

The factor that is converting detector counts[4] into photon numbers is called *gain*. The *gain* of a CCD can be modified in order to adjust its dynamic range. This is usually done during commissioning of the detector. After that, the *gain* is only changed on rare occasions.

To measure the *gain*, one can use flatfield images with different signal levels. The idea is to measure the signal and variance of detector counts in several pairs of images, at different light levels. The inverse slope of the linear relationship between variance and signal is equal to the *gain*[5]. The measured values for each CCD are listed in Table 2.1.

Multiplication of the raw images with the *gain* value provides photon number counts for each pixel.

2.3.2   Construction of the master bias images

For each of the 34 nights we constructed a master bias image using a set of raw bias exposures. First we determined and subtracted the bias level of each single image as the per-row average values of the overscan in x-direction, smoothing the averages over 10 rows (method 10, in Astro-WISE). The bias level was different for each CCD and varying between 100-200 detector counts. To construct the master bias image, we averaged the overscan corrected single images applying a 3σ-clipping algorithm.

---

[2] Astronomical Wide-field Imaging System for Europe

[3] http://www.astro-wise.org/docs/Manual.pdf

[4] measured in Analog-Digital-Units (ADU)

[5] for further details see e.g. http://www.mirametrics.com/tech_note_ccdgain.htm

Further we were using two raw bias images of each night to determine the readout noise of the detector. The readout noise was calculated as the RMS of the difference of the raw biases divided by $\sqrt{2}$. The average readout noise values for each CCD are shown in Table 2.1, an example master bias image of ccd50 is shown in Fig. 2.4.

2.3.3   Construction of the master flatfield images

In order to correct for variations in the pixel-to-pixel sensitivity, for inhomogeneous illumination of the CCDs and for dimming effects caused by dust pollution of the optical elements, we constructed a normalized sensitivity map for each night, a so called master flatfield image. Dividing the science images by the master flatfield we removed all of the linear effects.

In order to create a master flatfield image, one can either use images of a uniform illuminated screen that is placed within the telescope enclosure (domeflats) or images of the twilight sky (skyflats). One disadvantage of domeflats is that the light does not enter the telescope in parallel beams (since the dome screen is very close to the telescope). Therefore only the pixel-to-pixel variations are well represented whereas the illumination pattern and dimming effects are not. In case of skyflats, all light beams enter the telescope almost parallel. Pixel-to-pixel variations, illumination pattern and dimming effects are well represented. Unfortunately, skyflats can only be taken in perfectly clear sky conditions and in the limited twilight period. As a consequence, skyflats are not always available and the S/N is usually lower compared to domeflats.

To construct the master flatfield images, we combined domeflats and skyflats. Using a Fast-Fourier-Transformation algorithm, the master flatfield was constructed by extracting low spatial frequency components from the skyflat and high spatial frequencies from the domeflat (combine type 1, in Astro-WISE). An example master flatfield image of ccd50 is shown in Fig. 2.4.

2.3.4   Construction of the bad pixel masks

All pixels with non-linear response were considered to be not useful or 'bad' pixels. Pixels with values that are systematically too high (hot pixels) were identified as positive 5σ-outliers in the master bias images. Pixels with values that are systematically too low (cold pixels) were identified in the master flatfield images as pixels that are more than 6% below the local detector count level.

Combining the hot pixel maps (one for each master bias image) and the cold pixel maps (one for each master flatfield image) we constructed a master bad pixel mask for each of the 8 CCDs which we applied to all science images. In addition to hot and cold pixels we masked bad columns that have been identified by eye. The fraction of masked pixels is listed in Table 2.1 for each CCD. In Fig. 2.4 we show the bad pixel mask of ccd50 (right panel).

2.3.5   Data reduction of the science images

To all raw science images we applied an overscan correction and subtracted a normalized master bias image (see §2.3.2). Further we divided each science image by a master flatfield image (see §2.3.3). All nonlinear pixels and bad columns were flagged using the master bad pixel mask. In some images, tracks of coincidentally observed satellites were visible. We detected the tracks using a Hough transform (Duda & Hart, 1972) and masked all affected pixels.
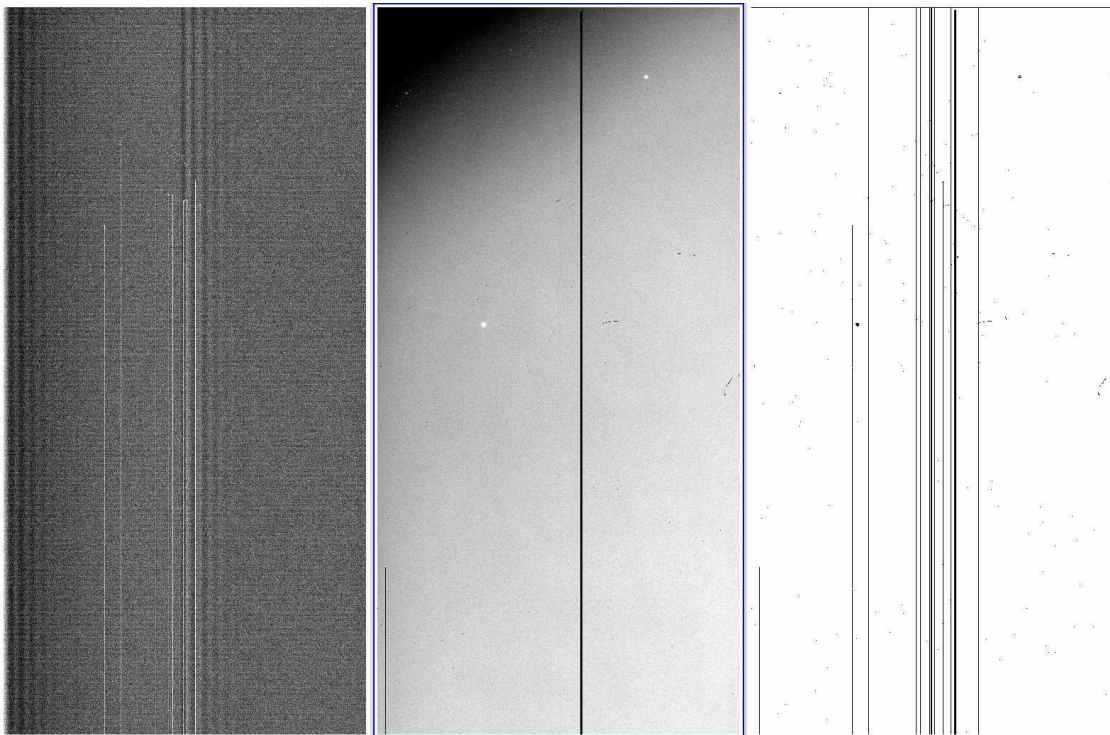
Figure 2.4: Example master bias image (left), master flatfield image (middle) and master bad pixel mask (right) of ccd50.

2.3.6   Cosmic ray filtering

Cosmic rays and high energy particles originate from radio-active decay within the camera and hit the detector during the exposure and readout process. This is visible as very narrow peaks in the images (cosmics). We identified cosmics using a 5-parameter Gaussian fit (for elongated cosmics) and a 3-parameter Gaussian fit (for circular cosmics) to all local maxima in each image. If the FWHM of a local maximum was found to be smaller than 1.5 pixel (0.36 arcsec) and if the amplitude of the Gaussian fit was more than 5σ higher than the local background, the local maximum was considered to be a cosmic and all pixels that are 2σ higher than the local background were masked.

2.3.7 Astrometry

All images of one CCD roughly map the same part of the sky. However, small shifts of the individual exposures (smaller than 20 pixels) arise from a limited pointing accuracy and dithering[6].

For the following data reduction steps, it was necessary to align all images with a sub-pixel precision. In Astro-WISE, this is done with the LDAC tools (Deul *et al.*, 1995). There are two possibilities for calculating the astrometric solution: astrometry of one image relative to an external reference catalog (e.g. USNO-A2.0, Monet (1998)) and astrometry of one image relative to a reference image. The first method is used to a achieve a good absolute astrometric calibration whereas the second method is better in achieving a good relative astrometry (because of a higher number of reference stars and smaller proper motion[7] effects).

We calculated the absolute astrometric solution only for the best seeing image. The positions and brightnesses of several hundred stars were measured with SExtractor (Bertin & Arnouts, 1996) and compared to the USNO-A2.0 catalog. Using least-square methods, a transformation was calculated that corrects for a shift, a rotation and a 3rd order polynomial distortion.

For all other images we performed a relative astrometric calibration in order to optimize the overlap of all sources in the whole field of view of one CCD. The procedure of deriving the relative astrometric solution is the same as for absolute astrometry with the only difference that we replaced the USNO-A2.0 reference catalog by a catalog that has been extracted from the reference image (see §2.5.1). Typically 300-400 reference stars were used to derive the relative astrometric solutions of the 4266 single images. Fig. 2.5 shows the spatial residuals of one astrometic solution. In Fig. 2.6 we plot a RMS-histogram of all astrometric solutions with RMS $\leq$ 0.1 arcsec. Only 12 images had an RMS larger than 0.1 and were not used in the following.

After calculating the astrometric solution (either with absolute or relative astrometry), each image was resampled to a new grid with a smaller pixel scale of 0.2 arcsec/pixel using the program SWarp[8]. The redistribution of the flux was done with a LANCZOS3 interpolation algorithm.

---

[6] the pointing of the telescope is shifted on purpose by a few pixels in order to avoid that the stars always fall on the same pixel on the detector which would increase the amount of correlated noise in the light curves

[7] due to small differences in the motion of the stars in the Milky Way, the stellar positions on the sky are changing with time; this effect is larger for closer stars

[8] http://terapix.iap.fr

DATE_OBS = 2006-07-30 02:50:57   <DRA>   = 0.00198 +- 0.03715

<RA> = 204.44238   <DDEC> = 0.00010 +- 0.02423

<DEC> = -66.56024   RMS = 0.04440

N = 368   CHIP: ccd50   Max = 0.12013

Residuals for
Sci-TESTJKOPPENH-WFI-------#84 . . . 0dd6bc054008d62cf88baca5f.fits
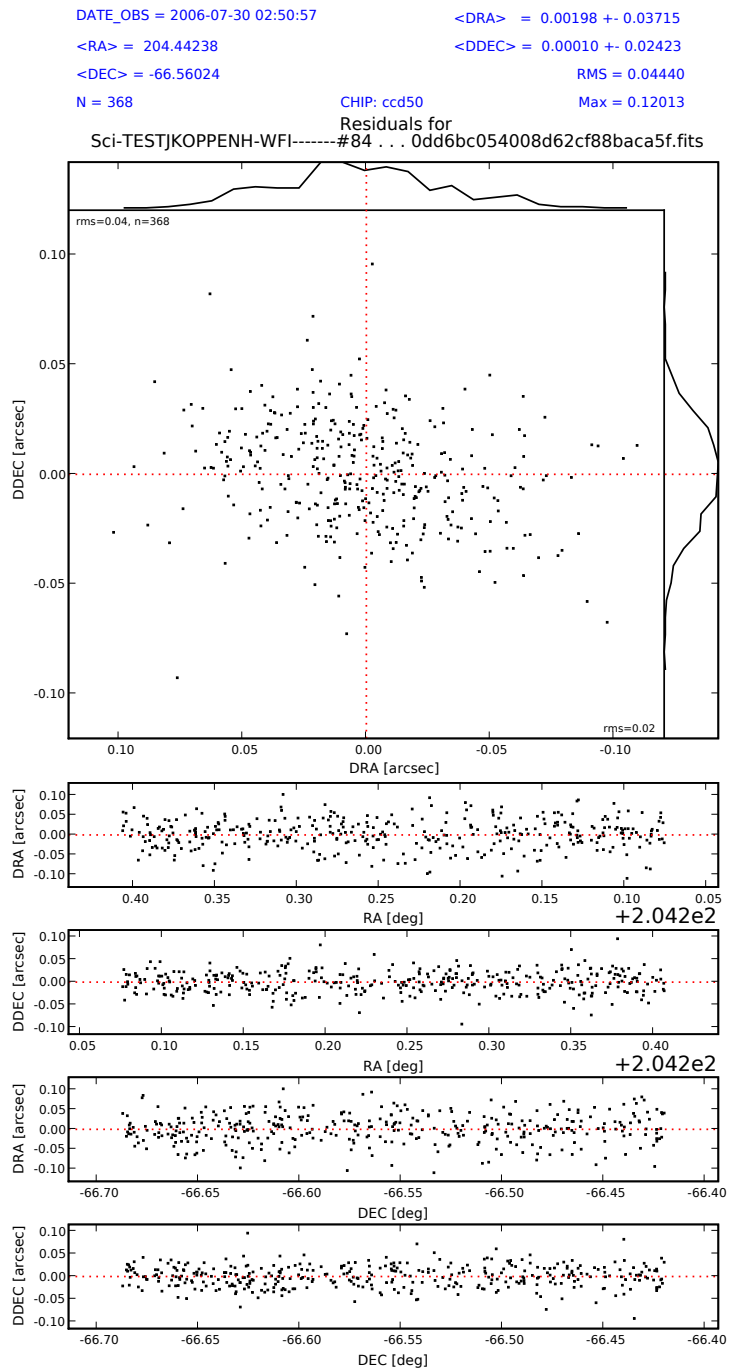
Figure 2.5: Spatial residuals of an arbitrary astrometric solution.
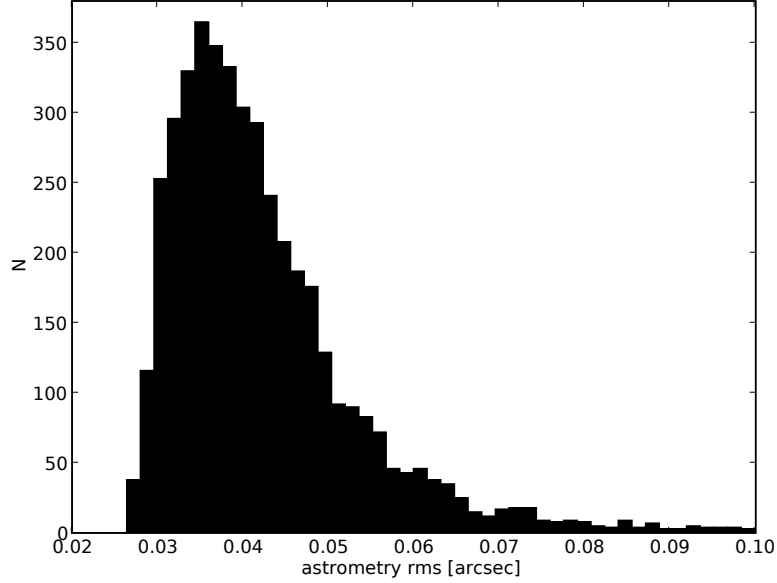
Figure 2.6: RMS histogram of all astrometric solutions. The median value is 0.04 arcsec. We use all images with an RMS smaller than 0.1 arcsec.

2.4 UBVRI Photometry

In order to determine absolute magnitudes and colors for each star in our target field, we performed a photometric calibration. On March 25th 2006, we obtained 3 dithered U-band exposures (filter #877) of OTSF-1a. Furthermore, on March 28th 2006, we obtained 3 dithered exposures in B-, V-, R- and I-band (filter #878, #843, #844 and #879). Table 2.2 list the observing conditions of the photometric calibration images.

We transformed the measured magnitude $m_{meas,i}$ (see below) of each star i into a calibrated magnitude $m_{cal,i}$ according to the following formula:

$$m_{cal,i} = m_{meas,i} + 2.5 \cdot log(exptime) - E_f \cdot airmass + C_f \cdot color_i + ZP_{f,c} \quad . \tag{2.1}$$

The first correction term normalizes the measurements to 1s exposure time. The second term corrects for extinction in the Earth's atmosphere[9] with a filter-dependent extinction coefficient E_f. The third term accounts for differences in the transmission curve of the WFI filters to the Johnson-Cousins filter system. Lastly, the zeropoint $ZP_{f,c}$ (which is different for each filter and CCD) is added to account for overall throughput of the telescope-camera system.

---

[9] the airmass is the amount of air that the light from a distant source has to pass until it enters the telescope; in plane parallel approximation, the airmass is equal to 1/cos(z) with z being the zenith distance

filter	airmass	exposure time	seeing
U	1.26	3x300s	1.15"
B	1.40	3x30s	1.05"
V	1.38	3x24s	0.85"
R	1.36	3x10s	0.90"
I	1.35	3x17s	1.00"

Table 2.2: Observing conditions of the images used for the photometric calibration.

	U	B	V	R	I
ext	0.48	0.23	0.18	0.16	0.11
col	0.05	0.25	-0.13	0.00	0.03

Table 2.3: Extinction and color coefficients. The B, V, R and I-band extinction coefficients have been measured whereas the U-band extinction coefficient and all color coefficients were taken from the WFI web page.

The color coefficients are fixed properties of the WFI-filters and have been published on the WFI web page[10]. The extinction coefficients and zeropoints, however, change with time and have to be measured using standard star observations. For the calibration in B-, V- R- and I-band, 4 observations of standard star fields (Landolt, 1992) were taken at various airmasses. This enabled us to determine the extinction coefficients and zeropoints in these bands. For the U-band calibration, there were only 2 Landold standard star field observations available, taken at almost exactly the same airmass. Therefore, we had to use the U-band extinction coefficient published on the WFI web page.

After standard reduction of the images (as described in §2.3), we performed aperture photometry on all stars in the Landolt fields and compared the measurements to the values in the reference catalog. In order to have almost all flux within the aperture (independent from seeing), it is important to use a big aperture when measuring the reference star fluxes. We used an aperture with 30 pixel diameter ($\hat{=}$ 6 arcsec). We compare our measurements to a reference catalog that has been exported from Astro-WISE which contains measurements from Landolt, Stetson (Stetson, 2000) and from the Sloan Digital Sky Survey (SDSS) Data Release 5 (Adelman-McCarthy *et al.*, 2007). SDSS measurements were transformed into the Johnson-Cousins filter system using the equations given in Jester *et al.* (2005).

In order to derive the extinction coefficients E_f for B-, V-, R- and I-band, we first corrected the measured values $m_{meas,i}$ for exposure time and color term (see eq. 2.1) and then fitted a linear function to the residuals as a function of airmass. We iteratively clipped 2.5σ outliers in order to improve the stability of the fit.

We assumed that the extinction coefficient is independent of CCD number and used the average of the values we obtained for the individual CCDs. Table 2.3 lists the measured extinction coefficients for B-, V-, R- and I-band as well as the extinction coefficient of the U-band and the color coefficients that were taken from the WFI web page.

After the extinction and color term correction, we derived a zeropoint for each CCD and filter by fitting a constant offset to the residuals. Table 2.4 lists our measured zeropoints. The errors of the zeropoints were estimated from the RMS of the final residuals.

---

[10]http://www.eso.org/sci/facilities/lasilla/instruments/wfi/inst/zeropoints/

CCD	ZP_U [mag]	ZP_B [mag]	ZP_V [mag]	ZP_R [mag]	ZP_I [mag]
ccd50	22.32±0.06	24.77±0.03	24.12±0.04	24.46±0.05	23.36±0.09
ccd51	22.20±0.11	24.88±0.02	24.24±0.03	24.55±0.03	23.48±0.05
ccd52	22.20±0.09	24.66±0.04	24.01±0.03	24.37±0.06	23.29±0.07
ccd53	22.18±0.06	24.83±0.05	24.20±0.03	24.55±0.09	23.42±0.08
ccd54	22.24±0.12	24.80±0.03	24.15±0.04	24.54±0.09	23.41±0.08
ccd55	22.25±0.12	24.89±0.05	24.24±0.04	24.58±0.07	23.47±0.09
ccd56	22.14±0.10	24.82±0.04	24.19±0.04	24.51±0.05	23.39±0.05
ccd57	22.21±0.11	24.66±0.04	24.03±0.03	24.39±0.06	23.31±0.07

Table 2.4: Measured U-, B-, V-, R- and I-band zeropoints of each CCD.

As an example we plot the residuals of the photometric calibration in B-band. In Fig. 2.7, we show the residuals after correcting for all but the extinction term as a function of the airmass. The slope of the fit to the residuals (black line) reveals the extinction coefficient E_B. In Fig. 2.8, we show the residuals after correcting for all but the color term as a function of color. The black line which corresponds to C_B=0.25 fits well to the residuals which confirms the color coefficient taken from the WFI web page.

In order to check if we had to correct for zeropoints variations over the field of view of one CCD (known as illumination correction), we plot the residuals as a function of x- and y-position on the CCD (Fig. 2.9). We found no strong trends and therefore used a constant zeropoint for each CCD. We plot the final residuals as a function of Universal Time (UT) in order to proof that the night was indeed photometric (Fig. 2.10).
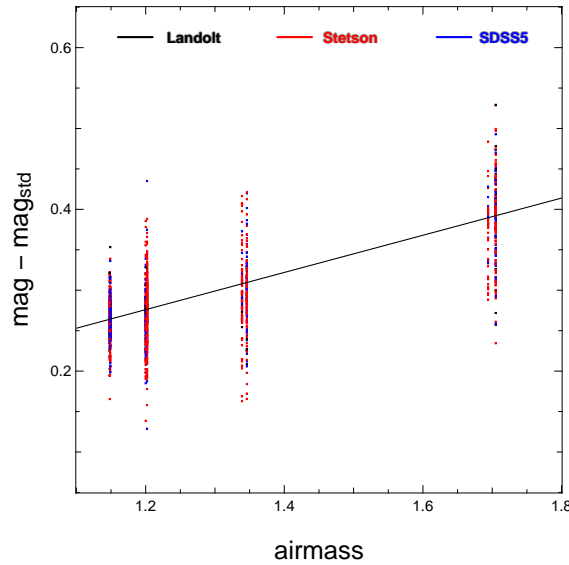
Figure 2.7: Residuals of the photometric B-band calibration as a function of airmass. Different colors represent different reference catalogs. Using a linear fit to the residuals (black line) we determined the extinction coefficient.
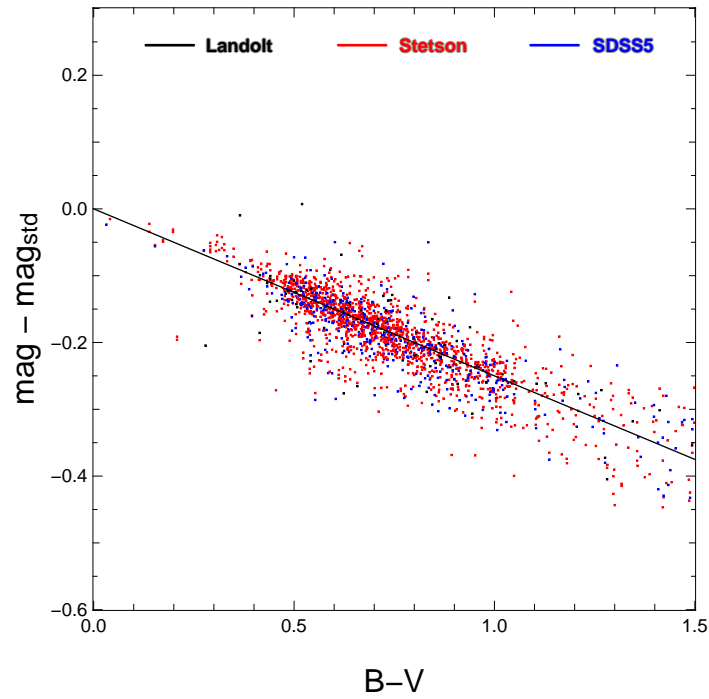
Figure 2.8: Residuals of the photometric B-band calibration as a function of color. The inverse slope of the black line represents the color coefficient that we obtained from the WFI web page which fits well the observed residuals.
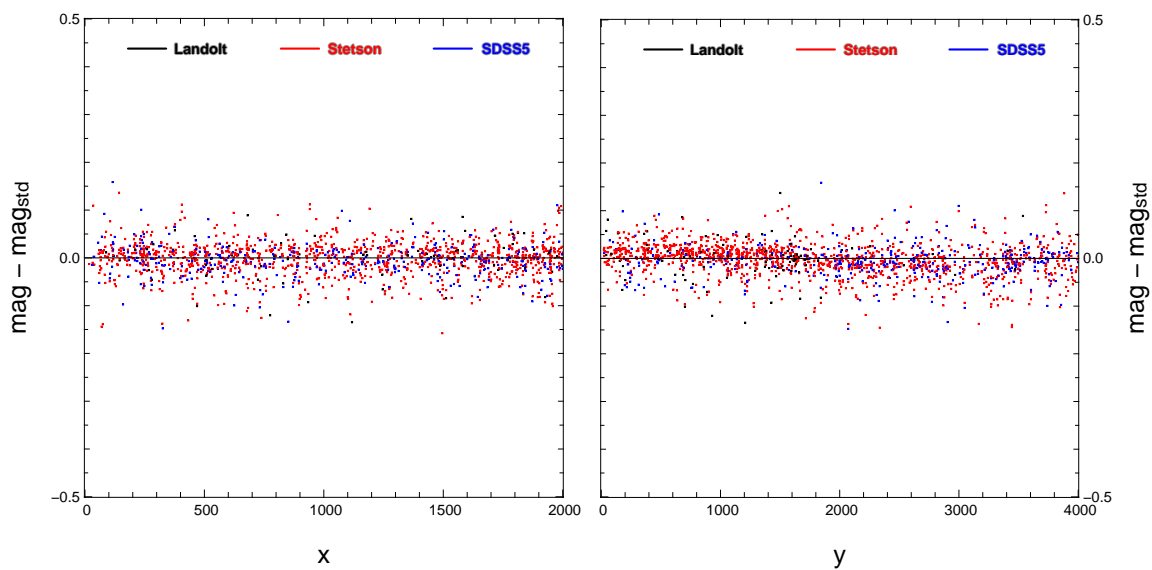
Figure 2.9: Final residuals of the photometric B-band calibration as a function of x- and y-position.
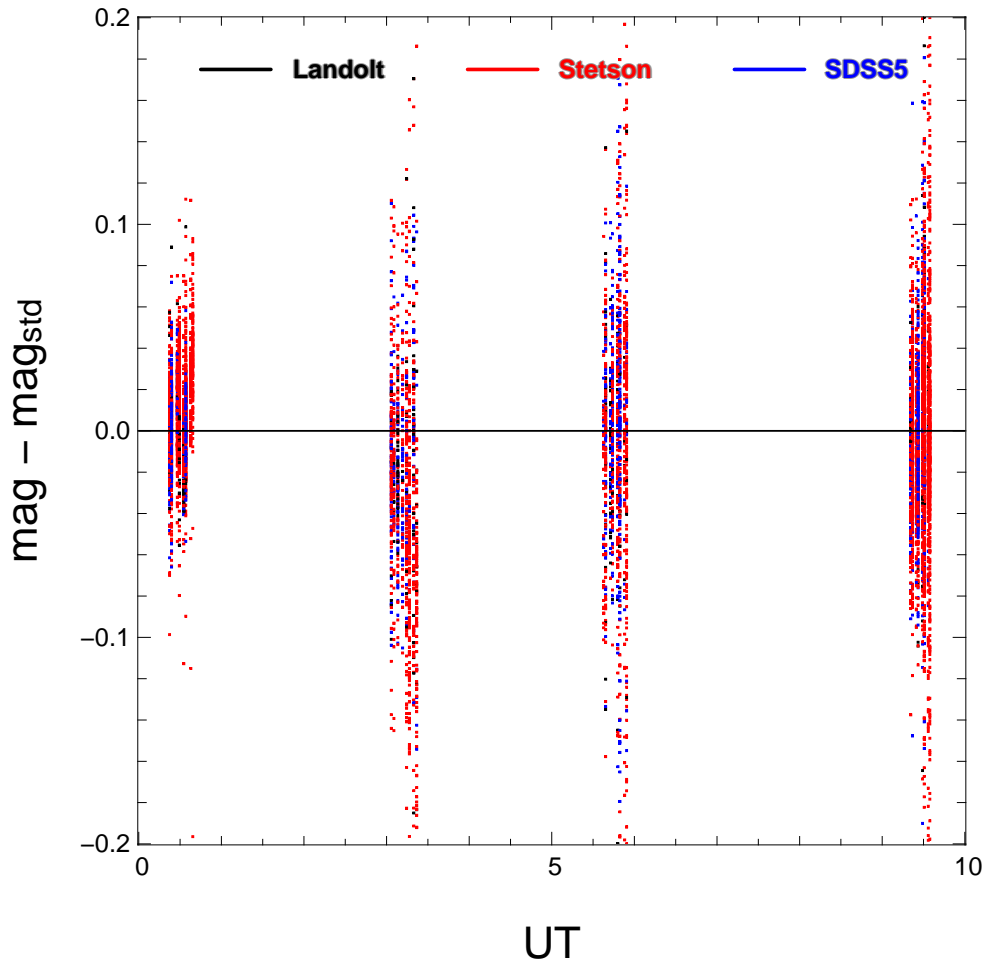
Figure 2.10: Final residuals of the photometric B-band calibration as a function of universal time. No strong trends are visible indicating photometric conditions for this particular night.

In order to derive the U-, B-, V-, R- and I-band magnitudes of all stars in our target field, we performed aperture photometry on each of the OTSF-1a images (3 per filter). Since the field is very crowded, the sources lie all very close to each other. Neighboring stars would corrupt the measurements, therefore we could not use a big aperture. For faint sources, a big aperture (such as 30 pixel) is also not the best choice in terms of S/N, since the background dominates the stellar photons in the outer regions of the PSF. Increasing the aperture size results in a large increase in background noise but only a small increase in signal.

In order to optimize the S/N we used SExtractor with different aperture sizes on one of the R-band images and plotted the median of the photometric errors of all stars as a function of aperture radius (Fig. 2.11). The highest photometric precision was achieved with a 15 pixel aperture (red line) which we used in the following.
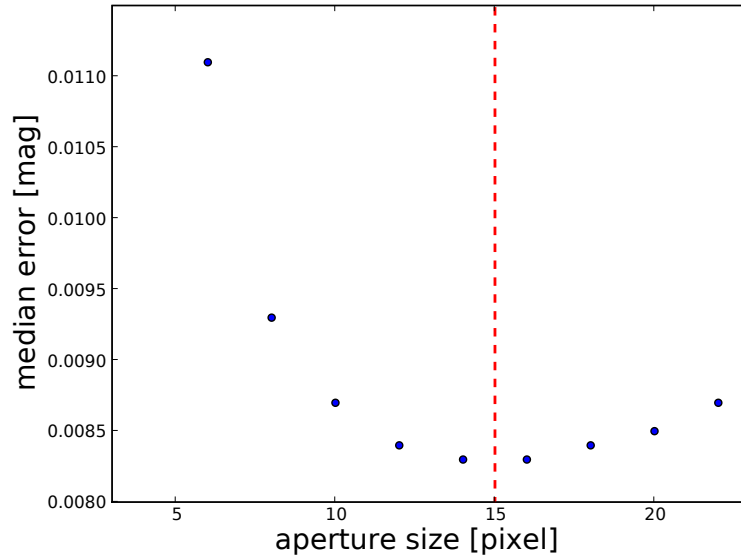
Figure 2.11: Photometric precision vs. aperture size for one of the R-band images. The optimal aperture diameter is 15 pixel which corresponds to 3 arcsec.

Since we cut-off the PSF at a shorter radius we were loosing some flux and the previously determined zeropoints are not valid without correcting for this effect. An aperture correction has to be applied that is depending on the PSF shape, where a broader PSF needs a higher correction. Using bright stars we estimated the difference between a 30 pixel aperture and a 15 pixel aperture. For sources with no bright close neighbors the difference between the two measurements was equal to the aperture correction. For blended sources the 30 pixel aperture gave a too high value therefore the difference was larger (more negative).

In Fig. 2.12 we plot the difference between a 30 pixel aperture and a 15 pixel aperture for all source in one of the V-band exposures. The red line marks the aperture correction we derived. Note that we calculated this correction for each of the 3 exposure and then used the average value for the correction.

Fig 2.13 shows the aperture correction as a function of PSF radius. Images with a broader PSF needed a larger (more negative) correction since more flux was lost in the smaller aperture.

Using eq. 2.1 and applying the aperture corrections to the measurements, we were able to derive the absolute U-, B-, V-, R-, and I-band magnitudes of each star in our target field. Since we had 3 observations of OTSF-1a in each band, we obtained 3 independent measurements. In order to eliminate outliers, we used the median value.
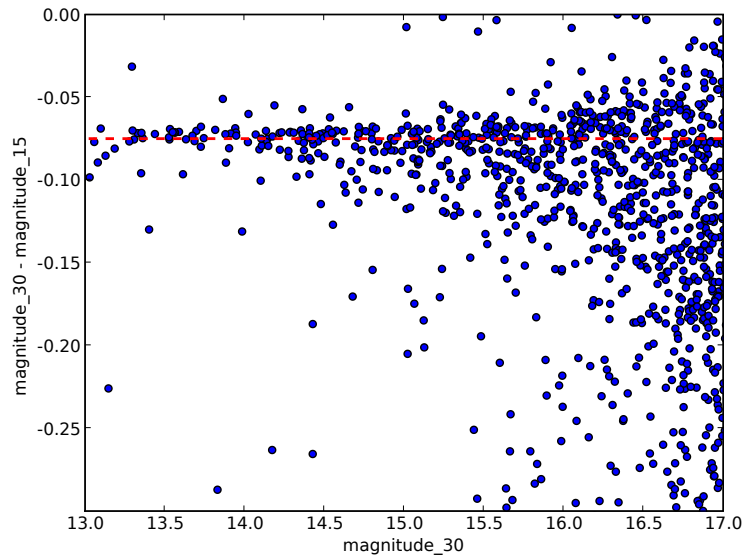
Figure 2.12: Determination of the aperture correction for one of the V-band exposures. Crowding results in down-scattering of points because neighboring sources lead to an overestimation in the object brightness when using a large aperture.
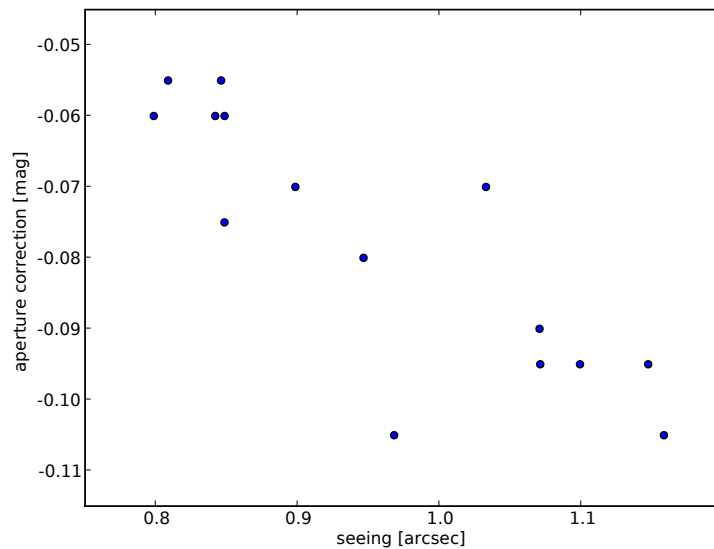
Figure 2.13: The aperture correction is correlated with the seeing. Because more flux is lost outside the aperture, a larger PSF usually needs a larger (more negative) aperture correction. However, since not only the size but also the shape of the PSF is varying, there is not a direct relationship between aperture correction and seeing.

In a final step we corrected our measurements for Galactic extinction. From Schlegel *et al.* (1998)
we obtained the total reddening for extragalactic objects E(B-V) = 0.698. Assuming a standard
extinction law, this translates in E(U-B) = 0.64 · E(B-V) = 0.45 (Binney & Merrifield, 1998). Since
our target stars are located inside the Galaxy, the actual reddening will be lower than the extragalactic
reddening (depending on the individual distance of each star). Fig. 2.14 shows the UBV color-color
plot of the OTSF-1a stars after correcting for an average reddening of half the extragalactic value[11].
Yellow and red lines indicate the location of main-sequence dwarfs and luminosity class III giants.
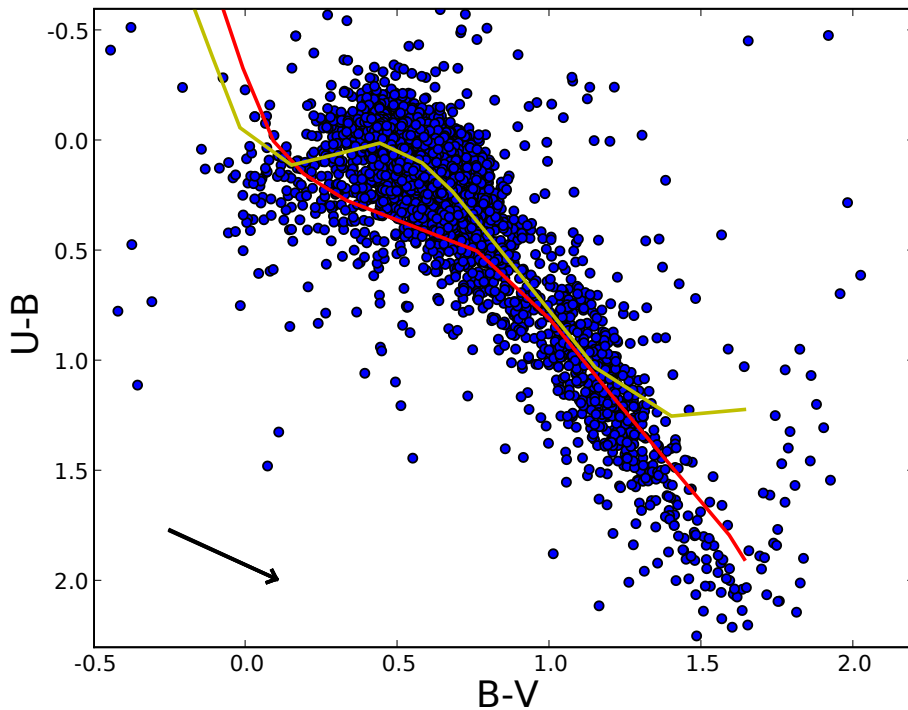
Figure 2.14: UBV color-color diagram of the 3 000 brightest stars in the OTSF-1a field. We corrected
all stars for an average reddening of E(B-V) = 0.35 (black arrow) which is half the value for extra-
galactic objects at that position of the sky (Schlegel *et al.*, 1998). The yellow and red lines show
the position of the main-sequence and luminosity class III giants (according to Binney & Merrifield
(1998)).

---

[11] for individual sources (i.e. our detected transit candidates) we performed a more detailed analysis and derived individual
   extinction values and distances (see §2.7.1)

2.5 Difference Imaging Analysis

Difference imaging was first developed by Tomaney & Crotts (1996) and further improved by Alard & Lupton (1998). The technique has become the most successful method used for the creation of high precision light curves in crowded fields like the Milky Way Bulge, the Large Magellanic Cloud or the Andromeda Galaxy (M31). A quantitative comparison of difference imaging to aperture and PSF-photometry can be found in Montalto *et al.* (2007).

The method uses a reference image which is a stack of the best seeing images. This reference image is degraded by convolution in order to match the seeing of each single image in the dataset. Subtracting the convolved reference image from a single image, one gets a so called difference image with all constant sources being removed. Variable sources are visible as positive or negative PSF-shaped residuals (see Fig. 2.16).

2.5.1 Construction of the reference image

For each CCD we created a stack of the 15 best seeing images. We performed absolute astrometry on the very best image then and used the astrometrically calibrated image as a reference for relative astrometry on the remaining 14 images. After regridding we expanded all 15 images to the same size and created an error image using the following formula:

$$\sigma = \sqrt{\frac{N'_{ADU}}{gain} + RN^2/p^2} \tag{2.2}$$

with N'_{ADU} being the pixel values of the regridded image, RN being the readout noise in e^- in the raw image and p being the pixel scale ratio between raw and regridded image (i.e. $0.238/0.2 = 1.19$). In our data reduction pipeline, error images store the 1σ uncertainties of each pixel. The above formula provides an initial estimate of the error of the regridded images where we neglected the noise that was introduced by the flatfield division and the bias subtraction which is only a small contribution to the total noise. In all subsequent data reduction steps the error images were calculated using Gaussian error propagation.

We subtracted the background in the best seeing image by iteratively fitting a 2-dimensional 2nd order polynomial while clipping positive outliers (i.e. stars). The 14 other images were photometrically aligned (scaled and background subtracted) by measuring amplitudes and local background levels of 100 stars and by comparing them to the background-subtracted best image. We fitted a constant scale and a 2nd order polynomial background.

Using an isolated star, we measured the PSF characteristics (FWHM and angle) in each image and replaced masked regions by the pixel values of the image with the most similar PSF. This was done in order to ensure a homogeneous PSF over the whole field in the stacked image. The final reference image we constructed as the seeing and background weighted combination of the photometrically aligned and bad pixel replaced images. Fig 2.15 shows the reference image and the reference error image for ccd50.
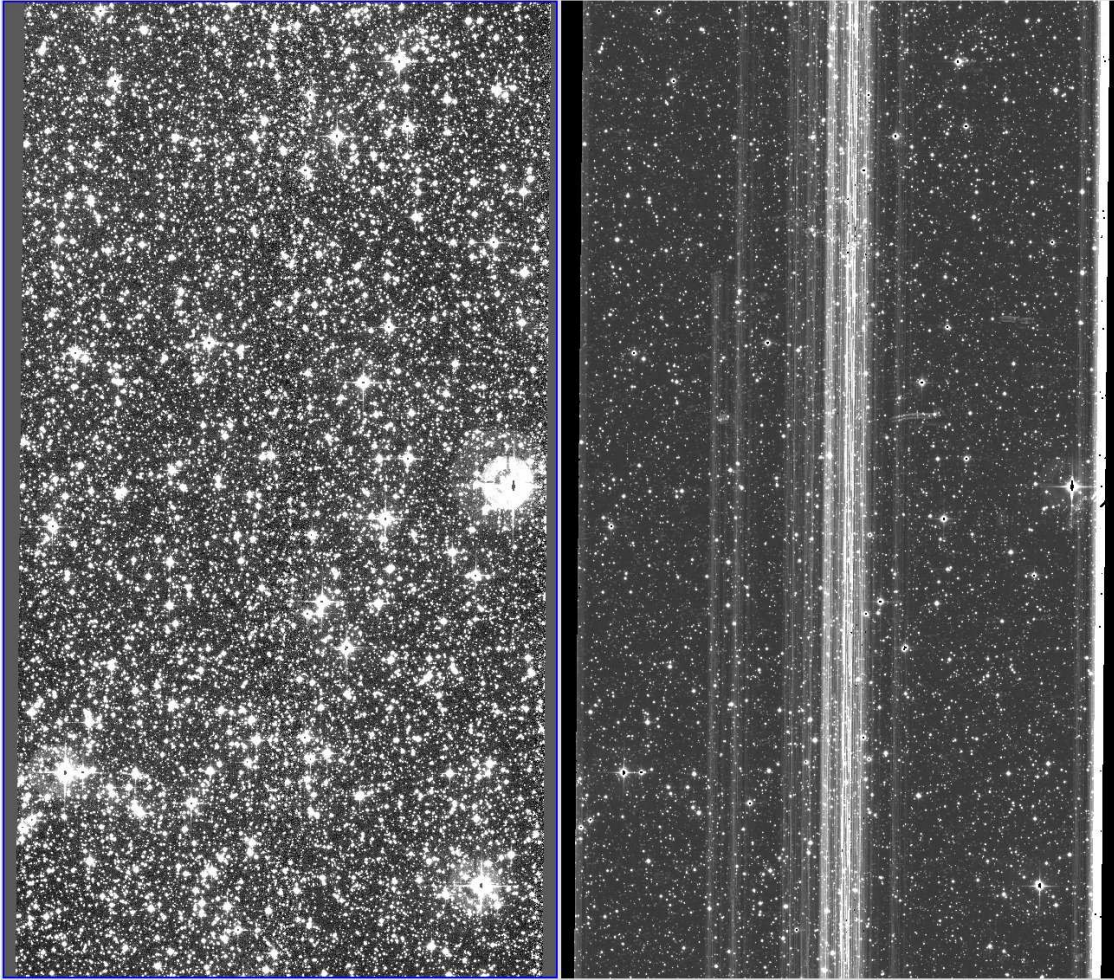
Figure 2.15: Reference image and corresponding error image of ccd50. Since masked pixels are on different x- and y-positions on the 15 regridded input images, the stacking process removed all bad pixel regions in the reference image. Nevertheless, bad pixel regions have a larger uncertainty, visible as brighter areas in the error image.

2.5.2   Construction of the difference images

In difference imaging, the reference image $R(u,v)$ is convolved with a kernel $K(u,v)$ in order to match the PSF of each of the single images. In addition a 2-dimensional polynomial surface $B(x,y)$ accounts for background differences. The convolved image $C(x,y)$ can therefore be calculated as:

$$C(x,y) \equiv R(u,v) \otimes K(u,v) + B(x,y) \quad . \tag{2.3}$$

Since the convolution always results in a degradation of the PSF, the reference image has to be constructed using the best seeing images.

The optimal kernel can be approximated using a superposition of N kernel base functions $k_i(x,y)$:

$$K(u,v) = \sum_{i=1}^{N} k_i(u,v) \quad . \tag{2.4}$$

Alard & Lupton (1998) proposed to use 2-dimensional Gaussian functions modulated with polynomials of the order p_i as kernel base functions:

$$K(u,v) = \sum_{i=1}^{N} \exp -\frac{u^2+v^2}{2\sigma_i^2} \sum_{j=0}^{p_i} \sum_{k=0}^{p_i-j} a_{ijk} u^j v^k \quad . \tag{2.5}$$

We used $N=4$ kernel base functions with $\sigma_i=\{0.1,1,4,12\}$ and $p_i=\{0,4,6,2\}$ and a kernel size of 41x41 pixel. The total number of coefficients a_{ijk} is 50. Together with 10 free parameters b_{mn} of a 3rd order background polynomial $B(x,y)$ we had a total of 60 free parameters which we determined via χ^2-minimization of the following expression:

$$\chi^2 = \sum_{x,y} \frac{1}{\sigma_{x,y}^2} [(R \otimes K)(x,y) + B(x,y) - S(x,y)]^2 \quad . \tag{2.6}$$

We subtracted the convolved image $C(x,y)$ from each single image $S(x,y)$ and in this way we obtained a difference image $D(x,y)$ for each single image:

$$D(x,y) = \frac{S(x,y) - C(x,y)}{|K|} \quad , \tag{2.7}$$

with

$$|K| = \sum_{u,v} K(u,v) \tag{2.8}$$

being the norm of the kernel. Using this normalization, the difference image has the same flux level as the reference image which is important for the following steps.

We used almost all pixels to determine the optimal kernel and background coefficients. Only pixels that belong to variable objects were not taken into account since these would have destroyed the normalization of the kernel. As we did not know a priori which pixel belong to variable objects, we first created a subset of difference images without masking any pixel, identified variable objects and masked them in the second run when we created all difference images.

In most cases, the PSF is varying over the field of view of the detector. In order to account for that, Alard (2000) proposed to use a space-varying kernel with the coefficients a_i being functions of the position on the CCD. However, in this case, the minimization procedure to derive the coefficients $a_i(x,y)$ is much more time consuming. A faster approach is to split each image in subfields and to determine a kernel in each of the subfields independently. In our case we used 4x8 subfields with a size of approximately 600x600 pixel. Fig. 2.16 shows a zoom-in on one of the regridded images and the corresponding difference image (i.e. S(x,y) and D(x,y)).
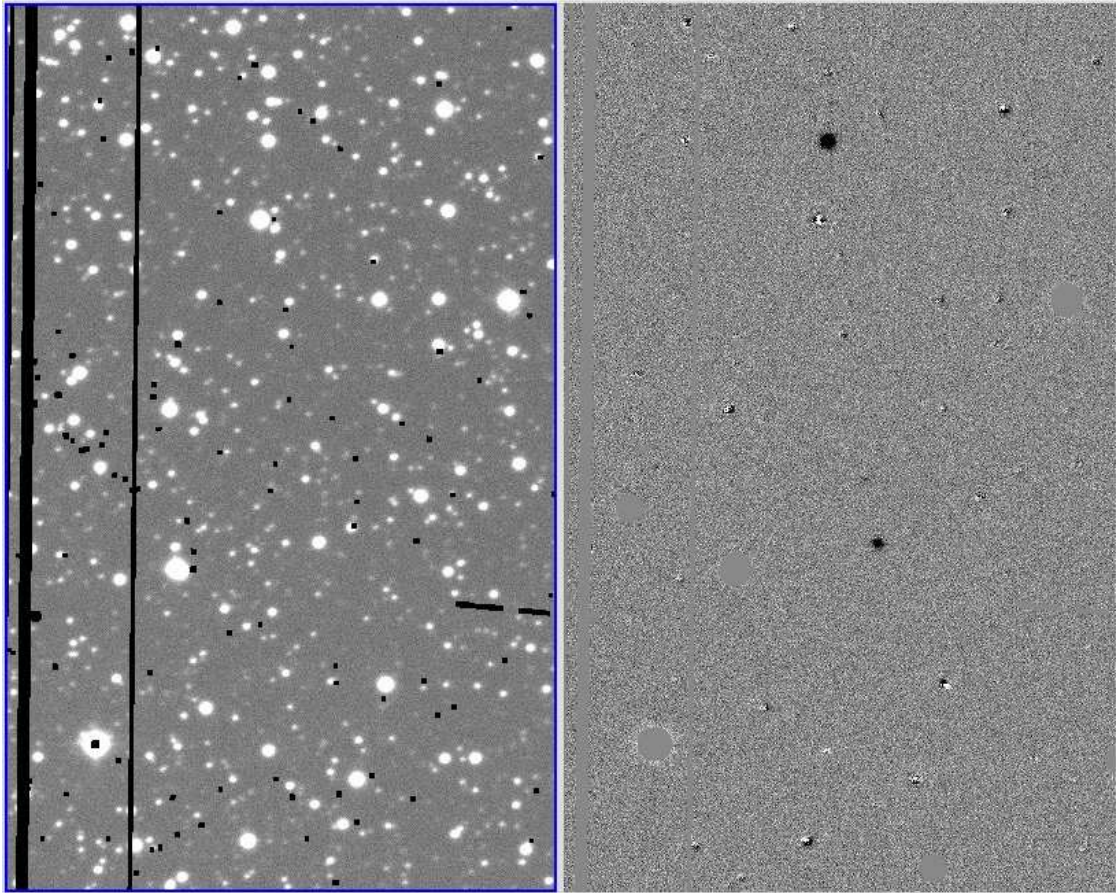
Figure 2.16: Example regridded image and the corresponding difference image. Two variable sources are visible as negative PSF-shaped residuals (black spots). All constant sources are subtracted leaving only noise in the difference image.

2.5.3 Light curve extraction

Using the difference images we were able to measure the differential flux of each source. Adding the flux in the reference image, we got the total flux in each single exposure. The flux measuriement in the reference image has to be done very carefully because sources located close to each other can affect the measurements. An overestimation of the reference image flux due to blending leads to an underestimation of the amplitude of any brightness variation of a variable object (see below).

One method to measure accurate fluxes in crowded fields is iterative PSF-photometry. Using bright isolated stars, the PSF is extracted and resampled on a finer grid. Fig. 2.17 illustrates the process of the PSF determination. Pixelization effects that are visible in the single isolated stars (upper panel) are removed by combining 6 PSF-reference stars that are centered on different sub-pixel positions.
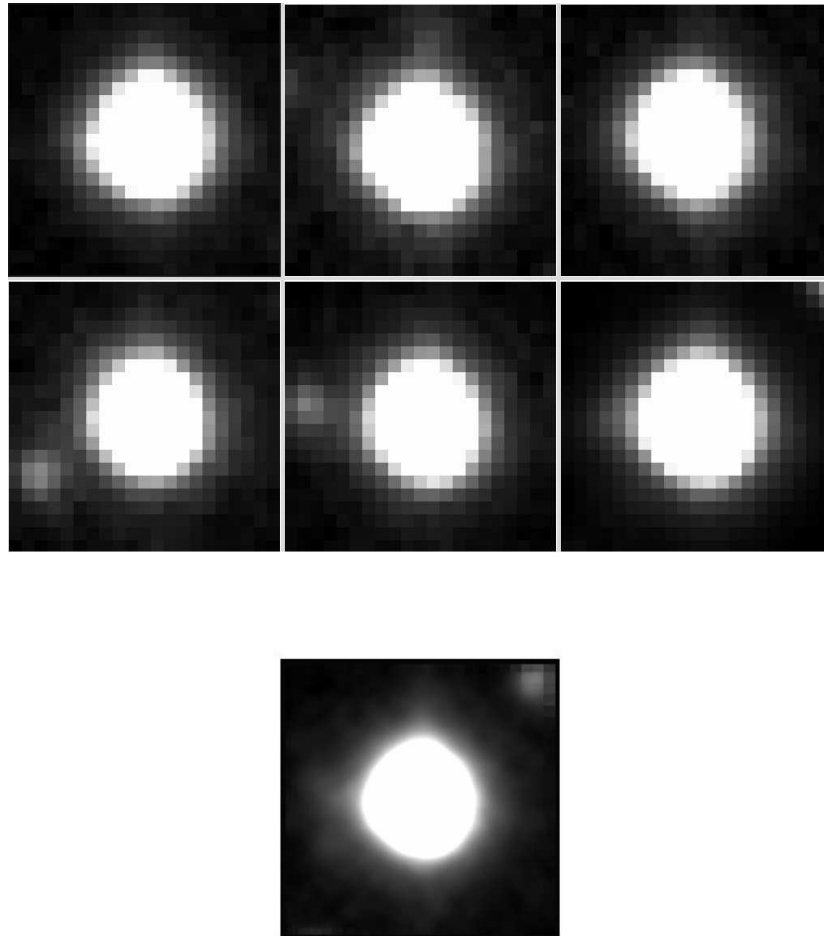
Figure 2.17: Determination of the PSF in the reference image. The PSF of 6 isolated stars is aligned, resampled on a finer grid and afterwards combined.

The extracted PSF was used to measure an initial flux value of each source. In the following iterations, all neighboring sources were subtracted before measuring the flux of a source making use of the improved fluxes that have been measured in the previous step. This was done, until all measured fluxes converged.

The photometry on the difference image was easier, because all non-variable sources have already been subtracted. We measured the fluxes with PSF-photometry where we extracted the PSF from the normalized convolved reference image C'(x,y) combining the same isolated stars we used to measure the fluxes in the reference image. Note that in this way we obtained the differential fluxes with respect to the reference image and later on measured the correct amplitudes of all variations (e.g. transit depths).

In a final step, we normalized all light curves to 1 (i.e. divided by the median value) and applied a barycentric time correction using the formulae of Meeus (1982) as implemented in the *skycalc* program by J. Thorstensen[12].

---

[12]http://www.dartmouth.edu/ physics/faculty/thorstensen.html

2.6   Light Curve Analysis

In this section we describe the light curve analysis and candidate selection process. For each CCD we extracted the light curves of the 2 000 brightest sources. In order to identify variable stars, we calculated the reduced χ^2 of a constant baseline fit. In Fig. 2.18 we plot the RMS of all light curves with reduced $\chi^2 \leq 1.5$ as a function of the R-band magnitude. We overplot the theoretical RMS for 25s exposure time, airmass 1.4, sky brightness of 20.3 mag/arcsec^2 and 1.5 arcsec seeing (black line). The expected precision has almost been reached, which demonstrates the power of the difference imaging technique. However, small systematic effects, such as correlated noise could still be present in our light curves and might have increased the RMS. In the next chapter we describe how we corrected for systematic effects.
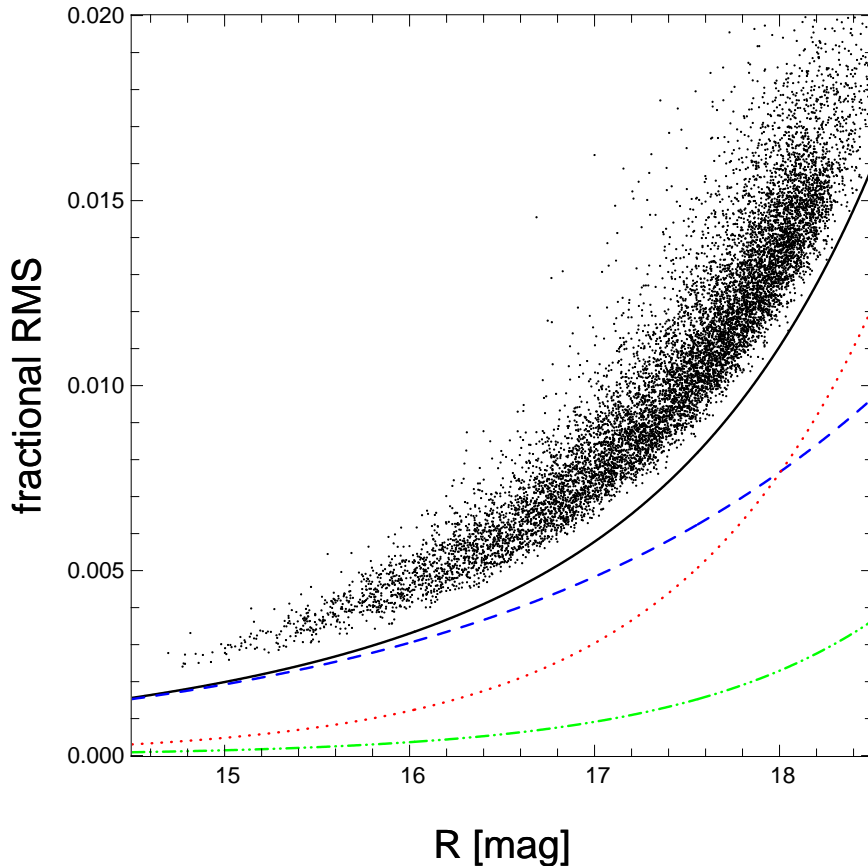
Figure 2.18: RMS of all non-variable light curves. The solid black line shows the RMS that is expected for a 25s exposure at airmass 1.4 assuming a sky brightness of 20.3 mag/arcsec^2 (4 days from full moon) and a seeing of 1.5 arcsec. The other lines show the individual noise contributions, namely the photon noise of the object (dashed blue line) the background noise (dotted red line) and the readout noise (dashed-dotted green line).

2.6.1 Systematics removal

The analysis of the photometric scatter of individual light curves in large data sets (such as the OGLE-III light curves) has shown that the RMS that was reached for faint sources is comparable to the expected value, but for bright sources an RMS excess was found that is limiting the photometric precision to 4-5 mmag. This excess was attributed to correlated noise (also known as 'red noise', see e.g. Pont *et al.* (2006) or Snellen *et al.* (2007)).
In order to correct for red noise in large data sets, Tamuz *et al.* (2005) have developed an algorithm called *sysrem* which has turned out to be very successful in reducing systematic effects for bright stars and is now used in most transit surveys.

The initial idea of the *sysrem* algorithm was to correct for differential extinction: since the spectral energy distribution of each star has a different slope within the transmission range of the filter, the (wavelength-dependent) extinction is slightly different for each star (depending on its color). As shown in §2.4, the extinction is proportional to the airmass ($E_f \cdot airmass$). The difference imaging technique only corrects for a constant E_f for all stars (by the normalization of the kernel). Therefore we can expect to see a residual of the form $c_i \cdot a_j$ for each star i and image j with a color-dependent differential extinction coefficient c_i and airmass a_j. In the following, we consider a data set consisting of N light curves with M data points. In order to remove differential extinction effects, we have to find for each star i the value c_i that minimizes the expression

$$S_i^2 = \sum_j \frac{(r_{ij} - c_i a_j)^2}{\sigma_{ij}^2} \quad , \tag{2.9}$$

where r_{ij} is the flux difference of data point j to the average flux in light curve i and σ_{ij} is the uncertainty of the measurement. Assuming we know the airmasses a_j, we can find the best c_i as

$$c_i = \frac{\sum_j \frac{r_{ij} a_j}{\sigma_{ij}^2}}{\sum_j \frac{a_j}{\sigma_{ij}^2}} \tag{2.10}$$

and subtract the residuals $c_i \cdot a_i$ from each light curve.

In its generalized form, the *sysrem* algorithm corrects for any linear systematic effect that can be represented as $c_i \cdot a_j$. Starting with an initial set of 'generalized airmasses' a_j[13], we calculate the 'generalized colors' c_i that minimize Eq. 2.9. Then we turn the problem around and ask are what the best values of a_j that minimize the expression

$$S_j^2 = \sum_i \frac{(r_{ij} - c_i a_j)^2}{\sigma_{ij}^2} \quad , \tag{2.11}$$

given the 'generalized colors' c_i, we derived in the previous step. Minimization of S^2 with respect to a_j results in

$$a_j = \frac{\sum_i \frac{r_{ij} c_i}{\sigma_{ij}^2}}{\sum_j \frac{c_i}{\sigma_{ij}^2}} \quad . \tag{2.12}$$

---

[13] in practice, one may start with the actual airmass

After calculating the improved values a_j, we start again using eq. 2.10 to calculate better values of c_i. Repeating this process, the a_j and c_i converge typically after a few iterations to a final set of 'generalized airmasses' and 'generalized colors' which are not necessarily the true airmasses of the observations or the true colors of the stars. Instead, c_i and a_j could be related to other parameters like e.g. the position on the CCD, the moon phase or the seeing.

Using the final values a_j and c_i, we subtract the residuals from each light curve. In this way, we remove only the most prominent systematic effect. Subsequently applying the *sysrem* algorithm to the corrected light curves, we remove all significant systematic effects.

Sysrem is very robust against the choice of initial values for a_j. The algorithm identifies and removes systematic effects without any prior knowledge of their origin (as long as they are linear and appear in many stars of the sample). If all measurements have the same uncertainties σ_{ij}, the *sysrem* algorithm is identical to a principal component analysis.

Sysrem can only work efficiently, if all light curves of variable stars are identified and removed from the sample. Therefore, we fitted a constant baseline to each light curve and plotted the histogram of reduced χ^2 in Fig. 2.19. We applied the algorithm to all light curves with $\chi^2 \leq 1.5$ (70% of all light curves) and subtracted 4 systematic effects.

Fig. 2.20 shows the RMS of the light curves before (black dots) and after the *sysrem* correction (red dots). The algorithm reduced the RMS of the light curves by only a small amount. We therefore conclude, that systematic effects in our data set are not as prominent as it is the case for other surveys. Note that we already reach ~ 3 mmag precision in the uncorrected light curves. Note also, that there is no strong deviation from the expected precision for bright stars but rather a constant offset for the whole magnitude range which indicates an overestimated throughput of the telescope rather than the presence of red noise.
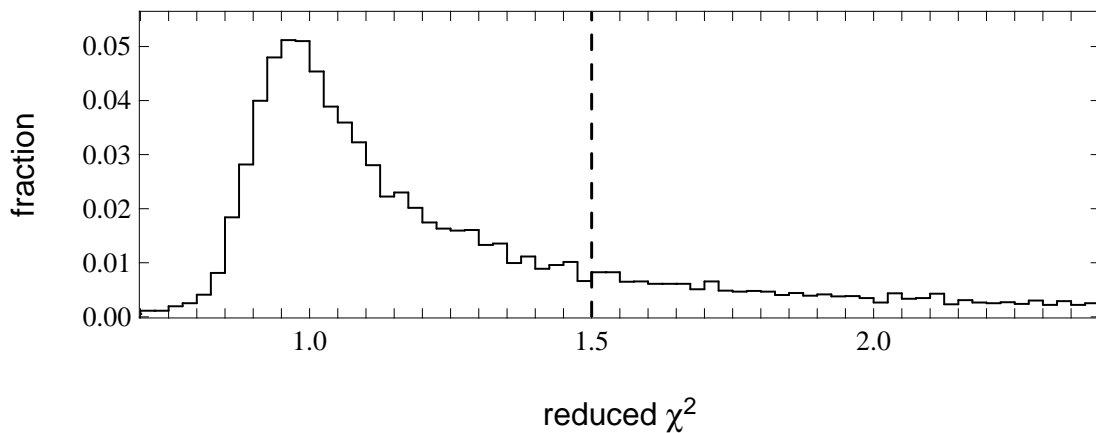
Figure 2.19: Histogram of the reduced χ^2 for a constant baseline fit to all light curves. We apply the *sysrem* algorithm to all light curves with a reduced $\chi^2 \leq 1.5$.
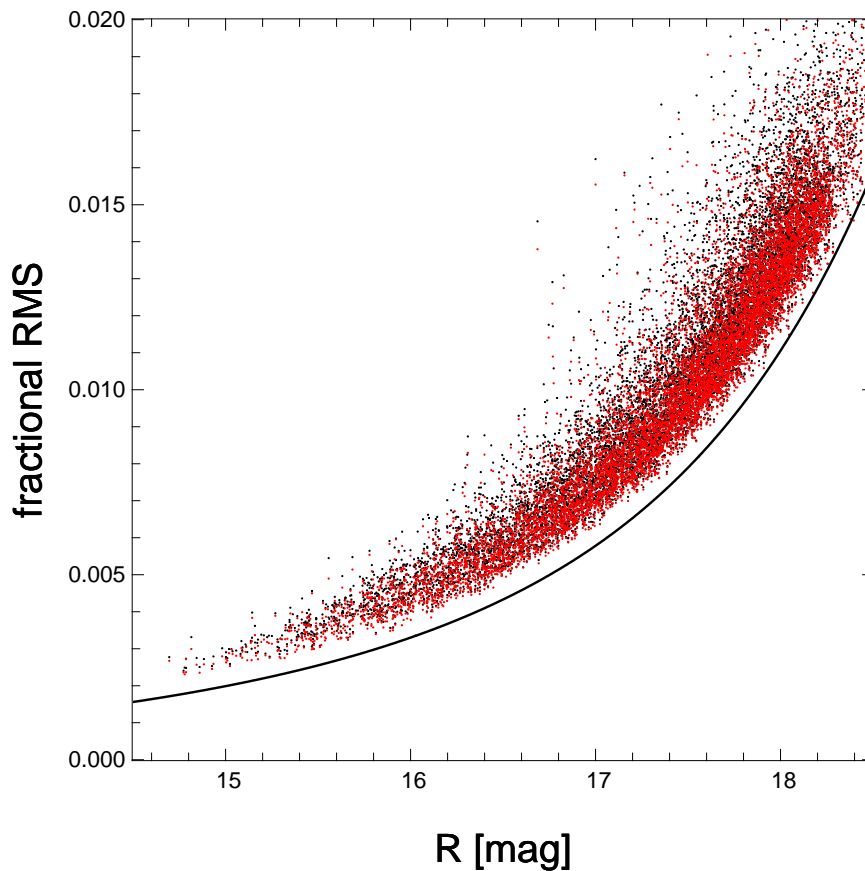
Figure 2.20: RMS before (black) and after (red) application of the *sysrem* algorithm.

Since other groups reported more significant improvements using *sysrem* (e.g. Pont *et al.*, 2006; Snellen *et al.*, 2007; Raetz *et al.*, 2009), we performed a test to verify our implementation. For one CCD, we created a new set of light curves running the difference imaging software with unoptimized standard parameters (i.e. lower background order, bigger subfields, etc.) and extracted the light curves in the same way as before. Then we ran *sysrem* on the new set of light curves and compare the RMS before and afterwards (Fig. 2.21).

Naturally, using an unoptimized pipeline, the RMS of the light curves is higher compared to the optimized pipeline (Fig 2.20). However, the *sysrem* algorithm was able to remove a large fraction of it. This demonstrates, on the one hand, the power of the *sysrem* algorithm but, on the other hand, it shows that optimizing the data reduction pipeline is very important in order to reduce the amount of systematic effects in the light curves.
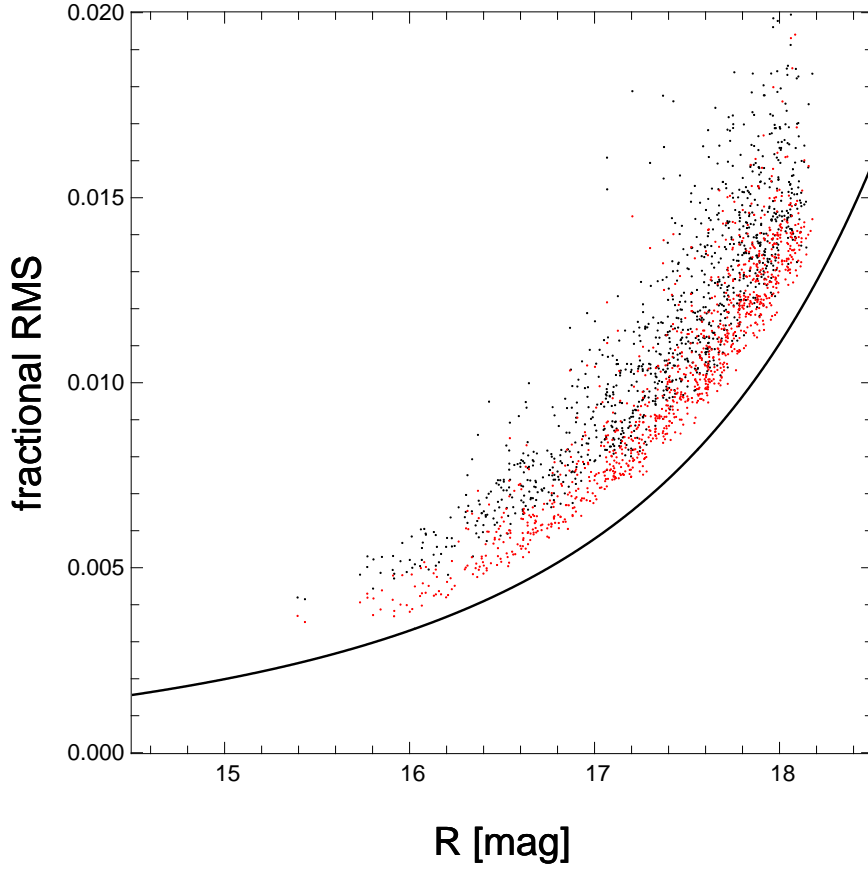
Figure 2.21: RMS after application of the *sysrem* algorithm for an unoptimized pipeline.

2.6.2   Box-fitting analysis

In order to find transiting planet candidates in our large set of light curves, a fast detection algorithm was needed. In the past years the box-fitting least squares (BLS) algorithm proposed by Kovács *et al.* (2002) has proven to be one of the most efficient algorithms. In the following, we explain the algorithm and introduce two important quantities: the S/N of a transit light curve and the signal detection efficiency (SDE).

Consider a transiting planet light curve that is showing cyclical brightness drops with period p. In a simplistic view the flux is a two level system with values H and L. The time spend in the lower level L (i.e. the transit duration) is $\tau \cdot p$, where τ is the fractional transit length (see eq. 1.18). For Hot Jupiters, τ is on the order of 0.01 to 0.1 (Defaÿ *et al.*, 2001) which corresponds to absolute transit durations of typically to 2-3 hours. Together with the epoch of the transit t_0 the light curve is characterized by five parameters: p, τ, H, L and t_0.

The individual errors of each measurement σ_i are taken into account by giving each point $\{x_i\}$ a weight $\omega_i = \sigma_i^{-2}[\sum_{j=1}^{n} \sigma_j^{-2}]^{-1}$. Applying an offset to all points in the light curve we further require that the arithmetic average of the values $\{\omega_i x_i\}$ is zero.

In the following we consider the light curve to be folded with a test period p. The new sequence of points is named $\{x_i'\}$ and the corresponding weights $\{\omega_i'\}$. In order to find the best-fitting box, the expression

$$D = \sum_{i=1}^{i_1-1} \omega_i'(x_i'-H)^2 + \sum_{i=i2+1}^{n} \omega_i'(x_i'-H)^2 + \sum_{i=i_1}^{i_2} \omega_i'(x_i'-L)^2 \tag{2.13}$$

has to be minimized with respect to H and L. This results in the arithmetic averages in each of the two regions

$$L = \frac{s}{r} \quad \text{and} \quad H = -\frac{s}{1-r} \tag{2.14}$$

with

$$s = \sum_{i=i_1}^{i=i_2} \omega_i' x_i' \quad \text{and} \quad r = \sum_{i=i_1}^{i=i_2} \omega_i' \quad . \tag{2.15}$$

Using this, eq. 2.13 transforms into

$$D = \sum_{i=1}^{n} \omega_i' x_i'^2 - \frac{s^2}{r(1-r)} \quad , \tag{2.16}$$

where the first term in eq. 2.16 is independent of the period. In order to minimize with respect to the parameters τ and t_0, we determine for all possible pairs (i_1, i_2) the minimum of the second term in equation 2.16:

$$SR := -min\left\{-\left[\frac{s^2(i_1,i_2)}{r(i_1,i_2)[1-r(i_1,i_2)]}\right]^{\frac{1}{2}}\right\} = max\left\{\left[\frac{s^2(i_1,i_2)}{r(i_1,i_2)[1-r(i_1,i_2)]}\right]^{\frac{1}{2}}\right\} \quad . \tag{2.17}$$

In fact, we test only those pairs (i_1, i_2) that correspond to a fractional transit length τ in a physical meaningful range, e.g. [0.01...0.1]. In order to further increase the speed of the algorithm by reducing the number of pairs (i_1, i_2), it has been proposed by Kovács *et al.* (2002) to divide the folded light curve in N bins (with N being smaller than the number of data points in the light curve) and use only the average values of each bin in the box-fitting process.

Note that in eq. 2.17, we switched the sign in order to make SR positive. A high SR means a low χ^2 of the fit. Determining the maximum SR for each period p one gets the best fitting box represented by the values of L, H, τ and t_0. Plotting the maximum SR value for each period p over $1/p$ we obtain the SR-spectrum which we normalized to the maximum SR value.

In the SR-spectrum, good detections are visible as narrow peaks that build a high contrast to the noisy other SR values. In many cases, additional peaks at twice or half of the best period[14] are visible. As an example we show the SR-spectrum of our best candidate in Fig. 2.24.

---

[14] or even higher order harmonics and sub-harmonics

A measure for the significance of a detection is the so called signal detection efficiency (SDE):

$$SDE := \frac{SR_{peak} - <SR>}{sd(SR)} \quad , \tag{2.18}$$

where $<SR>$ is the average SR value and $sd(SR)$ is the standard deviation of all SR values.

We applied the BLS-algorithm to all *sysrem*-corrected light curves and tested 4 001 different periods equally spaced in $1/p$ between 0.9 and 9.1 days. We used 1 000 bins in the folded light curves. For each light curve we determined the best fitting period p, epoch t_0, transit depth $\Delta F / F$ and fractional transit length τ. In addition, we determine the number of transits, number of data points during a transit, the S/N of the light curve and the SDE of each detection and calculate the reduced χ^2 of the box-fit.
As an additional very useful parameter, we measured the variations that are in the out-of-transit part of the light curve: after the masking the detected signal (i.e. removing all points within a distance of $0.75 \cdot \tau$ from t_0), we ran the BLS-algorithm again on the remaining data points. We compared the S/N found in the masked light curve, $S/N_{removed}$ hereafter, to the S/N found in the unmasked light curve. In the case of variable stars the difference between the two values S/N - $S/N_{removed}$ was very low, whereas for a transiting planet the difference was high, since no variation was left after the masking of the transit.

In order to identify all interesting transiting planet candidates and to reject variable stars and other false positives, we applied a number of selection criteria to the light curves that have been selected by the BLS-algorithm. In particular we required:

   i) # transits ≥ 2

   ii) $S/N \geq 12$

   iii) reduced $\chi^2 \leq 1.5$

   iv) S/N - $S/N_{removed} \geq 4.7$

A minimum of two transits is required in order to determine the period of the orbit[15]. According to Kovács *et al.* (2002), a S/N of 12 is required for the BLS-algorithm to work efficiently. The last two selection criteria were optimized using Monte-Carlo simulations and are discussed in §2.8.

---

[15]candidates showing only one transit are unlikely to be detected by the BLS-algorithm and even if they were detected, the follow-up of such a candidate would be difficult

2.7 pre-OmegaTranS Candidates

Among 200 light curves that passed the detection criteria presented in the previous chapter, we identified 4 transiting planet candidates (POTS-C1, POTS-C2, POTS-C3 and POTS-C4). The remaining detections are classified as variable stars or false detections caused by systematic outliers and are clearly distinguishable from the 4 candidates. We calculated the Tingley-Sackett parameter (see §1.5.1) for each candidate and searched for ellipsoidal variations in the out-of-transit parts of the light curves (see §1.5.2). According to these tests, POTS-C1 is the most reliable candidate (see Fig. 2.22). POTS-C3 has the lowest quality, since the candidate has a Tingley-Sackett parameter of 1 and shows indications of ellipsoidal variations. Fig 2.23 shows 1.5x1.5 arcmin finding charts of all candidates. In the following, we discuss each candidate in detail.
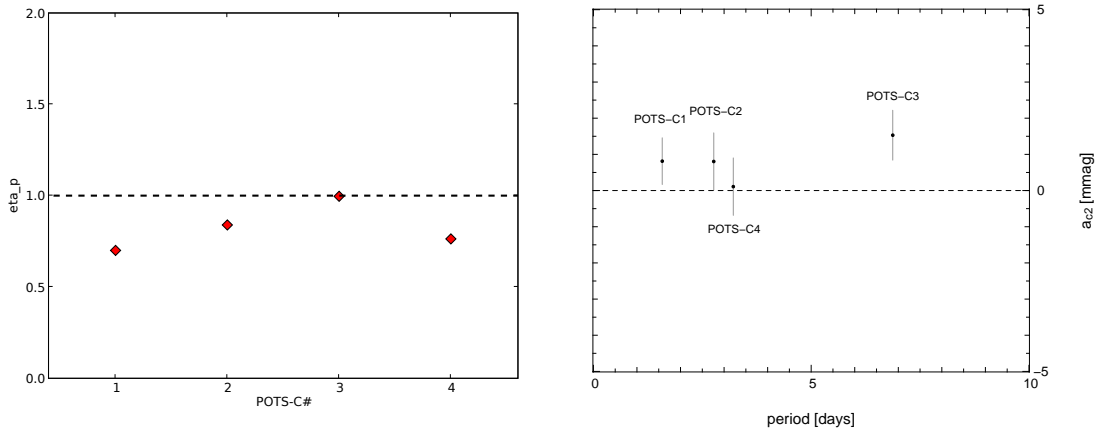
Figure 2.22: Tingley-Sackett parameter and ellipsoidal variations of the pre-OmegaTranS candidates.

2.7.1 POTS-C1

The most interesting candidate was detected close to the image center on ccd52. The S/N of the detection is 38.2, the highest value of all candidates found in the pre-OmegaTranS survey. In Fig. 2.24 we show the SR-spectrum of the detection. The highest peak is located at p_1=1.58 days (SDE=4.63). There is also a peak at twice the period p_2=3.16 with similar significance (SDE=4.55). Looking at the epochs of the 3 observed transits, we found that the separation between the first and the second transit is $2 \cdot p_1 = p_2 = 3.16$ days and the separation between the first and the third transit is $36 \cdot p_1 = 18 \cdot p_1 = 56.88$ days. Since we have no observations at odd epochs of p_1, in principle both periods are possible. However, we believe that p_1 is the correct period given the higher SDE and considering the strong selection effect of the transit method towards finding shorter period planets (see §1.3.6). The detailed light curve fitting also supports the conclusion, that p_1 is the correct period (see below).
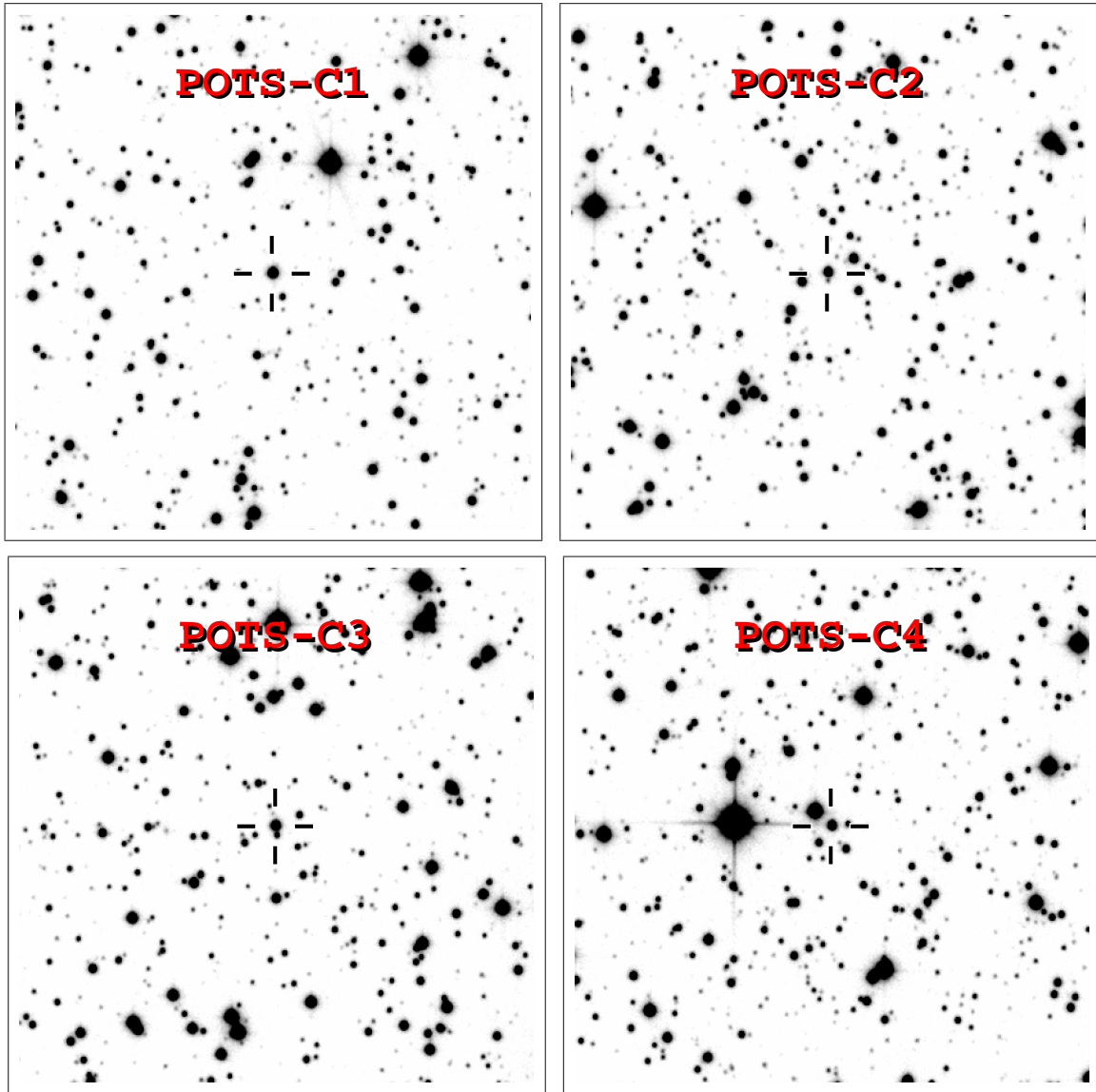
Figure 2.23: Finding chart of POTS-C1, POTS-C2, POTS-C3 and POTS-C4. The field of view is 1.5x1.5 arcmin. North is up and East is left.

We extracted the UBVRI magnitudes of POTS-C1 from the photometric calibration (see §2.4). The uncorrected (V-I) of POTS-C1 is 1.80 mag, indicating that the host star is a late K-dwarf. In addition, we identified POTS-C1 to be identical to source 13342613-6634520 in the 2MASS catalog (Skrutskie *et al.*, 2006) and extracted its JHK magnitudes.

In order to estimate the intrinsic color $(V\text{-}I)_0$, we iteratively fitted a distance (using absolute and measured apparent magnitude), calculated the extinction (using an average value of E(B-V)/kpc = 0.21 mag, as derived in the field selection process [Barbieri (2007)]) and determined the spectral type by least-squares fitting of the extinction corrected colors UBVRIJHK to reference colors taken

from Binney & Merrifield (1998)[16]. The fitting procedure converged for a K6V star at a distance of 970 pc with an extinction of E(B-V)=0.21 mag.
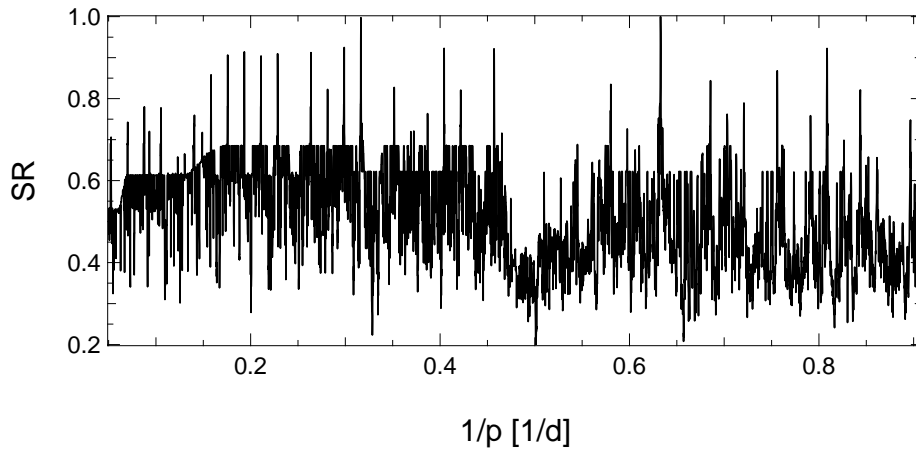
Figure 2.24: SR-spectrum of POTS-C1. Two peaks of comparable significance are visible at p_1=1.58 days and p_2=3.16 days.
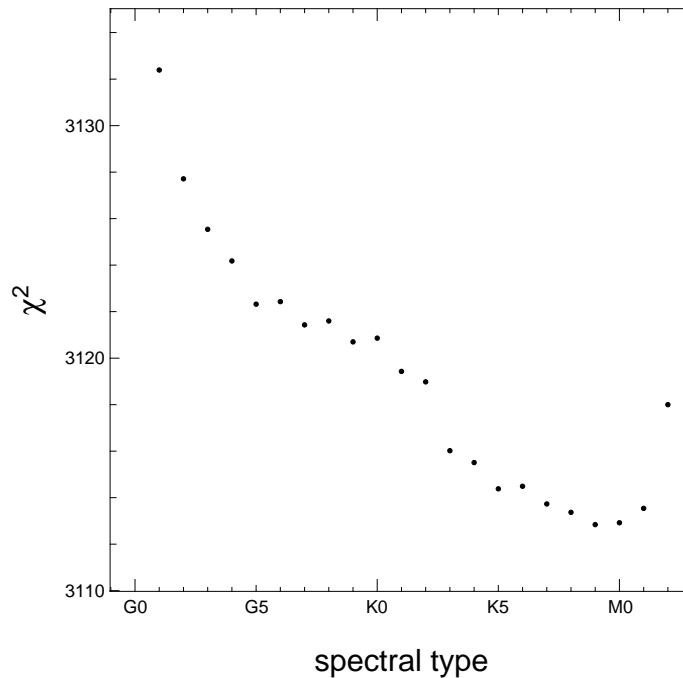
Figure 2.25: χ^2 of the converged fit as a function of the spectral type of the host star (N_{dof}=3056).

---

[16]a similar approach has been recently used by Sale *et al.* (2009) to derive a high resolution extinction map of the Milky Way using 3 bands (r', i' and H_α)
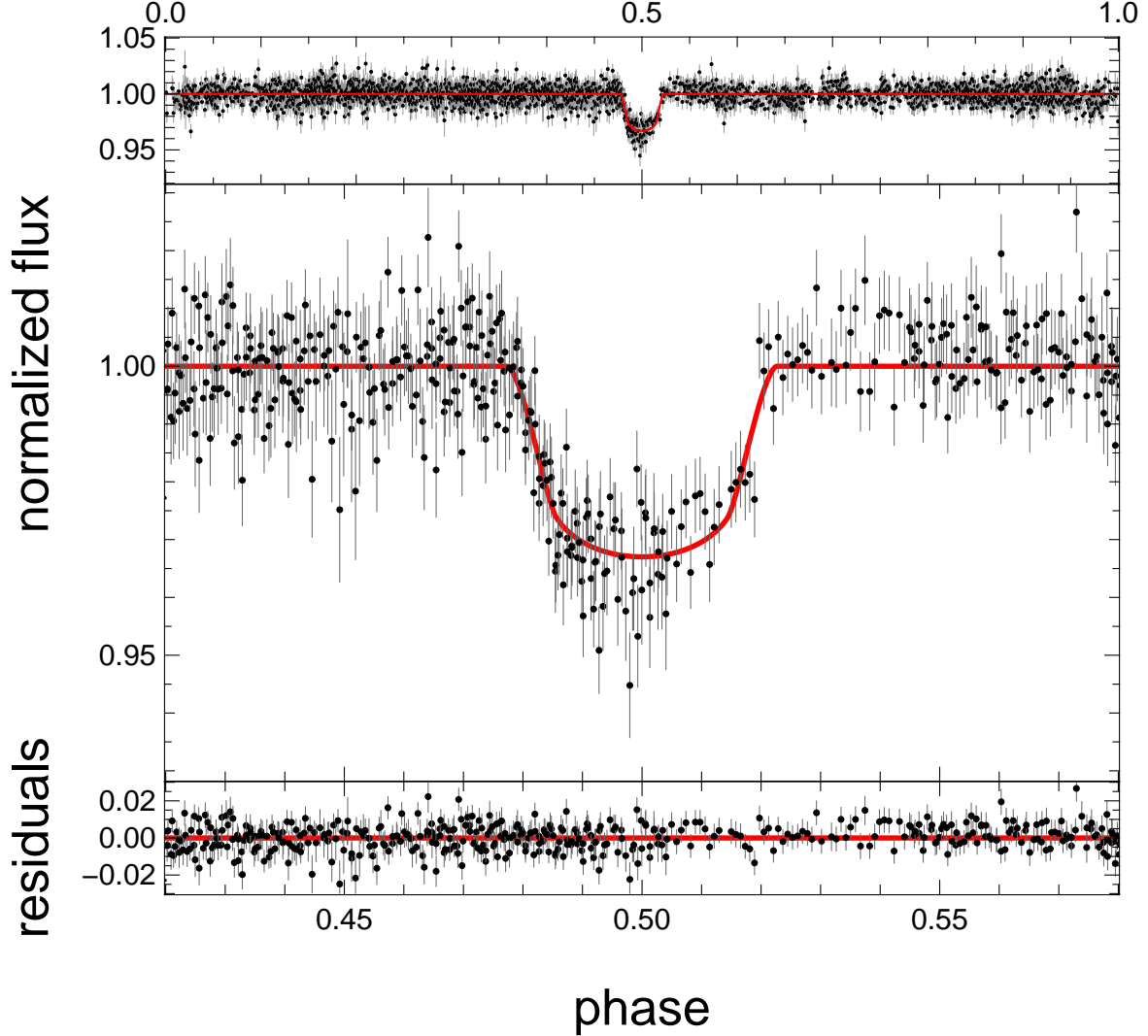
Figure 2.26: Folded R-band light curve of POTS-C1. The red line shows the best fitting model with the parameters listed in Table 2.5.

In order to measure all parameters of the POTS-C1 system, we fitted an analytical transit light curve model according to the equations of Mandel & Agol (2002) with a quadratic limb-darkening parameterization of the form:

$$I(r) = \gamma_1(1 - \sqrt{1-r^2}) + \gamma_2(1 - \sqrt{1-r^2})^2 \quad , \tag{2.19}$$

where r is the normalized radial coordinate on the disk (i.e. $0 \leq r \leq 1$) and γ_1 and γ_2 are the quadratic limb-darkening coefficients taken from Claret (2000).

The free parameters of the fit were period p, epoch t_0, inclination i and planetary radius R_{pl}. We fitted a scale in order to normalize the light curve to 1. In an iterative process, we minimized the χ^2 with respect to one parameter after the other until all parameters converged.

From the extinction corrected color of the star we had only a rough estimate of its spectral type and thus we did not know its limb-darkening coefficients. We therefore performed the fitting for several spectral types and subtypes ranging from A0V to M5V and searched for the absolute minimum χ^2 of all fits. In the case of POTS-C1 the best fit was achieved for a K9V star (see Fig. 2.25) with a χ^2 of 3112.83 which is in good agreement with the spectral type that has been derived from the colors.

In the same way we determined the best fit with the second possible period p_2. We found a minimum χ^2 of 3114.36 for a spectral type of M2V. The slightly larger χ^2 indicates that p_1 is more likely the correct period.

In order to increase the accuracy of the fitting and to derive precise uncertainties of the system parameters, we minimized the χ^2 on a grid centered on the minimum previously found with the iterative process. The resulting final parameters including error estimates are listed in Table 2.5 together with all other parameters of the POTS-C1 system. In Fig. 2.26 we show the folded light curve together with the best fit. Fig. 2.27 shows the individual transits (1 full transit and 2 ingress parts).

The best fitting planetary radius of POTS-C1b is 1.02 R_{Jup}, a value that is comparable to most transiting planets detected so far. However, the host star, a late K-dwarf, is one of the smallest stars known to host a transiting planet (see §1.4) making POTS-C1 a very interesting candidate.
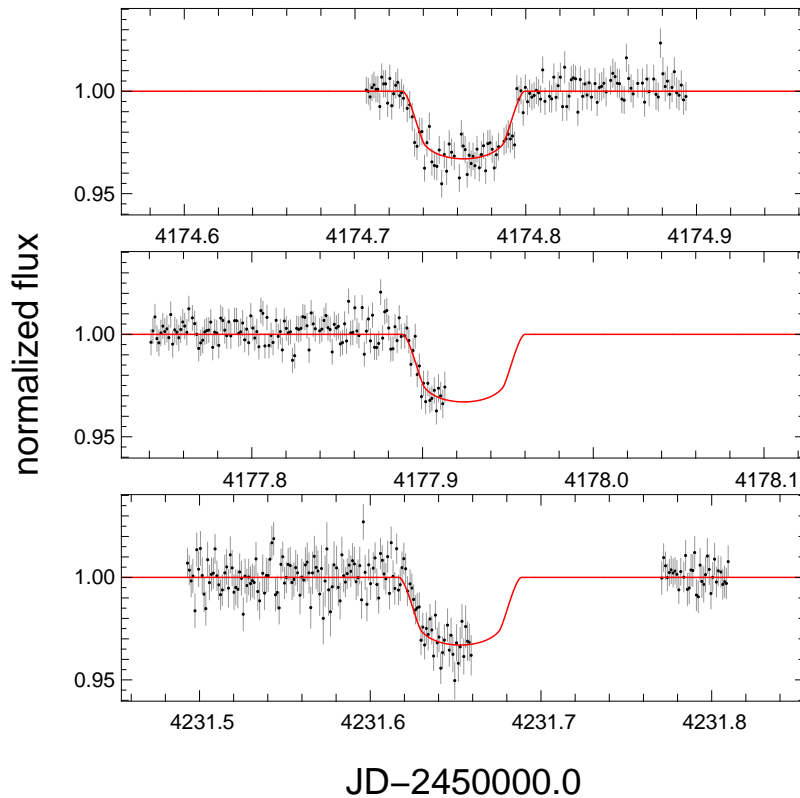
Figure 2.27: Unfolded R-band light curve of POTS-C1 showing three individual transits of POTS-C1b.

	POTS-C1	POTS-C2
Stellar parameters:		
RA (J2000.0)	$13^h34^m26^s.1$	$13^h37^m32^s.1$
DEC (J2000.0)	$-66°34'52''$	$-66°50'41''$
U	20.89 ± 0.10 mag	20.90 ± 0.12
B	19.54 ± 0.04 mag	19.90 ± 0.04
V	17.94 ± 0.03 mag	18.50 ± 0.03
R	17.01 ± 0.06 mag	17.70 ± 0.06
I	16.14 ± 0.07 mag	16.91 ± 0.07
J	15.17 ± 0.06 mag	15.93 ± 0.12
H	14.38 ± 0.04 mag	15.16^a
K	14.24 ± 0.08 mag	15.09^a
d	0.90 kpc	1.49 kpc
E(*B-V*)	0.19 mag	0.32 mag
(*R-I*)	0.87 mag	0.79 mag
(*R-I*)$_0$	0.71 mag	0.53 mag
spectral type	K7V^b / K9V^c	K4V^b / G0V^c
Planetary and orbital parameters:		
p	$1.58025319\pm3.174\cdot10^{-5}$ days	$2.76311360\pm9.662\cdot10^{-5}$ days
t_0	$2\,454\,231.6527187\pm1.0465\cdot10^{-3}$ days	$2\,454\,241.3666309\pm1.7152\cdot10^{-3}$ days
R_{pl}	1.025 ± 0.016 R$_{Jup}$	1.981 ± 0.039 R$_{Jup}$
i	$86.46\pm0.16°$	$84.63\pm0.14°$
a_{pl}	0.0218^d AU	0.0392^e AU
reduced χ^2	1.02 (N$_{dof}$=3051)	0.95 (N$_{dof}$=2892)
Light Curve and detection properties:		
S/N	38.2	38.0
$S/N_{removed}$	10.8	11.1
SDE	4.63	5.27
τ	0.036	0.031
$\Delta F/F$	0.029	0.024
# transits	3 (1 full, 2 ingress)	3 (2 full, 1 ingress)
# transit points	83	128
RMS	0.0089	0.0129

^{a} no error estimate is available

^{b} from colors

^{c} from light curve fit

^{d} assuming a K9 host star with $M_\star = 0.55\ M_\odot$

^{e} assuming a G0 host star with $M_\star = 1.05\ M_\odot$

Table 2.5: Planetary and stellar parameters of the POTS-C1 and POTS-C2 systems.

2.7.2 POTS-C2

A second candidate was detected on ccd57. The S/N of 38.0 is equally high compared to POTS-C1. The best fitting period p_1=2.76 days (SDE=5.27) is of much larger significance than the second best period (SDE=4.33). 3 different transits (2 full transit and 1 ingress part) comprise a total of 128 data points.
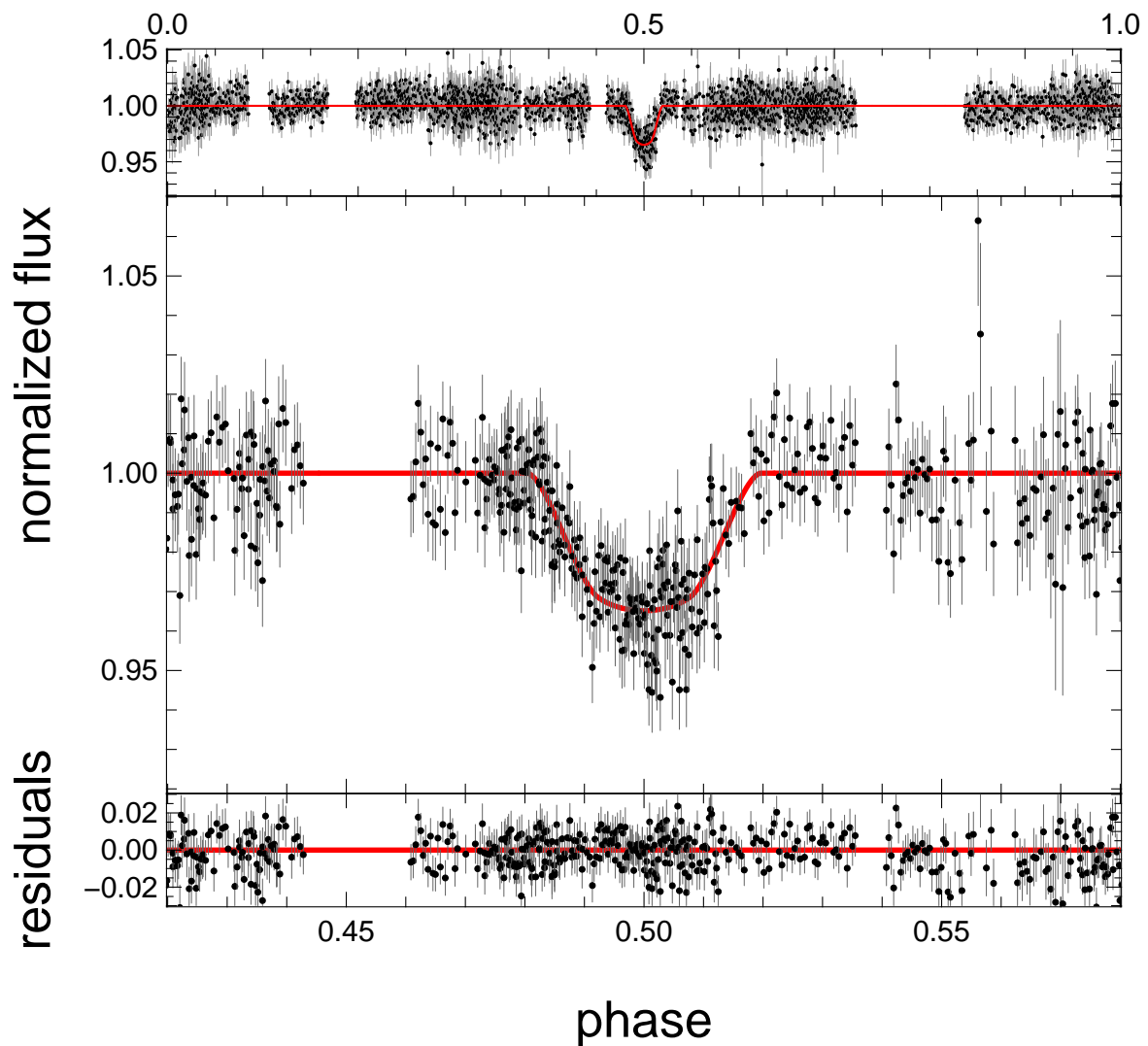
Figure 2.28: Folded R-band light curve of POTS-C2. The red line shows the best fitting model with the parameters listed in Table 2.5.

POTS-C2 is identical to 2MASS source 13342613-6634520. Iterative fitting of spectral type and distance/extinction converged for a K4V star at a distance of 1.49 kpc with an extinction of E(B-V)=0.32 mag.

The light curve fitting resulted in a minimum χ^2 of 2741.51 for a G0V star which is different to the spectral type that has been derived from the colors. Fig. 2.28 shows the folded light curve together with the best fitting model.

With a best fitting planetary radius of 1.98 R_{Jup}, POTS-C2b is very large for a planet. However, since the radius of the host star is not known with good precision, the candidate might be actually smaller. Nevertheless, POTS-C2 is a candidate of much lower quality than POTS-C1.
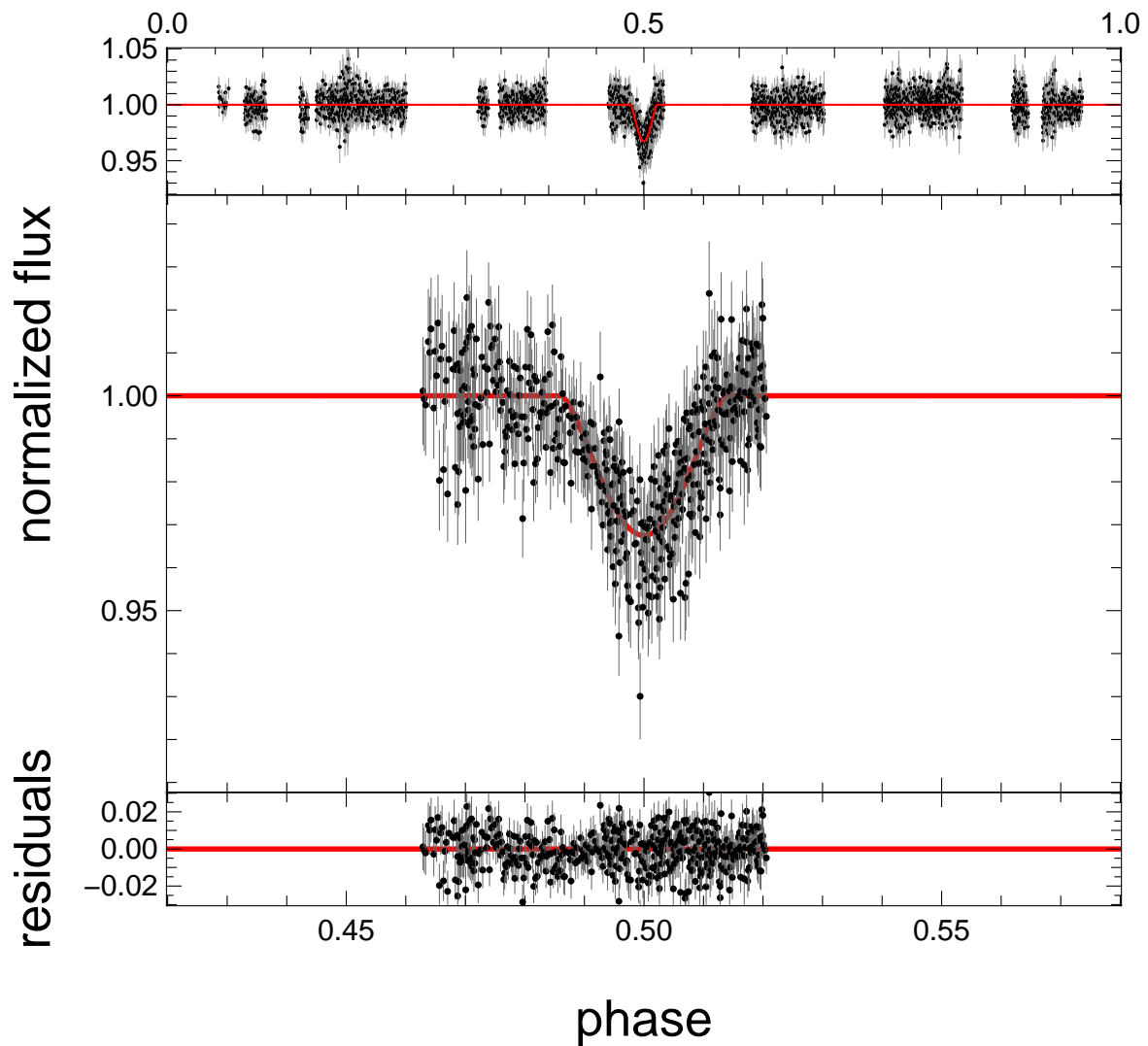
Figure 2.29: Folded R-band light curve of POTS-C3. The red line shows the best fitting model with the parameters listed in Table 2.6.

2.7.3 POTS-C3

A third candidate was detected on ccd54 with a S/N of 37.6. The best fitting period is p_1=6.87 days. 2 observed transits (1 full transit and 2 ingress parts) comprise a total of 182 data points.
POTS-C3 is identical to 2MASS source 13323523-64244520. Iterative fitting of spectral type and distance/extinction converged for a F6V star at a distance of 1.38 kpc with an extinction of E(B-V)=0.30 mag.

The light curve fitting resulted in a minimum χ^2 of 3400.88 for a A0V star which is very different to the spectral type derived from the colors (note, that A0V was the earliest spectral type we fitted, earlier types might give an even better fit). Fig. 2.29 shows the folded light curve together with the best fitting model.
The best fitting planetary radius is 6.7 R_{Jup} - by far too large for a planet. The inconsistency of the derived spectral types, the V-shaped transit signal, a large Tingley-Sackett parameter and possible ellipsoidal variations (see Fig. 2.22) and last but not least the large radius make POTS-C3 a candidate of low quality. A grazing eclipsing binary system is a more likely scenario.

2.7.4 POTS-C4

A fourth candidate was detected on ccd51 with a S/N of 25.6. The best fitting period is 3.21 days. 2 different transits comprise a total of 97 data points.
Because of its faintness, POTS-C4 is not included in the 2MASS catalog and therefore no JHK magnitudes were avaliable. Iterative fitting of spectral type and distance/extinction converged for a F6V star at a distance of 1.82 kpc with an extinction of E(B-V)=0.39 mag.

The light curve fitting resulted in a minimum χ^2 of 3495.09 for a A4V star which is different to the spectral type that has been derived from the colors. Fig. 2.30 shows the folded light curve together with the best fitting model.
The large radius of the primary and the deep transit depth result in a radius of 3.16 R_{Jup}. POTS-C4b is therefore most likely too large to be a planet.

	POTS-C3	POTS-C4
Stellar parameters:		
RA (J2000.0)	$13^h32^m52^s.3$	$13^h36^m39^s$
DEC (J2000.0)	$-66°45'20''$	$-66°34'51''$
U	19.44±0.12 mag	19.94±0.11 mag
B	19.05±0.03 mag	19.53±0.02 mag
V	17.96±0.04 mag	18.37±0.03 mag
R	17.40±0.09 mag	17.69±0.03 mag
I	16.81±0.08 mag	17.04±0.05 mag
J	15.85 mag[a]	—
H	15.52 mag[a]	—
K	14.73 mag[a]	—
d	1.38 kpc	1.82 kpc
E(*B-V*)	0.30 mag	0.39 mag
(*R-I*)	0.59 mag	0.65 mag
(*R-I*)$_0$	0.49 mag	0.54 mag
spectral type	F6V[b] / A0V[c]	F6V[b] / A4V[c]
Planetary and orbital parameters:		
p	$6.87296277±4.0309·10^{-4}$ days	$3.21169909±2.9061·10^{-4}$ days
t_0	$2\,454\,181.6255139±2.2784·10^{-3}$ days	$2\,454\,184.6568274±3.8515·10^{-3}$ days
R_{pl}	$6.710±0.077\ R_{Jup}$	$3.162±0.083\ R_{Jup}$
i	$83.59±0.01°$	$82.96±0.16°$
a_{pl}	0.1009 AU[d]	0.0552 AU[e]
reduced χ^2	1.10 (N$_{dof}$=3083)	1.15 (N$_{dof}$=3034)
Light Curve and detection properties:		
S/N	37.6	25.6
S/N$_{removed}$	8.2	10.1
SDE	3.82	3.40
τ	0.020	0.025
$\Delta F/F$	0.025	0.027
# transits	2	2
# transit points	182	97
RMS	0.0116	0.0125

[a] no error estimate is available

[b] from colors

[c] from light curve fit

[d] assuming a A0V host star with $M_\star = 2.90\ M_\odot$

[e] assuming a A4V host star with $M_\star = 2.18\ M_\odot$

Table 2.6: Planetary and stellar parameters of the POTS-C3 and POTS-C4 systems.
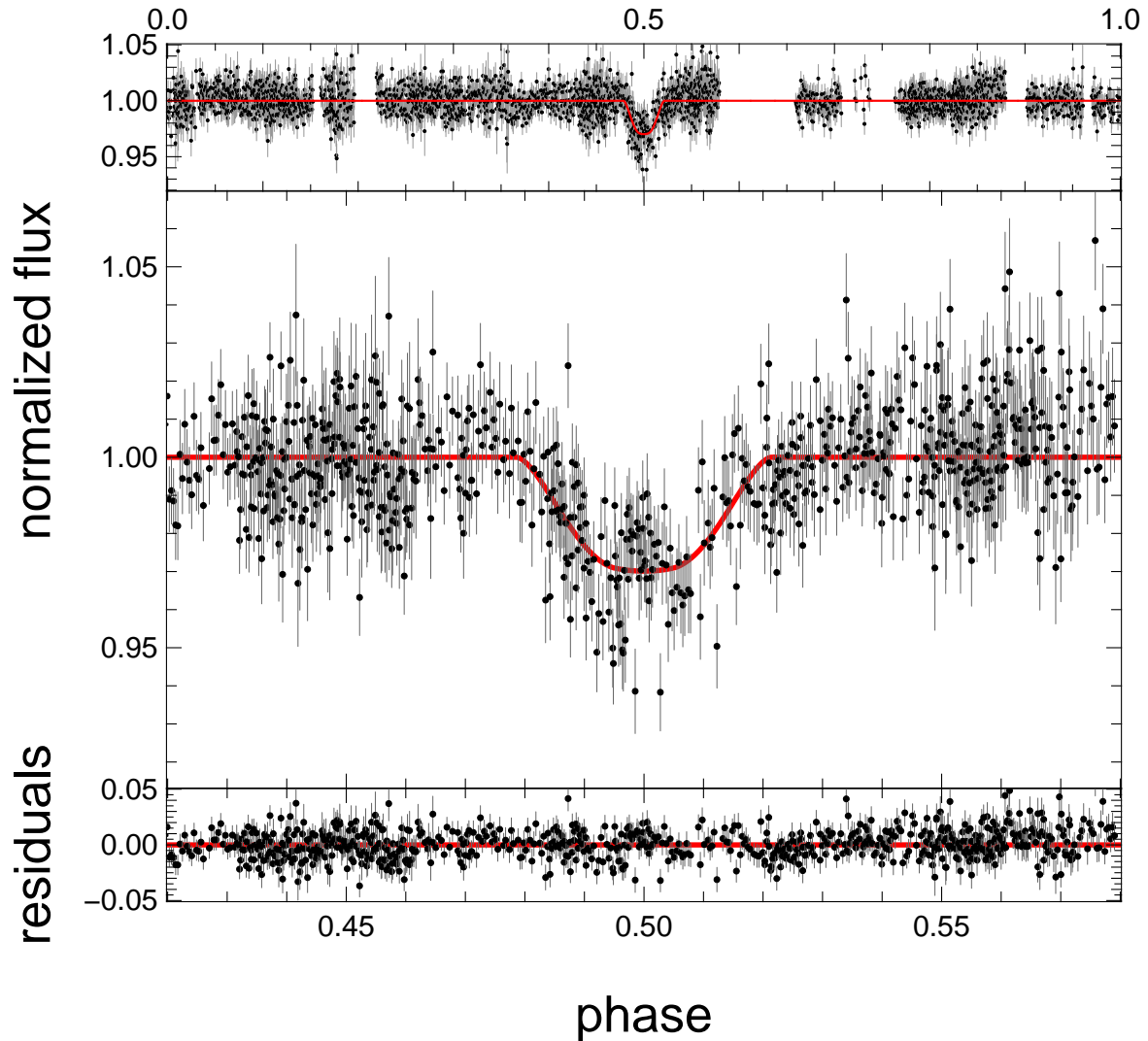
Figure 2.30: Folded R-band light curve of POTS-C4. The red line shows the best fitting model with the parameters listed in Table 2.6.

2.7.5 Follow-up strategy

In order to confirm the planetary nature of the candidates, it is essential to determine the mass of the transiting objects using spectroscopic follow-up observations (see §1.5.5). Since all of our candidates are very faint, we will need a high resolution echelle spectrograph on a 8m-class telescope. Therefore we have submitted a proposal (program 383.C-0821) to ESO for high resolution spectroscopic follow-up observations using the UVES[17] instrument (Dekker *et al.*, 2000) which is mounted on the Very Large Telescope (VLT) at Paranal Observatory in Chile. A total of 10h have been granted in period P83 (March-September 2009).

---

[17]Ultra-Violet-Echelle-Spectrograph

We will use the combination of UVES and FLAMES[18] (Pasquini *et al.*, 2002) which enables us to simultaneously observe objects that are located within a circle of 25 arcmin diameter. The positions of our candidates allow us to observe our best candidate POTS-C1 together with either POTS-C3 or POTS-C4. The remaining five fibers will be used for follow-up of eclipsing binaries and for observations of RV reference stars.

With the granted time we will be able to execute 10 observing blocks with each of them having 1h execution time (45min exposure + 15min overhead). According to the UVES exposure time calculator[19], we will be able to achieve a RV precision of about 100-150 m/s for our candidates. The expected RV variation can be calculated using eq. 1.11. Assuming a mass of 1 M_{Jup} and assuming the spectral type of POTS-C1, POTS-C3 and POTS-C4 is K9V, A0V and A4V, we expect RV variations of 460 m/s, 90 m/s and 120 m/s respectively. Since we know the period and epoch of the orbit, even 10 measurements will enable us to derive a mass of POTS-C1b and therefore confirm or reject their planetary nature. 5 measurements of POTS-C3 and POTS-C4 will reveal or rule out a high mass of the candidates. Moreover, the spectra will asses the spectral typing.

In addition to the spectroscopic follow-up, we plan to observe upcoming transits of POTS-C1b with GROND, a 7 chanel imager mounted on the 2.2m telescope at LaSilla Observatory in Chile (for details of the observational and data reduction strategy see §3). In a two week period of MPE guaranteed time in April 2009, we will have 3 chances to observe a transit of POTS-C1b. The light curves in the 4 optical bands (g', r', i' and z') will provide very important information about the candidate systems and contribute significantly to the follow-up success (as demonstrated in Snellen *et al.* (2009), see §3).

2.8   Detection Efficiency

In order to study the detection efficiency of the pre-OmegaTranS survey and to estimate the expected number of detections, we perform detailed Monte-Carlo simulations. We followed a backward approach injecting artificial transit signals into the light curves that were extracted from the WFI data and applied the BLS-algorithm trying to recover the correct period. Fig. 2.31 illustrates the different inputs to the simulations.

For the input stellar population we used a Besançon model of the OTSF-1a target field which provided us with a distribution of stellar masses $M_\star$ and radii $R_\star$ as well as apparent R-band magnitude m_R and limb-darkening coefficients γ_1 and γ_2 (determined from T_{eff} and log g, according to Claret (2000)).

We tested two different planet populations with periods equally distributed between 1 and 3 days (Very Hot Jupiters) and periods equally distributed between 3 and 5 days (Hot Jupiters). For both populations we distributed the planetary radii R_{pl} equally between 1.0 and 1.25 R_{Jup}. For the planet fraction f_{planet} we used the values of Gould *et al.* (2006a) who found $f_{HJ} = 1/320$ and $f_{VHJ} = 1/710$ analyzing the OGLE-III survey. Note that according to these numbers there are about 50 HJ and 23 VHJ in our field. Assuming an typical transit probability of $\sim$5%, there are on average only 3-4 planets that could be detected - even with infinite observation time.

---

[18]Fiber Large Array Multi Element Spectrograph

[19]http://www.eso.org/observing/etc/bin/gen/form?INS.NAME=UVES+INS.MODE=spectro
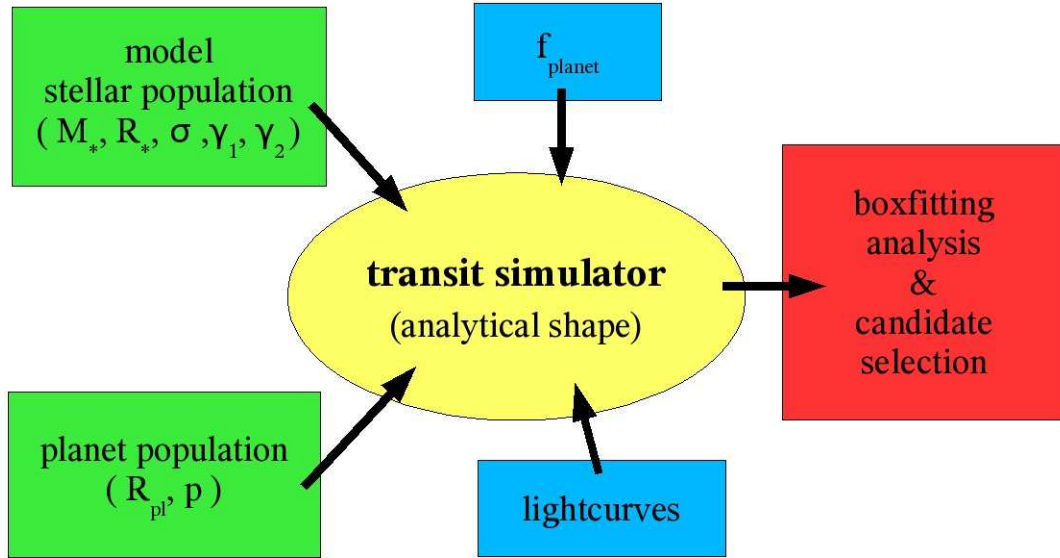
Figure 2.31: Overview of the simulation inputs.

For each of the 15996 light curves[20] we randomly picked one star of the stellar population requiring the apparent R-band magnitude of the star in the Besançon model to match the magnitude of the star the light curve belongs to (as derived in from the photometric calibration, see §2.4). Then we decided randomly whether the star has a planet or not, depending on the fraction of stars having a planet of this type. If the star had a planet, we randomly picked a VHJ or HJ from one of the input planet distributions and created a star-planet pair which we attributed a randomly oriented inclination vector. If the inclination vector was resulting in a transiting orbit[21], we injected an artificial transit signal into the light curve using the stellar and planetary parameters, the inclination and a random epoch. The transits were simulated according to the formulae of Mandel & Agol (2002). After the simulation of the light curves, we applied the BLS-algorithm and checked whether or not the detected period matched the simulated period (allowing for twice and half the correct value).

One simulation run was finished after each light curve had been picked once. In this way one run represents one possible outcome of the pre-OmegaTranS survey. Since in the majority of cases the star has no planet or the inclination was such that no transits were visible, there were in general only a few transit light curves per run. We performed 500 000 simulation runs and averaged over all results. After running the BLS-algorithm, we applied the detection cuts listed in §2.6.2. A total of 132 723 simulated VHJ and HJ light curves passed the first two criteria (i.e. had a S/N higher than 12.0 and showed 2 individual transits or more). However, applying these cuts on the 15 996 pre-OmegaTranS light curves resulted in 5 589 detections. The majority of these detections are to be considered as false positive detections (noisy light curves, variable stars or light curves with uncorrected systematic effects).

---

[20] we removed the light curves of the 4 candidates

[21] the geometric probability transiting orbit mainly depends on stellar radius and semi-major axis of the orbit, see eq. 1.14

In order to lower the false positive rate and to decrease the number of light curves that have to be inspected by eye, we optimized the last two criteria using the results from the simulations. For a given maximum number of false positives we determine the optimal detection cuts S/N-$S/N_{removed}$ and reduced χ^2, for which as few as possible simulated true detections are lost. Fig. 2.32 shows the fraction of all simulated detections that were lost due to the additional two detection cuts as a function of the maximum allowed number of false positives (left panel). With the optimized detection cuts (dashed blue lines), we reduced the number of false positive detections by 96.4% to a total of 200 and lost only 15.1% of all simulated true detections. Note that the majority of the true detections were lost due to a high reduced χ^2 value indicating a variable host star. These candidates would be very difficult to follow-up and confirm anyway. In the right panel of Fig. 2.32 we plot S/N-$S/N_{removed}$ vs. reduced χ^2 of 200 false positives (red dots) and simulated true detections (black dots).
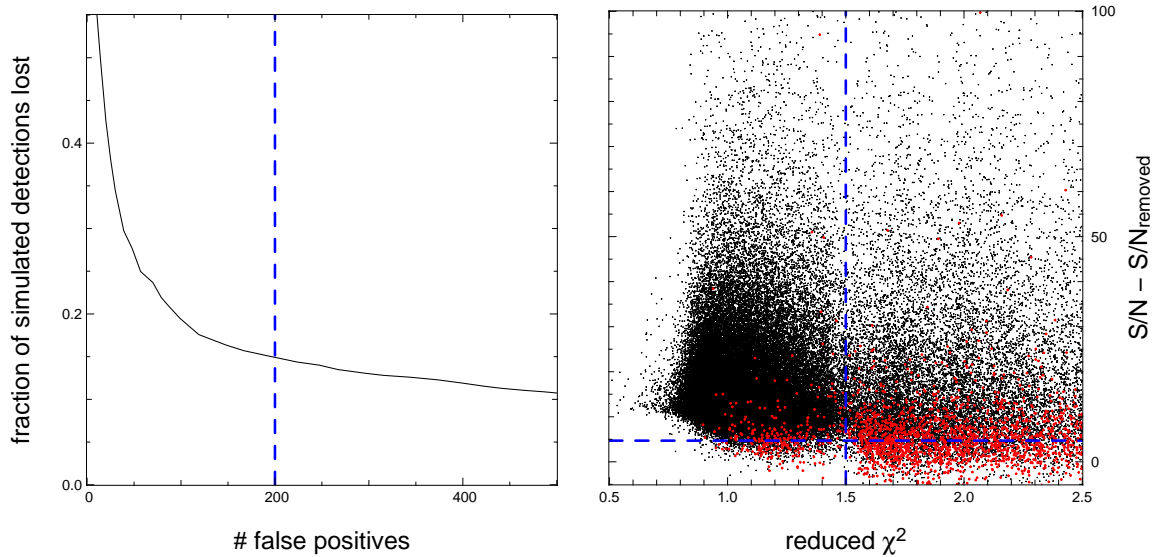
Figure 2.32: Optimizing the detection cuts of the pre-OmegaTranS project. Simulated detections are shown as black points whereas false detections are shown in red. The blue line marks the location of the optimized detection cuts. Only 15.1% of the true detections were lost while the number of false detections is reduced by 96.4% to 200.

Applying all 4 detection cuts to the simulated light curves led to 115 311 detections in 500 000 runs. Table 2.7 shows the fraction of all runs that resulted in 0, 1, 2 or 3 detections. According to our simulations, the chance to detect a planet (VHJ or HJ) was 21%. Fig. 2.33 shows the S/N distribution of all planets detected in our simulations. In Fig. 2.34 we show the expected magnitude and spectral type distribution of the host stars.

The detection of one good candidate (POTS-C1) is consistent with the results of our simulations although a null result would have been more likely. However, the planet fractions we use in our simulations have uncertainties of a factor of 2. Also the Besançon model might not well enough represent the distribution of stellar parameters in the pre-OmegaTranS fields. Due to low number statistics, we cannot conclude on any of these explanations since a 'by chance' detection is also a possible explanation.

number of detections	VHJ [%]	HJ [%]	both [%]
0	87.74	90.45	79.37
1	11.48	9.08	18.35
2	0.75	0.45	2.11
3	0.03	0.02	0.16
4	0.00	0.00	0.01

Table 2.7: Expected number of detections for the pre-OmegaTranS project.

Looking at the expected spectral type distribution (Fig. 2.33) we find our candidate to be atypically red. Note that this makes POTS-C1 very interesting for follow-up studies, since not many planets transiting low mass stars have been found so far (see §1.4).
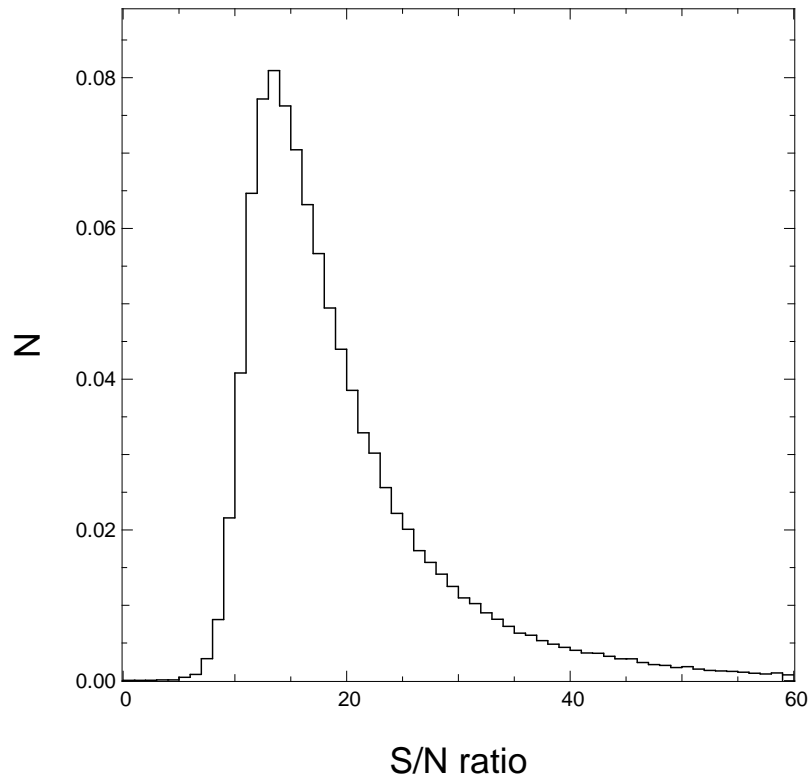
Figure 2.33: Expected S/N distribution of VHJ and HJ detections for the pre-OmegaTranS project. We show only the combined distribution since the results for VHJ and HJ are almost identical.
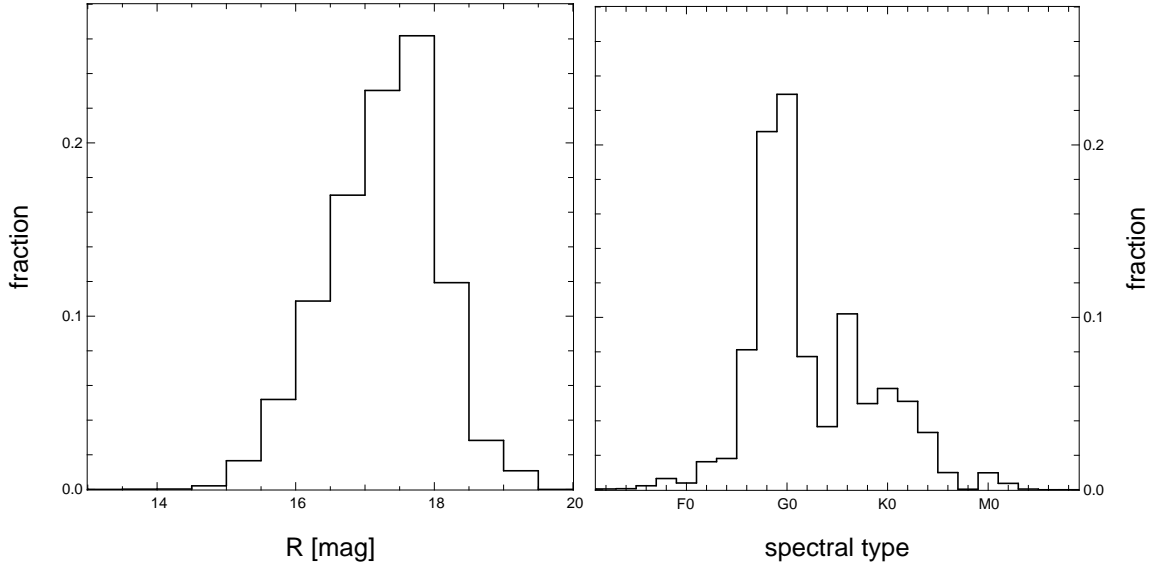
Figure 2.34: Expected host star magnitude and spectral type distribution for the pre-OmegaTranS project. Also here, the individual results for VHJ and HJ are almost identical.

2.9 Survey Byproducts: Variable Stars

Among the 16 000 light curves extracted from the pre-OmegaTranS images, we identified more than one hundred variable stars. The majority of these are short-period eclipsing binary systems but also pulsating stars and one flare star were found. We detected periodically variable sources using 4 different detection algorithms:

- BLS-algorithm (see §2.6.2): The BLS-algorithm has turned out to be very useful in the search for detached eclipsing binary systems. We tested 50 000 periods ranging from 0.1 to 100 days allowing box lengths between 0.01 and 0.4 phase units.

- LS-algorithm: To search for sinusoidal variations such as pulsating stars or contact eclipsing binary systems we used the Lomb-algorithm (Lomb, 1976) in the interpretation of Scargle (1982) for unevenly sampled data. The LS-algorithm is based on a Fourier analysis. For each light curve, the algorithm provided us a power-spectrum in the frequency range of 0.001 days^{-1} to $1\,000$ days^{-1} in which we searched for significant peaks. We used the implementation of Goessl (2007).

- LK-algorithm: The Lafler-Kinman-algorithm (Lafler & Kinman, 1965) provides a measurement of the smoothness of the folded light curve. For each test period we calculated the sum of the squared flux-differences of subsequent points in the folded light curve[22]: $LK(p) = \sum_{i=1}^{N-1}(F_{i+1} - F_i)^2$. We calculated the LK-spectrum for 20 000 periods between 0.01 and 1 000 days and search for minima of $LK(p)$.

---

[22] the points have to be sorted according to their phase value

- PDM-algorithm: The Phase-Dispersion-Method (Stellingwerf, 1978) is based on a technique to minimizes the sample variance of the phase diagram. For each test period the folded light curve was divided into m=100 segments with n_m data points and the segment-variances are summed up: $PDM(p) = \sum_{j=1}^{m} \sum_{i=1}^{n_m} (F_i - \bar{F}_j)^2 / (n_m - 1)$ with $\bar{F}_j$ being the flux-average in segment j. We tested 20 000 trial periods between 0.01 and 1 000 days.

For each light curve, we followed-up the best three periods of each of the four detection algorithm resulting in 12 possible periods. In order to find and refine the correct period, we used a String-Length-algorithm (Clarke, 2002) with 10 000 test periods within 1% of each detected period. The SL-algorithm is similar to the LK-algorithm but instead of summing up the flux-differences the sum is calculated over the 2-dimensional distance in the phase-folded light curve: $SL(p) = \sum_{i=1}^{N-1} \left[(F_{i+1} - F_i)^2 + (\phi_{i+1} - \phi_i)^2 \right]$. Finally, each light curve was folded using the period that resulted in the lowest SL-value and inspected by eye.

In the following we present a selection of the most interesting variable stars found in the pre-OmegaTranS dataset. The full catalog of variable sources will be available soon at www.usm.uni-muenchen.de/∼koppenh/. More detailed informations about the different types of variable stars can be found in Hoffmeister *et al.* (1984).
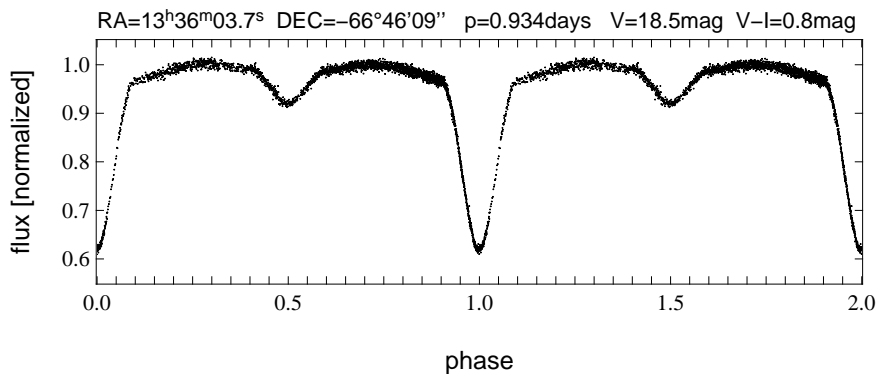
Figure 2.35: POTS-V5606989: An example of a detached eclipsing binary system of Algol type - the most common type. The two components have a different surface brightness which result in a deep primary eclipse and a shallow secondary eclipse.

RA=13^{h}33^{m}15.6^s DEC=−66°40'52"   p=2.196days   V=??.?mag V−I=?.?mag
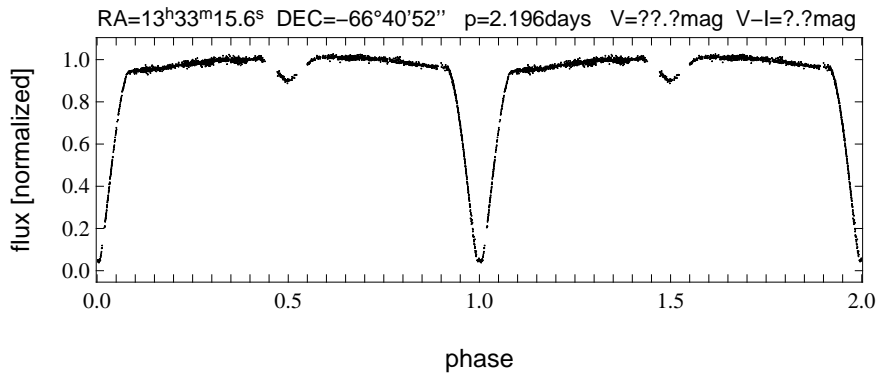
Figure 2.36: POTS-V5300024: Algol type eclipsing binary with an extremely deep primary eclipse. The system must consist of a large secondary that is eclipsing a bright but small primary causing the brightness to drop by 96%. Because the star is located very close the border of the field, no magnitude and color information is available.

RA=13^{h}37^{m}35.4^s DEC=−66°46'15"   p=0.903days   V=14.0mag V−I=1.0mag
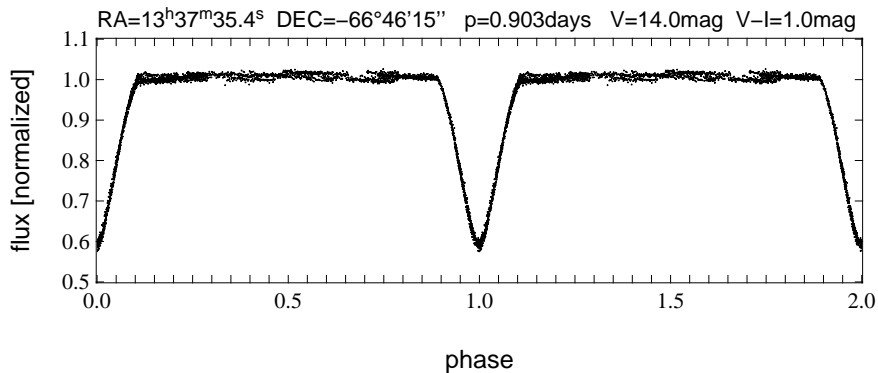
Figure 2.37: POTS-V5706871: Algol type eclipsing binary with no visible secondary eclipse. The total light is completely dominated by the primary component.

RA=13^{h}36^{m}39.7^s DEC=−66°34'48"   p=1.458days   V=16.4mag V−I=1.1mag
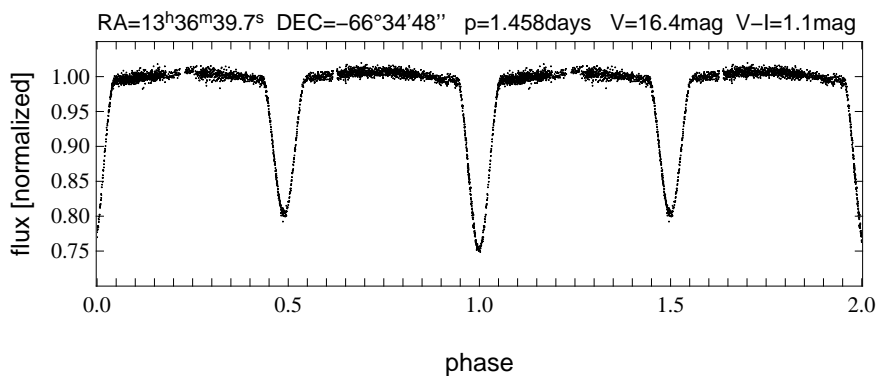
Figure 2.38: POTS-V5104049: An example of a detached eclipsing binary system of RX Her type. The two components have very similar radii and luminosities causing the light curve to show two eclipses of almost identical depth and shape.

RA=13^{h}36^{m}36.2^s DEC=−66°46'17''   p=0.924days   V=16.5mag V−I=0.9mag
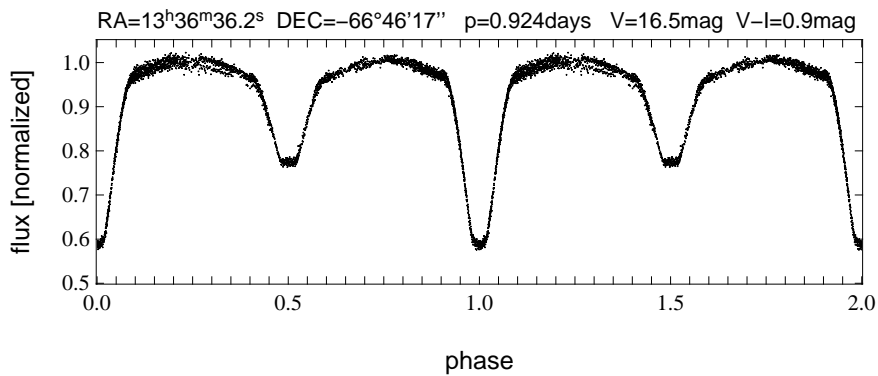
Figure 2.39: POTS-V5606939: An example of a detached eclipsing binary system of AR Lac type. In this system, a total eclipse of the secondary occurs - visible as a flat part in the light curve at phase 0.5 and 1.5.

RA=13^{h}36^{m}10.7^s DEC=−66°29'20''   p=0.637days   V=17.4mag V−I=1.2mag
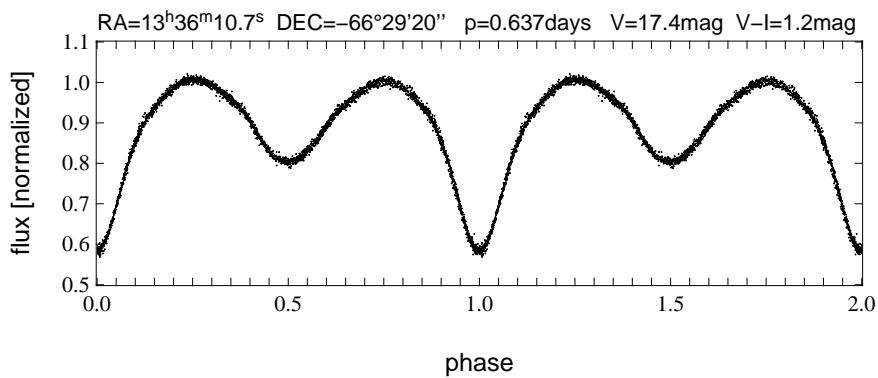
Figure 2.40: POTS-V5107329: β Lyr type eclipsing binary. This close contact system consists of components with different surface brightnesses. The ligthcurve is characterized by strong ellipsoidal variations in between two eclipses of unequal depth.

RA=13^{h}37^{m}10.7^s DEC=−66°46'27''   p=0.334days   V=17.7mag V−I=1.2mag
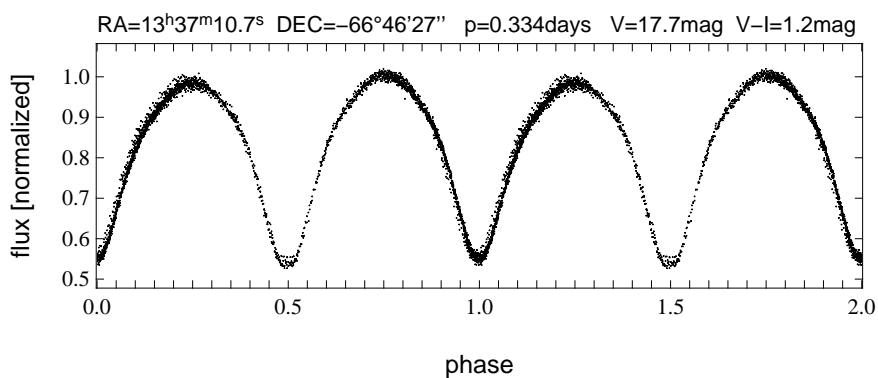
Figure 2.41: POTS-V5707071: Contact eclipsing binary system of W Uma type. Like the β Lyr type systems, there are strong ellipsoidal variations visible. Two almost identical components result in very similar primary and secondary eclipses.

RA=13^{h}35^{m}16.0^s DEC=−66°28'19''   p=0.355days   V=17.6mag   V−I=1.4mag
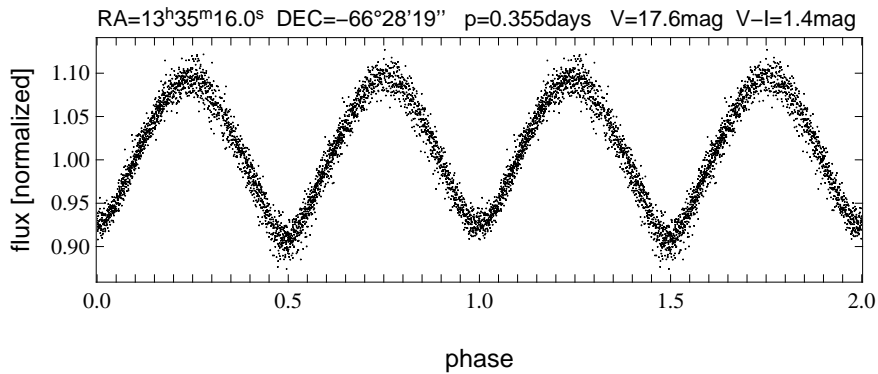
Figure 2.42: POTS-V5207790: Non-eclipsing binary contact system with strong ellipsoidal varia-tions. Not many systems of this type had been found in the past, because the accuracy needed to detect the small variations was only reached for bright stars. However, current photometric surveys reach a precision of a few mmag also for fainter stars. In the pre-OmegaTranS light curve dataset we have identified ∼20 objects of this type.

RA=13^{h}34^{m}06.4^s DEC=−66°37'34''   p=0.314days   V=18.6mag   V−I=1.7mag
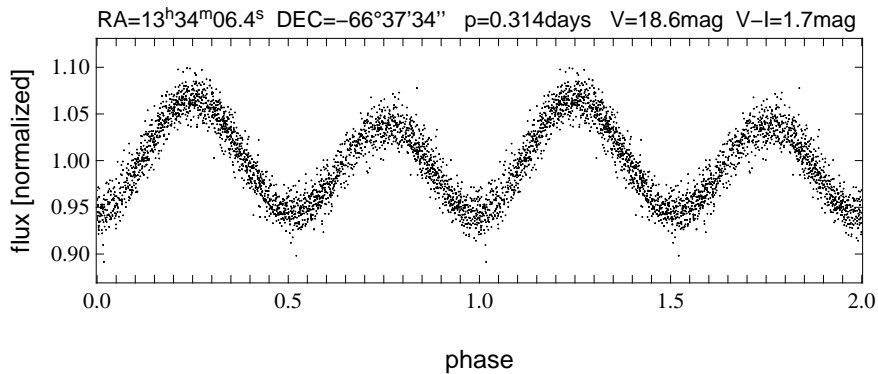
Figure 2.43: POTS-V5303056: Another non-eclipsing binary with ellipsoidal variations on a 5% level.

RA=13^{h}35^{m}52.4^s DEC=−66°33'06''   p=1.866days   V=17.7mag   V−I=1.3mag
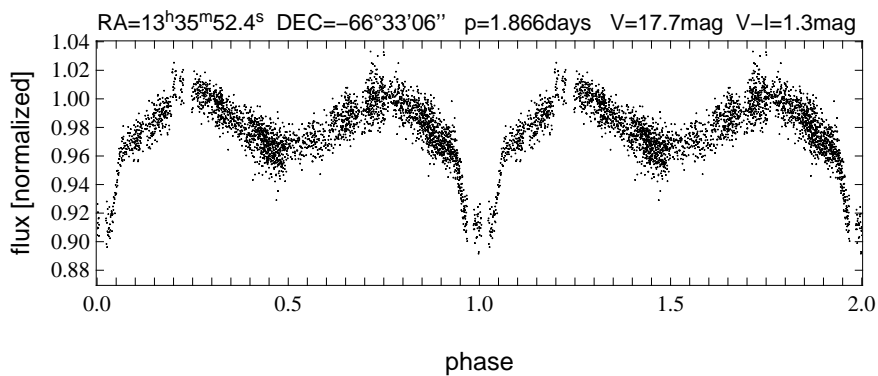
Figure 2.44: POTS-V5105074: Ellipsoidal variations on a 2% level with a grazing primary eclipse.
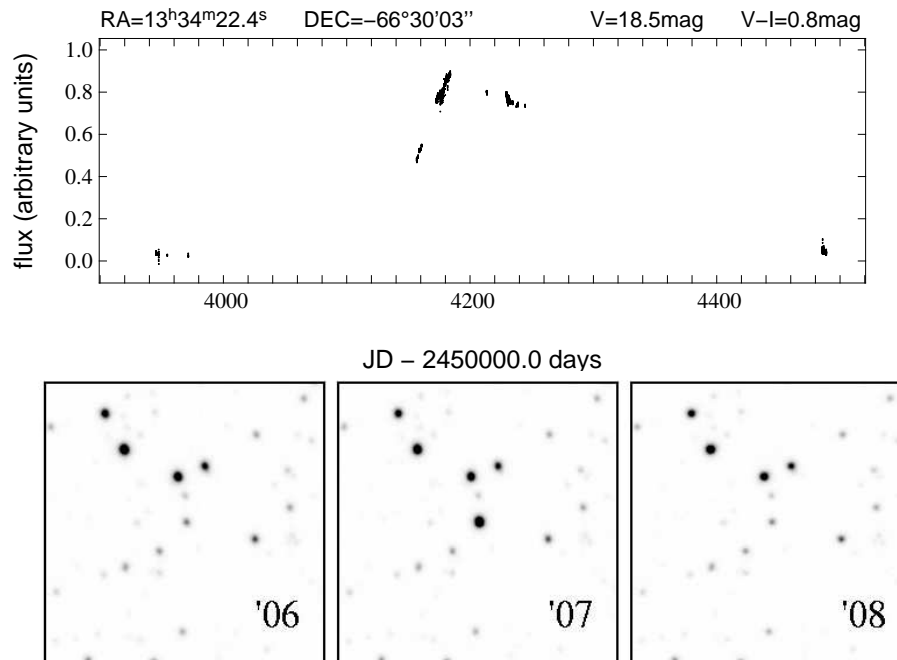
Figure 2.45: POTS-V5206701: This interesting object was very faint in 2006 and 2008 but showed a nova-like outburst in 2007 with a brightness-increase of more than a factor of 20.
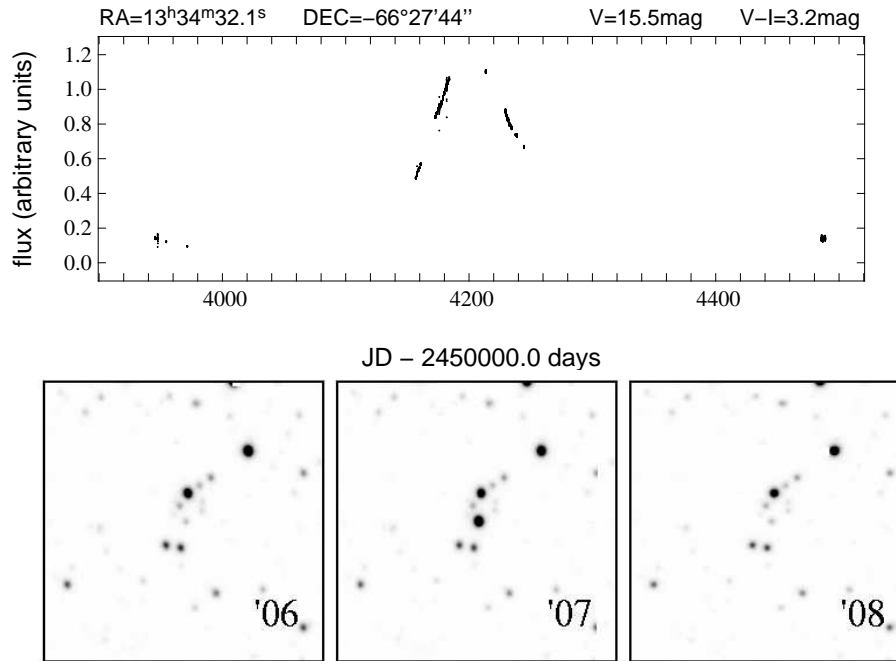
Figure 2.46: POTS-V5209654: Very red long periodically variable star, presumably a Mira type pulsating star. Note that the maximum is almost in sync with POTS-V5206701 (see Fig. 2.45). The two objects are actually very close to each other (∼2'), however, the different color and shape of the variation rules out a physical connection of the observed phenomena.
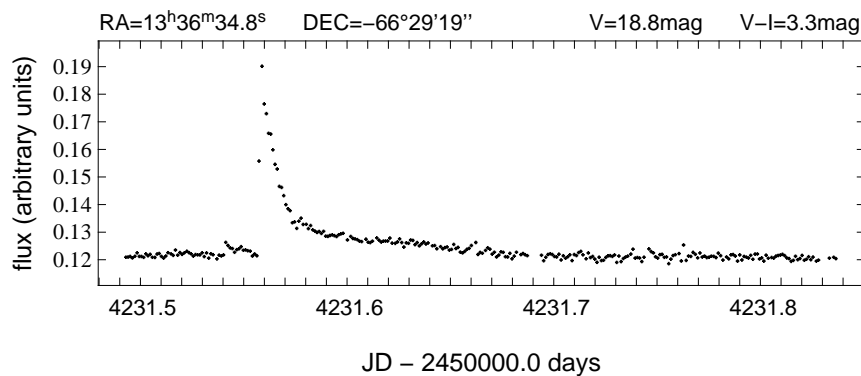
Figure 2.47: POTS-V5107359: A UV Cet type flare star showing a single outburst on May 11th 2007.

2.10 Conclusion

Analyzing the light curves of 16 000 stars, we identified 4 transiting planet candidates. Using light curve diagnostics and consistency checks we were able to provide strong evidence for a planetary nature of one of the candidates (POTS-C1). With both spectroscopic and photometric follow-up observations we will soon be able to derive the mass of the candidate. In case our expectations will be met and POTS-C1b will be confirmed as a planet, the detection will be of high scientific value. With a spectral type of K7, POTS-C1 would be the second lowest mass host star around which a transiting planet was found (only GJ436, an M-dwarf, has a lower mass).

We estimate the luminosity of POTS-C1 to be 0.1 $L_\odot$. Given the close distance of 0.02 AU, the irradiation at the surface of POTS-C1 is 250 times higher than the Solar constant. Due to the close distance to the star, POTS-C1b will most likely be tidally locked.

In the course of the pre-OmegaTranS project we set-up and optimized the data reduction pipeline. We have proven to be able to produce high precision lightcurves with only a minimum level of systematic noise. Therefore we are now in a good position to start the OmegaCam Transit Survey and search for low-mass planets around M-dwarfs and Jupiters in open clusters.

Chapter 3

Follow-up of OGLE2-TR-L9

This Chapter is based on Snellen *et al.* (2009). The photometric observations of the OGLE-II microlens monitoring campaign have been taken in the period 1997−2000. All light curves of this campaign have recently become public. Our analysis of these data has revealed 13 low-amplitude transiting objects among ∼15700 stars in three Carina fields towards the Galactic disk. One of these objects, OGLE2-TR-L9 (P∼2.5 days), turned out to be an excellent transiting-planet candidate. In this section, we report on our investigation of the true nature of OGLE2-TR-L9. By re-observing the photometric transit, we attempt to determine the transit parameters to high precision, and, by spectroscopic observations, to estimate the properties of the host star and determine the mass of the transiting object by means of radial velocity measurements.

High precision photometric observations were obtained in g', r', i', and z' band simultaneously, using the new GROND detector, mounted on the MPI/ESO 2.2m telescope at La Silla. Eight epochs of high-dispersion spectroscopic observations were obtained using the fiber-fed FLAMES/UVES Echelle spectrograph, mounted on ESO's Very Large Telescope at Paranal.

The photometric transit, now more than 7 years after the last OGLE-II observations, was re-discovered only ∼8 minutes from its predicted time. The primary object is a rapidly rotating F3 star with $v\sin i$=39.33±0.38 km/s, T=6933±58 K, log g = 4.25±0.01, and [Fe/H] = −0.05±0.20. The transiting object is an extra-solar planet with M_p=4.5±1.5 M_{Jup} and R_p=1.61±0.04R_{Jup}.

Since this is the first planet detected orbiting a fast rotating star, the uncertainties in both the radial velocity measurements and the planetary mass are larger than for most other planets discovered to date. The rejection of possible blend scenarios was based on a quantitative analysis of the multi-color photometric data. A stellar blend scenario of an early F-star with a faint eclipsing-binary system is excluded, due to 1) the consistency between the spectroscopic parameters of the star and the mean density of the transited object as determined from the photometry, and 2) the excellent agreement between the transit signal as observed at four different wavelengths.

3.1   Transit Photometry with GROND
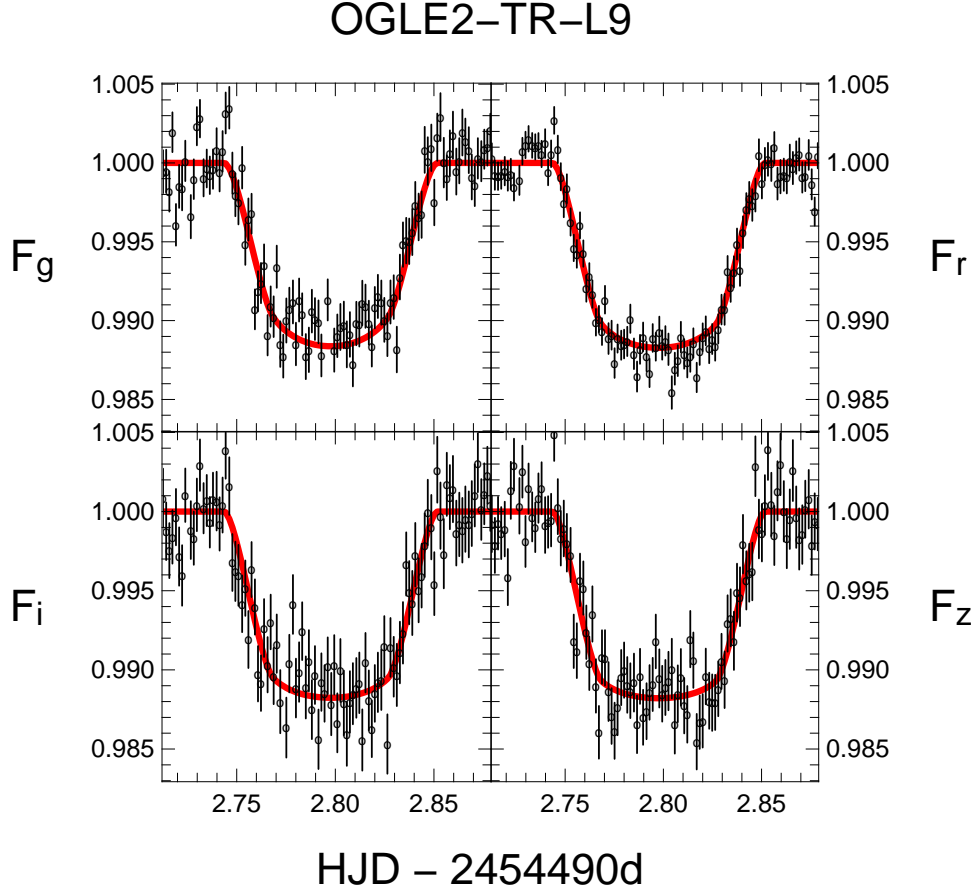
Figure 3.1: Transit light curves of OGLE2-TR-L9 in g′, r′, i′ and z′ observed simultaneously with the GROND instrument, mounted on the MPI/ESO 2.2m telescope. The line shows the best model fit for the combined light curves, as discussed in the text.

3.1.1   Data acquisition and analysis

We observed one full transit of OGLE-TR-L9 with GROND (Greiner *et al.*, 2008), which is a gamma ray burst follow-up instrument mounted on the MPI/ESO 2.2m telescope at the La Silla observatory. GROND is a 7-channel imager that allows to take 4 optical (g′r′i′z′) and 3 near infrared (JHK) exposures simultaneously. On January 27, 2008, a total of 104 images in each optical band and 1248 images in each near infrared band were taken. The JHK-images turned out to have insufficient signal-to-noise ratio to be able to detect the transit, and will not be considered further. Using exposure times of 66 seconds and a cycle rate of 2.5 minutes, we covered a period of about 4 hours centered on the predicted transit time.

filter	γ_1	γ_2
g′	0.3395	0.3772
r′	0.2071	0.3956
i′	0.1421	0.3792
z′	0.0934	0.3682

Table 3.1: Limb-darkening coefficients used for the transit fitting, taken from Claret (2004) for a star with metallicity $[Fe/H] = 0.0$, surface gravity log $g = 4.5$, and effective temperature $T_{eff} = 7000$K.

All optical images were reduced with the *mupipe* software developed at the University Observatory in Munich[1]. After the initial bias and flat-field corrections, cosmic rays and bad pixels were masked, and the images were resampled to a common grid. The frames did not suffer from detectable fringing, even in the z-band. Aperture photometry[2] was performed on OGLE2-TR-L9 and eight to ten interactively selected reference stars, after which light curves were created for each of the 4 bands. The aperture radius was chosen to be 12 pixels, corresponding to 1.9 arcseconds, and the seeing was typically 1.1 arcseconds during the observations. The sky was determined in an annulus between 20 and 30 pixels from the object positions. The rms in the individual light curves of the reference stars was in all cases lower than 0.3%, which provided typical precisions in the relative fluxes superior to 0.2%.

3.1.2 Fitting the transit light curves

The light curves in g′, r′, i′, and z′, were fitted with analytic models presented by Mandel & Agol (2002). We used quadratic limb-darkening coefficients taken from Claret (2004), for a star with metallicity [Fe/H]=0.0, surface gravity log g=4.5, and effective temperature T_{eff}=7000K (close to the spectroscopic parameters of the star as determined below). The values of the limb-darkening coefficients are given in Table 3.1.

Using a simultaneous fit to all 4 light curves, we derived the mean stellar density, M_{star} / R_{star}^3 in solar units, the radius ratio R_{planet} / R_{star}, the impact parameter β_{impact} in units of R_{star}, and the timing of the central transit. With a scaling factor for each band, eight free parameters could be fitted.

The light curves and the model fits are shown in Fig. 3.1, and the resulting parameters are listed in Table 3.2. The model fits the light curves well except for the g-band light curve, which is attributed to the significantly more noisy light curve, and the poorly determined baseline, particularly before ingress.

3.2 Spectroscopic Observations with UVES/FLAMES

We observed OGLE2-TR-L9 with the UV-Visual Echelle Spectrograph (UVES; Dekker *et al.* (2000)), mounted at the Nasmyth B focus of UT2 of ESO's Very Large Telescope (VLT) at Paranal, Chile.

---

[1] http://www.usm.lmu.de/∼arri/mupipe/

[2] note that for a bright object like OGLE-TR-L9, aperture photometry performs better than the difference imaging technique (see §2.5) which is limited to ∼ 2-3 mmag due to systematic effects. Since there are many equally bright or brighter reference stars in the vicinity of OGLE-TR-L9 we achieved a better precision with aperture photometry, see below

The aims of these observations were to estimate the spectroscopic parameters of the host star, and to determine the radial velocity variations. The observations were performed in fiber mode, with UVES connected to the FLAMES fiber facility (Pasquini *et al.*, 2002), with 7 science fibers and with simultaneous thorium-argon wavelength calibration (*UVES7 mode*).

Apart from our main target, fibers were allocated to two other OGLE-II transit candidates from S07 (OGLE2-TR-L7 and OGLE2-TR-L12), and three random stars within the 25′ FLAMES field. In addition, one fiber was positioned on the empty sky. A setup with a central wavelength of 580 nm was used, resulting in a wavelength coverage of 4785−6817Å over two CCDs, at a resolving power of R=47000. Since the upper CCD was found to cover only a small number of strong stellar absorption lines, in addition to being affected by significant telluric contamination, only the lower CCD (4785−5729Å) was used for further analysis.

Eight observations were taken in Director's Discretionary Time, in service mode during December 2007 and January 2008, and spread in such a way that the data would be evenly distributed across the orbital phases of our main target (see Table 3.3). The data were analyzed using the *midas*-based UVES/FLAMES pipeline provided by ESO, which results in fully reduced, wavelength-calibrated spectra. Since we were concerned with the wavelength calibration of the fifth epoch (see below), we also analyzed the data using purpose-build IDL routines. No significant differences in the wavelength solutions were found. The resulting signal-to-noise per resolution element, in the central part of the orders, varied between ∼10 and 20 during the different epochs (see Table 3.3).

3.2.1 Determination of stellar spectroscopic parameters
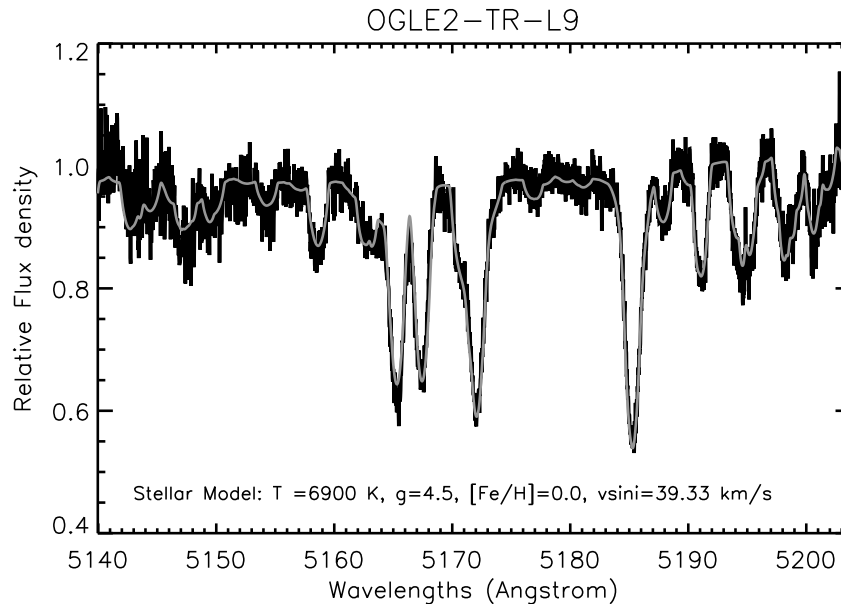
Figure 3.2: The central part of one order of the combined UVES spectrum of OGLE2-TR-L9, with overplotted a synthetic spectrum with T=6900 K, g=4.5, [Fe/H]=0, and v*sin*i = 39.33 km/sec.

Transit:		
ρ_s	=	0.4260±0.0091 ρ_{sun}
R_p/R_s	=	0.10847±0.00098
β_{impact}	=	0.7699±0.0085
t_0	=	2 454 492.79765±0.00039 HJD
P	=	2.4855335±7×10^{-7} d
Host star:		
Coord. (J2000)	=	11^h 07^m 55.29^s $-61°$ $08'$ $46.3''$
I mag	=	13.974
I−J mag	=	0.466±0.032
J−K mag	=	0.391±0.049
T	=	6933±58 K
log g	=	4.47±0.13*
log g	=	4.25±0.01**
$[Fe/H]$	=	−0.05±0.20
vsini	=	39.33±0.38 km/s
R_s	=	1.53±0.04 R_{sun}
M_s	=	1.52±0.08 M_{sun}
Age	<	0.66 Gyr
Planetary Companion:		
K	=	510±170 m/s
i	=	79.8±0.3°
a	=	0.0413±0.0005 AU
R_p	=	1.61±0.04 R_{Jup}
M_p	=	4.5±1.5 M_{Jup}

*Determined from the spectroscopic analysis
**Determined from mean stellar density combined with the
   evolutionary tracks

Table 3.2: The transit, host star, and planetary companion parameters as determined from our photometric and spectroscopic observations.

The spectroscopic parameters of the star, vsini, surface temperature, surface gravity, and metallicity, were determined from the SNR-weighted, radial velocity shifted combination of the eight epochs taken with UVES. This combined spectrum has a signal-to-noise ratio of ~42 in the central areas of the orders. Detailed synthetic spectra were computed using the interactive data language (IDL) interface SYNPLOT (I. Hubeny, private communication) to the spectrum synthesis program SYNSPEC (Hubeny *et al.*, 1994), utilizing Kurucz model atmospheres[3]. These were least-squares fitted to each individual order of the combined UVES spectrum. The final atmospheric parameters were taken as the average values across the available orders. The uncertainties in the fitted parameters estimated using a χ-square analysis and from the scatter between the orders, provided similar results, of which the latter are adopted.

---

[3] http://kurucz.harvard.edu/grids.html

HJD	Orbital	SNR	RV	BiS
-2450000	Phase		km s^{-1}	km s^{-1}
4465.8421	0.157	19.0	1.090±0.224	-0.076±0.482
4466.8583	0.566	16.6	1.204±0.276	0.173±0.380
4468.7219	0.316	11.2	0.842±0.212	-0.233±0.683
4472.7447	0.934	14.7	1.105±0.231	-0.492±0.460
4489.6749	0.746	9.0	2.345±0.376	0.123±1.101
4490.8382	0.214	15.3	0.472±0.318	0.235±0.339
4493.7697	0.393	19.9	1.187±0.187	-0.150±0.432
4496.7703	0.601	19.0	1.190±0.272	0.418±0.545

Table 3.3: Spectroscopic observations of OGLE2-TR-L9 taken with UVES/FLAMES. The first three columns give the Heliocentric Julian Date, the planet's orbital phase at the time of observation, and the signal-to-noise ratio of the spectra per resolution element in the center of the middle order. Column 4 and 5 give the radial velocity and the bisector span measurements.

The best-fit solution parameters and their uncertainties are given in Table 3.2. One order of the combined UVES spectrum is shown in Fig. 3.2, showing the Mg$_b$ 5170$\mathring{A}$ complex, with the synthetic spectrum with T=6900 K, log g=4.5, [Fe/H]=0, and vsini = 39.33 km/sec, overplotted.

3.2.2   Radial velocity measurements

The orders of the eight spectra were first cosine-tapered to reduce edge effects. Cross-correlations were performed using the best-fit velocity-broadened synthetic spectrum, as determined above, as a reference. The spectrum of the sky-fiber indicated that the sky contribution was typically of the order of ~0.5%. However, for the observation at 0.74 orbital phase (epoch 5), the relative sky levels were an order of magnitude larger, due to a combination of bad seeing and a full moon. We therefore subtracted the sky spectrum from all target spectra before cross-correlation.

The resulting radial velocity data are presented in Table 3.3, after correction to heliocentric values. The uncertainties are estimated from the variation of the radial velocity fits between the different orders. The final radial velocity data as function of orbital phase (the latter determined from the transit photometry), are shown in Figure 3.3. The data were fitted with a sine function with amplitude, K, and a zero-point, V_0, as free parameters. The radial velocity amplitude was determined at K = 510 ± 170 m/s, with V_0 = +0.2 km/s.

We also determined the variations in the bisector span (following Queloz *et al.* (2001)) as function of both radial velocity and orbital phase which are shown in Fig. 3.4. We performed a least-squares fit of the bisector span measurements as function of orbital phase with a sinusoid, but no significant variations at a level of -0.01 ± 0.140 km s^{-1} were found. Although this means that there is no indication that the measured radial velocity variations are due to line-shape variations, caused by either stellar activity or blends of more than one star, the errors are very large, making any claim based on the bisector span uncertain.
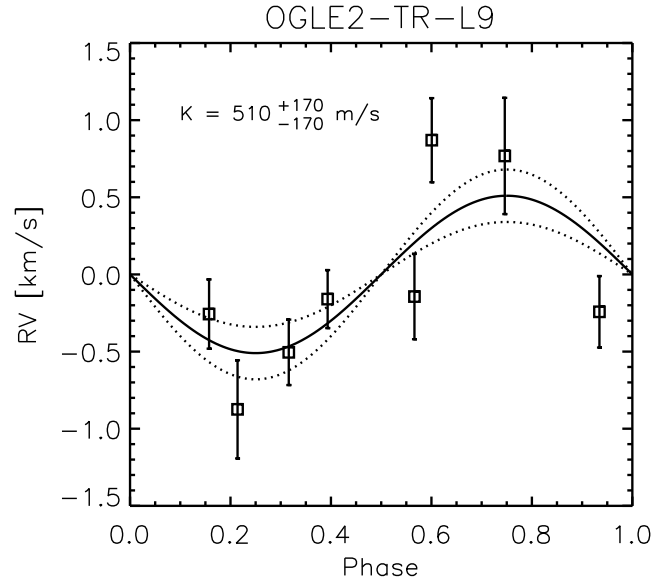
Figure 3.3: The radial velocity measurements of OGLE2-TR-L9 as function of orbital phase from the ephemeris of the transit photometry.

3.3 Estimation of the Stellar and Planetary Parameters

3.3.1 Stellar mass, radius, and age

The transit photometry provides an estimate of the mean density of the host star, while the spectroscopic observations yield its surface temperature, surface gravity, and metallicity. The stellar evolutionary tracks of Siess *et al.* (2000) were used subsequently to estimate the star's mass, radius, and age, resulting in $M_s = 1.52 \pm 0.08$ M_{Sun}, $R_s = 1.53 \pm 0.04$ R_{Sun}, and an age of <0.66 Gyr. These parameters correspond to a surface gravity of $\log g = 4.25 \pm 0.01$, which is in reasonable agreement, but about 1.7σ lower than the spectroscopic value. It should be realized that it is notoriously difficult to obtain reliable log g values from spectra at relatively low signal-to-noise ratio.

3.3.2 Planetary mass and radius

Using the values obtained from the transit fit to the GROND light curves, the radial velocity curve fit, and the stellar parameters derived above, we obtain a planetary mass of $M_p = 4.5 \pm 1.5$ M_{Jup} and a planetary radius of $R_p = 1.61 \pm 0.04$ R_{Jup}. The semi-major axis of the orbit is a=0.0413 $\pm$ 0.0005 AU and the mean density of the planet is 1.44 ± 0.49 g cm^{-3}.

This implies that OGLE2-TR-L9b is one of the largest known transiting hot Jupiters, only TrES-4b and WASP-12b are marginally larger, although its mean density is similar to that of Jupiter. Even so, OGLE2-TR-L9b is significantly larger than expected for an irradiated $\sim$4.5 M_{Jup} planet (Fressin *et al.*, 2007).
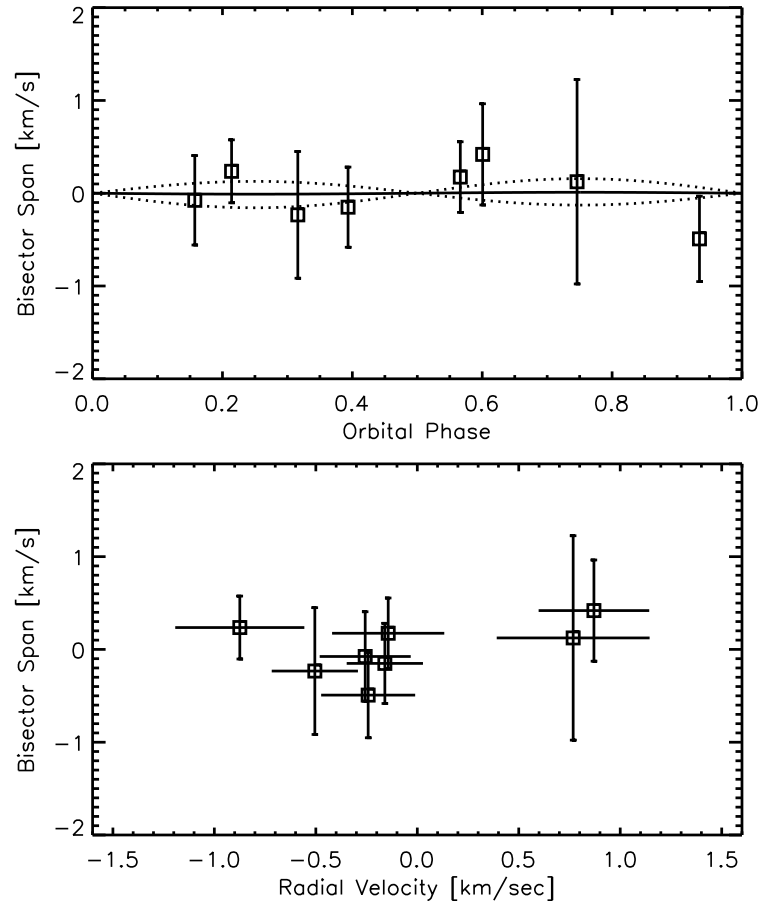
Figure 3.4: Bisector variations as function of orbital phase (top panel) and radial velocity value (bottom panel). The solid line and dashed lines in the top panel indicate the least-squares fit to the sinusoidal variation in the bisector span and its uncertainty at -0.01 ± 0.140 km s^{-1}.

3.4   Rejection of Blended Eclipsing Binary Scenarios

Large photometric transit surveys are prone to produce a significant fraction of false interlopers among genuine, transiting, extra-solar planets. If the light from a short-period eclipsing stellar binary is blended with that from a third, brighter star, the combined photometric signal can mimic a transiting exoplanet. Although the radial velocity variations induced by an eclipsing binary should be orders of magnitude larger than those caused by a planet, the blending of the spectral lines with those from the brighter, third star could produce variations in the overall cross-correlation profile that have significantly smaller amplitudes, possibly as small as expected for giant planets. Since this would be accompanied with significant line-shape variations, bisector span analyses are often used to reject a blended eclipsing binary scenario.
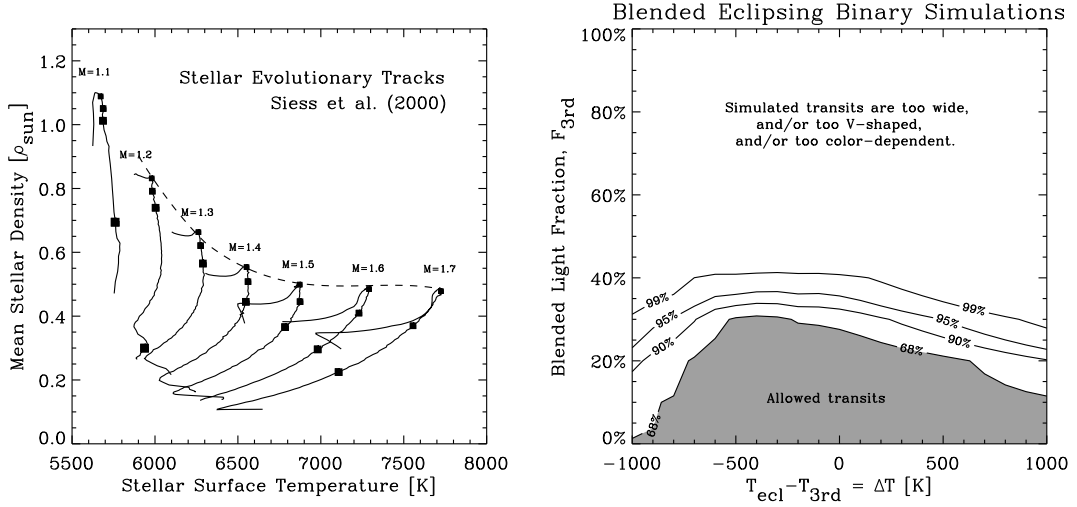
Figure 3.5: The upper panel shows the stellar surface temperature, T_s, versus the mean density, ρ_s, for evolutionary tracks of Siess *et al.* (2000). The filled squares on each track indicate stellar ages of 0.1, 0.5, and 1×10^9 years, (and 5×10^9 years for $M \leq 1.2 M_{Sun}$), with larger symbols indicated higher ages. The dashed line indicates the maximum possible ρ_s for a given stellar surface temperature. The bottom panel shows the confidence intervals from the χ-square analysis of all possible blended eclipsing binary scenarios fitted to the GROND light curves. On the x-axis the difference in surface temperature between the eclipsed and the third star is shown, and on the y-axis the fraction of the total light coming from the third star in r'-band. It shows that the combined g'r'i'z' light curves can only be fitted including a low level ($\lesssim 30\%$) of light contamination.

Although no significant variations in the bisector span are observed in OGLE2-TR-L9, it could be argued that this is due to the low signal-to-noise ratio of the data. We show however that a blended eclipsing binary scenario can be rejected anyway, because of the following observations:

1 Transit light curves from g' to z' band: As can be seen in Fig. 3.1, there is an excellent agreement between the light curves from g to z band. This means that if the transit was actually caused by a background eclipsing binary blended with a bright foreground star, the colors (and thus the surface temperatures) of the eclipsed binary star and foreground star should be very similar.

2 Transit shape and spectral classification: The mean stellar density determined from the transit photometry is in excellent agreement with that inferred from the spectral classification, both being consistent with an early F-star. Using the argument above, this means that if this is a blend, then both the foreground star and the eclipsed binary star should be early F stars.

However, if we now assume that a significant fraction of the light originates from a foreground star, and we remove this contribution from the light curve, the transit can no longer be fitted by an early F-star, but only by a star of significantly higher mean density, implying a cooler, less massive star, again in contradiction with point 1). This implies that the early F-star *is* the transited object, and that a blended eclipsing binary scenario can be rejected.

To explore further the possible role of additional light from a blended star, we performed a quantitative analysis, simulating background eclipsing binary systems with their light diluted by that from a third star. We first used the stellar evolutionary tracks of Siess *et al.* (2000) to determine the full range of stellar parameters that can be present in eclipsing binaries, of which only the stellar surface temperature, T_{ecl}, and the mean stellar density, ρ_{ecl} of the eclipsed star are of interest in the simulations. We note that the evolutionary status of the third star is not important, since we do not restrict ourselves to physical triple systems, but also include chance-alignments of back- and foreground stars. As is indicated in the top panel of Fig. 3.5, where the stellar evolutionary tracks are shown, there is a maximum possible mean-stellar density for a given surface temperature. This was used as a boundary condition in the simulations.

In our simulations we varied two parameters, 1) the difference between the surface temperature of the eclipsed star and that of the third star, ΔT (-1000 K$<\Delta T<+1000$ K), and 2) the fraction of light originating from the third (possibly unrelated) star, F_{3rd} ($0<F_{3rd}< 99\%$). The combined light of the eclipsing binary and third star should produce a spectrum which with a surface temperature of $T_{comb} = 6933$ K. Therefore, a simple linear relation between T_{comb} and the surface temperatures of the individual stars was assumed, such that $T_{ecl} = T_{comb} - \frac{F_{3rd}}{1+F_{3rd}}\Delta T$. We note that any small fraction of light that could originate from the eclipsing star is simply added to F_{3rd}. In this way, each combination of F_{3rd} and ΔT, results in a T_{ecl} and a maximum possible ρ_{ecl}. It also results in a fractional contribution of light from the third star that varies over the four filters.

For each combination of F_{3rd} and ΔT, model eclipsing binary light curves fitted to the g'r'i'z' GROND data, using as before the algorithms of Mandel & Agol (2002), in which the binary size ratio and the impact parameter were completely free to vary, and ρ_{ecl} was retricted to be below the upper limit set by T_{ecl}. In this way, all possible blended eclipsing binary scenarios were simulated, independently of whether or not the third star is physically related to the binary. The bottom panel of Fig. 3.5 shows the confidence contours of the χ-square analysis of all possible blended eclipsing binary scenarios. It shows that the combined g'r'i'z' data can only be fitted by light curves of eclipsing binaries with a low level $\lesssim 30\%$ (90% confidence level) of blended light, meaning that most light in the stellar spectrum must originate from the eclipsed star.

Scenarios in which the stellar spectrum is dominated by a third star with a small contribution from a background eclipsing binary, can be strongly rejected. The transit light curves produced by those rejected scenarios are simply too wide, too V-shaped, and/or too color dependent to fit the GROND data. One scenario that we cannot reject, is a small contribution from a blended star. For example, it could in principle be possible that the light from the transited F3 star is diluted at a $\sim 30\%$ level with light from another F-star (with a similar v*sin*i and radial velocity, otherwise it would show up in the spectra). In this case, the transiting planet would be $\sim 30\%$ more massive (and $\sim 15\%$ larger) than determined above, by no means outside the planet mass range.

We note that for most transiting planets presented in the literature, such a low-level contamination scenario can not be excluded, since the variations in the bisector span would be orders of magnitude smaller than in the case of a blended eclipsing stellar binary. This is because the radial velocity variations in the latter case are 10^{2-3} times larger than in the first case.

There have been several reports of blended eclipsing binaries hiding out as transiting planets, most notably by Mandushev *et al.* (2005) and Torres *et al.* (2004). However, these studies dealt with very low signal-to-noise ratio light curves, whereas the true nature of these systems would have been easily established by high quality photometric data similar to that presented in this paper.

Mandushev *et al.* (2005) rejected a transiting planet scenario for the rapidly rotating ($v\sin i$=34 km/s) F5 star GSC 01944-02289, in favour of a blended eclipsing binary. This system was shown to be a hierarchical triple consisting of an eclipsing binary with G0V and M3V components, in orbit around a slightly evolved F5 dwarf. The latter star in this scenario contributes for ∼89% to the total light from the system. Although they claim that the true nature of this system was not revealed by their BVI light curves, the color difference between the G0V and F5V star implies that the transit must be 25-30% deeper in I-band than in B-band. However, no quantitative analysis of the light curves was presented, and the authors claimed that the true nature of the system was only brought to light by spectroscopic means.

In a similar fashion, Torres *et al.* (2004) presented the case of OGLE-TR-33, which was identified as a triple system consisting of an eclipsing binary with F4 and K7-M0 components orbiting a slightly evolved F6 star. However, the photometry in this study relied solely on the original I-band OGLE-III data, resulting in a relatively low SNR transit detection for which the ingress and bottom of the transit were not well covered. They also claimed that the blended eclipsing binary was only revealed by spectroscopy. However, their best-fit planet model already pointed towards a very unlikely planet radius of ∼3 R_{Jup}, and the V-shaped transit produced by the blended eclipsing binary would have been easily detected by our high precision photometry. We note that while Torres *et al.* (2004) and Mandushev *et al.* (2005) only considered physical triple systems, our analysis presented above covers all possible scenarios, including those involving chance-alignment of background or foreground stars.

3.5   Discussion

More than seven years and >1000 orbital periods after the last observations of OGLE2-TR-L9, we have rediscovered the transit signal only 8 minutes from its predicted time (from S07). Our study not only shows that an observing campaign with long time intervals between measurements can produce reliable light curves, it also shows that it produces extremely accurate orbital periods.

OGLE2-TR-L9b is the first extra-solar planet discovered transiting a rapidly rotating (vsini=39 km/s) F-star. OGLE2-TR-L9 is also the star with the highest surface temperature (T=6933 K) of all main-sequence stars that host an exoplanet known to date. It is therefore not surprising that the uncertainties in the radial velocity variations are higher than for most other transiting exoplanets presented in the literature. Only because of the high mass of OGLE2-TR-L9b, we were able to detect its radial velocity signature. We note, however, that since a blend scenario can be rejected at high significance, an upper limit to the mass of OGLE2-TR-L9b would have been sufficient to claim the presence of a transiting, extra-solar planet, although of unknown mass. Similar arguments have to be used in the case of future detection of the transits of Earth-size planets from Kepler or CoRoT, since their radial velocity signature may be too small to measure.

OGLE2-TR-L9b has a significantly larger radius than expected for a planet of about 4.5 times the mass of Jupiter, even if it is assumed that 0.5% of the incoming stellar luminosity is dissipated at the planet's center (Fressin *et al.*, 2007). However, it is not the only planet found to be too large (e.g. CoRoT-exo-2b, TrES-4b, and XO-3b). Several mechanisms have been proposed to explain these 'bloated' radii, such as more significant core heating and/or orbital tidal heating (see Liu *et al.* (2008) for a recent detailed discussion).

The measured vsini and estimated stellar radius have been combined to infer a rotation period of the host star of $\sim$1.97$\pm$0.04 days. This implies that the rotation of the star is not locked to the orbital period of OGLE2-TR-L9b. A vsini of 39 km/sec is within the normal range for stars of this spectral type. The mean vsini of F5 to F0 stars in the solar neighbourhood range from 10^2 to 10^3 km/sec respectively. We note that the vsini of OGLE2-TR-L9a is only $\sim$9% of the expected break-up velocity for a star of this mass and radius. Assuming the general Roche model for a rotating star (e.g. Seidov (2004)), the ratio of polar to equatorial radius of OGLE2-TR-L9a will be on the order of, $1 - \frac{1}{2}(v/v_{max})^2 \sim 0.996$. Thus, the rotational flattening of the host star is not expected to influence the transit shape significantly. OGLE2-TR-L9 is expected to exhibit a strong Rossiter-McLaughlin effect. Simulation using a segmented stellar surface predict an amplitude of 230 m/sec.

Chapter 4

Optimization of the Pan-Planets Survey Strategy

4.1 Abstract

This Chapter is based on Koppenhoefer *et al.* (2009). Using Monte Carlo simulations we analyze the potential of the upcoming transit survey Pan-Planets. The analysis covers the simulation of realistic light curves (including the effects of ingress/egress and limb-darkening) with both correlated and uncorrelated noise as well as the application of a box-fitting least squares detection algorithm. In this work we show how simulations can be a powerful tool in defining and optimizing the survey strategy of a transiting planet survey.

We find the Pan-Planets project to be competitive with all other existing and planned transit surveys with the main power being the large 7 square degree field of view. In the first year we expect to find up to 25 Jupiter-sized planets with periods below 5 days around stars brighter than V = 16.5 mag. The survey will also be sensitive to planets with longer periods and planets with smaller radii. After the second year of the survey, we expect to find up to 9 Warm Jupiters with periods between 5 and 9 days and 7 Very Hot Saturns around stars brighter than V = 16.5 mag as well as 9 Very Hot Neptunes with periods from 1 to 3 days around stars brighter than i' = 18.0 mag.

4.2 The Pan-Planets Survey

The Panoramic Survey Telescope and Rapid Response System (PanSTARRS) is an Air Force funded project aiming at the detection of killer asteroids that have the potential of hitting the Earth in the near future. The prototype mission PanSTARRS1 is using a 1.8m telescope at the Haleakala Observatories (Maui, Hawaii) to monitor 3π of the sky over a 3.5 yr period starting in early 2009. The telescope is equipped with the largest CCD camera in the world to date that samples a field of 7 sq.deg. on a 1.4 Gigapixel array (Kaiser, 2004) with a pixel-size of 0.258 arcsec.

To make use of the large amount of data that will be collected, a science consortium of institutes from USA, Germany, UK and Taiwan has defined 12 Key Science Projects, out of which one is the Pan-Planets transit survey. A total of 120h per year have been dedicated to this project during the 3.5 yr lifetime of the survey. The actual observing time will be less due to bad weather and technical downtime. We account for a 33% loss in our simulations.

In the first two years, Pan-Planets will observe 3 to 7 fields in the direction of the Galactic plane. Exposure and read-out time will be 30s and 10s respectively. The observations will be scheduled in 1h or 3h blocks. The target magnitude range will be 13.5 to 16.5 mag in the Johnson V-band. The magnitude range is extended to i' = 18 when searching for Very Hot Neptunes (see §4.4.6). More detailed informations about Pan-Planets are presented in Afonso et al. (in prep.).

4.3 Simulations

The goal of this work is to study the expected number of planets that will be detected by the Pan-Planets project as a function of different survey strategies, with a variety of different parameters like number of fields (3 to 7), length of a single observing block (1h and 3h) and level of residual red noise (0 mmag, 1 mmag, 2 mmag, 3 mmag and 4 mmag). In total we simulate about 100 different combinations of these parameters for each of 5 different planet populations (see §4.3.2).

In our simulations we follow a full Monte-Carlo approach, starting with the simulation of light curves with realistic transit signals. Systematic effects coming from data reduction steps on image basis, such as differential imaging or PSF-photometry are taken into account by adding non-Gaussian correlated noise, the so called red noise (Pont *et al.*, 2006), to our light curves (see §4.3.4). We apply a box-fitting least squares algorithm to all simulated light curves in order to test whether a transiting planet is detected or not.

For each star in the input stellar distribution (§4.3.1) we decide randomly whether it has a planet or not, depending on the fraction of stars having a planet of this type. In the case it has a planet, we randomly pick a planet from the input planet distribution (§4.3.2) and create a star-planet pair which is attributed a randomly oriented inclination vector resulting in a transiting or non-transiting orbit (the geometric probability for a transiting orbit depends on stellar radius and semi-major axis of the orbit). In the case of a transiting orbit, the light curve is simulated based on stellar and planetary parameters and the observational dates we specified (see §4.3.5). The shape of the transit is calculated according to the formulae of Mandel & Agol (2002) and includes the effects of ingress/egress and limb-darkening. We add uncorrelated Gaussian (white) and correlated non-Gaussian (red) noise to our light curves. Details about our noise model are given in §4.3.3 and §4.3.4. After the simulation of the light curves, we apply our detection algorithm and our detection cuts as described in §4.3.6, and count how many planets we detect.

One simulation run is finished after each star has been picked once. In this way one run represents one possible outcome of the Pan-Planets survey. Since in the majority of cases the star has no planet or the inclination is such that no transits are visible, there are in general only a few transiting light curves per run. For each planet population and each set of survey parameters we simulate 25 000 runs. For the selected survey strategy we increase the precision to 100 000 runs. The numbers we list in our results are averages over these runs. The scatter of the individual outcomes allows us to derive errors for our estimates.

4.3.1 Input stellar distribution

We make use of a Besançon model[1] (Robin *et al.*, 2003) for the spectral type and brightness distributions of stars in our target fields. A model of 1 sq.deg centered around RA = $19^h47^m41\overset{s}{.}7$, DEC = $+17^d01^m52^s$ (l = 54.5, b = -4.2) is scaled to the actual survey area assuming a constant density. The parameters taken from the model are stellar mass M_{star}, effective temperature T_{eff}, surface gravity $\log g$, metallicity $[Fe/H]$ and apparent MegaCam[2] i'-band AB-magnitude $m_{i'}$. The model also provides colors which we use to determine the apparent Johnson V-band magnitude m_V, according to the following formula derived by Smith *et al.* (2002) :

$$V = g' - 0.55 \cdot (g' - r') - 0.03 \tag{4.1}$$

The stellar radii R_{star} are calculated using $\log g$ and M_{star} according to $R_{star} = \text{sqrt}(G \times M_{star} / g)$. Furthermore, T_{eff}, $\log g$, and $[Fe/H]$ are used to determine quadratic limb-darkening coefficients according to Claret (2004) which are based on synthetic ATLAS spectra (Claret, 2000).

In total we find 3 440 F-, G-, K- and M-dwarfs[3] per sq.deg. that are not saturated (i.e. $m_{i'} \geq 13$ mag) and are brighter than our radial velocity follow-up limit (i.e. $m_V \leq 16.5$ mag). Fig. 4.1 shows the input stellar distribution.

For VHN we extend the target magnitude range to $m_{i'} \leq 18$ mag. We find 34 000 M-dwarfs in this range.

---

[1] http://bison.obs-besancon.fr/modele/
[2] http://www.cfht.hawaii.edu/Instruments/Imaging/Megacam/
[3] we refer to dwarfs as stars of luminosity class IV-VI
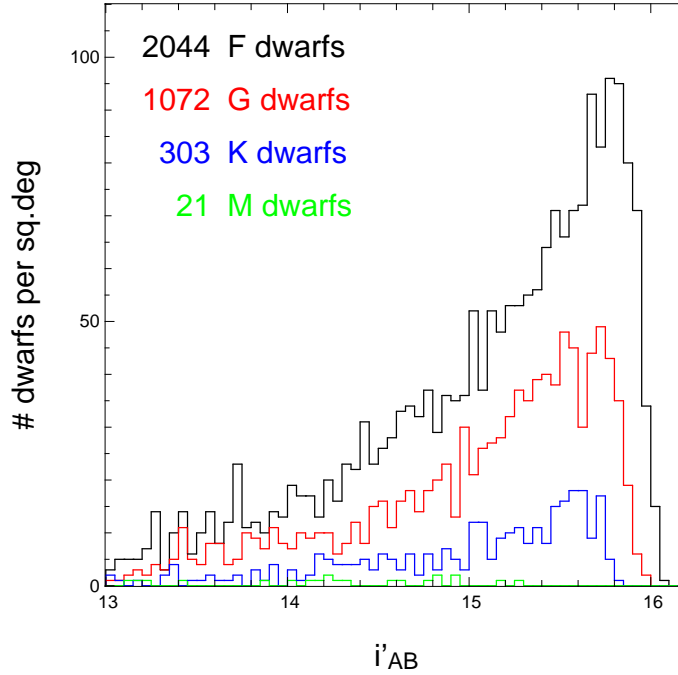
Figure 4.1: Total number and magnitude histogram of F-, G-, K- and M-dwarfs (top to bottom) with $m_{i'} \geq 13$ mag and $m_V \leq 16.5$ mag in our target population. Note that the cut on the visual magnitude results in an brighter cut in i' for the later type stars due to their redder color.

4.3.2   Input planet distributions

We test five different planetary populations:

   i) Very Hot Jupiters (VHJ), with radii of 1.0-1.25 R_J and periods between 1 and 3 days

  ii) Hot Jupiters (HJ), with radii of 1.0-1.25 R_J and periods between 3 and 5 days

 iii) Warm Jupiters (WJ), with radii of 1.0-1.25 R_J and periods between 5 and 10 days

 iv) Very Hot Saturns (VHS), with radii of 0.6-0.8 R_J and periods between 1 and 3 days

  v) Very Hot Neptunes (VHN), with radii of 0.3 R_J and periods between 1 and 3 days

Within the given ranges the radii and periods are homogeneously distributed.
Our predicted yields depend on the frequency of stars that have a planet for each of the five population. These frequencies are not known to a very good precision and not many estimates have been published so far. Gould *et al.* (2006a) performed a detailed study of the OGLE-III survey and derived frequencies of Very Hot Jupiters and Hot Jupiters by comparing the number of detected planets in the OGLE-III survey to the number of stars the survey was sensitive to. They found at 90% confidence level $0.1408 \cdot (1^{+1.10}_{-0.54})$% of all late type dwarfs to have a VHJ and $0.3125 \cdot (1^{+1.37}_{-0.59})$% to have a HJ. Fressin *et al.* (2007) published comparable results analyzing the same survey.

For VHJ and HJ we use the frequencies published by Gould *et al.* (2006a). The frequency of WJ we speculate to be the same as for HJ which is consistent with the OGLE-III results (see §4.5). Further we assume the frequencies for VHS and VHN to be 0.714% (same as for VHJ) and 5% respectively.

4.3.3   White noise model

For the white noise in our light curves we add four different Gaussian components: stellar photon noise, sky background, readout and scintillation noise. The photon noise of each star is estimated using a preliminary exposure time calculator which has been calibrated by observations taken during a pre-commissioning phase of the PanSTARRS1 telescope. We assume the sky background to be 20.15 mag per square arcsecond which corresponds to a seven day distance to full moon. The readout noise is assumed to be 8 e^- per pixel. The scintillation noise is estimated to be 0.5 mmag according to the formula of Young (1967, 1993) and is only of importance at the very bright end of our target distribution. Fig. 4.2 shows the white noise as function of magnitude as well as the individual contributions.

For our calculations we assume a seeing of 1.2 arcsec, airmass of 1.4, extinction coefficient of 0.08 and PSF fitting radius of 1.0 arcsec. At the faint end (i' = 18 mag) the number of photons is of the order of 15,500 for the object and 7,800 for the sky and therefore well outside the Poisson statistics regime.
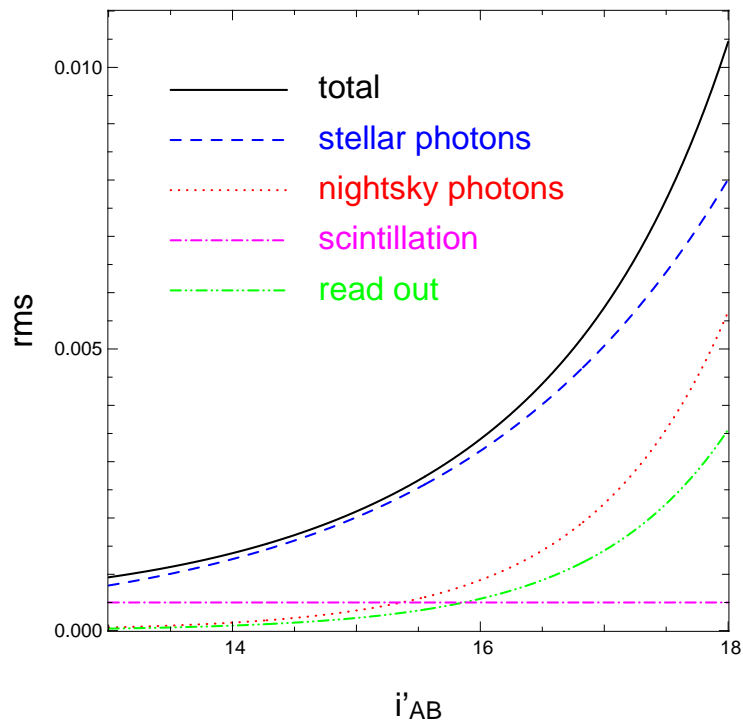
Figure 4.2: Total white noise and contributions of the four components.

4.3.4   Residual red noise model

As detailed analyses of light curve datasets have shown, all transit surveys suffer from non-Gaussian correlated noise sources, also known as red noise. E.g. Pont *et al.* (2006) analyzed the OGLE-III light curves and calculated binned averages of subsets containing n data points. They found the standard deviation σ of these averages can be parameterized to a good approximation by the following formula:

$$\sigma = \sqrt{\frac{\sigma_{white}^2}{n} + \sigma_{red}^2} \qquad (4.2)$$

with σ_{white} being the single point rms of the white noise component and σ_{red}^2 being a constant red noise contribution. With this equation one can model how the red noise decreases the signal-to-noise ratio (S/N) of a transit light curve.

Application of algorithms to remove systematic effects, such as *Sysrem* (Tamuz *et al.*, 2005) or *TFA* (Kovács *et al.*, 2005) have been successfully applied by several groups resulting in a significant reduction of the level of red noise (e.g. Snellen *et al.*, 2007). However, a small fraction of the correlated noise always remained.

In our simulations we want to account for this residual red noise (RRN). A simple model would be to increase the level of Gaussian noise by a certain amount and therefore assume that the correlated nature is of minor importance. For studies based only on S/N calculations one could also use a parameterization like equation 4.2. Since we are simulating light curves, we want to introduce a different approach. We model the RRN by adding superimposed sine waves of different wavelengths and amplitudes. This allows us to include the effects the correlated noise has on the efficiency of the detection algorithm, which could get confused by noise that is correlated on timescales of a typical transit duration.

We add RRN according to the following model:

$$\Delta_{flux}(t) = \sum_i A_i \cdot sin(\frac{\pi}{\tau_i}t + p_{0,i}) \qquad (4.3)$$

with normalized amplitude A_i, timescale τ_i and random phase shift $p_{0,i}$ of each component i. The phase shift is calculated for each observing block independently and therefore changing with time for a single light curve. This is done in order to avoid introducing strong periodic signals that are coherent over a timescale longer than a day.

For each model we start with relative amplitudes A_i' which are normalized in such a way that the rms of the added RRN (rms_{red}) is of value 1 mmag, 2 mmag, 3 mmag or 4 mmag:

$$rms_{red} = \sqrt{\frac{\sum_i A_i^2}{2}} \quad . \qquad (4.4)$$

In order to analyze the influence of the timescales and amplitudes on our results we construct a total of 9 different red noise models with each of them having 3 or 4 components. Table 4.1 gives an overview of the parameters of our red noise models. We refer to models 1 to 3 as 'fixed parameter' models because for these we select arbitrary fixed values for A_i' and τ_i which we use for all light curve. For models 4 to 9 we draw the relative amplitudes and timescales randomly in a given range and for each light curve individually. Fig. 4.3 shows $\Delta_{flux}(t)$ for the fixed parameter models.

model	A'_1	A'_2	A'_3	A'_4	τ_1[min]	τ_2[min]	τ_3[min]	τ_4[min]
1	1	2	3	4	355	169	111	48
2	2	3	4	1	169	131	111	88
3	3	4	1	2	131	99	61	27
4	1-4	1-4	1-4	1-4	300-400	200-300	100-200	0-100
5	1-4	1-4	1-4	1-4	250-300	200-250	150-200	100-150
6	1-4	1-4	1-4	1-4	250-300	200-250	150-200	—
7	1-4	1-4	1-4	1-4	250-300	200-250	—	100-150
8	1-4	1-4	1-4	1-4	250-300	—	150-200	100-150
9	1-4	1-4	1-4	1-4	—	200-250	150-200	100-150

Table 4.1: Dimensionless relative amplitudes A'_i and timescales τ_i of our different red noise models. Models 1 to 3 are fixed parameter models whereas for the others we draw random values within a given range for each single light curve individually. The timescales are chosen to cover the range of expected transit durations.
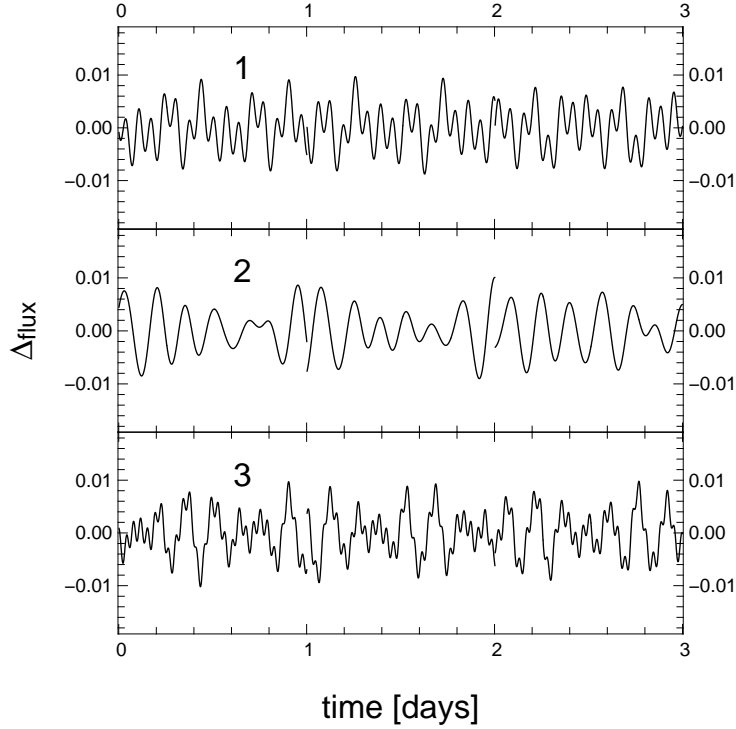
Figure 4.3: $\Delta_{flux}(t)$ for the fixed parameter models 1 to 3. Because the random phase shift is calculated for each day individually there are discontinuities visible at integer day positions (local noon). In our simulation we calculate the phase shift for each observing block in order to ensure continuity within an observing block.

4.3.5 Epochs of the observations

For each year the Pan-Planets survey has been granted a total of 120h hours which will be executed in 1h or 3h blocks. Assuming a 33% loss due to bad weather we expect the data to be taken in 81 or 27 nights per year depending on our survey strategy. The actual epochs of the observations we use to construct our light curves are computed in the following way. For each night in which our target field is visible for at least 3h we calculate the range of visibility, namely the time the field is higher than airmass 2 on the sky. This results in a 183 day period starting on April 26th and ending on October 24th. We randomly pick nights during the period of visibility and place the observing block arbitrarily within the time span our target is higher than airmass 2, as calculated earlier.

In our simulations we test 5 different scenarios with alternate observations of 3 to 7 fields during the observing block. The time for one exposure and readout is assumed to be 40s. Therefore the different number of fields transform into cycle rates between 120s and 280s. Using the selected nights, the random position of a block within a night and the cycle rate we construct a table of observational dates which we use as input to the light curve simulations. For each simulation run (which represents one possible outcome of the survey) we draw new observational dates. Table 4.2 summarizes the observational parameter depending on the survey strategy.

# of fields	block size	cycle rate	# of data points per night	# of data points per year
3	1h	120s	30	2430
4	1h	160s	23	1863
5	1h	200s	18	1458
6	1h	240s	15	1215
7	1h	280s	13	1053
3	3h	120s	90	2430
4	3h	160s	68	1863
5	3h	200s	54	1458
6	3h	240s	45	1215
7	3h	280s	39	1053

Table 4.2: Cycle rate and number of data points per night and year depending on observational strategy.

4.3.6   Light curve analysis

Each simulated light curve is analyzed by our detection algorithm which is a box-fitting least squares (BLS) algorithm proposed by Kovács *et al.* (2002). The program folds the light curves with trial periods in the range from 0.9 to 9.1 days and finds the best χ^2 fitting box corresponding to a fractional transit length[4] τ between 0.01 and 0.1. For each detection the BLS-algorithm provides period, S/N and the number of individual transits. For a successful detection we require the period found to match the simulated period within 0.2% (see Fig. 4.4). In addition, we impose the S/N to be larger than 16 (see §4.3.7) and the number of transits to be at least equal to 3. The planet is also considered being detected if the measured period is half or twice the simulated period (to within 0.2%). This can easily happen in case of unevenly sampled light curves. For later analysis we store all input parameters of the simulation and output parameters of the detection algorithm in a table.

4.3.7   Signal-to-noise cut

To model a transit survey, it is very important to have a transparent and reproducible procedure of applying cuts in the process of selecting the candidates. The most important value is the minimum S/N. The S/N of a transit light curve is defined as the transit depth divided by the standard deviation of the photometric average of all measurements taken during a transit. For a light curve with N uniformly spaced data points with individual Gaussian error σ, transit depth δ and a fractional transit length τ this is:

$$S/N = \frac{\delta}{\sigma/\sqrt{N\tau}} \quad .$$
(4.5)

---

[4] the fractional transit length is defined as the transit duration divided by the period
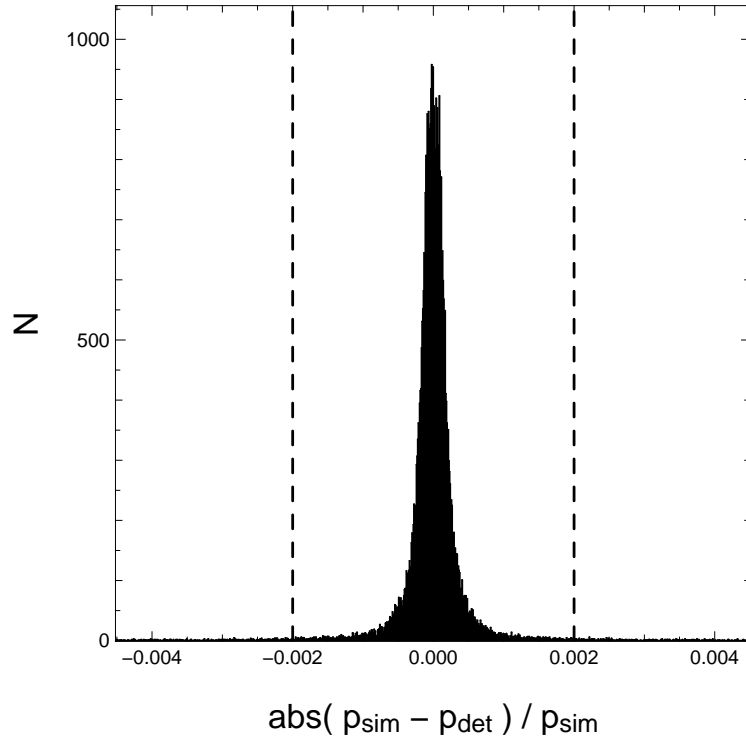
Figure 4.4: Deviation of the detected period p_{det} from the simulated period p_{sim} of a number of arbitrary selected observation runs. For a successful detection we require the detected period to deviate less than 0.2% (dashed line).

In the presence of red noise the value of the S/N is reduced. Also the actual shape of the transit, which is determined by limb-darkening and ingress/egress, has an impact on the S/N. This effect is included implicitly in our simulation.

Since the probability of finding a planet is small, the majority of transit surveys use a low S/N cut of about 10. This results in a high number of statistical and physical false positives[5] and has made it necessary to include non-reproducible selection procedures such as "by-eye" rejection. Pushing the S/N cut to the detection limit makes it therefore difficult to model the detection efficiency.

In the Pan-Planets survey we expect to find a very high number of candidates already in the first year which will require a high amount of radial velocity follow-up resources. The best candidates have the highest S/N and will be followed-up first. We will most likely not be able to follow-up all candidates down to the detection threshold of ~ 12 and therefore use a somewhat larger S/N cut. In this work we calculate the expected number of detections using a S/N cut of 16.

---

[5] statistical false positives are purely noise generated detections whereas physical false positives are true low amplitude variations (like e.g. in a blended binary system)

4.4 Results

In this section we summarize the results of a total of 7.6 million simulation runs. The computation time was 230 000 CPU hours which we distributed over a 486 CPU beowulf cluster.

In §4.4.1 we show which block size (1h or 3h) is more efficient for the Pan-Planets survey. In §4.4.2 we compare the different RRN models. Section §4.4.3 addresses the question of the optimal number of fields (3 to 7). In §4.4.4 we summarize the actual number of VHJ, HJ, WJ, VHS we expect to find using our preferred survey strategy. Finally, we show the results in the case of observing the same fields during the second year of the survey instead of monitoring new ones (§4.4.5). In §4.4.6 we study the potential to find Very Hot Neptunes transiting M-dwarfs.

Error estimates are only given for the final numbers in §4.4.4 and §4.4.5. All numbers we present are scaled from the 1 sq.deg. Besançon model to the actual survey area of $N_{fields} \times 7$ sq.deg assuming a constant spectral type and magnitude distribution and a homogeneous density.

In order to check whether there are 7 fields of comparable density, we count the total number of stars in the USNO-A2.0 catalog and compare it to the total number of stars in the Besançon model for a set of different Galactic longitudes (Table 4.3). We assumed an average color (m_{USNO_R}-$m_{i'}$) of 0.25 mag. In the range $43.5 \leq l \leq 61.5$ the number of stars in the Besançon model agrees well with the number of stars. The USNO density varies at a level of 30% with the average being ~14 000, close to the density we assume in our simulations (l = 54.5). With a diameter of 3 deg. a total of 7 Pan-Starrs fields fit in this range.

4.4.1 Influence of the size of the observing blocks

We investigate the influence of the observing block size on the number of detections in the Pan-Planets survey. Table 4.4 lists the average number of VHJ and HJ found with 1h and 3h blocks after the application of our detection cuts, as described in §4.3.7.

The first three columns list the planet population and the survey strategy (i.e. number of fields and observing block size). The fourth column shows the average numbers of all simulated transiting planet light curves having a S/N of 16 or more (without requiring 3 transits and without running the detection algorithm). Here the numbers are very similar comparing the 1h to the 3h block strategies.

To understand this, one has to consider that a planet spends a certain fraction of its orbit in transit phase (also known as fractional transit length τ). This fraction depends mainly on the inclination and period of the orbit as well as the radius of the host star. For a given τ the average number of points in transit ($N \cdot \tau$) only depends on the total number of observations N and is therefore independent of the block size. The same applies to the S/N which, for fixed transit depth and photometric noise properties, depends only on the number of points in transit to a good approximation. Therefore, if only a minimum S/N is required, the number of detections is comparable for a strategy with 1h blocks and with 3h blocks, with minor differences arising from limb-darkening and ingress/egress effects.

Although the number of points in transit is the same for both strategies, one 3h block covers on average a bigger part of the transit compared to a 1h block. As a consequence the average number of individual transits must be lower in the case of 3h blocks. If we impose the additional cut of requiring at least 3 transits to be visible in the light curve (column 5), the expected number of planets found is lower for the 3h blocks compared to the 1h blocks. With a 3h block strategy the number of light

l	b	# USNO-A2.0	# Besançon model
deg	deg	$13.25 \leq m_{USNO\_R} \leq 16.25$	$13 \leq m_{i'} \leq 16$
40.5	-4.2	7748	15103
41.5	-4.2	8439	14623
42.5	-4.2	10670	14352
43.5	-4.2	14814	14248
44.5	-4.2	14248	14208
45.5	-4.2	10906	13754
46.5	-4.2	14910	13645
47.5	-4.2	17018	13194
48.5	-4.2	17065	13175
49.5	-4.2	14482	12959
50.5	-4.2	14295	12370
51.5	-4.2	14424	12459
52.5	-4.2	16737	12260
53.5	-4.2	15890	11997
54.5	-4.2	14131	11770
55.5	-4.2	14555	11705
56.5	-4.2	15682	11456
57.5	-4.2	14562	11370
58.5	-4.2	13195	11058
59.5	-4.2	11301	10877
60.5	-4.2	11194	10436
61.5	-4.2	9188	10489
62.5	-4.2	6181	10139
63.5	-4.2	4968	9903

Table 4.3: Total number of stars per sq.deg. according to the USNO-A2.0 catalog and the Besançon model.

curves passing the S/N cut and having 3 or more transits is on average 53% lower for HJ and 26% lower for VHJ. For the longer period HJ this effect is stronger due to the fact that the number of visible transits is lower in general.

In order the planet to be considered detected (as described in §4.3), we not only require S/N $\geq$ 16 and at least 3 visible transits, but also that the BLS-algorithm finds the correct period (allowing for twice and half the correct value). The impact of this additional selection cut is shown in columns 6-10 for light curves with 0 mmag, 1 mmag, 2 mmag, 3 mmag and 4 mmag RRN[6]. Without RRN, most planets are found by the BLS-algorithm. The loss is marginally higher in the case of 3h blocks which is a consequence of the generally lower number of transits, since the BLS-algorithm is more efficient if more transits are present. Comparing the results for 1h and 3h blocks we find that in case the RRN level is 2 mmag, the number of detected planets without RRN is on average 59% lower for HJ and 30% lower for VHJ in the 3h block case.

---

[6] we restrict ourself here to RRN of model 4 - our favored model (see §4.4.2)

population	fields	block	S/N $\geq$ 16	$\geq$ 3 transits	0mmag	1mmag	2mmag	3mmag	4mmag
VHJ	3	1h	13.13	11.39	10.95	10.18	7.73	5.33	3.61
VHJ	4	1h	16.09	13.91	13.37	12.54	9.82	7.00	4.82
VHJ	5	1h	18.53	16.12	15.52	15.06	12.06	8.66	6.10
VHJ	6	1h	20.67	18.00	17.34	16.75	14.00	10.17	7.38
VHJ	7	1h	22.44	19.57	18.87	18.44	15.76	11.72	8.44
VHJ	3	3h	12.50	8.16	7.50	6.45	4.04	2.57	1.61
VHJ	4	3h	15.04	9.95	9.16	8.32	5.32	3.39	2.15
VHJ	5	3h	17.69	11.88	10.95	9.66	6.48	4.23	2.75
VHJ	6	3h	20.09	13.61	12.54	11.01	7.84	5.23	3.21
VHJ	7	3h	21.43	14.64	13.47	12.51	9.03	6.09	3.84
HJ	3	1h	15.93	10.83	9.75	8.65	5.52	3.36	2.06
HJ	4	1h	18.31	12.11	10.87	10.07	6.97	4.37	2.74
HJ	5	1h	20.54	13.69	12.22	11.40	8.43	5.30	3.37
HJ	6	1h	22.45	14.82	13.22	12.32	9.41	6.15	4.07
HJ	7	1h	23.60	15.54	13.78	13.16	10.28	6.86	4.45
HJ	3	3h	14.06	4.98	3.91	2.91	1.49	0.85	0.53
HJ	4	3h	16.30	5.78	4.49	3.54	1.88	1.04	0.66
HJ	5	3h	18.22	6.45	4.97	4.09	2.31	1.34	0.84
HJ	6	3h	20.06	7.04	5.38	4.49	2.74	1.56	0.98
HJ	7	3h	21.59	7.60	5.73	5.07	3.20	1.89	1.15

Table 4.4: Influence of the block size shown on the basis of the number of planets detected in a 1 yr campaign after applying different detection cuts.

Including RRN, fewer planets are detected by the BLS-algorithm and the discrepancy between 1h and 3h blocks increases. For a typical RRN level of 2 mmag we find on average 71% less HJ and 45% less VHJ with 3h blocks compared to 1h blocks.

As an additional test we perform the same analysis for a campaign with twice the amount of observing time spread over 2 years. This would correspond to a strategy where we stay on the same target fields in the second year of the Pan-Planets survey. Also in this case, 1h blocks are more efficient than 3h blocks. Assuming the RRN level is 2 mmag, we find that the number of detected planets is on average 34% lower for HJ and 59% lower for VHJ in the 3h block case. The details of the simulations for a 2 yr campaign can be found in §4.4.5. In the following we restrict our results to 1h blocks.

4.4.2   Influence of the residual red noise model

In this section we compare the results of nine different RRN models which have been introduced in §4.3.4. In addition, we compare the red noise models to a scenario where we add additional uncorrelated white noise by the same amount as the RRN level. Table 4.5 shows the number of HJ and VHJ found with a 1h block strategy and 2 mmag RRN for each of the 9 different red noise models, as well as for the increased white noise model.

In general the increased white noise model results in a significantly higher number of detections compared to the RRN models (on average 22% and 39% higher for VHJ and HJ respectively). This shows that the effect of the RRN on the efficiency of the BLS-algorithm is strong and needs to be taken into account in our simulations.

Comparing the individual RRN models to each other we find that for the fixed parameter models (1 to 3) the number of detections is 8% and 13% higher for VHJ and HJ respectively than for the random models (4 to 9). The individual results of the random models are all very similar and vary only by a few percent. In the following we restrict our results to the red noise model 4, since it is the most general of all models with 4 components and random timescales ranging from 0 to 400 minutes.

4.4.3   Influence of the number of fields

In order to optimize the survey with respect to the number of alternating fields monitored during an observing block, we compare the number of detections for each of the 5 strategies (3 to 7 fields). We do not test more than 7 fields, because it is not sure if we can find a higher number of fields with comparable density (see §4.4). Note also, that with more than 7 fields, the number of data points per light curve would be less than 1 000 and the cycle rate longer than 5 minutes which would complicate the process of eliminating false positives on the basis of the light curve shape[7]. We limit our simulations to the above selected 1h blocks (see §4.4.1) and 2 mmag RRN of model 4 (see §4.4.2). In general, the total number of detections depends on the number of fields in two counteracting ways: on the one hand, observing more fields results in more target stars and therefore more transiting planet systems that can be detected; on the other hand, observing more fields results in a lower number of data points per light curve and thus the S/N of each transit candidate is shifted to a lower value. The latter effect is stronger for faint stars because the S/N is generally lower whereas for brighter stars the S/N is high enough in most cases.

The number of detections in the first year of the Pan-Planets survey for different number of fields is shown in Table 4.6. For all planet populations (i.e. VHJ, HJ, WJ and VHS) we find more planets with a higher number of fields. The loss in S/N is over-compensated by the higher number of target stars. In Fig. 4.5 we show the S/N distributions of VHJ detections for a 3 field and a 7 field strategy. The S/N distribution of VHJ peaks at a higher level than our cut of 16, even for the 7 field strategy, which explains why observing more fields results in more detections.

---

[7] it is important to well sample the ingress/egress part of the transits which has a duration of approximately 15-20 minutes

population	# of fields	model 1	model 2	model 3	model 4	model 5	model 6	model 7	model 8	model 9	white
VHJ	3	9.10	8.26	8.72	7.73	7.90	7.80	7.84	7.85	7.75	10.91
VHJ	4	11.30	10.31	11.17	9.82	9.81	9.88	9.92	9.97	9.83	13.30
VHJ	5	13.53	12.66	13.34	12.06	11.95	12.29	12.43	12.23	12.08	15.08
VHJ	6	15.81	14.66	15.01	14.00	14.16	14.12	14.01	13.89	14.23	17.11
VHJ	7	17.24	16.13	16.97	15.76	15.77	15.95	15.85	15.74	15.81	18.44
HJ	3	7.04	6.01	6.74	5.52	5.63	5.69	5.61	5.54	5.60	9.39
HJ	4	8.51	7.37	7.99	6.97	6.80	6.91	6.89	6.91	7.00	10.51
HJ	5	9.84	8.83	9.75	8.43	8.32	8.29	8.33	8.32	8.45	12.10
HJ	6	11.13	10.08	10.53	9.41	9.42	9.41	9.37	9.51	9.41	13.15
HJ	7	11.77	10.78	11.37	10.28	10.39	10.39	10.42	10.31	10.31	13.64

Table 4.5: Influence of the red noise model for 1h blocks and a RRN level of 2 mmag.

# fields	VHJ	HJ	WJ	VHS
3	7.73	5.52	1.60	2.26
4	9.82	6.97	1.95	2.63
5	12.06	8.43	2.44	3.05
6	14.00	9.41	2.61	3.40
7	15.76	10.28	2.78	3.51

Table 4.6: Number of planets found in the first year depending on the number of target fields, assuming 1h blocks and 2 mmag RRN (model 4).
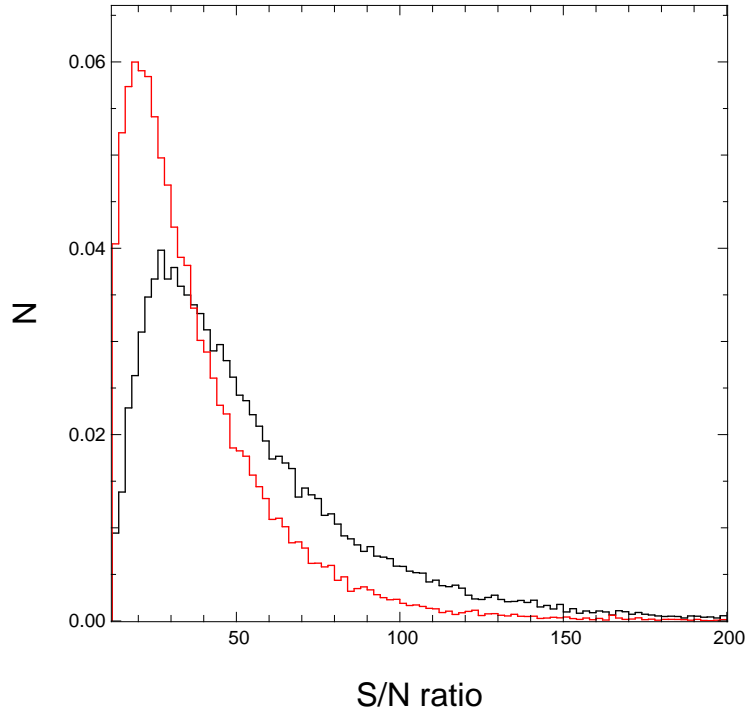
Figure 4.5: Normalized S/N distribution of VHJ detections for a 3 field strategy (black) and a 7 field strategy (red) assuming 1h blocks and 2 mmag RRN (model 4).

In the case of a 2 yr campaign the situation is the same. For all four planet populations it is more efficient to observe a higher number of fields (see Table 4.7). Therefore we conclude that observing 7 fields is the most efficient strategy and restrict our results in the following to 7 fields.

4.4.4   The expected number of detections in the Pan-Planets survey

In the previous sections we have identified our preferred survey strategy with 1h blocks and alternating among 7 fields. In addition we selected RRN model 4 as our preferred one. For these parameters we performed more detailed simulations in order to calculate the expected number of detections of the Pan-Planets project (including error estimates) and to study the parameter distributions of the detected

# fields	VHJ	HJ	WJ	VHS
3	11.16	11.90	4.85	3.95
4	14.72	15.21	6.18	5.07
5	17.96	18.34	7.46	5.94
6	21.25	21.22	8.66	6.68
7	24.13	23.55	9.48	7.49

Table 4.7: Number of planets found after 2 years depending on the number of target fields, assuming 1h blocks and 2 mmag RRN (model 4).

planets in detail. For each of 4 different RRN levels (1 mmag, 2 mmag, 3 mmag and 4 mmag) and 4 planet populations (VHJ, HJ, WJ and VHS) we performed 25 000 simulation runs. The number of detections depending on the level of RRN are shown in Table 4.8. Fig. 4.6 shows the cumulative distribution of the host star brightness for each planet populations for 2 mmag of RRN (model 4).

Our predicted numbers are affected by two sources of uncertainties. The first and dominant one is the uncertainty of the planet frequency taken from Gould *et al.* (2006a) which is caused by the low number statistics of the OGLE detections. This uncertainty is not included in Table 4.8 and must be taken into account by scaling all of our HJ results by a factor of $1^{+1.37}_{-0.59}$ and all of our VHJ results by a factor of $1^{+1.10}_{-0.54}$, as published in Gould *et al.* (2006a).

The second uncertainty is a direct result of our simulations. Each simulation run represents one possible outcome of 1 sq.deg. of the Pan-Planets survey. Since the simulated observational epochs change from one run to the other and since in each run different stars are attributed to planets with different orbital parameters, an intrinsic scatter in the number of planets in found in each run. The combination of 49 randomly chosen runs represents one possible outcome of the full 49 sq.deg. survey (7 fields). From the histogram of these combinations we derive 68% confidence intervals for our predicted numbers.

4.4.5 Number of expected detections in a two year campaign

The Pan-Planets project has a lifetime of 3.5 years. In the previous sections we focus mainly on the first year of the survey. In this section we show the results of our simulations for a 2 year campaign. In particular, we address the question whether the project is more efficient if we stay on the same fields or if we choose new targets assuming that we find fields with similar densities (see §4.6).

Table 4.9 shows the number of planets detected in a 2 yr campaign for four different levels of RRN. Except for VHJ, we more than double the number of detections for each planet population. For the longer period WJ the gain is a factor of 3. In a 1 yr campaign most of these planets show less than 3 transits and are not detected. Adding the observations of the second year, the number of transits increases and many of the previously undetected planets are found.
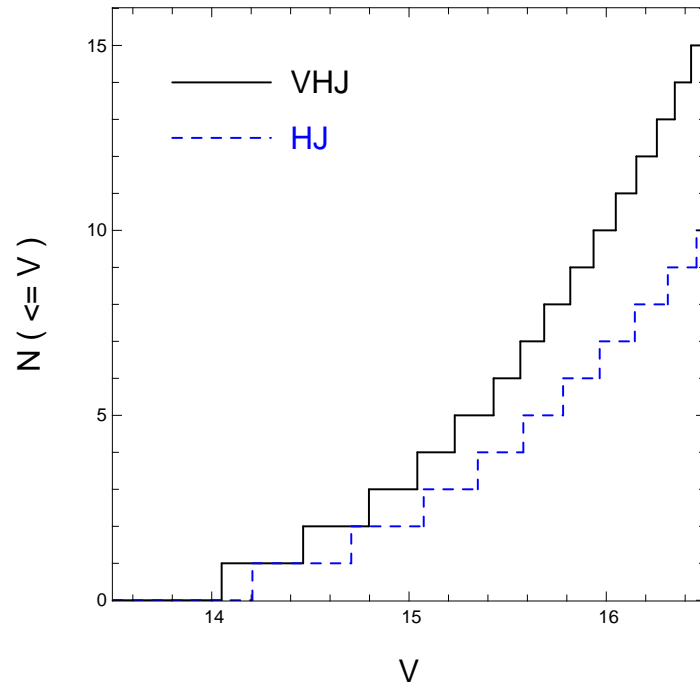
Figure 4.6: Cumulative host star brightness distributions for each planet population for a 1 yr campaign with 2 mmag RRN (model 4).
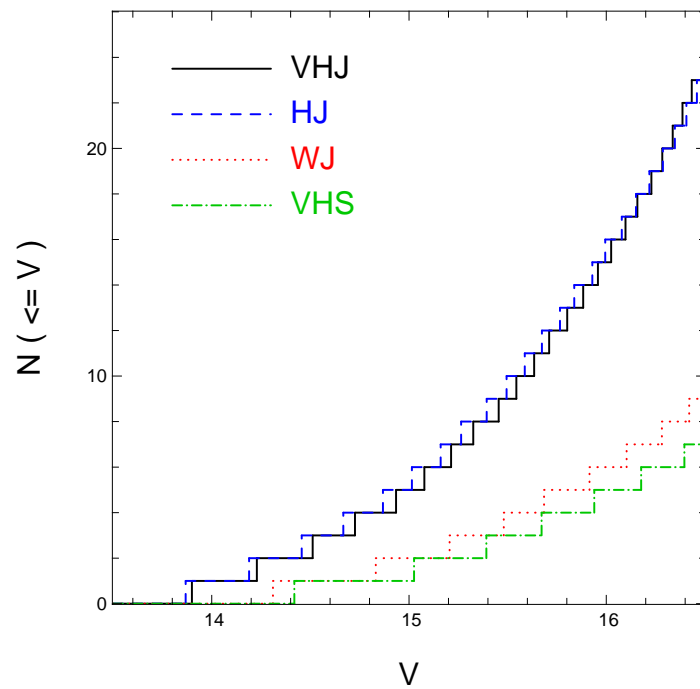
Figure 4.7: Cumulative host star brightness distributions for each planet population for a 2 yr campaign with 2 mmag RRN (model 4).

RRN level	VHJ	HJ	WJ	VHS
1 mmag	18.4 ± 4.3	13.2 ± 3.7	3.8 ± 2.0	5.2 ± 2.3
2 mmag	15.8 ± 4.0	10.3 ± 3.2	2.8 ± 1.7	3.5 ± 1.9
3 mmag	11.7 ± 3.5	6.9 ± 2.7	$1.8^{+1.4}_{-1.3}$	1.9 ± 1.4
4 mmag	8.4 ± 2.9	4.5 ± 2.1	$1.1^{+1.1}_{-0.9}$	$0.9^{+1.0}_{-0.7}$

Table 4.8: Number of planets found in the first year for our selected survey strategy as a function of residual red noise level (model 4).

In addition, staying on the same fields in the second year increases the S/N of all transit light curves, due to the higher number of data points taken during a transit. Planets that have an insufficiently high S/N after the first year are detected after the second year. This is particularly true for VHS.

Fig. 4.8 shows the fraction of all transiting Jupiter-sized planets (VHJ, HJ, WJ) that are detected in the first year of the survey (lower black line) and in the 2 yr campaign (upper red line). In the first year, the average efficiencies are 26.3%, 10.6% and 4.3% for VHJ, HJ and WJ respectively. Planets that have been missed do not have the required S/N, show less than 3 transits in the light curve, or the BLS-algorithm found a wrong period. Extending the survey to the second year increases the efficiency significantly to 39.8%, 24.0% and 14.3% for VHJ, HJ and WJ respectively.
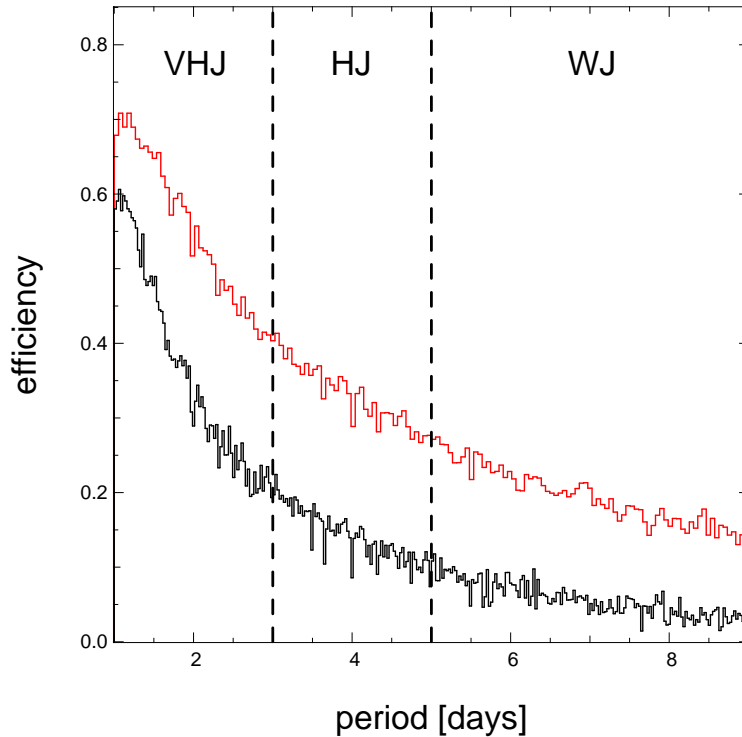
Figure 4.8: Fraction of all transiting VHJ, HJ and WJ that are detected as a function of period for a 1 yr campaign (lower black line) and a 2 yr campaign (upper red line).

RRN level	VHJ	HJ	WJ	VHS
1 mmag	28.1 ± 5.3	29.3 ± 5.4	12.4 ± 3.5	10.6 ± 3.3
2 mmag	24.1 ± 4.9	23.6 ± 4.9	9.5 ± 3.1	7.5 ± 2.7
3 mmag	19.0 ± 4.4	16.5 ± 4.1	6.1 ± 2.5	4.0 ± 2.1
4 mmag	14.4 ± 3.8	10.9 ± 3.3	4.0 ± 2.0	2.1 ± 1.5

Table 4.9: Number of planets found with 160h of observations in 2 years for our selected survey strategy as a function of residual red noise level (model 4).

RRN level	1 yr	2 yr
1 mmag	5.7 ± 2.4	16.6 ± 4.1
2 mmag	3.5 ± 1.9	9.7 ± 3.1
3 mmag	2.4 ± 1.6	6.3 ± 2.5
4 mmag	1.7 ± 1.4	4.6 ± 2.2

Table 4.10: Number of VHN detections after the first and second year of the Pan-Planets survey for our selected survey strategy for different residual red noise levels (model 4).

4.4.6 The detection of Very Hot Neptunes

In this section we study the potential to find Very Hot Neptunes transiting M-dwarfs. The radius ratio between planet and star is much higher for low mass stars which results in much deeper transits and therefore a higher detection probability. According to the Besançon model there are a total of 34 000 M-dwarfs brighter than AB-magnitude $m_{i'} = 18$ mag in 7 fields of 7 sq.deg. each. These objects are particularly interesting, since the composition of planets in this mass range is rather unknown (gaseous, icy or rocky). Also the habitable zone is much closer to the star due to its lower surface temperature. Note, that only one planet transiting an M-dwarf has been detected so far.

We consider all transiting VHN candidates down to host star brightnesses of $m_{i'} = 18$ mag to be interesting objects, although the spectroscopical follow-up will be very challenging. New high resolution near infrared spectrographs will help to confirm these very red objects.

To study the potential of Pan-Planets to find transiting VHN we perform simulations for the whole input stellar distribution and analyze the spectral type distribution of the hosts stars of all successful detections (Fig. 4.9). The Pan-Planets survey is sensitive to close-in Neptune-sized planets around late K- and early M-dwarfs if the frequency of these stars hosting Neptunes is as large as 5%. The number of VHN detections after the first and the second year is listed in Table 4.10 for 4 different residual red noise levels. Assuming 2 mmag of RRN we expect to find 3 VHN after the first and 9 VHN after the second year.

Further we analyze the distance distributions of all detected VHJ, VHS and VHN systems (Fig. 4.10). The volume probed strongly depends on the radius of the planet. For lower mass radius the transit depth is generally smaller and therefore the photometric precision needed to detect the transits must be higher, which is only the case for closer and thus brighter systems. Note that for HJ and WJ the distance distributions are very similar to the VHJ distribution.
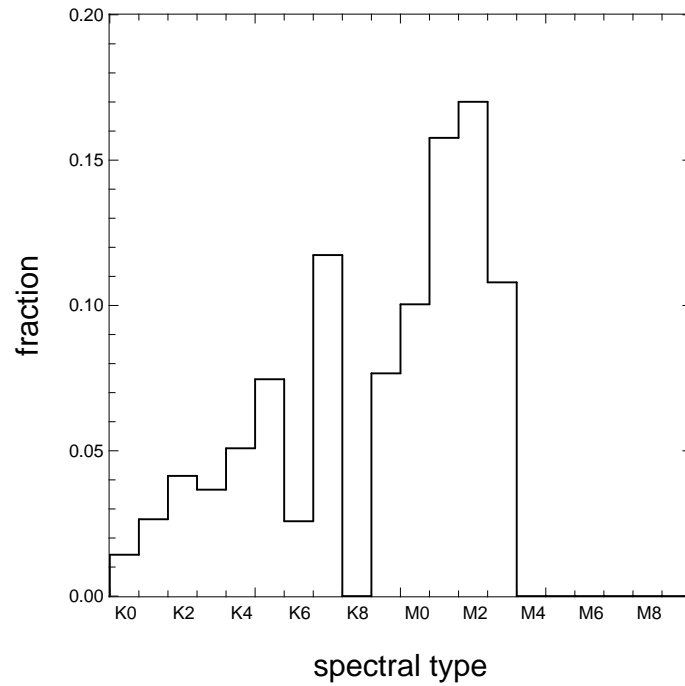
Figure 4.9: Host star spectral type distribution of all detected VHN for a 2 yr campaign with 2 mmag RRN (model 4). Pan-Planets is sensitive to VHN transiting late K- and early M-dwarfs.
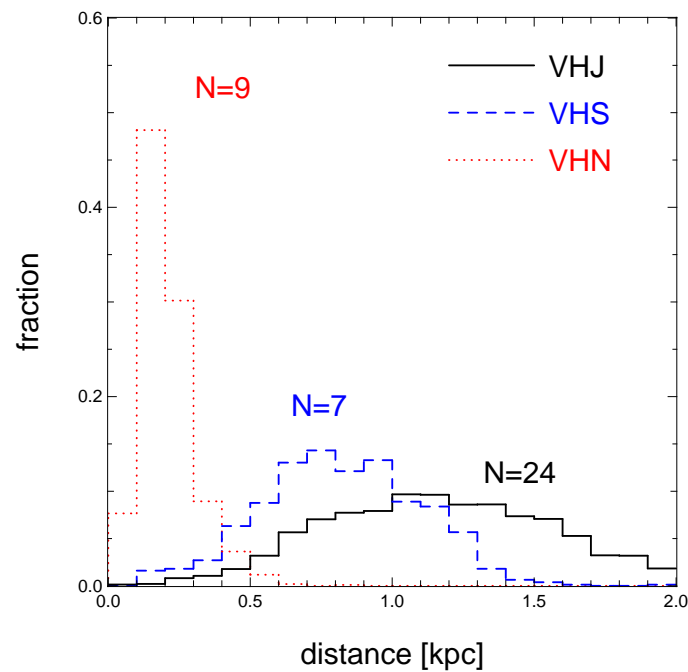
Figure 4.10: Distance distribution of the detected VHJ, VHS and VHN for a 2 yr campaign with 2 mmag RRN (model 4). Due to the lower transit depth smaller planets can only be detected around closer stars.

4.5   Consistency Check

Gould *et al.* (2006a) have modeled the OGLE-III survey in order to derive absolute frequencies of HJ and VHJ. In our simulations we are using these frequencies to predict the number of detections for the Pan-Planets survey. In order to verify our results we performed a consistency check by modeling the OGLE-III survey and comparing the results to the actual number of planets found. We limit this test to the 3 Carina fields where 3 planets have been found (1 HJ, 2 VHJ). The 2 bulge fields that have also been observed during the OGLE-III campaign are more difficult to model due to a stronger blending and a higher uncertainty in the input stellar distribution.

We obtained the Besançon model population of the 3 Carina fields (CAR100, CAR104, CAR105) for stars in the magnitude range of $13.7 \leq I_{mag} \leq 17.0$. The overall noise level as a function of magnitude has been determined by Gould *et al.* (2006a) to be:

$$\sigma = -0.723 + 0.1544 \cdot I_{mag} - 0.01094 \cdot I_{mag}^2 + 0.000259 \cdot I_{mag}^3 \quad . \tag{4.6}$$

In their simulations Gould *et al.* (2006a) did not include correlated noise sources, instead they account for systematics by using an increased S/N cut. In order to be as consistent as possible we follow the same procedure and do not split the over-all noise in red and white noise components (as we did in the Pan-Planets simulations). We use the radius and period distributions for HJ and VHJ introduced in §4.3.2. The epochs of the observations were taken from the light curve of OGLE-TR-74[8] with 1,200 epochs taken from February to May 2002.

After simulating the light curves in the same way as described in §4.3 we run the BLS-algorithm and check for a correct period recovery. In addition we apply the following cuts which have been used by the OGLE group and are summarized in detail in Section 3 and Table 1 in Gould *et al.* (2006a): the transit depth δ must be smaller than 0.04 mag ($\sim$3.62%); the S/N greater than 11.6; the signal detection efficiency[9] larger than 3.8; the number of transits is required to be at least 3; and finaly, the color $(V - I)_0$ must be greater than 0.4. Note that we have not imposed any cut on the transit depth in our simulations for the Pan-Planets survey since a Jupiter-sized planet transiting an M-dwarf can have a fairly high transit depth. Further we do not use a color since in our simulations we include only late type dwarfs a priori.

In total we simulated 50 000 runs for each of the five planet populations. On average we find 2.18 VHJ and 1.46 HJ which is in reasonable good agreement with the actual number of 2 VHJ and 1 HJ found by the OGLE group.

According to our simulations the OGLE-III carina survey was not sensitive to one of the other 3 planet populations we tested. We find on average 0.45 WJ, 0.12 VHS and zero VHN which is agreement with none being found by OGLE.

---

[8] one of the OGLE-III candidates
[9] quality parameter provided by the BLS-algorithm for each detection

4.6 Conclusion

The aim of this work was to study the influence of the survey strategy on the efficiency of the Pan-Planets project and to predict the number of detections for an optimized strategy.
Our calculations are based on the simulation of realistic light curves including the effects of limb-darkening, ingress/egress and observational window functions. In addition we have introduced a model to simulate correlated (red) noise which allows us to include the effects of correlated noise on the efficiency of the BLS-algorithm. Our approach can be applied to any transit survey as well.

Below we summarize the caveats and assumptions that were made in our simulations:

- Our results depend on the spectral type and magnitude distribution of the Besançon model. The model does not include second order substructure such as spiral arms.

- We neglect the effects of blending. Due to crowding into the direction of the Galactic disk some stars are blended by neighboring sources.

- We assume all planets that are detected by the BLS-algorithm to be followed-up and confirmed spectroscopically. In particular, we assume that no true candidate is rejected by any candidate selection process. The detailed follow-up strategy of the Pan-Planets survey will be presented in Afonso et al. (in prep.).

- Our simulations are done for 1 sq.deg. and the results are scaled to the actual survey area. We assume that all fields (3, 4, 5, 6 or 7 case) have homogeneous densities and non-varying (or similar) stellar populations. Simple number counts on the USNO-catalog showed that we can find up to 7 fields with similar total number of stars (see §4.4). For a larger number of fields, the assumption of a constant density might be too optimistic since we are restricted to fields that are close to each other in order to keep the observational overhead low.

- Our results directly scale with the assumed planet frequencies. The values of 0.14% and 0.31% we use for VHJ and HJ have uncertainties of a factor of 2. For WJ, VHS and VHN we have used hypothetical values of 0.31%, 0.14% and 5% respectively. After completion of the Pan-Planets survey we will be able to derive more accurate absolute frequencies for all five planet populations.

- The quality of the data is assumed to be homogeneously good over the whole detector area. Bad pixel regions and gaps between the individual CCDs are not taken into account and result in an effective field of view that is smaller than 7 sq.deg.

Comparing different observing strategies we found that observing more fields is more efficient. Concerning the observation time per night, we compared 1h blocks to 3h blocks and found the shorter ones to be more efficient. This is still the case for a 2 yr campaign.

For a RRN level of 2 mmag we expect to find up to 15 VHJ and 10 HJ in the first year around stars brighter than V = 16.5 mag. The survey will also be sensitive to planets with longer periods (WJ) and smaller radii (VHS and VHN). Assuming that the frequencies of stars with WJ and VHS is 0.31% and 0.14% respectively, we expect to find up to 2 WJ and 3 VHS in the same magnitude range.

We found that observing the same fields in the second year of the 3.5 yr lifetime of the survey is more efficient than choosing new fields. We expect to find up to 24 VHJ, 23 HJ, 9 WJ and 7 VHS. In particular for longer periods (HJ and WJ) and smaller radii (VHS) we will more than double the number of detections of the first year if we continue to observe the same targets.

We have investigated the potential of the Pan-Planets survey to detect VHN transiting M-dwarfs brighter than i' = 18 mag. Assuming the frequency of these objects is 5%, we expect to find up to 3 detections in the first year and up to 9 detections observing the same fields in the second year.

As a consistency check we modeled the OGLE-III Carina survey and found 2.18 VHJ, 1.46 HJ, 0.45 WJ, 0.12 VHS and zero VHN which is in agreement with the 2 VHJ and 1 HJ and the zero WJ, VHS and VHN that have been actually detected.

Chapter 5

Summary and Outlook

The search for extra-solar planets has become more and more important in the last years. The number of known planets is aready 331 (as of 20.3.2009) and new detections are published almost on a weekly basis. Not least a strong public interest motivates more and more astronomers to initiate new surveys and to participate in the search.

Direct imaging of extra-solar planets is extremely difficult, since in most cases the star out-shines the planet by orders of magnitudes. In addition, the very small apparent distance between planet and star due to the large interstellar distances complicates direct imaging. Therefore, a number of indirect techniques are used to detect extra-solar planets among which the transit method has a privileged position. The transit method aims to detect periodic luminosity changes that are caused by a companion passing in front of the star. Finding such a transiting planet has the advantage that its radius and therefore its density can be inferred by measuring the luminosity decrease of the star. In addition, transiting planets allow a detailed analysis of the composition of their atmospheres. Transiting planets are therefore very promising targets to look for signs of life. The work in hand considers several aspects of the search for extra-solar planets with the transit method.

In the first chapter, the most successful methods that led to the detection of extra-solar planets are introduced. In addition we summarize the formalisms that are important for the following chapters.

The second chapter presents the pre-OmegaTranS project, a photometric survey conducted with the 2.2m telescope in LaSilla/Chile. The goal of this project is the detection of transiting planets. A total of 16 000 stars have been analyzed in order to find the characteristic luminosity variations that are caused by a transiting planetary companion. We found four candidates among which one is very promising (POTS-C1b). The candidate is a Jupiter-sized object that is transiting a low-mass star. We found strong evidence for a planetary nature of the companion. Preparations for the confirmation of the candidate with photometric and spectroscopic follow-up observations have been initiated.

Chapter 3 demonstrates such a process of confirmation of a transit candidate in the case of OGLE2-TR-L9b. Using high resolution spectroscopic follow-up observations we were able to derive the mass of the candidate to be 4.5 Jupiter-masses. Additional photometric follow-up confirms without doubt the planetary nature of the candidate. With a radius of 1.6 Jupiter-radii, OGLE2-TR-L9b is

larger than expected for a planet of about 4.5 times the mass of Jupiter. Other planets (e.g. CoRoT-2b, TrES-4b and XO-3b) were also found to be too large. Several mechanisms have been proposed to explain these 'bloated' radii, such as more significant core heating and/or orbital tidal heating. Compared to the other 56 transiting planets that were found, OGLE2-TR-L9b is the planet with the hottest and most rapidly rotating host star.

This year, a new transit survey, Pan-Planets, will start observations using the PanSTARRS telescope at Haleakala Observatory in Hawaii. The telescope is equipped with the largest CCD camera that has been built so far. Each exposure maps seven sq.deg. of the sky in 1.4 billion pixels. The survey is led by the Max-Planck-Institute for Astronomy in Heidelberg (C. Afonso and Th. Henning). The focus of the first observing campaign of this project is the unbiased exploration of the mass-radius relationship of Jupiter-sized planets.
The University Observatory of the LMU is actively participating in the Pan-Planets project. In the course of this work, detailed Monte-Carlo simulations have been carried out in order to optimize the survey strategy of Pan-Planets and to estimate the number of detections that can be expected (chapter 4). We found that observing a high number of fields results in more detections. Furthermore, short observing blocks of 1h are favored over 3h observing blocks. According to our simulations, Pan-Planets will be able to find up to 25 planets of the size of Jupiter already in the first year. The project is therefore one of the most promising transit searches in the near future. We will contribute to the photometric identification of transit candidates as well as to their spectroscopic confirmation.

Another future project is OmegaTranS, which will start observations in early 2010. The main focus of this survey will be the search for low-mass planets around M-dwarfs and Hot Jupiters in open stellar clusters. The data reduction pipeline of OmegaTranS has been developed and optimized in the course of the pre-OmegaTranS project (chapter 2). This will enable us to achieve quick results.

Last but not least, we are a member of the RoPACS project[1], which is a near infrared search for rocky planets around cool stars. The observations have already been started and first candidates are being examined.

The knowledge and experience gained in this work is very useful for all of our future projects. Not only the software but also the skills that have been developed are of great value and enable us to increasingly take part in one of the most fascinating fields of astronomy.

---

[1] http://www.star.herts.ac.uk/ dpi/RoPACS/

Appendix A

Astrophysical Constants and Acronyms

AU	$1.50 \; 10^{11}$ m
pc	$3.09 \; 10^{16}$ m
$M_\odot$	$1.99 \; 10^{30}$ kg
M_{Jup}	$1.90 \; 10^{27}$ kg
M_{Earth}	$5.97 \; 10^{24}$ kg
$R_\odot$	$6.96 \; 10^{8}$ m
R_{Jup}	$7.14 \; 10^{7}$ m
R_{Earth}	$6.37 \; 10^{6}$ m
$L_\odot$	$3.84 \; 10^{26}$ W

Table A.1: Astrophysical constants used throughout this work.

ADU	Analog Digital Unit
Astro-WISE	Astronomical Wide-field Imaging System for Europe
BLS	Box-fitting Least Squares
CCD	Charge Coupled Device
CHZ	Continuous Habitable Zone
ESO	European Southern Observatory
FWHM	Full Width Half Maximum
GHZ	Galactic Habitable Zone
GROND	Gamma Ray burst Optical/Near-infrared Detector
HJ	Hot Jupiter
HZ	Habitable Zone
HRD	Hertzsprung-Russell Diagram
HST	Hubble Space Telescope
OmegaTranS	OmegaCam Transit Survey
OTSF	OmegaTranS Survey Field
PanSTARRS	Panoramic Survey Telescope and Rapid Response System
Pan-Planets	PanSTARRS Planet Survey
POTS	Pre-Omegacam Transit Survey
PSF	Point Spread Function
RoPACS	Rocky Planets Around Cool Stars
RMS	Root Mean Squares
RRN	Residual Red Noise
SDE	Signal Detection Efficiency
SDSS	Sloan Digital Sky Survey
S/N	Signal to Noise ratio
USNO	US Naval Observatory
VHJ	Very Hot Jupiter
VHN	Very Hot Neptune
VHS	Very Hot Saturn
WFI	Wide Field Imager
WJ	Warm Jupiter

Table A.2: Acronyms used throughout this work.

Bibliography

Aarseth, S. J., Lin, D. N. C., & Palmer, P. L. 1993: *Evolution of Planetesimals. II. Numerical Simulations*, ApJ, 403, 351

Abe, F., Bennett, D. P., Bond, I. A., Eguchi, S., Furuta, Y., Hearnshaw, J. B., Kamiya, K., Kilmartin, P. M., Kurata, Y., Masuda, K., Matsubara, Y., et al. 2004: *Search for Low-Mass Exoplanets by Gravitational Microlensing at High Magnification*, Science, 305, 1264

Adelman-McCarthy, J. K., Agüeros, M. A., Allam, S. S., Anderson, K. S. J., Anderson, S. F., Annis, J., Bahcall, N. A., Bailer-Jones, C. A. L., Baldry, I. K., Barentine, J. C., Beers, T. C., et al. 2007: *The Fifth Data Release of the Sloan Digital Sky Survey*, ApJS, 172, 634

Agol, E., Steffen, J., Sari, R., & Clarkson, W. 2005: *On detecting terrestrial planets with timing of giant planet transits*, MNRAS, 359, 567

Aigrain, S., Barge, P., Deleuil, M., Fressin, F., Moutou, C., Queloz, D., Auvergne, M., & Baglin, A. 2008: *The CoRoT Exoplanet Programme: Exploring the Gas-Giant/Terrestrial Planet Transition*, in Astronomical Society of the Pacific Conference Series, Vol. 384, 14th Cambridge Workshop on Cool Stars, Stellar Systems, and the Sun, ed. S. P. P. S. D. E. M. B. J. Messina, 270–+

Alard, C. 2000: *Image subtraction using a space-varying kernel*, A&AS, 144, 363

Alard, C. & Lupton, R. H. 1998: *A Method for Optimal Image Subtraction*, ApJ, 503, 325

Artymowicz, P. 2004: *Dynamics of Gaseous Disks with Planets*, in Astronomical Society of the Pacific Conference Series, Vol. 324, Debris Disks and the Formation of Planets, ed. L. Caroff, L. J. Moon, D. Backman, & E. Praton, 39–+

Baade, D., Meisenheimer, K., Iwert, O., Alonso, J., Augusteijn, T., Beletic, J., Bellemann, H., Benesch, W., Böhm, A., Böhnhardt, H., Brewer, J., et al. 1999: *The Wide Field Imager at the 2.2-m MPG/ESO telescope: first views with a 67-million-facette eye.*, The Messenger, 95, 15

Baglin, A., Auvergne, M., Barge, P., Michel, E., Catala, C., Deleuil, M., & Weiss, W. 2007: *The CoRoT mission and its scientific objectives*, in American Institute of Physics Conference Series, Vol. 895, Fifty Years of Romanian Astrophysics, ed. C. Dumitrache, N. A. Popescu, M. D. Suran, & V. Mioc, 201–209

Bakos, G., Noyes, R. W., Kovács, G., Stanek, K. Z., Sasselov, D. D., & Domsa, I. 2004: *Wide-Field Millimagnitude Photometry with the HAT: A Tool for Extrasolar Planet Detection*, PASP, 116, 266

Barbieri, M. 2007: *Fields Selection for Transiting Planets Surveys and Application to the ΩTranS Survey*, in Astronomical Society of the Pacific Conference Series, Vol. 366, Transiting Extrapolar Planets Workshop, ed. C. Afonso, D. Weldrake, & T. Henning, 78–+

Barranco, J. A. & Marcus, P. S. 2000: *Vortices in Protoplanetary Disks and the Formation of Planetesimals*, in Studying Turbulence Using Numerical Simulation Databases, 8. Proceedings of the 2000 Summer Program, p. 97, 97–+

Beaulieu, J.-P., Bennett, D. P., Fouqué, P., Williams, A., Dominik, M., Jørgensen, U. G., Kubas, D., Cassan, A., Coutures, C., Greenhill, J., Hill, K., et al. 2006: *Discovery of a cool planet of 5.5 Earth masses through gravitational microlensing*, Nat, 439, 437

Beichman, C., Lawson, P., Lay, O., Ahmed, A., Unwin, S., & Johnston, K. 2006: *Status of the terrestrial planet finder interferometer (TPF-I)*, in Society of Photo-Optical Instrumentation Engineers (SPIE) Conference Series, Vol. 6268, Society of Photo-Optical Instrumentation Engineers (SPIE) Conference Series

Benedict, G. F., McArthur, B. E., Forveille, T., Delfosse, X., Nelan, E., Butler, R. P., Spiesman, W., Marcy, G., Goldman, B., Perrier, C., Jefferys, W. H., et al. 2002: *A Mass for the Extrasolar Planet Gliese 876b Determined from Hubble Space Telescope Fine Guidance Sensor 3 Astrometry and High-Precision Radial Velocities*, ApJ, 581, L115

Bennett, D. P., Bond, I., Cheng, E., Friedman, S., Garnavich, P., Gaudi, B. S., Gilliland, R., Gould, A., Greenhouse, M. A., Griest, K., Kimble, R. A., et al. 2004: *The Microlensing Planet Finder: completing the census of extrasolar planets in the Milky Way*, in Society of Photo-Optical Instrumentation Engineers (SPIE) Conference Series, Vol. 5487, Society of Photo-Optical Instrumentation Engineers (SPIE) Conference Series, ed. J. C. Mather, 1453–1464

Bennett, D. P., Bond, I. A., Udalski, A., Sumi, T., Abe, F., Fukui, A., Furusawa, K., Hearnshaw, J. B., Holderness, S., Itow, Y., Kamiya, K., et al. 2008: *A Low-Mass Planet with a Possible Sub-Stellar-Mass Host in Microlensing Event MOA-2007-BLG-192*, ApJ, 684, 663

Bertin, E. & Arnouts, S. 1996: *SExtractor: Software for source extraction.*, A&AS, 117, 393

Biller, B. A., Kasper, M., Close, L. M., Brandner, W., & Kellner, S. 2006: *Discovery of a Brown Dwarf Very Close to the Sun: A Methane-rich Brown Dwarf Companion to the Low-Mass Star SCR 1845-6357*, ApJ, 641, L141

Binney, J. & Merrifield, M. 1998, Galactic astronomy (Galactic astronomy / James Binney and Michael Merrifield. Princeton, NJ : Princeton University Press, 1998. (Princeton series in astrophysics) QB857 .B522 1998 ($35.00))

Bodenheimer, P. 2004: *Planet Formation in Disks*, in Astronomical Society of the Pacific Conference Series, Vol. 323, Star Formation in the Interstellar Medium: In Honor of David Hollenbach, ed. D. Johnstone, F. C. Adams, D. N. C. Lin, D. A. Neufeeld, & E. C. Ostriker, 329–+

Boley, A. C. 2009: *The Two Modes of Gas Giant Planet Formation*, ApJ, 695, L53

Bond, I. A., Udalski, A., Jaroszyński, M., Rattenbury, N. J., Paczyński, B., Soszyński, I., Wyrzykowski, L., Szymański, M. K., Kubiak, M., Szewczyk, O., Żebruń, K., et al. 2004: *OGLE 2003-BLG-235/MOA 2003-BLG-53: A Planetary Microlensing Event*, ApJ, 606, L155

Boss, A. P. 1997: *Giant planet formation by gravitational instability.*, Science, 276, 1836

Boss, A. P. 2002: *Evolution of the Solar Nebula. V. Disk Instabilities with Varied Thermodynamics*, ApJ, 576, 462

Bouchy, F., Pont, F., Melo, C., Santos, N. C., Mayor, M., Queloz, D., & Udry, S. 2005: *Doppler follow-up of OGLE transiting companions in the Galactic bulge*, A&A, 431, 1105

Bouchy, F., Queloz, D., Deleuil, M., Loeillet, B., Hatzes, A. P., Aigrain, S., Alonso, R., Auvergne, M., Baglin, A., Barge, P., Benz, W., et al. 2008: *Transiting exoplanets from the CoRoT space mission. III. The spectroscopic transit of CoRoT-Exo-2b with SOPHIE and HARPS*, A&A, 482, L25

Brown, T. M., Charbonneau, D., Gilliland, R. L., Noyes, R. W., & Burrows, A. 2001: *Hubble Space Telescope Time-Series Photometry of the Transiting Planet of HD 209458*, ApJ, 552, 699

Burrows, A., Hubeny, I., Budaj, J., & Hubbard, W. B. 2007: *Possible Solutions to the Radius Anomalies of Transiting Giant Planets*, ApJ, 661, 502

Cameron, A. C., Bouchy, F., Hébrard, G., Maxted, P., Pollacco, D., Pont, F., Skillen, I., Smalley, B., Street, R. A., West, R. G., Wilson, D. M., et al. 2007: *WASP-1b and WASP-2b: two new transiting exoplanets detected with SuperWASP and SOPHIE*, MNRAS, 375, 951

Campbell, B. & Walker, G. A. H. 1979: *Precision radial velocities with an absorption cell*, PASP, 91, 540

Capaccioli, M., Mancini, D., & Sedmak, G. 2002: *VST: a dedicated wide-field imaging facility at Paranal*, in Society of Photo-Optical Instrumentation Engineers (SPIE) Conference Series, Vol. 4836, Society of Photo-Optical Instrumentation Engineers (SPIE) Conference Series, ed. J. A. Tyson & S. Wolff, 43–52

Chabrier, G., Baraffe, I., Allard, F., & Hauschildt, P. 2000: *Deuterium Burning in Substellar Objects*, ApJ, 542, L119

Charbonneau, D., Allen, L. E., Megeath, S. T., Torres, G., Alonso, R., Brown, T. M., Gilliland, R. L., Latham, D. W., Mandushev, G., O'Donovan, F. T., & Sozzetti, A. 2005: *Detection of Thermal Emission from an Extrasolar Planet*, ApJ, 626, 523

Charbonneau, D., Brown, T. M., Latham, D. W., & Mayor, M. 2000: *Detection of Planetary Transits Across a Sun-like Star*, ApJ, 529, L45

Charbonneau, D., Brown, T. M., Noyes, R. W., & Gilliland, R. L. 2002: *Detection of an Extrasolar Planet Atmosphere*, ApJ, 568, 377

Chauvin, G., Lagrange, A.-M., Dumas, C., Zuckerman, B., Mouillet, D., Song, I., Beuzit, J.-L., & Lowrance, P. 2004: *A giant planet candidate near a young brown dwarf. Direct VLT/NACO observations using IR wavefront sensing*, A&A, 425, L29

Chauvin, G., Lagrange, A.-M., Zuckerman, B., Dumas, C., Mouillet, D., Song, I., Beuzit, J.-L., Lowrance, P., & Bessell, M. S. 2005: *A companion to AB Pic at the planet/brown dwarf boundary*, A&A, 438, L29

Chyba, C. F. & Hand, K. P. 2005: *ASTROBIOLOGY: The Study of the Living Universe*, ARA&A, 43, 31

Chyba, C. F. & McDonald, G. D. 1995: *The Origin of Life in the Solar System: Current Issues*, Annual Review of Earth and Planetary Sciences, 23, 215

Claret, A. 2000: *A new non-linear limb-darkening law for LTE stellar atmosphere models. Calculations for -5.0 <= log[M/H] <= +1, 2000 K <= T_{eff} <= 50000 K at several surface gravities*, A&A, 363, 1081

Claret, A. 2004: *A new non-linear limb-darkening law for LTE stellar atmosphere models III. Sloan filters: Calculations for -5.0 <= log [M/H] <= +1, 2000 K <= T_{eff} <= 50 000 K at several surface gravities*, A&A, 428, 1001

Clarke, D. 2002: *String/Rope length methods using the Lafler-Kinman statistic*, A&A, 386, 763

Cocconi, G. & Morrison, P. 1959: *Searching For Interstellar Communications*, Nat, 184, 844

Cochran, W. D., Redfield, S., Endl, M., & Cochran, A. L. 2008: *The Spin-Orbit Alignment of the HD 17156 Transiting Eccentric Planetary System*, ApJ, 683, L59

Cockell, C. S., Herbst, T., Léger, A., Absil, O., Beichman, C., Benz, W., Brack, A., Chazelas, B., Chelli, A., Cottin, H., Coudé Du Foresto, V., et al. 2009: *Darwin - an experimental astronomy mission to search for extrasolar planets*, Experimental Astronomy, 23, 435

Cumming, A., Butler, R. P., Marcy, G. W., Vogt, S. S., Wright, J. T., & Fischer, D. A. 2008: *The Keck Planet Search: Detectability and the Minimum Mass and Orbital Period Distribution of Extrasolar Planets*, PASP, 120, 531

Cumming, A., Marcy, G. W., & Butler, R. P. 1999: *The Lick Planet Search: Detectability and Mass Thresholds*, ApJ, 526, 890

de Mooij, E. J. W. & Snellen, I. A. G. 2009: *Ground-based K-band detection of thermal emission from the exoplanet TrES-3b*, A&A, 493, L35

Deeg, H. 1998: *Photometric Detection of Extrasolar Planets by the Transit-Method*, in ASP Conf. Ser. 134: Brown Dwarfs and Extrasolar Planets, 216–+

Defaÿ, C., Deleuil, M., & Barge, P. 2001: *A Bayesian method for the detection of planetary transits*, A&A, 365, 330

Dekker, H., D'Odorico, S., Kaufer, A., Delabre, B., & Kotzlowski, H. 2000: *Design, construction, and performance of UVES, the echelle spectrograph for the UT2 Kueyen Telescope at the ESO Paranal Observatory*, in Society of Photo-Optical Instrumentation Engineers (SPIE) Conference Series, Vol. 4008, Society of Photo-Optical Instrumentation Engineers (SPIE) Conference Series, ed. M. Iye & A. F. Moorwood, 534–545

Deming, D., Harrington, J., Laughlin, G., Seager, S., Navarro, S. B., Bowman, W. C., & Horning, K. 2007: *Spitzer Transit and Secondary Eclipse Photometry of GJ 436b*, ApJ, 667, L199

Deming, D., Harrington, J., Seager, S., & Richardson, L. J. 2006: *Strong Infrared Emission from the Extrasolar Planet HD 189733b*, ApJ, 644, 560

Deming, D., Seager, S., Richardson, L. J., & Harrington, J. 2005: *Infrared radiation from an extrasolar planet*, Nat, 434, 740

Demory, B.-O., Gillon, M., Barman, T., Bonfils, X., Mayor, M., Mazeh, T., Queloz, D., Udry, S., Bouchy, F., Delfosse, X., Forveille, T., et al. 2007: *Characterization of the hot Neptune GJ 436 b with Spitzer and ground-based observations*, A&A, 475, 1125

Deul, E. R., Holl, A., Guglielmo, F., Borsenberger, J., deBatz, B., Bertin, E., Copet, E., Epchtein, N., Fouque, P., Lacombe, F., LeBertre, T., et al. 1995: *Data processing for the DENIS project*, Memorie della Societa Astronomica Italiana, 66, 549

Dominik, M., Albrow, M. D., Beaulieu, J.-P., Caldwell, J. A. R., DePoy, D. L., Gaudi, B. S., Gould, A., Greenhill, J., Hill, K., Kane, S., Martin, R., et al. 2002: *The PLANET microlensing follow-up network: results and prospects for the detection of extra-solar planets*, Planetary and Space Science, 50, 299

Dong, S., Bond, I. A., Gould, A., Kozłowski, S., Miyake, N., Gaudi, B. S., Bennett, D. P., Abe, F., Gilmore, A. C., Fukui, A., Furusawa, K., et al. 2009: *Microlensing Event MOA-2007-BLG-400: Exhuming the Buried Signature of a Cool, Jovian-Mass Planet*, ApJ, 698, 1826

Drake, A. J. 2003: *On the Selection of Photometric Planetary Transits*, ApJ, 589, 1020

Duda, R. O. & Hart, P. E. 1972: *Use of the Hough Transformation To Detect Lines and Curves in Pictures*, Commun. Assoc. Comput. Mach., 15, 11

Dunham, E. W., Mandushev, G. I., Taylor, B. W., & Oetiker, B. 2004: *PSST: The Planet Search Survey Telescope*, PASP, 116, 1072

Ecuvillon, A., Israelian, G., Santos, N. C., Mayor, M., & Gilli, G. 2006: *Abundance ratios of volatile vs. refractory elements in planet-harbouring stars: hints of pollution?*, A&A, 449, 809

Ehrenfreund, P., Irvine, W., Becker, L., Blank, J., Brucato, J. R., Colangeli, L., Derenne, S., Despois, D., Dutrey, A., Fraaije, H., Lazcano, A., et al. 2002: *Astrophysical and astrochemical insights into the origin of life.*, Reports on Progress in Physics, 65, 1427

Feinberg, G. & Shapiro, R. 1980, Life beyond earth: the intelligent earthling's guide to life in the universe. (Life beyond earth: the intelligent earthling's guide to life in the universe., by Feinberg, G.; Shapiro, R.. New York, NY (USA): William Morrow, 480 p.)

Fischer, D. A., Laughlin, G., Butler, P., Marcy, G., Johnson, J., Henry, G., Valenti, J., Vogt, S., Ammons, M., Robinson, S., Spear, G., et al. 2005: *The N2K Consortium. I. A Hot Saturn Planet Orbiting HD 88133*, ApJ, 620, 481

Fischer, D. A., Marcy, G. W., Butler, R. P., Vogt, S. S., Frink, S., & Apps, K. 2001: *Planetary Companions to HD 12661, HD 92788, and HD 38529 and Variations in Keplerian Residuals of Extrasolar Planets*, ApJ, 551, 1107

Fischer, D. A. & Valenti, J. 2005: *The Planet-Metallicity Correlation*, ApJ, 622, 1102

Ford, E. B., Rasio, F. A., & Yu, K. 2003: *Dynamical Instabilities in Extrasolar Planetary Systems*, in Astronomical Society of the Pacific Conference Series, Vol. 294, Scientific Frontiers in Research on Extrasolar Planets, ed. D. Deming & S. Seager, 181–188

Fortney, J. J., Marley, M. S., & Barnes, J. W. 2007: *Planetary Radii across Five Orders of Magnitude in Mass and Stellar Insolation: Application to Transits*, ApJ, 659, 1661

Fressin, F., Guillot, T., Morello, V., & Pont, F. 2007: *Interpreting and predicting the yield of transit surveys: giant planets in the OGLE fields*, A&A, 475, 729

Gammie, C. F. 2001: *Nonlinear Outcome of Gravitational Instability in Cooling, Gaseous Disks*, ApJ, 553, 174

Gaudi, B. S., Bennett, D. P., Udalski, A., Gould, A., Christie, G. W., Maoz, D., Dong, S., McCormick, J., Szymański, M. K., Tristram, P. J., Nikolaev, S., et al. 2008: *Discovery of a Jupiter/Saturn Analog with Gravitational Microlensing*, Science, 319, 927

Goessl, C. 2007: *Finding Cepheid Variable Stars in Northern Dwarf Galaxies of the Local Group*, PhD thesis, AA(Universitäts-Sternwarte der LMU, Scheinerstrasse 1, 81679 München, Germany)

Goldreich, P. & Soter, S. 1966: *Q in the Solar System*, Icarus, 5, 375

Goldreich, P. & Tremaine, S. 1979: *The excitation of density waves at the Lindblad and corotation resonances by an external potential*, ApJ, 233, 857

Gonzalez, G. 1998: *Spectroscopic analyses of the parent stars of extrasolar planetary system candidates*, A&A, 334, 221

Gonzalez, G., Brownlee, D., & Ward, P. 2001: *The Galactic Habitable Zone: Galactic Chemical Evolution*, Icarus, 152, 185

Gould, A., Dorsher, S., Gaudi, B. S., & Udalski, A. 2006a: *Frequency of Hot Jupiters and Very Hot Jupiters from the OGLE-III Transit Surveys toward the Galactic Bulge and Carina*, Acta Astronomica, 56, 1

Gould, A., Udalski, A., An, D., Bennett, D. P., Zhou, A.-Y., Dong, S., Rattenbury, N. J., Gaudi, B. S., Yock, P. C. M., Bond, I. A., Christie, G. W., et al. 2006b: *Microlens OGLE-2005-BLG-169 Implies That Cool Neptune-like Planets Are Common*, ApJ, 644, L37

Greiner, J., Bornemann, W., Clemens, C., Deuter, M., Hasinger, G., Honsberg, M., Huber, H., Huber, S., Krauss, M., Krühler, T., Küpcü Yoldaş, A., et al. 2008: *GROND - a 7-Channel Imager*, PASP, 120, 405

Grießmeier, J.-M., Stadelmann, A., Penz, T., Lammer, H., Selsis, F., Ribas, I., Guinan, E. F., Motschmann, U., Biernat, H. K., & Weiss, W. W. 2004: *The effect of tidal locking on the magnetospheric and atmospheric evolution of "Hot Jupiters"*, A&A, 425, 753

Haisch, Jr., K. E., Lada, E. A., & Lada, C. J. 2001: *Disk Frequencies and Lifetimes in Young Clusters*, ApJ, 553, L153

Halbwachs, J. L., Arenou, F., Mayor, M., Udry, S., & Queloz, D. 2000: *Exploring the brown dwarf desert with Hipparcos*, A&A, 355, 581

Halbwachs, J. L., Mayor, M., & Udry, S. 2005: *Statistical properties of exoplanets. IV. The period-eccentricity relations of exoplanets and of binary stars*, A&A, 431, 1129

Harrington, J., Luszcz, S., Seager, S., Deming, D., & Richardson, L. J. 2007: *The hottest planet*, Nat, 447, 691

Hart, M. H. 1979: *Habitable Zones about Main Sequence Stars*, Icarus, 37, 351

Hébrard, G., Bouchy, F., Pont, F., Loeillet, B., Rabus, M., Bonfils, X., Moutou, C., Boisse, I., Delfosse, X., Desort, M., Eggenberger, A., et al. 2008: *Misaligned spin-orbit in the XO-3 planetary system?*, A&A, 488, 763

Hoffmeister, C., Richter, G., & Wenzel, W. 1984, Veraenderliche Sterne (Berlin: Springer, 1984, 2. ueberarb. Aufl.)

Holman, M. J. & Murray, N. W. 2005: *The Use of Transit Timing to Detect Terrestrial-Mass Extrasolar Planets*, Science, 307, 1288

Houghton, R. A. 2003: *The Contemporary Carbon Cycle*, Treatise on Geochemistry, 8, 473

Hubeny, I., Lanz, T., & Jeffery, C. S. 1994: *SYNSPEC: a User's Guide*, Newsl. on Analysis of Astronomical Spectra, 20

IAU. 2006: *Definition of a Planet in the Solar System*, Symposium 2006, Resolution 5B

Ida, S. & Lin, D. N. C. 2004: *Toward a Deterministic Model of Planetary Formation. II. The Formation and Retention of Gas Giant Planets around Stars with a Range of Metallicities*, ApJ, 616, 567

Jester, S., Schneider, D. P., Richards, G. T., Green, R. F., Schmidt, M., Hall, P. B., Strauss, M. A., Vanden Berk, D. E., Stoughton, C., Gunn, J. E., Brinkmann, J., et al. 2005: *The Sloan Digital Sky Survey View of the Palomar-Green Bright Quasar Survey*, AJ, 130, 873

Johnson, J. A., Winn, J. N., Narita, N., Enya, K., Williams, P. K. G., Marcy, G. W., Sato, B., Ohta, Y., Taruya, A., Suto, Y., Turner, E. L., et al. 2008: *Measurement of the Spin-Orbit Angle of Exoplanet HAT-P-1b*, ApJ, 686, 649

Jones, D. J., Diddams, S. A., Ranka, J. K., Stentz, A., Windeler, R. S., Hall, J. L., & Cundiff, S. T. 2000: *Carrier-Envelope Phase Control of Femtosecond Mode-Locked Lasers and Direct Optical Frequency Synthesis*, Science, 288, 635

Jorissen, A., Mayor, M., & Udry, S. 2001: *The distribution of exoplanet masses*, A&A, 379, 992

Joshi, Y. C., Pollacco, D., Cameron, A. C., Skillen, I., Simpson, E., Steele, I., Street, R. A., Stempels, H. C., Christian, D. J., Hebb, L., Bouchy, F., et al. 2009: *WASP-14b: 7.3 M_J transiting planet in an eccentric orbit*, MNRAS, 392, 1532

Jurić, M. & Tremaine, S. 2008: *Dynamical Origin of Extrasolar Planet Eccentricity Distribution*, ApJ, 686, 603

Kaiser, N. 2004: *Pan-STARRS: a wide-field optical survey telescope array*, in Presented at the Society of Photo-Optical Instrumentation Engineers (SPIE) Conference, Vol. 5489, Ground-based Telescopes. Edited by Oschmann, Jacobus M., Jr. Proceedings of the SPIE, Volume 5489, pp. 11-22 (2004)., ed. J. M. Oschmann, Jr., 11–22

Kalas, P., Graham, J. R., & Clampin, M. 2005: *A planetary system as the origin of structure in Fomalhaut's dust belt*, Nat, 435, 1067

Kashyap, V. L., Drake, J. J., & Saar, S. H. 2008: *Extrasolar Giant Planets and X-Ray Activity*, ApJ, 687, 1339

Kasting, J. F. 1988: *Runaway and moist greenhouse atmospheres and the evolution of earth and Venus*, Icarus, 74, 472

Kasting, J. F., Whitmire, D. P., & Reynolds, R. T. 1993: *Habitable Zones around Main Sequence Stars*, Icarus, 101, 108

Kepler, S. O., Costa, J. E. S., Castanheira, B. G., Winget, D. E., Mullally, F., Nather, R. E., Kilic, M., von Hippel, T., Mukadam, A. S., & Sullivan, D. J. 2005: *Measuring the Evolution of the Most Stable Optical Clock G 117-B15A*, ApJ, 634, 1311

Kipping, D. M. 2009: *Transit timing effects due to an exomoon*, MNRAS, 392, 181

Kjeldsen, H., Bedding, T. R., Butler, R. P., Christensen-Dalsgaard, J., Kiss, L. L., McCarthy, C., Marcy, G. W., Tinney, C. G., & Wright, J. T. 2005: *Solar-like Oscillations in α Centauri B*, ApJ, 635, 1281

Klahr, H. H. & Bodenheimer, P. 2003: *Turbulence in Accretion Disks: Vorticity Generation and Angular Momentum Transport via the Global Baroclinic Instability*, ApJ, 582, 869

Kley, W. & Crida, A. 2008: *Migration of protoplanets in radiative discs*, A&A, 487, L9

Kley, W., Peitz, J., & Bryden, G. 2004: *Evolution of planetary systems in resonance*, A&A, 414, 735

Knutson, H. A., Charbonneau, D., Allen, L. E., Fortney, J. J., Agol, E., Cowan, N. B., Showman, A. P., Cooper, C. S., & Megeath, S. T. 2007: *A map of the day-night contrast of the extrasolar planet HD 189733b*, Nat, 447, 183

Knutson, H. A., Charbonneau, D., Burrows, A., O'Donovan, F. T., & Mandushev, G. 2009: *Detection of A Temperature Inversion in the Broadband Infrared Emission Spectrum of TrES-4*, ApJ, 691, 866

Koch, D. G., Borucki, W., Dunham, E., Geary, J., Gilliland, R., Jenkins, J., Latham, D., Bachtell, E., Berry, D., Deininger, W., Duren, R., et al. 2004: *Overview and status of the Kepler Mission*, in Society of Photo-Optical Instrumentation Engineers (SPIE) Conference Series, Vol. 5487, Society of Photo-Optical Instrumentation Engineers (SPIE) Conference Series, ed. J. C. Mather, 1491–1500

Konacki, M. & Wolszczan, A. 2003: *Masses and Orbital Inclinations of Planets in the PSR B1257+12 System*, ApJ, 591, L147

Koppenhoefer, J., Afonso, C., Saglia, R. P., & Henning, T. 2009: *Investigating the potential of the Pan-Planets project using Monte Carlo simulations*, A&A, 494, 707

Korycansky, D. G. & Pollack, J. B. 1993: *Numerical calculations of the linear response of a gaseous disk to a protoplanet*, Icarus, 102, 150

Kovács, G., Bakos, G., & Noyes, R. W. 2005: *A trend filtering algorithm for wide-field variability surveys*, MNRAS, 356, 557

Kovács, G., Zucker, S., & Mazeh, T. 2002: *A box-fitting algorithm in the search for periodic transits*, A&A, 391, 369

Kuijken, K., Bender, R., Cappellaro, E., Muschielok, B., Baruffolo, A., Cascone, E., Iwert, O., Mitsch, W., Nicklas, H., Valentijn, E. A., Baade, D., et al. 2002: *OmegaCAM: the 16k×16k CCD camera for the VLT survey telescope*, The Messenger, 110, 15

Kuiper, G. P. 1951: *O the Origin of the Solar System*, in 50th Anniversary of the Yerkes Observatory and Half a Century of Progress in Astrophysics, ed. J. A. Hynek, 357–+

Lafler, J. & Kinman, T. D. 1965: *An RR Lyrae Star Survey with Ihe Lick 20-INCH Astrograph II. The Calculation of RR Lyrae Periods by Electronic Computer.*, ApJS, 11, 216

Landolt, A. U. 1992: *UBVRI photometric standard stars in the magnitude range 11.5-16.0 around the celestial equator*, AJ, 104, 340

Laughlin, G. & Adams, F. C. 1997: *Possible Stellar Metallicity Enhancements from the Accretion of Planets*, ApJ, 491, L51+

Lee, J. W., Kim, S.-L., Kim, C.-H., Koch, R. H., Lee, C.-U., Kim, H.-I., & Park, J.-H. 2009: *The sdB+M Eclipsing System HW Virginis and its Circumbinary Planets*, AJ, 137, 3181

Lenzen, R., Hartung, M., Brandner, W., Finger, G., Hubin, N. N., Lacombe, F., Lagrange, A.-M., Lehnert, M. D., Moorwood, A. F. M., & Mouillet, D. 2003: *NAOS-CONICA first on sky results in a variety of observing modes*, in Presented at the Society of Photo-Optical Instrumentation Engineers (SPIE) Conference, Vol. 4841, Society of Photo-Optical Instrumentation Engineers (SPIE) Conference Series, ed. M. Iye & A. F. M. Moorwood, 944–952

Levison, H. F., Lissauer, J. J., & Duncan, M. J. 1998: *Modeling the Diversity of Outer Planetary Systems*, AJ, 116, 1998

Lin, D. N. C. 1997: *Planetary Formation in Protostellar Disks*, in Astronomical Society of the Pacific Conference Series, Vol. 121, IAU Colloq. 163: Accretion Phenomena and Related Outflows, ed. D. T. Wickramasinghe, G. V. Bicknell, & L. Ferrario, 321–+

Lin, D. N. C., Bodenheimer, P., & Richardson, D. C. 1996: *Orbital migration of the planetary companion of 51 Pegasi to its present location*, Nat, 380, 606

Lineweaver, C. H., Fenner, Y., & Gibson, B. K. 2004: *The Galactic Habitable Zone and the Age Distribution of Complex Life in the Milky Way*, Science, 303, 59

Liu, X., Burrows, A., & Ibgui, L. 2008: *Theoretical Radii of Extrasolar Giant Planets: the Cases of TrES-4, XO-3b, and HAT-P-1b*, ApJ, 687, 1191

Loeillet, B., Shporer, A., Bouchy, F., Pont, F., Mazeh, T., Beuzit, J. L., Boisse, I., Bonfils, X., da Silva, R., Delfosse, X., Desort, M., et al. 2008: *Refined parameters and spectroscopic transit of the super-massive planet HD 147506b*, A&A, 481, 529

Lomb, N. R. 1976: *Least-squares frequency analysis of unequally spaced data*, Ap&SS, 39, 447

Lovelace, R. V. E., Li, H., Colgate, S. A., & Nelson, A. F. 1999: *Rossby Wave Instability of Keplerian Accretion Disks*, ApJ, 513, 805

Mandel, K. & Agol, E. 2002: *Analytic Light Curves for Planetary Transit Searches*, ApJ, 580, L171

Mandushev, G., Torres, G., Latham, D. W., Charbonneau, D., Alonso, R., White, R. J., Stefanik, R. P., Dunham, E. W., Brown, T. M., & O'Donovan, F. T. 2005: *The Challenge of Wide-Field Transit Surveys: The Case of GSC 01944-02289*, ApJ, 621, 1061

Marcy, G. W. & Butler, R. P. 1992: *Precision radial velocities with an iodine absorption cell*, PASP, 104, 270

Marcy, G. W., Butler, R. P., Fischer, D., Vogt, S. S., Lissauer, J. J., & Rivera, E. J. 2001: *A Pair of Resonant Planets Orbiting GJ 876*, ApJ, 556, 296

Marois, C., Macintosh, B., Barman, T., Zuckerman, B., Song, I., Patience, J., Lafrenière, D., & Doyon, R. 2008: *Direct Imaging of Multiple Planets Orbiting the Star HR 8799*, Science, 322, 1348

Masset, F. S., D'Angelo, G., & Kley, W. 2006: *On the Migration of Protogiant Solid Cores*, ApJ, 652, 730

Masset, F. S. & Papaloizou, J. C. B. 2003: *Runaway Migration and the Formation of Hot Jupiters*, ApJ, 588, 494

Matsumura, S., Takeda, G., & Rasio, F. A. 2008: *On the Origins of Eccentric Close-In Planets*, ApJ, 686, L29

Mayer, L., Quinn, T., Wadsley, J., & Stadel, J. 2002: *Formation of Giant Planets by Fragmentation of Protoplanetary Disks*, Science, 298, 1756

Mayor, M., Pepe, F., Queloz, D., Bouchy, F., Rupprecht, G., Lo Curto, G., Avila, G., Benz, W., Bertaux, J.-L., Bonfils, X., dall, T., et al. 2003: *Setting New Standards with HARPS*, The Messenger, 114, 20

Mayor, M. & Queloz, D. 1995: *A Jupiter-Mass Companion to a Solar-Type Star*, Nat, 378, 355

Mayor, M., Udry, S., Lovis, C., Pepe, F., Queloz, D., Benz, W., Bertaux, J.-L., Bouchy, F., Mordasini, C., & Segransan, D. 2009: *The HARPS search for southern extra-solar planets. XIII. A planetary system with 3 super-Earths (4.2, 6.9, and 9.2 M$_{Earth}$)*, A&A, 493, 639

Mazeh, T., Naef, D., Torres, G., Latham, D. W., Mayor, M., Beuzit, J., Brown, T. M., Buchhave, L., Burnet, M., Carney, B. W., Charbonneau, D., et al. 2000: *The Spectroscopic Orbit of the Planetary Companion Transiting HD 209458*, ApJ, 532, L55

McArthur, B. E., Endl, M., Cochran, W. D., Benedict, G. F., Fischer, D. A., Marcy, G. W., Butler, R. P., Naef, D., Mayor, M., Queloz, D., Udry, S., et al. 2004: *Detection of a Neptune-Mass Planet in the ρ Cancri System Using the Hobby-Eberly Telescope*, ApJ, 614, L81

McCullough, P. R., Stys, J. E., Valenti, J. A., Fleming, S. W., Janes, K. A., & Heasley, J. N. 2005: *The XO Project: Searching for Transiting Extrasolar Planet Candidates*, PASP, 117, 783

McLaughlin, D. B. 1924: *Some results of a spectrographic study of the Algol system.*, ApJ, 60, 22

Meeus, J. 1982, Astronomical formulae for calculators (Richmond, Va., U.S.A. : Willmann-Bell, c1982. 2nd ed., enl. and rev.), 43–+

Mejía, A. C., Durisen, R. H., & Pickett, B. K. 2003: *Gravitational Instabilities in Disks with Radiative Cooling*, in Astronomical Society of the Pacific Conference Series, Vol. 294, Scientific Frontiers in Research on Extrasolar Planets, ed. D. Deming & S. Seager, 287–290

Militzer, B., Hubbard, W. B., Vorberger, J., Tamblyn, I., & Bonev, S. A. 2008: *A Massive Core in Jupiter Predicted from First-Principles Simulations*, ApJ, 688, L45

Monet, D. G. 1998: *The 526,280,881 Objects In The USNO-A2.0 Catalog*, in Bulletin of the American Astronomical Society, Vol. 30, Bulletin of the American Astronomical Society, 1427–+

Montalto, M., Piotto, G., Desidera, S., de Marchi, F., Bruntt, H., Stetson, P. B., Arellano Ferro, A., Momany, Y., Gratton, R. G., Poretti, E., Aparicio, A., et al. 2007: *A new search for planet transits in NGC 6791*, A&A, 470, 1137

Murphy, M. T., Udem, T., Holzwarth, R., Sizmann, A., Pasquini, L., Araujo-Hauck, C., Dekker, H., D'Odorico, S., Fischer, M., Hänsch, T. W., & Manescau, A. 2007: *High-precision wavelength calibration of astronomical spectrographs with laser frequency combs*, MNRAS, 380, 839

Murray, N., Paskowitz, M., & Holman, M. 2002: *Eccentricity Evolution of Migrating Planets*, ApJ, 565, 608

Narita, N., Enya, K., Sato, B., Ohta, Y., Winn, J. N., Suto, Y., Taruya, A., Turner, E. L., Aoki, W., Yoshii, M., Yamada, T., et al. 2007: *Measurement of the Rossiter-Laughlin Effect in the Transiting Exoplanetary System TrES-1*, PASJ, 59, 763

Narita, N., Sato, B., Ohshima, O., & Winn, J. N. 2008: *A Possible Spin-Orbit Misalignment in the Transiting Eccentric Planet HD 17156b*, PASJ, 60, L1+

Nelson, R. P. 2005: *On the orbital evolution of low mass protoplanets in turbulent, magnetised disks*, A&A, 443, 1067

Nelson, R. P., Papaloizou, J. C. B., Masset, F., & Kley, W. 2000: *The migration and growth of protoplanets in protostellar discs*, MNRAS, 318, 18

Neuhäuser, R., Guenther, E. W., Wuchterl, G., Mugrauer, M., Bedalov, A., & Hauschildt, P. H. 2005: *Evidence for a co-moving sub-stellar companion of GQ Lup*, A&A, 435, L13

Noyes, R. W., Bakos, G. Á., Torres, G., Pál, A., Kovács, G., Latham, D. W., Fernández, J. M., Fischer, D. A., Butler, R. P., Marcy, G. W., Sipőcz, B., et al. 2008: *HAT-P-6b: A Hot Jupiter Transiting a Bright F Star*, ApJ, 673, L79

O'Donovan, F. T., Charbonneau, D., Bakos, G. Á., Mandushev, G., Dunham, E. W., Brown, T. M., Latham, D. W., Torres, G., Sozzetti, A., Kovács, G., Everett, M. E., et al. 2007: *TrES-3: A Nearby, Massive, Transiting Hot Jupiter in a 31 Hour Orbit*, ApJ, 663, L37

Okamoto, Y. K., Kataza, H., Honda, M., Yamashita, T., Onaka, T., Watanabe, J.-i., Miyata, T., Sako, S., Fujiyoshi, T., & Sakon, I. 2004: *An early extrasolar planetary system revealed by planetesimal belts in β Pictoris*, Nat, 431, 660

Oliver, B. M. 1973: *Project cyclops study: Conclusions and recommendations*, Icarus, 19, 425

Paardekooper, S.-J. & Mellema, G. 2006: *Halting type I planet migration in non-isothermal disks*, A&A, 459, L17

Papaloizou, J. C. B., Nelson, R. P., Kley, W., Masset, F. S., & Artymowicz, P. 2007: *Disk-Planet Interactions During Planet Formation*, in Protostars and Planets V, ed. B. Reipurth, D. Jewitt, & K. Keil, 655–668

Pasquini, L., Avila, G., Blecha, A., Cacciari, C., Cayatte, V., Colless, M., Damiani, F., de Propris, R., Dekker, H., di Marcantonio, P., Farrell, T., et al. 2002: *Installation and commissioning of FLAMES, the VLT Multifibre Facility*, The Messenger, 110, 1

Pasquini, L., Döllinger, M. P., Weiss, A., Girardi, L., Chavero, C., Hatzes, A. P., da Silva, L., & Setiawan, J. 2007: *Evolved stars suggest an external origin of the enhanced metallicity in planet-hosting stars*, A&A, 473, 979

Pepe, F. A. & Lovis, C. 2008: *From HARPS to CODEX: exploring the limits of Doppler measurements*, Physica Scripta Volume T, 130, 014007

Perryman, M. A. C. 2000: *Extra-solar planets.*, Reports of Progress in Physics, 63, 1209

Pinsonneault, M. H., DePoy, D. L., & Coffee, M. 2001: *The Mass of the Convective Zone in FGK Main-Sequence Stars and the Effect of Accreted Planetary Material on Apparent Metallicity Determinations*, ApJ, 556, L59

Pollacco, D. L., Skillen, I., Cameron, A. C., Christian, D. J., Hellier, C., Irwin, J., Lister, T. A., Street, R. A., West, R. G., Anderson, D., Clarkson, W. I., et al. 2006: *The WASP Project and the SuperWASP Cameras*, PASP, 118, 1407

Pollack, J. B., Hubickyj, O., Bodenheimer, P., Lissauer, J. J., Podolak, M., & Greenzweig, Y. 1996: *Formation of the Giant Planets by Concurrent Accretion of Solids and Gas*, Icarus, 124, 62

Pont, F., Zucker, S., & Queloz, D. 2006: *The effect of red noise on planetary transit detection*, MN-RAS, 373, 231

Queloz, D., Eggenberger, A., Mayor, M., Perrier, C., Beuzit, J. L., Naef, D., Sivan, J. P., & Udry, S. 2000: *Detection of a spectroscopic transit by the planet orbiting the star HD209458*, A&A, 359, L13

Queloz, D., Henry, G. W., Sivan, J. P., Baliunas, S. L., Beuzit, J. L., Donahue, R. A., Mayor, M., Naef, D., Perrier, C., & Udry, S. 2001: *No planet for HD 166435*, A&A, 379, 279

Raetz, S., Mugrauer, M., Schmidt, T. O. B., Roell, T., Eisenbeiss, T., Hohle, M., Seifahrt, A., Koeltzsch, A., Vaňko, M., Broeg, C., Koppenhoefer, J., et al. 2009: *Observations of the transiting planet TrES-2 with the AIU Jena telescope in Großschwabhausen*, in IAU Symposium, Vol. 253, IAU Symposium, 436–439

Rasio, F. A. & Ford, E. B. 1996: *Dynamical instabilities and the formation of extrasolar planetary systems*, Science, 274, 954

Rasool, S. I. & de Bergh, C. 1970: *The runaway greenhouse and accumulation of CO_2 in the Venus atmosphere*, Nat, 226, 1037

Reichert, J., Holzwarth, R., Udem, T., & Hänsch, T. W. 1999: *Measuring the frequency of light with mode-locked lasers*, Optics Communications, 172, 59

Robin, A. C., Reylé, C., Derrière, S., & Picaud, S. 2003: *A synthetic view on structure and evolution of the Milky Way*, A&A, 409, 523

Rossiter, R. A. 1924: *On the detection of an effect of rotation during eclipse in the velocity of the brigher component of beta Lyrae, and on the constancy of velocity of this system.*, ApJ, 60, 15

Rousset, G., Lacombe, F., Puget, P., Hubin, N. N., Gendron, E., Fusco, T., Arsenault, R., Charton, J., Feautrier, P., Gigan, P., Kern, P. Y., et al. 2003: *NAOS, the first AO system of the VLT: on-sky performance*, in Presented at the Society of Photo-Optical Instrumentation Engineers (SPIE) Conference, Vol. 4839, Society of Photo-Optical Instrumentation Engineers (SPIE) Conference Series, ed. P. L. Wizinowich & D. Bonaccini, 140–149

Ruden, S. P. 1999: *The Formation of Planets*, in NATO ASIC Proc. 540: The Origin of Stars and Planetary Systems, 643–+

Safronov, V. S. 1972, Evolution of the protoplanetary cloud and formation of the earth and planets. (Evolution of the protoplanetary cloud and formation of the earth and planets., by Safronov, V. S.. Translated from Russian. Jerusalem (Israel): Israel Program for Scientific Translations, Keter Publishing House, 212 p.)

Sale, S. E., Drew, J. E., Unruh, Y. C., Irwin, M. J., Knigge, C., Phillipps, S., Zijlstra, A. A., Gänsicke, B. T., Greimel, R., Groot, P. J., Mampaso, A., et al. 2009: *High spatial resolution Galactic 3D extinction mapping with IPHAS*, MNRAS, 392, 497

Santos, N. C., Mayor, M., Naef, D., Pepe, F., Queloz, D., Udry, S., Burnet, M., Clausen, J. V., Helt, B. E., Olsen, E. H., & Pritchard, J. D. 2002: *The CORALIE survey for southern extra-solar planets. IX. A 1.3-day period brown dwarf disguised as a planet*, A&A, 392, 215

Sartoretti, P. & Schneider, J. 1999: *On the detection of satellites of extrasolar planets with the method of transits*, A&AS, 134, 553

Saumon, D. & Guillot, T. 2004: *Shock Compression of Deuterium and the Interiors of Jupiter and Saturn*, ApJ, 609, 1170

Scargle, J. D. 1982: *Studies in astronomical time series analysis. II - Statistical aspects of spectral analysis of unevenly spaced data*, ApJ, 263, 835

Schlegel, D. J., Finkbeiner, D. P., & Davis, M. 1998: *Maps of Dust Infrared Emission for Use in Estimation of Reddening and Cosmic Microwave Background Radiation Foregrounds*, ApJ, 500, 525

Schmidt, T. O. B., Neuhäuser, R., Seifahrt, A., Vogt, N., Bedalov, A., Helling, C., Witte, S., & Hauschildt, P. H. 2008: *Direct evidence of a sub-stellar companion around CT Chamaeleontis*, A&A, 491, 311

Seidov, Z. F. 2004: *The generalized Roche model*, ArXiv Astrophysics e-prints

Siess, L., Dufour, E., & Forestini, M. 2000: *An internet server for pre-main sequence tracks of low- and intermediate-mass stars*, A&A, 358, 593

Silvotti, R., Schuh, S., Janulis, R., Solheim, J.-E., Bernabei, S., Østensen, R., Oswalt, T. D., Bruni, I., Gualandi, R., Bonanno, A., Vauclair, G., et al. 2007: *A giant planet orbiting the 'extreme horizontal branch' star V391 Pegasi*, Nat, 449, 189

Simon, A., Szatmáry, K., & Szabó, G. M. 2007: *Determination of the size, mass, and density of "exomoons" from photometric transit timing variations*, A&A, 470, 727

Sing, D. K. & López-Morales, M. 2009: *Ground-based secondary eclipse detection of the very-hot Jupiter OGLE-TR-56b*, A&A, 493, L31

Sirko, E. & Paczyński, B. 2003: *Ellipsoidal Variability in the OGLE Planetary Transit Candidates*, ApJ, 592, 1217

Skrutskie, M. F., Cutri, R. M., Stiening, R., Weinberg, M. D., Schneider, S., Carpenter, J. M., Beichman, C., Capps, R., Chester, T., Elias, J., Huchra, J., et al. 2006: *The Two Micron All Sky Survey (2MASS)*, AJ, 131, 1163

Smith, J. A., Tucker, D. L., Kent, S., Richmond, M. W., Fukugita, M., Ichikawa, T., Ichikawa, S.-i., Jorgensen, A. M., Uomoto, A., Gunn, J. E., Hamabe, M., et al. 2002: *The u'g'r'i'z' Standard-Star System*, AJ, 123, 2121

Snellen, I. A. G., Koppenhoefer, J., van der Burg, R. F. J., Dreizler, S., Greiner, J., de Hoon, M. D. J., Husser, T. O., Krühler, T., Saglia, R. P., & Vuijsje, F. N. 2009: *OGLE2-TR-L9b: an exoplanet transiting a rapidly rotating F3 star*, A&A, 497, 545

Snellen, I. A. G., van der Burg, R. F. J., de Hoon, M. D. J., & Vuijsje, F. N. 2007: *A search for transiting extrasolar planet candidates in the OGLE-II microlens database of the galactic plane*, A&A, 476, 1357

Snellgrove, M. D., Papaloizou, J. C. B., & Nelson, R. P. 2001: *On disc driven inward migration of resonantly coupled planets with application to the system around GJ876*, A&A, 374, 1092

Sozzetti, A., Torres, G., Latham, D. W., Stefanik, R. P., Korzennik, S. G., Boss, A. P., Carney, B. W., & Laird, J. B. 2009: *A Keck HIRES Doppler Search for Planets Orbiting Metal-Poor Dwarfs. II. On the Frequency of Giant Planets in the Metal-Poor Regime*, ApJ, 697, 544

Stellingwerf, R. F. 1978: *Period determination using phase dispersion minimization*, ApJ, 224, 953

Sterken, C., ed. 2005, Astronomical Society of the Pacific Conference Series, Vol. 335, The Light-Time Effect in Astrophysics: Causes and cures of the O-C diagram

Stetson, P. B. 2000: *Homogeneous Photometry for Star Clusters and Resolved Galaxies. II. Photometric Standard Stars*, PASP, 112, 925

Struve, O. 1952: *Proposal for a project of high-precision stellar radial velocity work*, The Observatory, 72, 199

Swain, M. R., Vasisht, G., & Tinetti, G. 2008: *The presence of methane in the atmosphere of an extrasolar planet*, Nat, 452, 329

Szabó, G. M., Szatmáry, K., Divéki, Z., & Simon, A. 2006: *Possibility of a photometric detection of "exomoons"*, A&A, 450, 395

Tamuz, O., Mazeh, T., & Zucker, S. 2005: *Correcting systematic effects in a large set of photometric light curves*, MNRAS, 356, 1466

Tanaka, H., Takeuchi, T., & Ward, W. R. 2002: *Three-Dimensional Interaction between a Planet and an Isothermal Gaseous Disk. I. Corotation and Lindblad Torques and Planet Migration*, ApJ, 565, 1257

Thorsett, S. E., Arzoumanian, Z., Camilo, F., & Lyne, A. G. 1999: *The Triple Pulsar System PSR B1620-26 in M4*, ApJ, 523, 763

Tinetti, G., Vidal-Madjar, A., Liang, M.-C., Beaulieu, J.-P., Yung, Y., Carey, S., Barber, R. J., Tennyson, J., Ribas, I., Allard, N., Ballester, G. E., et al. 2007: *Water vapour in the atmosphere of a transiting extrasolar planet*, Nat, 448, 169

Tingley, B. 2004: *Using color photometry to separate transiting exoplanets from false positives*, A&A, 425, 1125

Tingley, B. & Sackett, P. D. 2005: *A Photometric Diagnostic to Aid in the Identification of Transiting Extrasolar Planets*, ApJ, 627, 1011

Tomaney, A. B. & Crotts, A. P. S. 1996: *Expanding the Realm of Microlensing Surveys with Difference Image Photometry*, AJ, 112, 2872

Toomre, A. 1964: *On the gravitational stability of a disk of stars*, ApJ, 139, 1217

Torres, G., Konacki, M., Sasselov, D. D., & Jha, S. 2004: *Testing Blend Scenarios for Extrasolar Transiting Planet Candidates. I. OGLE-TR-33: A False Positive*, ApJ, 614, 979

Trilling, D. E., Benz, W., Guillot, T., Lunine, J. I., Hubbard, W. B., & Burrows, A. 1998: *Orbital Evolution and Migration of Giant Planets: Modeling Extrasolar Planets*, ApJ, 500, 428

Trilling, D. E., Lunine, J. I., & Benz, W. 2002: *Orbital migration and the frequency of giant planet formation*, A&A, 394, 241

Tsapras, Y., Street, R., Horne, K., Snodgrass, C., Dominik, M., Allan, A., Steele, I., Bramich, D. M., Saunders, E. S., Rattenbury, N., Mottram, C., et al. 2009: *RoboNet-II: Follow-up observations of microlensing events with a robotic network of telescopes*, Astronomische Nachrichten, 330, 4

Udalski, A. 2003: *The Optical Gravitational Lensing Experiment. Real Time Data Analysis Systems in the OGLE-III Survey*, Acta Astronomica, 53, 291

Udalski, A. 2007: *Transit Campaigns of the OGLE-III Survey*, in Astronomical Society of the Pacific Conference Series, Vol. 366, Transiting Extrapolar Planets Workshop, ed. C. Afonso, D. Weldrake, & T. Henning, 51—+

Udalski, A., Jaroszyński, M., Paczyński, B., Kubiak, M., Szymański, M. K., Soszyński, I., Pietrzyński, G., Ulaczyk, K., Szewczyk, O., Wyrzykowski, Ł., Christie, G. W., et al. 2005: *A Jovian-Mass Planet in Microlensing Event OGLE-2005-BLG-071*, ApJ, 628, L109

Udalski, A., Paczynski, B., Zebrun, K., Szymanski, M., Kubiak, M., Soszynski, I., Szewczyk, O., Wyrzykowski, L., & Pietrzynski, G. 2002a: *The Optical Gravitational Lensing Experiment. Search for Planetary and Low-Luminosity Object Transits in the Galactic Disk. Results of 2001 Campaign*, Acta Astronomica, 52, 1

Udalski, A., Pietrzynski, G., Szymanski, M., Kubiak, M., Zebrun, K., Soszynski, I., Szewczyk, O., & Wyrzykowski, L. 2003: *The Optical Gravitational Lensing Experiment. Additional Planetary and Low-Luminosity Object Transits from the OGLE 2001 and 2002 Observational Campaigns*, Acta Astronomica, 53, 133

Udalski, A., Szewczyk, O., Zebrun, K., Pietrzynski, G., Szymanski, M., Kubiak, M., Soszynski, I., & Wyrzykowski, L. 2002b: *The Optical Gravitational Lensing Experiment. Planetary and Low-Luminosity Object Transits in the Carina Fields of the Galactic Disk*, Acta Astronomica, 52, 317

Udalski, A., Szymanski, M. K., Kubiak, M., Pietrzynski, G., Soszynski, I., Zebrun, K., Szewczyk, O., & Wyrzykowski, L. 2004: *The Optical Gravitational Lensing Experiment. Planetary and Low-Luminosity Object Transits in the Fields of Galactic Disk. Results of the 2003 OGLE Observing Campaigns*, Acta Astronomica, 54, 313

Udalski, A., Zebrun, K., Szymanski, M., Kubiak, M., Soszynski, I., Szewczyk, O., Wyrzykowski, L., & Pietrzynski, G. 2002c: *The Optical Gravitational Lensing Experiment. Search for Planetary and Low- Luminosity Object Transits in the Galactic Disk. Results of 2001 Campaign – Supplement*, Acta Astronomica, 52, 115

Udem, T., Holzwarth, R., & Hänsch, T. W. 2002: *Optical frequency metrology*, Nat, 416, 233

Udry, S. & Santos, N. C. 2007: *Statistical Properties of Exoplanets*, ARA&A, 45, 397

Valenti, J. & Fischer, D. 2008: *Stellar Metallicity and Planet Formation*, in Astronomical Society of the Pacific Conference Series, Vol. 384, 14th Cambridge Workshop on Cool Stars, Stellar Systems, and the Sun, ed. G. van Belle, 292–+

Vidal-Madjar, A., Désert, J.-M., Lecavelier des Etangs, A., Hébrard, G., Ballester, G. E., Ehrenreich, D., Ferlet, R., McConnell, J. C., Mayor, M., & Parkinson, C. D. 2004: *Detection of Oxygen and Carbon in the Hydrodynamically Escaping Atmosphere of the Extrasolar Planet HD 209458b*, ApJ, 604, L69

Vidal-Madjar, A., Lecavelier des Etangs, A., Désert, J.-M., Ballester, G. E., Ferlet, R., Hébrard, G., & Mayor, M. 2003: *An extended upper atmosphere around the extrasolar planet HD209458b*, Nat, 422, 143

Ward, W. R. 1997: *Protoplanet Migration by Nebula Tides*, Icarus, 126, 261

Weidenschilling, S. J., Spaute, D., Davis, D. R., Marzari, F., & Ohtsuki, K. 1997: *Accretional Evolution of a Planetesimal Swarm*, Icarus, 128, 429

Werner, M. W., Roellig, T. L., Low, F. J., Rieke, G. H., Rieke, M., Hoffmann, W. F., Young, E., Houck, J. R., Brandl, B., Fazio, G. G., Hora, J. L., et al. 2004: *The Spitzer Space Telescope Mission*, ApJS, 154, 1

Winn, J. N. 2009: *Measuring accurate transit parameters*, in IAU Symposium, Vol. 253, IAU Symposium, 99–109

Winn, J. N., Johnson, J. A., Fabrycky, D., Howard, A. W., Marcy, G. W., Narita, N., Crossfield, I. J., Suto, Y., Turner, E. L., Esquerdo, G., & Holman, M. J. 2009: *On the Spin-Orbit Misalignment of the XO-3 Exoplanetary System*, ApJ, 700, 302

Winn, J. N., Johnson, J. A., Marcy, G. W., Butler, R. P., Vogt, S. S., Henry, G. W., Roussanova, A., Holman, M. J., Enya, K., Narita, N., Suto, Y., et al. 2006: *Measurement of the Spin-Orbit Alignment in the Exoplanetary System HD 189733*, ApJ, 653, L69

Winn, J. N., Johnson, J. A., Narita, N., Suto, Y., Turner, E. L., Fischer, D. A., Butler, R. P., Vogt, S. S., O'Donovan, F. T., & Gaudi, B. S. 2008: *The Prograde Orbit of Exoplanet TrES-2b*, ApJ, 682, 1283

Winn, J. N., Johnson, J. A., Peek, K. M. G., Marcy, G. W., Bakos, G. Á., Enya, K., Narita, N., Suto, Y., Turner, E. L., & Vogt, S. S. 2007: *Spin-Orbit Alignment for the Eccentric Exoplanet HD 147506b*, ApJ, 665, L167

Winn, J. N., Noyes, R. W., Holman, M. J., Charbonneau, D., Ohta, Y., Taruya, A., Suto, Y., Narita, N., Turner, E. L., Johnson, J. A., Marcy, G. W., et al. 2005: *Measurement of Spin-Orbit Alignment in an Extrasolar Planetary System*, ApJ, 631, 1215

Wolf, A. S., Laughlin, G., Henry, G. W., Fischer, D. A., Marcy, G., Butler, P., & Vogt, S. 2007: *A Determination of the Spin-Orbit Alignment of the Anomalously Dense Planet Orbiting HD 149026*, ApJ, 667, 549

Wolszczan, A. & Frail, D. A. 1992: *A planetary system around the millisecond pulsar PSR1257 + 12*, Nat, 355, 145

Yoo, J., DePoy, D. L., Gal-Yam, A., Gaudi, B. S., Gould, A., Han, C., Lipkin, Y., Maoz, D., Ofek, E. O., Park, B.-G., Pogge, R. W., et al. 2004: *OGLE-2003-BLG-262: Finite-Source Effects from a Point-Mass Lens*, ApJ, 603, 139

Young, A. T. 1967: *Photometric error analysis. VI. Confirmation of Reiger's theory of scintillation*, AJ, 72, 747

Young, A. T. 1993: *Scintillation noise in CCD photometry*, Observatory, 113, 41

Acknowledgments

Curriculum Vitae

Persönliche Daten

Name:	Johannes Manuel Koppenhöfer
Geburtsdatum:	10. August 1977
Geburtsort:	Bretten
Familienstand:	ledig
Anschrift:	Parkstr. 21, 82008 Unterhaching

Ausbildung

1984-1988	Grundschule Bretten-Büchig
1988-1997	Melanchthon-Gymnasium Bretten
1998-2001	Studium der Physik an der Technischen Hochschule Karlsruhe
2001-2005	Studium der Physik an der Ludwig-Maximilians-Universität München
2004-2005	Diplomarbeit an der Universitäts-Sternwarte München über "Suche nach Extra-Solaren Planeten: Spektroskopische Nachbeobachtungen, photometrische Transit-Suche und Simulationen"
2005	Diplom in Physik, LMU München
2005-2009	Promotion in Astronomie an der LMU München

Berufliche Tätigkeit

1997-1998	Zivildienst bei der Lebenshilfe e.V. in Bretten
2002-2003	Studentische Hilfskraft an der Universitäts-Sternwarte München